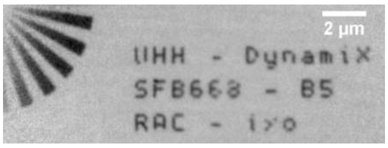

UNIVERSITÄT HAMBURG
FACHBEREICH PHYSIK

Time-resolved imaging of magnetic nanostructures in the visible and soft X-ray spectral range

Zeitaufgelöste Abbildung magnetischer Nanostrukturen im sichtbaren und weichen Röntgenspektralbereich

Dissertation
zur Erlangung des Doktorgrades
des Fachbereichs Physik
der Universität Hamburg

vorgelegt von

PHILIPP K. G. WESSELS

aus Lohne (Oldb.)

Hamburg
2014

Gutachter der Dissertation:	Prof. Dr. Markus Drescher Prof. Dr. Thomas Wilhein Prof. Dr. Hermann Dürr
Gutachter der Disputation:	Prof. Dr. Markus Drescher PD Dr. habil. Guido Meier
Datum der Disputation:	11.03.2014
Vorsitzender des Prüfungsausschusses:	PD Dr. habil. Michael Martins
Vorsitzende des Promotionsausschusses:	Prof. Dr. Daniela Pfannkuche
Leiter des Fachbereichs Physik:	Prof. Dr. Peter Hauschildt
Dekan der Fakultät für Mathematik, Informatik und Naturwissenschaften:	Prof. Dr. Heinrich Graener

Abstract

To unravel the nature of magnetism, an investigation at its fundamental length- and time-scales has to be tackled. Besides pure research interest of the processes occurring in nanoscopic magnetic systems in the femto- and picosecond range, advancing knowledge experiences promising applications toward faster non-volatile memory devices with increased data storage density. However, this exploration demands state-of-the-art experimental setups sensitive to detect the magnetization with superior spatial and temporal resolution. In this work two new instruments for time-resolved imaging of magnetic nanostructures have been set up:

A tabletop time-resolved scanning Kerr microscope (TR-SKM) capable of analyzing the dynamics of patterned magnetic media using the magneto-optic Kerr effect (MOKE) in combination with femtosecond laser pulses to carry out stroboscopic pump-probe experiments. With a novel pump approach utilizing a magnesium photocathode as electro-optical switch, the generation of intense, broadband electronic current pulses becomes possible for excitation of magnetic systems with the transported transient magnetic field. This enables jitter-free measurements on isolated spin-wave packets in permalloy ($\mathrm{Ni_{80}Fe_{20}}$) with a temporal resolution $< 30\,\mathrm{ps}$ and a spatial resolution $< 560\,\mathrm{nm}$. The spatially and temporally resolved data set permits a global analysis of the dynamic parameters defining the wave-packet. For the first time, a direct observation of backward volume modes with counterpropagating group and phase velocities in permalloy became possible.

For examinations requiring an increased spatial resolution, a mobile synchrotron radiation based full-field time-resolved magnetic transmission X-ray microscope (TR-MTXM) has been set up at the soft X-ray beamline P04 of the high-brilliance storage ring PETRA III at DESY with a temporal resolution $< 250\,\mathrm{ps}$ and a spatial resolution $< 65\,\mathrm{nm}$. The magnetization of a sample is accessible via the X-ray magnetic circular dichroism (XMCD). Experiments to stimulate magnetic permalloy nanostructures with synchronized femtosecond laser pulses as well as picosecond electronic current pulses of large amplitudes have been carried out. Vortex magnetization patterns were forced into a non-equilibrium state by aligning the majority of the magnetic moments into one direction and the evolution of the domain pattern destruction and recovery could be monitored in time. A reproducible recovery of the vortex pattern with stable chirality and polarity and unusually high vortex core velocities could be observed. Feasibility studies on non-reversible switching processes in need of an active reset stimulus in magnetic chains and arrays have been initiated.

Zusammenfassung

Um die Eigenschaften magnetischer Phänomene zu entschlüsseln, ist eine Beobachtung auf deren fundamentalen Längen- und Zeitskalen hilfreich. Neben rein wissenschaftlichen Interessen an nanoskaligen Magnetsystemen im Femto- und Pikosekunden-Bereich, versprechen tiefere Einblicke unter anderem Anwendungen hin zu schnelleren, nicht flüchtigen Speichermedien mit wachsender Datendichte. Allerdings verlangt diese Form der Beobachtung modernste Versuchsaufbauten, um die Magnetisierung einer Probe mit hoher räumlicher und zeitlicher Auflösung zu messen. Im Rahmen dieser Arbeit wurden zwei neue Instrumente zur zeitaufgelösten Abbildung magnetischer Nanostrukturen aufgebaut:

Ein kompaktes zeitauflösendes Raster-Kerr-Mikroskop (TR-SKM) für die Analyse der Dynamik strukturierter magnetischer Medien mittels des magnetooptischen Kerr-Effektes (MOKE) in Kombination mit Femtosekunden-Laserpulsen für stroboskopische Anrege-Abfrage Experimente. Eine neuartige Pumpquelle in Form eines elektrooptischen Schalters mittels einer Magnesium Fotokathode ermöglicht die Erzeugung intensiver, breitbandiger elektronischer Strompulse, um magnetische Systeme durch das transportierte dynamische Magnetfeld anzuregen. Dies ermöglicht jitterfreie Messungen an isolierten Spinwellenpaketen in Permalloy ($Ni_{80}Fe_{20}$) mit einer Zeitauflösung $< 30\,\mathrm{ps}$ und einer räumlichen Auflösung $< 560\,\mathrm{nm}$. Die orts- und zeitaufgelösten Daten lassen eine globale Analyse der dynamischen Parameter der Wellenpakete zu. Erstmals konnten Backward-Volume Moden mit einer entgegengesetzten Gruppen- und Phasengeschwindigkeit direkt in Permalloy nachgewiesen werden.

Für Versuche, die eine erhöhte Ortsauflösung benötigen, wurde zusätzlich ein mobiles synchrotronstrahlungsbasiertes Vollfeld-Röntgentransmissionsmikroskop mit Zeitauflösung (TR-MTXM) an der P04 Strahlführung der hoch-brillanten Speicherringquelle PETRA III bei DESY aufgebaut, die monochromatische weiche Röntgenstrahlung generiert. Dabei lässt sich die Magnetisierung einer Probe über den zirkularen magnetischen Röntgendichroismus (XMCD) mit einer Zeitauflösung $< 250\,\mathrm{ps}$ und einer Ortsauflösung $< 65\,\mathrm{nm}$ abbilden. Experimente zur Anregung von magnetischen Permalloy-Nanostrukturen mit einem synchronisierten Femtosekunden-Lasersystem und einem elektronischen Pikosekundenpulser mit hoher Feldstärke wurden durchgeführt. Magnetische Wirbelstrukturen konnten durch homogene Ausrichtung des Großteils der magnetischen Momente in einen Nichtgleichgewichtszustand überführt werden und sowohl bei Ausrichtung als auch Relaxation zeitlich beobachtet werden. Dabei war es möglich eine reproduzierbare Regeneration der Wirbelstruktur mit stabiler Chiralität und Polarität zu erreichen sowie ungewöhnlich hohe Kerngeschwindigkeiten zu beobachten. Zudem wurden Machbarkeitsstudien zu nicht-reversiblen Schaltvorgängen in magnetischen Ketten und Feldern initiiert, die einen aktiven Rückschaltimpuls benötigen.

Contents

Chapter 1

Introduction

Throughout history magnetism has fascinated mankind not only in a pure scientific background but also in its great potential of applications easing everyday life. The Greek philosopher THALES OF MILETUS already described the existence of a so called *lodestone* attracting iron pieces in the 6th century BC. Lodestones are naturally-occurring magnets of the mineral magnetite ($\mathrm{Fe_3O_4}$). One of the first applications was the alignment of small magnetized pieces in earth's magnetic field used in a compass for navigation. Many other applications followed and nowadays we are surrounded by magnetism. For instance, cash and credit cards as well as key cards use a magnetic strip for identification. Electric motors, generators and transformers rely on strong permanent magnets and fields produced by electromagnets and contribute in the transport sector and in electric power generation. Strong fields generated by superconducting coils are found in particle accelerators as bending and focusing elements as well as in medicine in magnetic resonance tomography (MRT) for detailed imaging of inner body parts.

This work deals with the dynamics of small magnetic structures ranging from length scales of a few micrometers ($1\,\mu\mathrm{m} = 10^{-6}\,\mathrm{m}$) down to nanometers ($1\,\mathrm{nm} = 10^{-9}\,\mathrm{m}$). Today, nanomagnets can be found in many biomedical applications [17, 159] and for example work as vessels for targeted drug delivery [10, 47, 193] and release [23] improving efficacy while minimizing side effects by controlled concentration of medication at the intended site of action. Also, a remote control of behavior and signal transport in cells [48, 141] and neurons [92] is possible and even the apoptosis (programmed cell death) can be triggered by applying external magnetic fields to the nanoparticles *in vitro* and *in vivo* [33]. This might lead to new concepts fighting cancer and yet the selective destruction of tumor cells has been reported [38, 49] even with small permalloy (a nickel-iron alloy composed of $\mathrm{Ni_{80}Fe_{20}}$) elements in a magnetic vortex state similar to the ones investigated in this work [113].

Likewise, magnetic nanostructures are routinely used in data storage devices such as hard-disk drives (HDDs). The demand for higher storage densities and faster access time in memory technology has to be based on primal knowledge of magnetization processes happening at time scales from picoseconds ($1\,\mathrm{ps} = 10^{-12}\,\mathrm{s}$) to femtoseconds ($1\,\mathrm{fs} = 10^{-15}\,\mathrm{s}$) and length scales of nanometers to single atoms at once. Advanced data storage devices rely on a high bit density[1] of nanomagnetic information units close to each other facing the superparamagnetic limit where the thermal energy is sufficient to destroy the stored information. Concepts like heat-assisted magnetic recording (HAMR)

---

[1] In 2013 hard disk drives with an areal density approaching $750\,\mathrm{Gbit/in^2}$ are commercially available.

are around to overcome this limit by using more stable recording media, however, writing those materials becomes harder and they have to be heated by a laser during the storage process. Another approach is the development of bit-patterned media (BPM) [174, 176] and information storage in lithographically prepared isolated single domain particles instead of grains in a continuous medium. Both, HAMR and BPM are not yet commercially available and therefore, the in this work investigated magnetic stability of nanostructures [99] and the behavior of arrays under read and write processes [2] are important research topics with direct applications. Magnetic nanodots [36] and storage units consisting only of a few atoms [139] as well as recently demonstrated read and write processes on magnetic skyrmions [171] represent only a few examples of the activity in the scientific community concerning this field. New memory techniques [160, 37] toward the replacement of random-access memory (RAM) elements in todays computers by non-volatile magnetoresistive RAM (MRAM) may lead to a universal memory concept [169].

Not only the size of storage devices but also the speed of data manipulation and access is of importance. There seemed to be a fundamental speed limit for the switching of magnetic structures by field-induced precessional motion of the magnetization because below pulse durations of a few picoseconds the switching becomes chaotic and was believed to be impossible to handle in a controlled manner [197, 12]. However, observations since 1996 on the feasibility to at least destroy the magnetization [15, 19, 186, 107] or manipulate the spin-system and domain walls [162] on a femtosecond time scale pushed this fundamental limit down by some orders of magnitude. The theoretical foundation of this effect was controversially debated in literature and eventually lead to an explanation by superdiffusive spin currents [13]. Later, advanced concepts of non-thermal magnetization control [114] and deterministic recording processes solely induced by the light of circular polarized femtosecond laser pulses [187] were demonstrated. Moreover, in small ferrimagnetic structures a single ultrashort heat stimulus induced by a linear polarized laser pulse is sufficient to switch the magnetization [156, 168]. For a review of the physics involved in ultrafast manipulation of magnetism, the reader is referred to [115, 18].

Another technological application of small magnetic devices is the creation of so-called spintronic devices [218, 27] as logical units to replace nowadays electronic circuits relying on the motion of charged particles by magnetic circuits. Basic logical elements like NOT gates [5], atomic OR elements [110] and shift registers [84, 160, 37, 5] have been reported in the literature. This work also deals with the investigation of spin-waves usable for magnetic transport of information between devices or for logic operations exclusively [88, 120, 112, 111, 98].

From a scientific point of view the ultimate goal in nanoscale magnetic research would be the combination of high spatial resolution with high temporal resolution in a single experiment to study magnetism at its fundamental length- and time-scales being able to create actual movies of the magnetization dynamics. The ideal experiment might look like a combination of atomic spatial resolution found in scanning probe microscopy with the temporal resolution available at modern pulsed light sources such as femtosecond laser systems, attosecond ($1\,\mathrm{as} = 10^{-18}\,\mathrm{s}$) high harmonic generation (HHG) experiments or intense free-electron laser (FEL) sources. In order to contribute to the research toward this goal, two new time-resolved imaging experiments have been set up:

- A laboratory laser-based time-resolved scanning Kerr microscope (TR-SKM) for larger (micrometer) but fast (femtosecond) systems being able to capture the dy-

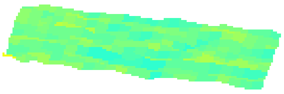

namics of magnetic structures with a time-resolution fundamentally limited by the laser pulse duration and a spatial resolution dominated by the wavelength of the laser pulses. This experiment relies on the magneto-optic Kerr effect (MOKE) in combination with a femtosecond laser for stroboscopic measurements of the time evolution of the magnetization and uses a novel in-house developed photoswitch to excite the magnetic system. The setup enables the observation of electron spin precession and spin-waves offering direct access to the important high frequency parameters of magnetic materials. Since the indirect discovery of spin-waves [24], techniques evolved allowing for direct imaging of the wave [41, 66] and the observation of effects like spin-wave interference [124], diffraction [143], tunneling [43] and even Bose-Einstein condensation (BEC) of magnons [42]. The constructed instrument is able to create and detect spin-wave packets similar to [161, 137] and the unique pump pulse parameters allowed a direct observation of backward volume modes with counterpropagating phase and group velocities in confined permalloy films for the first time. The here established creation of synchronized, broadband, short, defined and intense magnetic pump pulses is challenging but indispensable when aiming for the measurement of undisturbed isolated spin-wave packets.

- A synchrotron-based mobile and flexible full-field time-resolved magnetic transmission X-ray microscope (TR-MTXM) for slower (picoseconds) but smaller (nanometer) systems offering a time-resolution down to the synchrotron pulse duration at a spatial resolution limited by the X-ray optics. This experiment conducted at the soft X-ray beamline P04 at the high-brilliance synchrotron-radiation facility PETRA III is able to investigate the magnetization dynamics of previously excited nanoscale objects by X-ray magnetic circular dichroism (XMCD) spectromicroscopy [180, 191]. When it comes to analyzing magnetic information in real space with a sufficient spatial resolution, X-ray microscopy is a powerful tool [62, 63, 64, 26, 216] and with this setup the dynamics of artificially created single domain states in small permalloy structures could be observed. The analysis unrevealed new aspects in the dynamic characteristics of domain pattern destruction and recovery in magnetic vortices exposed to strong magnetic field pulses. The vortices represent a multibit memory cell [201, 199, 101, 205, 105] and allow information storage in four distinguishable magnetization configurations if a controlled manipulation and readout can be achieved. This work demonstrates a reproducible recovery into a defined vortex state and unexpected high vortex core velocities exceeding a reported threshold that should change the magnetization configuration [133, 83, 211]. Again, the availability of short and intense magnetic pump pulses is of key importance for all measurements together with a design of the newly constructed mobile X-ray microscopy endstation that allows for an easy set up and alignment procedure.

Combining both experiments shall give comprehensive insight into the dynamics of coupled nanomagnetic systems. This work provides feasibility studies for systematic investigations of the switching behavior in a proposed experiment sketched in figure 1.1. Here, the individual elements are artificially prepared in a way that they may interact by means of their stray field. A fraction of the initially aligned array is switched by a short and defined magnetic field- or laser-pulse. The adjacent bits now switch subsequently due to the coupling and a wave propagates through the array. One frame of the movie

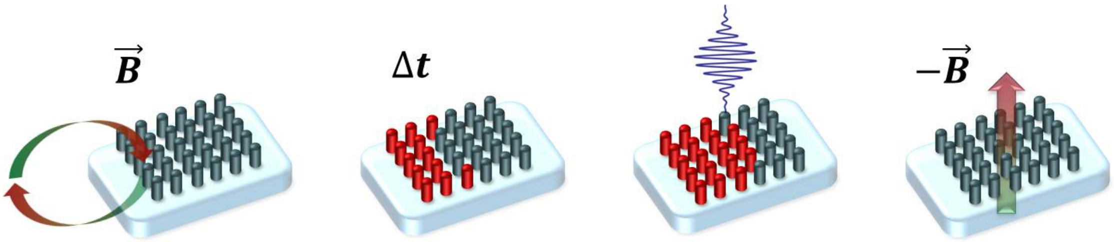

Figure 1.1: Pump-probe and reset sequence of a nanomagnetic array for the exploration of non-reversible switching processes. After excitation out of a defined initial state by a short and confined magnetic pump pulse the system evolves for a certain time Δt due to coupling via stray fields between the nanomagnets. Subsequently, the magnetic state is captured by a short probe pulse followed by a reset field forcing the whole array back to its initial state so that a new pump-probe and reset cycle with different Δt can begin.

capturing this dynamics can be recorded by taking a snapshot of the magnetization at a defined time-delay Δt after the excitation. In order to capture the next frame, the whole array is reset to its initial state by a magnetic field pulse and now the experiment starts over and over again recording other snapshots at different time-delays. This pump-probe approach is widely used in time-resolved (magnetic) imaging of fast processes and caught broad attention when the Nobel prize for chemistry was rewarded to AHMED ZEWAIL in 1999 honoring the development of femtochemistry [225]. Up to now mostly magnetic systems automatically relaxing to their initial ground state have been explored. Imaging of a non-reversible process with a final state being not identical with the initial one needs an active reset at the end of each cycle (figure 1.1) and this work demonstrates techniques toward non-reversible pump-probe imaging.

Understanding the involved interactions is of fundamental significance for modern storage technology and for future spintronic concepts if one thinks of a defined transport of information through a magnetic chain or recording in the aforementioned bit-patterned media. The complex dynamic phenomena of nanomagnetism need the insight gained with several experimental techniques and expertises in order to disentangle the physics and obtain a consistent theory of what is really happening at ultra-small length and ultra-short time scales. To name a few additional experimental approaches, the investigation of magnetism with HHG sources [175, 203, 198, 127], free-electron lasers [53, 78] or terahertz spectroscopy [106] is emerging leading to promising new research projects.

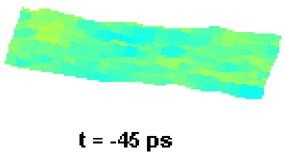

Chapter 2

Theory

The first chapter is intended to summarize the established theoretical background needed to cover most topics embedded in this work. It starts with explaining the origin and features of magnetism relevant to this work since the physical insight into the dynamics of magnetic nanostructures is the main goal. Special techniques are necessary to explore the world of small and fast magnetic structures and the reader is provided with background knowledge on the utilized magnetic contrast mechanisms and with basics on X-ray optics, photocathodes and coplanar waveguides needed to image and excite the samples. However, the calculation of specific parameters of the investigated samples goes along with the compilation of abstract common knowledge to provide examples on the one hand and to demonstrate anticipated characteristics for later comparison with the measurements.

2.1 Magnetism

Since the discovery of the magnetic properties of the *lodestone* mentioned in the introduction, the knowledge of magnetic phenomena improved massively. Figure 2.1 presents a rough overview of these phenomena sorted into their characteristic length- and timescales where the lodestone is represented by a macroscopic magnet in the top left.

A deeper understanding of the nature of magnetism was provided by the electrodynamic field theory of James Clerk Maxwell [145] describing electric and magnetic fields in an elegant way (see equations A.1 - A.4 in appendix A.1) as one unified force of the four fundamental interactions in physics. The Maxwell equations already are invariant under Lorentz transformations and thus consistent with the special relativity theory of Albert Einstein [52] stating that all physical laws have to be the same in every inertial system which means that the electric and magnetic field are just two representations of the same phenomenon.

According to Maxwell's equations the origin of magnetism is an electric current generated by moving charges. The question arises why an ordinary permanent magnet is able to produce a magnetic field without the obvious involvement of currents? In fact, currents are present and can be found by looking close enough into the structure of matter. Electrons with an electric charge $q = -e$ and mass m_e orbiting around atomic nuclei with an orbital momentum $\vec{l}$ resemble an electric current and thus lead to a magnetic dipole moment

$$\vec{m} = -\gamma \cdot \vec{l} \qquad \text{with} \qquad \gamma = g\frac{e}{2m_e}. \tag{2.1}$$

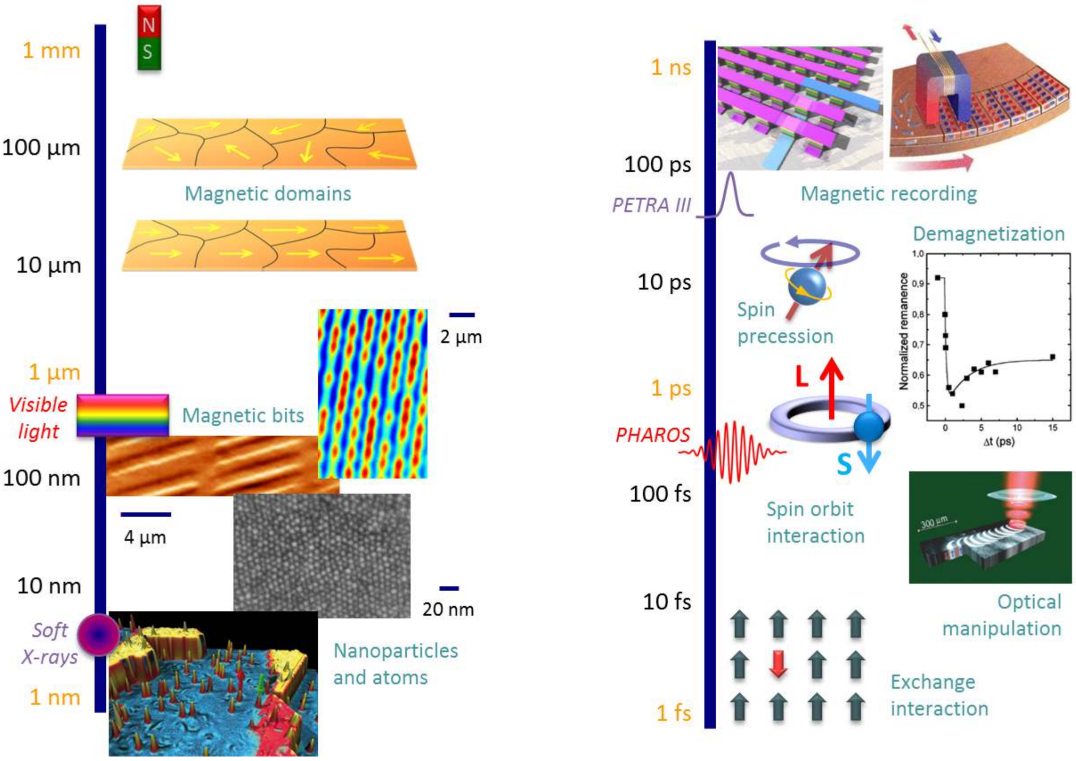

Figure 2.1: Magnetism in space and time: Fundamental magnetic systems and interactions on their natural length- and time-scales. This figure contains material from [103, 182, 200, 20, 140, 15, 187] [a].

Here, γ is called the gyromagnetic ratio with the Landé factor g close to unity relating the orbital moment to the magnetic moment. Additionally, quantum mechanics tells us that every electron carries a tiny magnetic moment itself originating from the spin $\vec{s}$ of the electron. However, due to the Heisenberg uncertainty principle [86], only one component along a quantization axis (here arbitrarily called z axis) of the angular momentum and spin vector is observable. To obtain the total magnetic moment originating from angular and spin momentum vector, a quantum mechanical approach has to be chosen. This means, $\vec{l}$ and $\vec{s}$ have to be replaced by the eigenvalues of the observable components of the angular and spin momentum operators $\langle \vec{l}_z \rangle$ and $\langle \vec{s}_z \rangle$ leading to

$$\langle \vec{m}_z \rangle = -\frac{\mu_B}{\hbar}\left[g_l \langle \vec{l}_z \rangle + g_s \langle \vec{s}_z \rangle \right] \qquad \text{with} \qquad \mu_B = \frac{e\hbar}{2m_e} \tag{2.2}$$

called the Bohr magneton. Additionally, the Landé factor $g_s \approx 2$ relating the magnetic moment to the electron spin momentum is approximately twice as large as the orbital momentum factor $g_l = 1$. The Dirac equation predicts an exact factor of $g_s = 2$. Small corrections to this value can accurately be calculated by quantum electrodynamics (QED). For an electron spin momentum with $g_s \approx 2$ the gyromagnetic ratio of equation 2.1 reads $\gamma \approx 176\,\mathrm{GHz/T}$.

Depending on how the different magnetic moments of the electrons add up or cancel

---

[a] This figure contains material reprinted with permission from the American Physical Society. For details and links to the articles see references [15, 187]

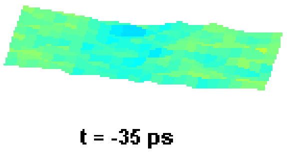

out in an atom, a net atomic magnetic moment may emerge. In condensed matter consisting of a lattice of many atoms, these magnetic moments again may add up or cancel out concerning the interactions between them. One of the strongest coupling is the exchange interaction resulting from the Coulomb repulsion force and the Pauli exclusion principle stating that two identical fermions[1] must not occupy the same quantum state at the same time and place. For the magnetic elements iron (Fe), cobalt (Co) and nickel (Ni) used in this thesis, the exchange interaction leads to a parallel alignment of the magnetic moments. A macroscopic net magnetic dipole moment density

$$\vec{M} = \frac{1}{V} \cdot \sum_n \vec{m}_n \tag{2.3}$$

called magnetization in a finite volume V is the result that generates a field itself which is called demagnetization field $\vec{H}_d$ inside the medium and stray field $\vec{H}_s$ outside the medium. The origin of those fields can be described by hypothetic magnetic surface charges[2] representing the sources and sinks of a magnetic field at the surface of a magnetized material and are a useful concept of understanding some magnetic phenomena as we see later. The relation between the total magnetic $\vec{B}$ field composed of the $\vec{H}$ field and the magnetization $\vec{M}$ is given by

$$\vec{B} = \mu_0 \left(\vec{H} + \vec{M} \right) \tag{2.4}$$

and illustrated in figure 2.2. Note that at a boundary between magnetic material and air in figure 2.2 only the normal component of the $\vec{B}$ field is continuous.

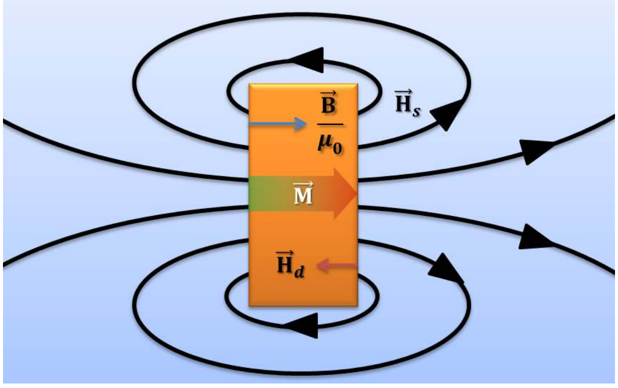

Figure 2.2: Ferromagnetic material with magnetization $\vec{M}$ generating a stray field $\vec{H}_s$ outside and a demagnetization field $\vec{H}_d$ inside the medium. The relation between $\vec{M}$, $\vec{H}$ and $\vec{B}$ according to equation 2.4 is illustrated.

In an external magnetic field $\vec{H}_{\text{ext}}$ the magnetization $\vec{M}$ can be realigned. The linear response to the external field, however, might not be isotropic and is described by the magnetic susceptibility $\overset{\leftrightarrow}{\chi}_m$ in the following way:

$$\vec{M} = \overset{\leftrightarrow}{\chi}_m \vec{H} \qquad \Rightarrow \qquad \vec{B} = \mu_0 \underbrace{(\mathbb{1} + \overset{\leftrightarrow}{\chi}_m)}_{\overset{\leftrightarrow}{\mu}_r} \vec{H}. \tag{2.5}$$

Materials that align their magnetic moments parallel to the field direction are called paramagnetic ($\chi_m > 0$) while materials generating a magnetization anti-parallel to an

---

[1] Fermions are particles with a half integer spin or, equivalently, with an antisymmetric wave-function under exchange of identical particle pairs.

[2] In reality isolated magnetic charges do not exist according to the Maxwell equation $\vec{\nabla} \cdot \vec{B} = 0$ and have not yet been observed experimentally.

external field are called diamagnetic ($\chi_m < 0$). If all dipole moments are completely aligned, the material has reached its saturation magnetization M_s.

2.1.1 Anisotropies and demagnetization field

The alignment of the magnetization might be preferred along one direction which is often called easy axis while the alignment along the opposite hard axis requires higher external fields. This phenomenon is called magnetic anisotropy and originates from several sources like e. g. the crystalline structure of condensed matter leading to the preferred alignment along one crystal axis. Besides this magnetocrystalline anisotropy there is also the shape anisotropy favoring certain directions due to the geometry of the magnetic material.

This work deals with the investigation of the magnetic properties of thin magnetic permalloy ($Ni_{80}Fe_{20}$) films or thin cobalt and platinum (Co/Pt) multilayers. Permalloy has a negligible magnetocrystalline anisotropy [219] and is dominated by the shape anisotropy with an easy axis in the sample plane. Contrary, the magnetocrystalline anisotropy in Co/Pt multilayers is tailored in a way that it dominates and the easy axis points out of the sample plane (see also figure 2.3).

Figure 2.3: A thin film of permalloy is dominated by the shape anisotropy aligning the magnetization inside the sample plane. A stack of Co/Pt multilayers dominated by the magnetocrystalline anisotropy aligns the magnetic moments of cobalt out of the sample plane (inspired by [191]).

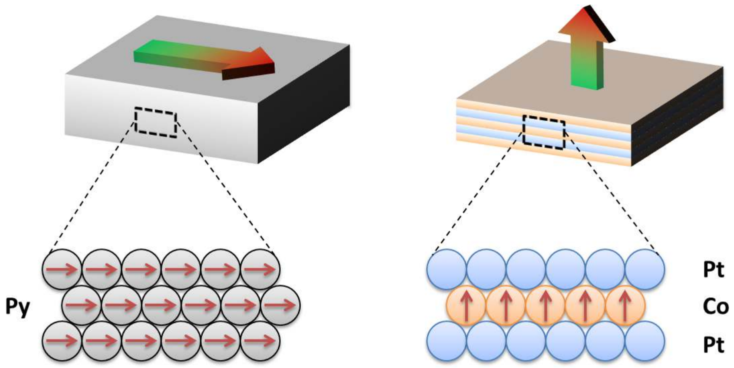

The origin of the shape anisotropy is understood by considering the demagnetization field. This explanation is inspired by the book of Stöhr and Siegmann [191] and based on the fact that the properties of thin cavities in a magnetic material are equivalent to the behavior of the inverse structure, namely thin magnetic films. One only has to interchange the stray field $\vec{H}_s$ with the demagnetization field $\vec{H}_d$ with an opposing sign.

Figure 2.4: Magnetic thin film with two cavities along and perpendicular to the magnetization direction of $\vec{M}$ and corresponding magnetic surface charges (+ and −). The image also shows the integration path $d\vec{l}$ as well as the closed surface S with surface normals $d\vec{s}$ for calculation of the demagnetization field $\vec{H}_d$ and stray field $\vec{H}_s$ (inspired by [191]).

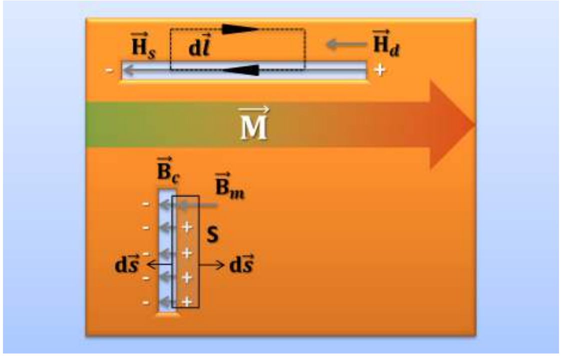

Consider a magnetic material with a cavity cut away in the direction of the magnetization with an integration path depicted in figure 2.4. Because of the absence of free

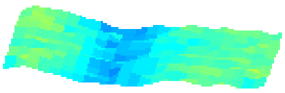

currents the line integral in Stokes' theorem has to vanish according to Ampere's law:

$$\oint \vec{H}\,\mathrm{d}\vec{l} = \int (\vec{H}_s - \vec{H}_d)\,\mathrm{d}\vec{l} = 0 \qquad \Rightarrow \qquad \vec{H}_s = \vec{H}_d. \tag{2.6}$$

The stray field $\vec{H}_s$ inside the cavity has to be quite small because the surface charges generating the field are far away from each other. So for a thin film magnetized in the sample plane, the demagnetization field $\vec{H}_d$ is small as well. Now, consider a cavity perpendicular to the magnetization direction and Gauss' theorem integrating the field B_c inside the cavity and B_m inside the material over the closed surface S indicated in figure 2.4. Together with $\vec{\nabla} \cdot \vec{B} = 0$ (absence of magnetic monopoles) we get

$$\iint_S (\vec{B}_c - \vec{B}_m)\,\mathrm{d}\vec{s} = 0 \qquad \Rightarrow \qquad \vec{B}_c = \vec{B}_m. \tag{2.7}$$

Since here the normal component of the magnetic induction $\vec{B}$ is continuous on the boundaries, the stray field inside the cavity reads according to equation 2.4 $\vec{H}_s = \vec{M}$ and is large due to the small distance between the virtual magnetic surface charges. Thus, a thin film magnetized perpendicular to the surface plane would experience a huge demagnetization field $\vec{H}_d = -\vec{M}$. For a spherical hollow inside a magnetized material the stray field computes to $H_s = \frac{1}{3}M$ and in general the demagnetization field for an arbitrary shape can be expressed like

$$\vec{H}_d = -\overset{\leftrightarrow}{N}(\vec{r}) \cdot \vec{M} \tag{2.8}$$

with N as the demagnetization factor that is a tensor for crystalline materials with possible spatial dependence on the position vector $\vec{r}$ as well. The trace of the demagnetization tensor has to fulfill the condition [179]

$$\mathrm{Tr}\left(\overset{\leftrightarrow}{N}\right) = \sum_i N_{ii} = N_{xx} + N_{yy} + N_{zz} = 1. \tag{2.9}$$

Analogously to the energy of a magnetic dipole moment in an external field being described by the scalar product between the two vectors $E = -\vec{B} \cdot \vec{m}$, the energy of a material with magnetization $\vec{M}$ in its own stray field $\vec{H}_s$ is given by

$$E_d = -\frac{\mu_0}{2} \int_V \vec{M}\vec{H}_s\,\mathrm{d}V \tag{2.10}$$

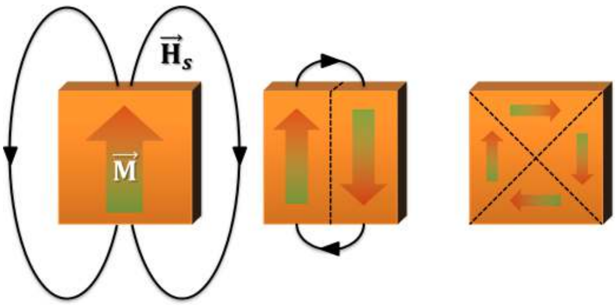

Figure 2.5: A uniform alignment of the magnetization $\vec{M}$ inside a ferromagnetic material results in a large stray field $\vec{H}_s$ that consumes a lot of energy according to equation 2.10 (left image). A division into two domains reduces the stray field (center image) and a flux closure structure of four domains minimizes the magnetostatic energy of the given geometry (right image).

and called demagnetization energy E_d.

In ferromagnetic materials the magnetization aligned by the exchange interaction will decay into zones with constant magnetization pointing in different directions called magnetic domains (figure 2.5). A uniform alignment would result in a large stray field H_s outside the material connected to the energy E_d of the configuration. The decay into multiple domains minimizes this energy because the outside stray field now only has to extend from one domain to another at the material boundaries. The domain structure in general depends on the external field and also on the anisotropies of the material. The domain size of a ferromagnetic material with saturation magnetization M_s and exchange constant A is given by the exchange length

$$l_{\mathrm{ex}} = \sqrt{\frac{2A}{\mu_0 M_s^2}} \tag{2.11}$$

because within this length the magnetization is dominated by exchange interaction and does not vary significantly. For permalloy the exchange length measures $l_{\mathrm{ex}} \approx 5\,\mathrm{nm}$ using its exchange constant $A = 13 \cdot 10^{-12}\,\mathrm{J/m}$ and saturation magnetization $M_s = 860\,\mathrm{kA/m}$.

2.1.2 Dynamics of magnetism

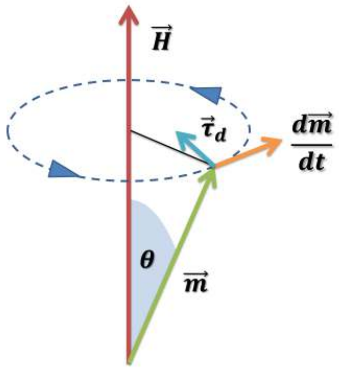

Figure 2.6: Precessional motion of a magnetic moment $\vec{m}$ around a magnetic field vector $\vec{H}$ driven by the torque $\frac{\mathrm{d}\vec{m}}{\mathrm{d}t}$. When damping is present an additional torque $\vec{\tau}_d$ pulls the magnetization into the direction of the field vector.

The energy of a magnetic dipole $\vec{m}$ in an external field $\vec{B}$ is given by $E = -\vec{B} \cdot \vec{m}$. In order to minimize this energy, the dipole experiences a torque $\vec{\tau} = \mu_0 \left[\vec{m} \times \vec{H}\right]$ analogously to a mechanical torque. The dynamics of this motion is described by

$$\frac{\mathrm{d}\vec{l}}{\mathrm{d}t} = \vec{\tau} \qquad \Rightarrow \qquad \frac{\mathrm{d}\vec{m}}{\mathrm{d}t} = -\gamma \cdot \mu_0 \left[\vec{m} \times \vec{H}\right] \tag{2.12}$$

and leads to Larmor precession with the angular frequency $\omega = \gamma \cdot \mu_0 |\vec{H}|$. This equation is only valid if no damping occurs. For dissipative systems a damping term in form of $\vec{\tau}_d = c \left[\vec{m} \times \frac{\mathrm{d}\vec{m}}{\mathrm{d}t}\right]$ with a damping coefficient c has to be introduced into equation 2.12. This leads to the Landau-Lifshitz-Gilbert (LLG) equation [129, 73, 74]

$$\frac{\mathrm{d}\vec{m}}{\mathrm{d}t} = -\gamma\mu_0 \left[\vec{m} \times \vec{H}\right] + \frac{\alpha}{|\vec{m}|} \left[\vec{m} \times \frac{\mathrm{d}\vec{m}}{\mathrm{d}t}\right] \tag{2.13}$$

$$\Rightarrow \left(1 + \alpha^2\right) \frac{\mathrm{d}\vec{m}}{\mathrm{d}t} = -\gamma\mu_0 \left[\vec{m} \times \vec{H}\right] - \frac{\gamma\alpha\mu_0}{|\vec{m}|} \left[\vec{m} \times \left(\vec{m} \times \vec{H}\right)\right] \tag{2.14}$$

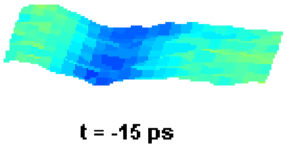

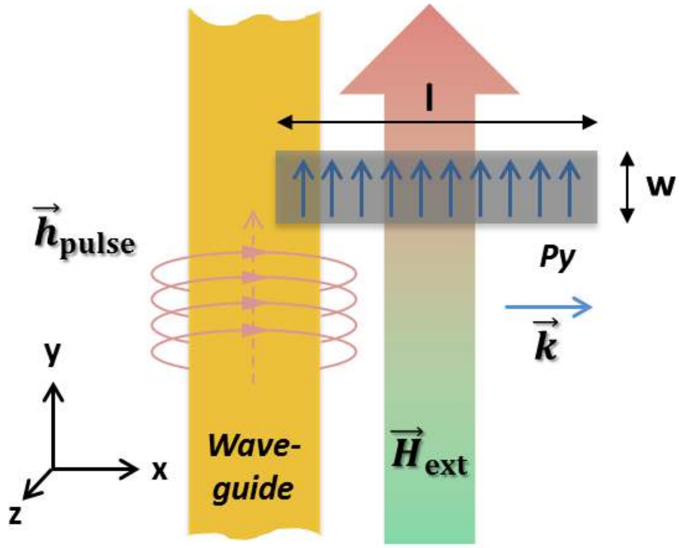

Figure 2.7: Schematic representation of the Damon-Eshbach spin-wave sample. A permalloy slab of width w, length l and thickness t magnetized in y direction by an external bias field $\vec{H}_\text{ext}$ is positioned with a certain overlap to the conductor of an electric waveguide. The system is pumped by a short current pulse generating a pulsed magnetic field $\vec{h}_\text{pulse}$ around the waveguide conductor.

with the phenomenological dimensionless damping parameter α that has a value of $\alpha = 0.008$ for permalloy [94]. Note that equation 2.13 can exactly be transformed into equation 2.14 by inserting $\frac{\mathrm{d}\vec{m}}{\mathrm{d}t}$ and applying vector algebra. Furthermore, the term $\left(1+\alpha^2\right)\frac{\mathrm{d}\vec{m}}{\mathrm{d}t}$ can be replaced by $\frac{\mathrm{d}\vec{m}}{\mathrm{d}t}$ to good approximation for small values of α.

The magnetic dipole moment $\vec{m}$ in equation 2.13 is replaceable by the magnetization $\vec{M} = \vec{m}_t/V$ when all elementary dipole moments coherently act as one big dipole moment $\vec{m}_t$. This simplification is called macrospin model. The LLG equation is the foundation for micromagnetic simulations predicting the dynamic behavior of extended systems by solving the LLG equation discretely on a grid and transferring the corresponding interactions between the grid cells. In order to obtain reasonable results, the grid size has to be smaller than the exchange length l_ex given by equation 2.11.

2.1.3 Spin-waves

If in a magnetized continuous medium the spin precession is inhomogeneously excited, the gyration of one magnetic moment may couple to adjacent magnetic moments. This leads to the emission of spin-waves also called magnons propagating through the medium. The coupling is mediated by exchange interaction at small wavelength or dipolar interactions at wavelength larger than the lattice constant. In this work the dynamics of spin-wave packets in thin rectangular films is investigated by exciting a fraction of the magnetic film with a magnetic field pulse and probing the magnetization spatially and temporally resolved in a pump-probe approach (figure 2.7). The introduction to the framework presented in this section is inspired by [119, 142, 123, 89, 90].

For dipolar spin-wave modes the description was first performed by Walker for spheroids [210] and by Damon and Eshbach for thin films [39] distinguishing between magnetostatic surface waves (MSSW) and backward volume magnetostatic waves (BVMSW). In the MSSW modes also called Damon-Eshbach modes, the magnetization of the sample is perpendicular to the propagation direction of the spin-wave. The amplitude of those modes decays exponentially with increasing distance from the surface of the film and the wave-vector of the MSSW modes only points into one particular direction. The group-velocity of MSSW modes is always positive. The BVMSW modes or backward volume modes experience a wave-vector parallel to the magnetization of the sample and can also exist beyond the surface. For small wave-vectors the group velocity of these modes is negative.

Ferromagnetic resonance

As we have seen above while deriving the LLG equation, the precession frequency of a magnetic moment $\vec{m}$ in an external field $\vec{H}_{\text{ext}}$ is given by $\omega = \gamma \cdot \mu_0 |\vec{H}_{\text{ext}}|$. Generally, in a medium with a magnetization $\vec{M}$ not only the external field has to be taken into account but also the demagnetization field $\vec{H}_d$. Here, we assume a slab magnetized in y-direction with the saturation magnetization ($M_y = M_s$) by an external field $\vec{H}_{\text{ext}}$. The slab is excited by a dynamic magnetic field (in this work a field pulse) $\vec{h}(t)$ and we are interested in the time dependent behavior of the magnetization $\vec{M}(t)$ and the resonance frequency f_r of the spin-precession (see also figure 2.7).

The magnetic field generated by the current in the waveguide has only components in x and z direction and thus external field and magnetization are given by

$$\vec{H}(t) = \begin{pmatrix} h_x(t) \\ H_{\text{ext}} \\ h_z(t) \end{pmatrix}, \qquad \vec{M}(t) = \begin{pmatrix} m_x(t) \\ M_s \\ m_z(t) \end{pmatrix}. \tag{2.15}$$

The total or effective field $\vec{H}_{\text{eff}}(t)$ now consist of the external fields combined in $\vec{H}(t)$ and the demagnetization field $\vec{H}_d(t)$ inside the medium according to equation 2.8. Assuming a diagonal demagnetization tensor $\overset{\leftrightarrow}{N}$ with diagonal elements $N_{ii} = N_i$ we obtain

$$\vec{H}_{\text{eff}}(t) = \vec{H}(t) + \vec{H}_d(t) = \vec{H}(t) - \overset{\leftrightarrow}{N} \cdot \vec{M}(t) = \begin{pmatrix} h_x(t) - N_x m_x(t) \\ H_{\text{ext}} - N_y M_s \\ h_z(t) - N_z m_z(t) \end{pmatrix}. \tag{2.16}$$

Inserting 2.15 and 2.16 into the Landau-Lifshitz-Gilbert equation 2.13 together with a harmonic oscillation ansatz $m_i(t) = m_i \cdot \mathrm{e}^{i(\omega t + \varphi)}$ leads to

$$\underbrace{\begin{pmatrix} \gamma\mu_0 \left[H_{\text{ext}} + M_s(N_x - N_y)\right] + i\alpha\omega & i\omega \\ -i\omega & \gamma\mu_0 \left[H_{\text{ext}} + M_s(N_z - N_y)\right] + i\alpha\omega \end{pmatrix}}_{\overset{\leftrightarrow}{X}} \cdot \begin{pmatrix} m_x(t) \\ m_z(t) \end{pmatrix}$$

$$= \gamma\mu_0 M_s \begin{pmatrix} h_x(t) \\ h_z(t) \end{pmatrix}. \tag{2.17}$$

This equation holds non trivial solutions if the determinant of the matrix

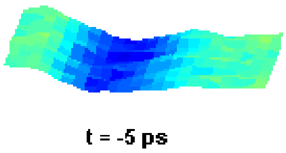

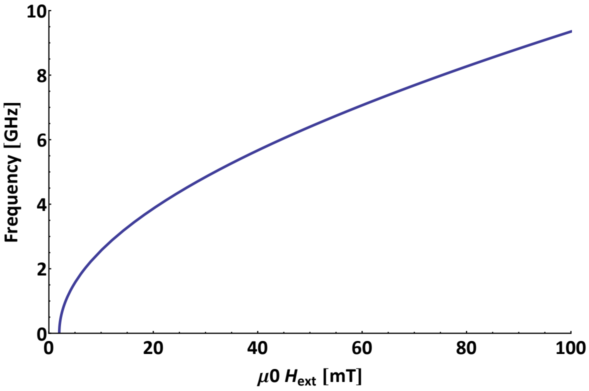

Figure 2.8: Ferromagnetic resonance (FMR) relating the resonant oscillation frequency f_r to an external field $\mu_0 H_{\text{ext}}$ for a permalloy slab with $N_x = 0$, $N_y = 0.002$ and $N_z = 0.998$ according to equation 2.20.

$$\det\left(\overset{\leftrightarrow}{X}\right) = \gamma^2\mu_0^2\left[H_{\text{ext}} + M_s(N_x - N_y)\right]\left[H_{\text{ext}} + M_s(N_z - N_y)\right] + i\alpha\omega\gamma\mu_0\left[2H_{\text{ext}} + M_s(N_x + N_z - 2N_y)\right] - \omega^2\left(1+\alpha^2\right) \tag{2.18}$$

vanishes leading to the resonance frequency

$$\omega_r = \frac{i\gamma\alpha\mu_0}{2(1+\alpha^2)}\left[2H_{\text{ext}} + M_s(N_x + N_z - 2N_y)\right] \pm \frac{\gamma\mu_0}{2(1+\alpha^2)}\sqrt{4\left[H_{\text{ext}} + M_s(N_x - N_y)\right]\left[H_{\text{ext}} + M_s(N_z - N_y)\right] - M_s^2(N_x - N_z)^2\alpha^2}. \tag{2.19}$$

In the undamped case ($\alpha = 0$), equation 2.19 transforms into the famous Kittel formula for the ferromagnetic resonance (FMR)

$$f_r = \frac{\omega_r}{2\pi} = \frac{\gamma\mu_0}{2\pi}\sqrt{\left[H_{\text{ext}} + M_s(N_x - N_y)\right]\left[H_{\text{ext}} + M_s(N_z - N_y)\right]} \tag{2.20}$$

discovered by Charles Kittel [117] and plotted for a system investigated in this work in figure 2.8.

For a thin, infinite film along the x direction the demagnetization tensor component $N_x = 0$ vanishes. The component N_y for a finite rectangular thin film element magnetized along y direction is given by [14, 100]

$$N_y(y) = \frac{1}{\pi}\left[\arctan\left(\frac{t}{2y+w}\right) - \arctan\left(\frac{t}{2y-w}\right)\right] \tag{2.21}$$

$$\Rightarrow N_y(y=0) = \frac{1}{\pi}\left[\arctan\left(\frac{t}{w}\right) - \arctan\left(\frac{-t}{w}\right)\right] \approx \frac{2t}{\pi w} \tag{2.22}$$

and is furthermore approximated to be constant over the stripe with the value at $y = 0$ being in the center of the slab. Because of equation 2.9 we get for the trace of the demagnetization tensor $N_x + N_y + N_z = N_y + N_z = 1$. In order to calculate the demagnetization factor N_x of a magnetized stripe along the elongated x-direction, the coordinates have to be exchanged ($y \Leftrightarrow x$) and the width w has to be replaced by the length l of the stripe.

With equation 2.22 we then get $N_y = 0.002$ and $N_z = 0.998$ for $w = 10\,\mu\text{m}$ and $t = 30\,\text{nm}$ and a resonance frequency $f_r = 7.08\,\text{GHz}$ of a permalloy film in an external field of $\mu_0 H_{\text{ext}} = 60\,\text{mT}$ according to equation 2.20.

Dynamic susceptibility

The reaction of the magnetization with respect to an external field is described by the magnetic susceptibility $\overset{\leftrightarrow}{\chi}_m$ in $\vec{M} = \overset{\leftrightarrow}{\chi}_m \cdot \vec{H}$ (equation 2.5). Equation 2.17 that describes the excitation geometry here and led to the FMR relation essentially is the inverse form of this equation and can be transformed via

$$\begin{pmatrix} m_x(t) \\ m_z(t) \end{pmatrix} = \overset{\leftrightarrow}{\chi} \cdot \begin{pmatrix} h_x(t) \\ h_z(t) \end{pmatrix} = \begin{pmatrix} \chi_{xx} & \chi_{xz} \\ \chi_{zx} & \chi_{zz} \end{pmatrix} \cdot \begin{pmatrix} h_x(t) \\ h_z(t) \end{pmatrix} \tag{2.23}$$

by inverting the matrix in equation 2.17 using $\overset{\leftrightarrow}{X}^{-1} = \mathrm{adj}\left(\overset{\leftrightarrow}{X}\right) / \det\left(\overset{\leftrightarrow}{X}\right)$. This leads to the dynamic susceptibility tensor

$$\overset{\leftrightarrow}{\chi} = \frac{\gamma\mu_0 M_s}{\det\left(\overset{\leftrightarrow}{X}\right)} \cdot \begin{pmatrix} \gamma\mu_0\left[H_{\text{ext}} + M_s(N_z - N_y)\right] + i\alpha\omega & -i\omega \\ i\omega & \gamma\mu_0\left[H_{\text{ext}} + M_s(N_x - N_y)\right] + i\alpha\omega \end{pmatrix} \tag{2.24}$$

which experiences a frequency dependence. The components related to the reaction of the magnetization z-component $m_z(t) = \chi_{zx}(\omega)h_x(t) + \chi_{zz}(\omega)h_z(t)$ accessible in the experimental setup read

$$\chi_{zx}(\omega) = \frac{i\omega\gamma\mu_0 M_s}{\det\left(\overset{\leftrightarrow}{X}\right)} \qquad \text{and} \qquad \chi_{zz}(\omega) = \frac{\gamma\mu_0 M_s \cdot \left(\gamma\mu_0\left[H_{\text{ext}} + M_s(N_x - N_y)\right] + i\alpha\omega\right)}{\det\left(\overset{\leftrightarrow}{X}\right)} \tag{2.25}$$

with $\det\left(\overset{\leftrightarrow}{X}\right)$ obtained from equation 2.18. The real and imaginary part of these components is plotted in figure 2.9 and shows a resonant response around f_r. Moreover,

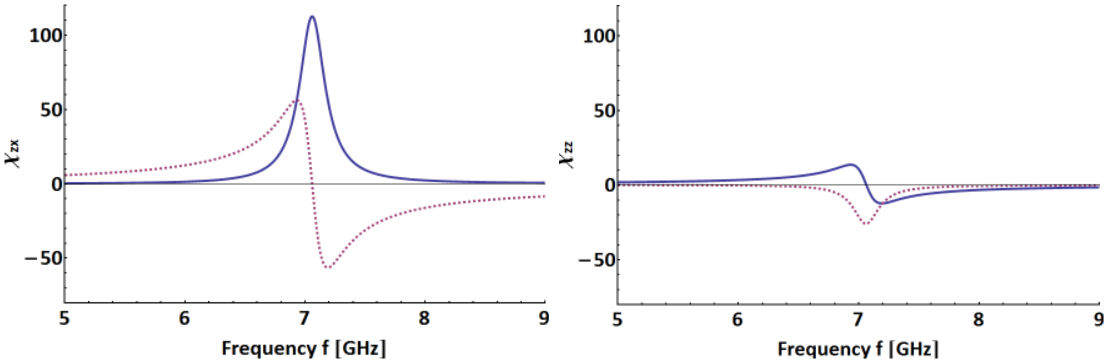

(a) Real (solid blue) and imaginary (dashed purple) part of the dynamic susceptibility component χ_{zx}.

(b) Real (solid blue) and imaginary (dashed purple) part of the dynamic susceptibility component χ_{zz}.

Figure 2.9: Real and imaginary part of the χ_{zx} and χ_{zz} components of the dynamic susceptibility tensor $\overset{\leftrightarrow}{\chi}$ according to equation 2.25 for a permalloy slab with $\mu_0 M_s = 1.040\,\mathrm{T}$ and $\alpha = 0.008$ in an external field of $\mu_0 H_{\text{ext}} = 60\,\mathrm{mT}$ using the demagnetization tensor components $N_x = 0$, $N_y = 0.002$ and $N_z = 0.998$.

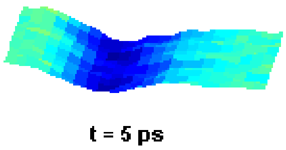

χ_{zx} and χ_{zz} are phase shifted by 90°. The real part generally resembles the excitation spectrum when driving the system with a short pulse that delivers a broad spectrum. The spectral width of the χ_{zx} component real part measures 259 MHz FWHM.

Quantized spin-wave modes and dispersion relation

The calculations sketched out here base on the work of Kalinikos and Slavin [104] who calculated the dispersion relation for a thin ferromagnetic film. The work was extended by Guslienko et. al. [79, 80] to small rectangular thin films. A reasonable approximation is neglecting the crystalline anisotropy of permalloy in all calculations [219].

In small magnetic rectangular structures, the spin-wave vector $\vec{k}$ is quantized according to the geometry boundaries namely width w, length l and thickness t of the film:

$$\vec{k} = \begin{pmatrix} k_{mx} \\ k_{ny} \\ k_{pz} \end{pmatrix} = \begin{pmatrix} \vec{\kappa}_{mn} \\ \frac{p\pi}{t} \end{pmatrix} \qquad \text{with} \qquad \vec{\kappa}_{mn} = \begin{pmatrix} k_{mx} \\ k_{ny} \end{pmatrix} = \begin{pmatrix} \frac{m\pi}{l_{\text{eff}}} \\ \frac{n\pi}{w_{\text{eff}}} \end{pmatrix} \qquad \forall \qquad m,n,p \in \mathbb{N}. \tag{2.26}$$

Because the structures in this work are thin films, propagation in z direction is neglected ($p = 0 \Rightarrow k_{pz} = 0$). Therefore, the $\vec{k}$ vector reduces to $\vec{\kappa}_{mn}$ from equation 2.26. A uniform radio-frequency (RF) field can only excite odd modes of k_{mx} and k_{ny} due to symmetry [118]. Furthermore, an effective stripe width w_{eff} and length l_{eff} is introduced [80] due to dipolar pinning at the stripe boundaries reducing the magnetization because of the emerging demagnetization field. Equation 2.27 notes the calculation of the effective width w_{eff} that can be transformed into the calculation of the effective length l_{eff} as well by replacing w with l:

$$w_{\text{eff}} = w\left(\frac{d}{d-2}\right) \qquad \text{with} \qquad d = \frac{2\pi}{\frac{t}{w}\left[1 - 2\ln\left(\frac{t}{w}\right)\right]}. \tag{2.27}$$

The calculation of the dispersion relation $f(k)$ is carried out in [79] and leads to

$$f(\vec{\kappa}_{mn}) = \frac{\gamma\mu_0}{2\pi}\sqrt{\left(H_{\text{eff}} + \frac{2A}{\mu_0 M_s}|\vec{\kappa}_{mn}|^2\right) \cdot \left(H_{\text{eff}} + \frac{2A}{\mu_0 M_s}|\vec{\kappa}_{mn}|^2 + M_s F_{mn}(\vec{\kappa}_{mn})\right)}. \tag{2.28}$$

Here, A is the exchange constant and

$$\begin{aligned} F_{mn}(\vec{\kappa}_{mn}) = 1 - P(\vec{\kappa}_{mn})&\left(\frac{k_{ny}^2}{|\vec{\kappa}_{mn}|^2}\right) \\ &+ P(\vec{\kappa}_{mn})\left[1 - P(\vec{\kappa}_{mn})\right]\left(\frac{M_s}{H_{\text{eff}} + \frac{2A}{\mu_0 M_s}|\vec{\kappa}_{mn}|^2}\right) \cdot \left(\frac{k_{mx}^2}{|\vec{\kappa}_{mn}|^2}\right) \end{aligned} \tag{2.29}$$

with

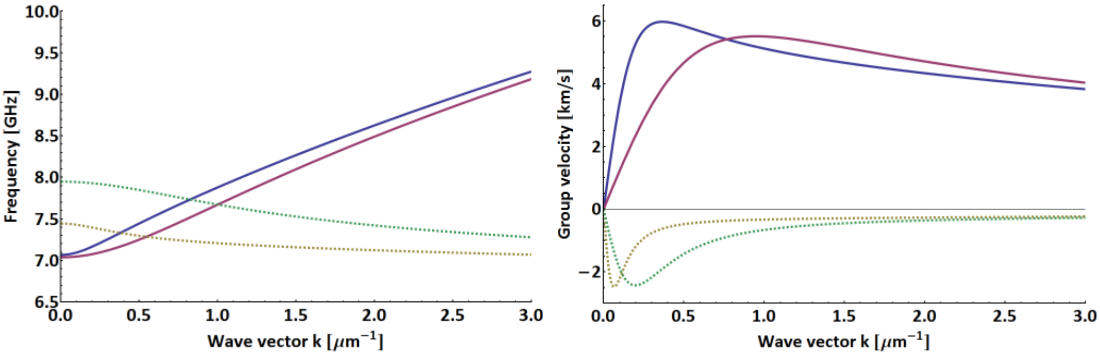

(a) Spin-wave dispersion relation $f(k)$ according to equation 2.28.

(b) Group velocities $v_g = \frac{\partial\omega}{\partial k}$ obtained by the first derivative of equation 2.28. The group velocity for the first DE mode peaks at $k = 0.37\,\mu\text{m}^{-1}$ with a value of $v_g = 5.98\,\text{km/s}$.

Figure 2.10: Spin-wave dispersion relation and group velocities for the first possible Damon-Eshbach (solid lines, blue $\vec{k}_1$ and red $\vec{k}_3$) and backward volume (dashed lines, yellow $\vec{k}_1$ and green $\vec{k}_3$) modes of a permalloy slab with $w = 10\,\mu\text{m}$, $l = 35\,\mu\text{m}$ and $t = 30\,\text{nm}$ in an external field of $\mu_0 H_{\text{ext}} = 60\,\text{mT}$.

$$P(\vec{\kappa}_{mn}) = 1 - \frac{1 - \exp\left(-|\vec{\kappa}_{mn}| \cdot t\right)}{|\vec{\kappa}_{mn}| \cdot t} \tag{2.30}$$

the dipole interaction tensor in order to take into account the dipolar coupling present in the system.

As demonstrated in the previous section the effective field H_{eff} in equation 2.28 is given by the external field H_{ext} and the demagnetization field $H_{\text{eff}} = H_{\text{ext}} - N_y(y=0) \cdot M_s$ but here only in the direction of the acting external field. The y component N_y of the demagnetization tensor is approximated by equation 2.22 [14, 100].

The single modes propagating with a phase velocity $v_{\text{ph}} = \omega/k$ in a rectangular permalloy structure will interfere generating a mode pattern consisting of the superposition of all excited modes. Since the amplitude a_m of the individual modes decreases with increasing mode number as $a_m \propto 1/m$ [118], only the first two odd modes are assumed to be dominant. Generally, these modes are phase shifted by an angle $\varphi = |\varphi_1 - \varphi_3|$ with respect to each other. Considering the aforementioned arguments, the z-component of the magnetization observable in the experiment can be described similar to [124, 123, 142, 161, 137] by

$$\begin{aligned} M_z(x,y,t) &\propto \mathrm{e}^{-\delta t} \cdot \exp\left(-\frac{(x - v_g \cdot t)^2}{2 \cdot [v_g \cdot \tau(t)]^2}\right) \\ &\cdot \left[a_1 \cdot \sin\left(\frac{\pi}{w_{\text{eff}}} \cdot y\right) \cdot \cos\left(kx - \omega t\right) + \frac{a_1}{3} \cdot \sin\left(\frac{3\pi}{w_{\text{eff}}} \cdot y\right) \cdot \cos\left(kx - \omega t + \varphi\right)\right] \end{aligned} \tag{2.31}$$

for a wave packet traveling with a group velocity of

$$v_g = \frac{\partial \omega}{\partial k} = v_{\text{ph}} + k \frac{\partial v_{\text{ph}}}{\partial k} \tag{2.32}$$

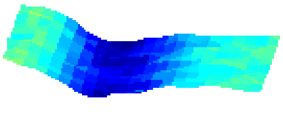

which may be negative for BV modes with small $\vec{k}$ vectors (see figure 2.10b) and in that case represents counterpropagation of phase and group velocity. Furthermore, the wave packet is temporally confined by its duration $\tau(t)$ which may experience a time-dependence if dispersion is present. The temporal damping constant δ is related to the dimensionless damping parameter α via the imaginary part in equation 2.19 and reads in the present case of low damping ($\alpha^2 \ll 1$ because $\alpha = 0.008$ for permalloy [94]):

$$\delta = \frac{\alpha \cdot \gamma \cdot \mu_0 \left[2H_{\text{ext}} + M_s\left(N_x + N_z - 2N_y\right)\right]}{2}. \tag{2.33}$$

If the wave packet duration $\tau(t)$ increases over time, the peak amplitude further diminishes with respect to time due to distribution of the constant total energy of the wave packet over the pulse duration. An additional decrease of the spin-wave amplitude with respect to the propagated distance may be present due to inelastic energy transfer between neighboring spins along the propagation path.

When we consider an excitation with a broadband pulse confined both in time and in space due a finite overlap with the waveguide (figure 2.7), the response related to the k_x components is more generally described by [137]

$$M_z(x,t) \propto \mathrm{e}^{-\delta t} \int_0^{k_c} P(k, \omega(k)) \cdot \sin\left(kx - \omega(k)t + \varphi\right) \mathrm{d}k \tag{2.34}$$

where $P(k,\omega(k))$ describes a weighting function of the $\vec{k}$-vectors due to the spectral density and k_c is a cut-off wave number useful for numeric integration. A representation of the pump pulse

$$h_x(x,t) = h_0 \cdot \Pi\left(\frac{x - \frac{\sigma_x}{2}}{\sigma_x}\right) \cdot \exp\left(-\frac{(t-t_0)^2}{2 \cdot \tau^2}\right) \tag{2.35}$$

used in the experiment is plotted in figure 2.11a with a Gaussian envelope of $\tau = 10\,\text{ps}$ duration and a spatial confinement given by a rectangular pulse function $\Pi(x)$ defining the overlap between magnetic layer and waveguide conductor of $\sigma_x = 5\,\mu\text{m}$. The weighting

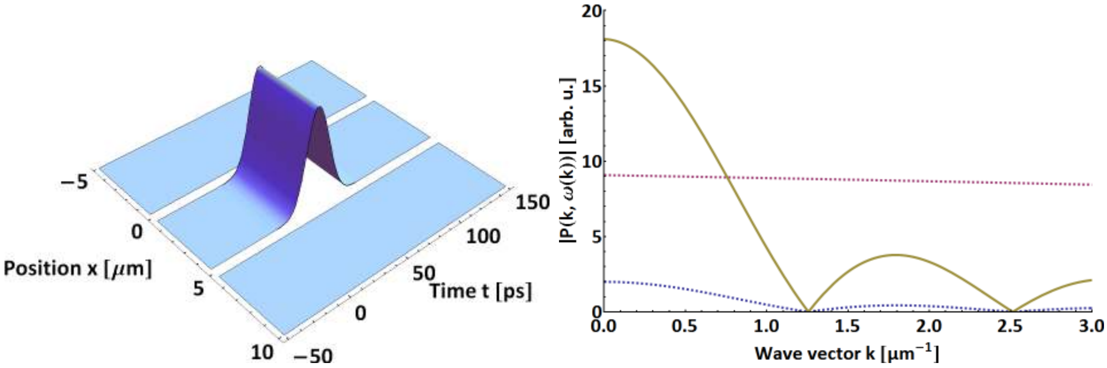

(a) Spatially and temporally confined Gaussian excitation pulse $h_x(x,t)$ of $\tau = 10\,\text{ps}$ duration and $\sigma_x = 5\,\mu\text{m}$ overlap with the magnetic system in real space.

(b) Spectral density of the excitation pulse $P(k,\omega(k)) \propto |h_x(k)| \cdot |h_x(\omega)|$ (solid yellow) containing the spatial part $|h_x(k)|$ (dashed blue) and temporal part $|h_x(\omega(k))|$ (dashed purple).

Figure 2.11: Excitation pulse in real space $h_x(x,t)$ and reciprocal space $h_x(k,\omega)$.

function now is generally composed of the modulus of the Fourier transformation in space and time $P(k, \omega(k)) \propto |h_x(k)| \cdot |h_x(\omega)|$ [137, 161] and depicted in figure 2.11b. The spatial part $|h_x(k)|$ resembles a sinc (k) function corresponding to the Fourier transform of the rectangular pulse. Since the transformation of a Gaussian gives another Gaussian, the temporal spectral shape $|h_x(\omega)|$ remains where $\omega(k)$ was obtained from the spin-wave dispersion relation in equation 2.28. Due to the broadband pulse, the temporal part is almost constant and the form of the excitation spectrum is dominated by the spatial confinement $|h_x(k)|$ [137]. It should be noted that the spectrum is only an approximation to get an idea of the shape and excitable wave vectors because the field distribution is not realistically modeled by a rectangular function as we see later in figure 4.3. A more accurate spectrum should be obtained by including the inhomogeneities of the excitation field in overlap with the magnetic system into the calculation.

2.1.4 Magneto-optic Kerr effect (MOKE)

The fact that the polarization plane of a linear polarized beam reflected by the surface of a magnetized medium is rotated is described by the magneto-optic Kerr effect (MOKE) and was first discovered by John Kerr [108, 109]. Phenomenologically, on a microscopic level the incoming light beam interacts with the electron cloud of the atoms inside the magnet and slightly polarizes the initially spherically symmetric charge distribution by driving its motion along the light field polarization. A present magnetic field inside the medium would lead to a Lorentz force $\vec{F} = q(\vec{v} \times \vec{B})$ on the quivering electrons perpendicular to the magnetic field direction adding another oscillation amplitude parallel to the direction of this force. Eventually, this oscillation of charged particles transfers photons into the reflected light field with an additional polarization component. A quantum description of the effect not explicitly presented in this work yields the insight that the spin-orbit interaction which couples the spin of the electron to its orbital motion connects the magnetic and optic properties.

An incident beam on a surface can be described in the basis of circular positive and negative helicity. In a more detailed calculation carried out in appendix A.1 it becomes obvious that different helicities experience individual indices of refraction

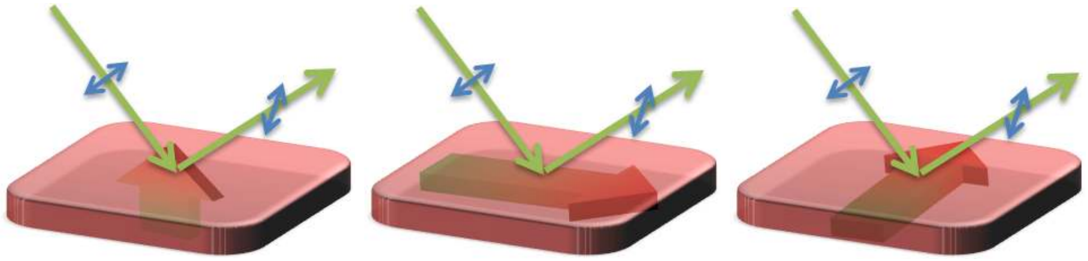

(a) Polar (P-MOKE) **(b)** Longitudinal (L-MOKE) **(c)** Transversal (T-MOKE)

Figure 2.12: Magneto-optic Kerr effect (MOKE) in polar, longitudinal and transversal configuration determined by the direction of the magnetization with respect to the incident beam.

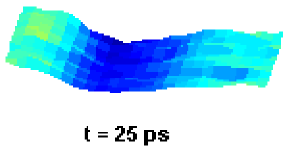

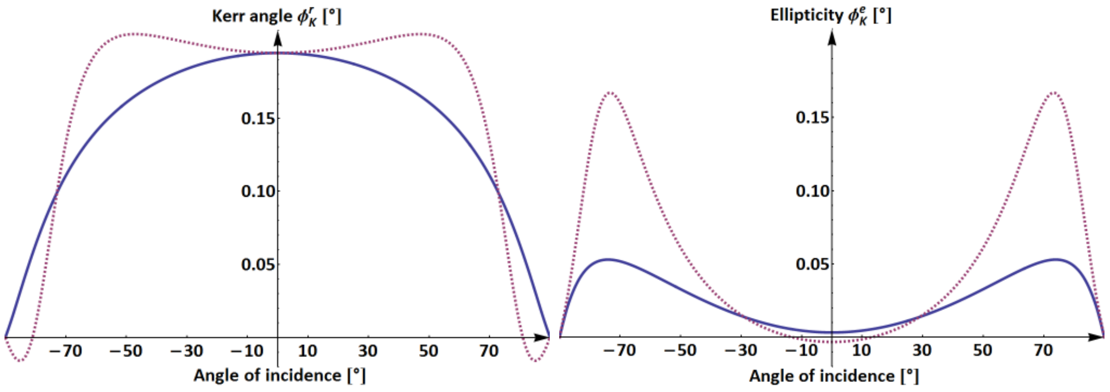

(a) Kerr rotation ϕ_K^r **(b)** Kerr ellipticity ϕ_K^e

Figure 2.13: Kerr rotation ϕ_K^r and ellipticity ϕ_K^e for bulk permalloy magnetized out of the sample plane with its saturation magnetization M_s in P-MOKE configuration according to equation A.69 and A.70 calculated with the theory in appendix A.1 and A.2 with the parameters $n = 1.69 + i2.69$ and $Q = 0.01012 - i0.005$ [152] for a wavelength of $\lambda = 515\,\text{nm}$. The solid blue curve applies for s-polarized light and the dashed purple curve for p-polarized light.

$$n^{\pm} \approx \underbrace{\sqrt{\mu_r \varepsilon_r}}_{n} \left(1 \mp \frac{1}{2}\vec{Q} \cdot \vec{e}_k\right) \tag{2.36}$$

with the Voigt vector $\vec{Q}$ [208, 130] introduced in appendix A.1 that describes the magneto-optic properties.

Using the Lorentz force, this is also understandable intuitively because right hand polarized light forces the electrons into right circular motion and vice versa. A magnetic field pointing into the photon propagation direction $\vec{e}_k$ leads to a Lorentz force toward or away from the center of the circle reducing or enlarging the radius of the orbit, respectively, giving rise to different optical properties for each helicity. That means after a certain distance L a phase difference is accumulated as well as a difference in absorption is experienced corresponding to a rotation of the polarization and a change in ellipticity:

$$\phi_K = \frac{\pi L}{\lambda}\left(n^+ - n^-\right) \approx -\frac{\pi n L}{\lambda}\vec{Q} \cdot \vec{e}_k. \tag{2.37}$$

Note that ϕ_K is is a complex number relating the Kerr rotation ϕ_K^r to the real part and the ellipticity ϕ_K^e to the imaginary part via the equations A.69 and A.70 in appendix A.1 and A.2 where the calculation of the Kerr angle is done explicitly. These values are depicted in figure 2.13 for permalloy with respect to the incident angle. The effect is maximal at 0° incident angle for the polar MOKE case which is used in this work. Note that for the wavelength of $\lambda = 515\,\text{nm}$ available in this setup also the ellipticity is negligible with respect to the Kerr rotation.

2.1.5 X-ray magnetic circular dichroism (XMCD)

Soft X-ray radiation is a superior tool for the investigation of magnetic nanostructures because it combines the advantage of a high spatial resolution due to the small wavelength with element specificity by selecting particular atomic transitions at an appropriate photon energy. Additionally, these advantages are extended by a magnetic contrast mechanism called X-ray magnetic circular dichroism (XMCD) discovered in the pioneering work by Gisela Schütz in 1987 [180] enabling the detection of the magnetization in a sample.

When working with circularly polarized light routinely available at bending magnets in a certain radiation cone and in helical undulators at 3^{rd} generation synchrotron radiation facilities (see also chapter 4.6), the orientation of the magnetic moment in atoms, clusters, molecules and condensed matter becomes observable with XMCD spectroscopy. Supplementary, the element specificity facilitates a disentanglement of the magnetization in compounds like alloys or multilayers where is it possible to map the magnetic contributions to the individual elements by analyzing XMCD data at the corresponding atomic transition edge. One possibility to obtain an XMCD signal is monitoring the transmitted X-ray intensity

$$I(z) = I_0 \cdot \mathrm{e}^{-\mu z} \qquad \text{with} \qquad \mu = \sigma \cdot \rho_T = \frac{\sigma \cdot N_A \cdot \rho}{M_m} \tag{2.38}$$

behind a sample of thickness $z = d$ given by the Lambert-Beer law with the absorption coefficient μ containing the cross section σ and the target particle density ρ_T computable via the molar mass M_m, material density ρ and the Avogadro constant $N_A = 6.022 \cdot 10^{23}\,\mathrm{mol}^{-1}$. Essentially, now the transmitted intensity of $3d$ transition metal elements at the L absorption edge differs for circular polarized light of opposite helicity with respect to the orientation of the magnetic moments projected onto the photon propagation direction. The change in the absorption coefficient μ is calculated by determining the cross section via Fermis golden rule[3]

$$|\mu| \propto |\langle\psi_f|H|\psi_i\rangle|^2 \cdot D\left(E_f\right). \tag{2.39}$$

Here, mutual helicities experience a varying density of final states $D\left(E_f\right)$ while the transition matrix element $|\langle\psi_f|H|\psi_i\rangle|^2$ remains constant for both polarizations.

The variable density of states becomes obvious by exemplifying the process more vividly in a picture shown in figure 2.14a. By absorbing a photon with defined helicity, a spin polarized electron can be released out of a spin-orbit split inner shell via the Fano effect discovered by Ugo Fano [58, 59] where the angular momentum of the photon is partly transferred to the electron spin via the spin-orbit coupling. This (virtual) electron may now be reabsorbed immediately in the $3d$ shell ($2p \rightarrow 3d$ transition) partly filled up to the Fermi energy E_F. Now, in a magnetized material the d valence band is unequally filled with spin-up and spin-down electrons with respect to the magnetization and since in a dipole transition the spin angular momentum remains constant, the density of final states $D\left(E_f\right)$ is different for the spin-polarized electrons and the transition rate changes. So to speak $D\left(E_f\right)$ acts as a detector probing the number of empty d states and thus the magnetization component in the propagation direction of the photon beam because the quantization axis is defined by the magnetization vector $\vec{M}$. This measurement can be carried out at both fine structure transitions from an initial $2p_{3/2}$ or $2p_{1/2}$ state referred to as L_3 and L_2 absorption edges, respectively. The XMCD contrast reverses from the L_3

---

[3] An almost identical equation for the transition matrix element in Fermis golden rule was first published by P. A. M. Dirac [46] and G. Wentzel [213] in 1927. Because of its significance, E. Fermi himself called it “Golden Rule No. 2” in his nuclear physics lectures [60].

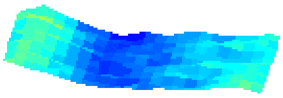

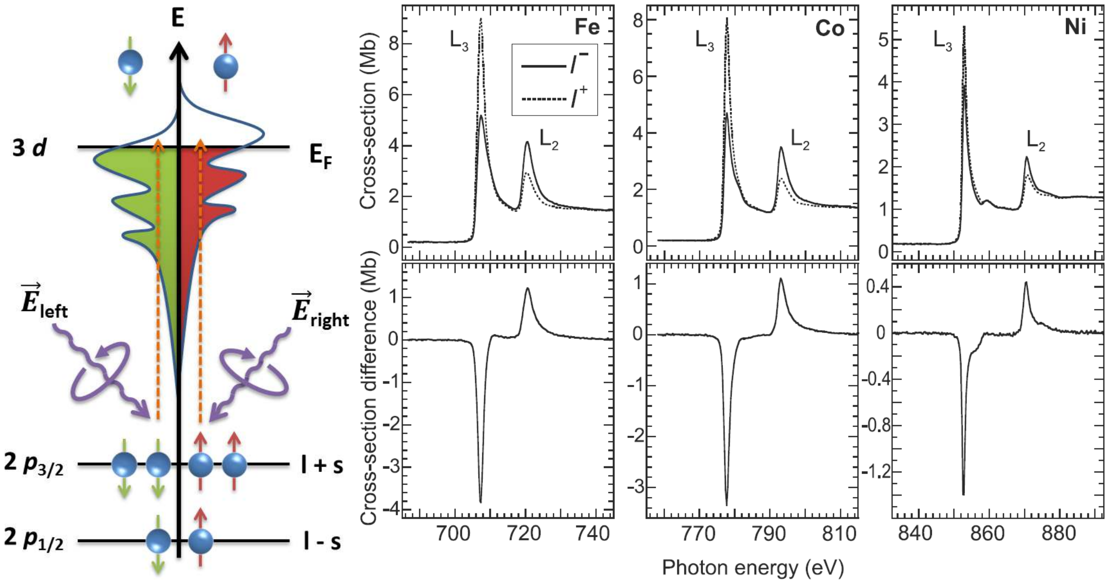

(a) Circular polarized light driving a $2p \rightarrow 3d$ transition selectively for spin-up or spin-down electrons depending on the photon helicity. Triggered transitions experience an unequal density of final states leading to an XMCD contrast.

(b) Absorption and XMCD spectra for iron, cobalt and nickel corrected for a 100 % circular polarized beam. The top graphs show the absorption spectra for the two photon helicities I^+ and I^- and the bottom graphs show the difference $I^- - I^+$ XMCD signal providing information about the sample magnetization. The cross section is given in Mb and one barn is defined as $10^{-24}\,\mathrm{cm}^2 = 10^{-28}\,\mathrm{m}^2$. The graph is taken from [191] and contains data from [29, 30].

Figure 2.14: Origin of the XMCD contrast and example spectra for the elemental ferromagnetic elements iron, nickel and cobalt.

to the L_2 absorption edge (compare figure 2.14b) because of the inverse spin polarization of the electron due to an opposite spin-orbit coupling, namely $l + s$ for $2p_{3/2}$ and $l - s$ for $2p_{1/2}$, that is responsible for the angular momentum transfer from the photon to the electron [190, 189].

Figure 2.14b presents the absorption of the in this work investigated ferromagnetic elements iron, cobalt and nickel at different photon helicities. By subtraction of both curves, the XMCD signal can be obtained. The difference cross section compared to the polarization averaged signal at the L_3 absorption edge typically measures $\sigma_{\mathrm{XMCD}}/\sigma = 23\,\%$ for iron and $\sigma_{\mathrm{XMCD}}/\sigma = 13\,\%$ for nickel. By obtaining a normalized difference signal for the acquired intensities $I^{\pm}$ this results in

$$\frac{I^+ - I^-}{I^+ + I^-} = \frac{I_0 \cdot \left[\mathrm{e}^{-(\mu+\mu_{\mathrm{XMCD}})d} - \mathrm{e}^{-(\mu-\mu_{\mathrm{XMCD}})d}\right]}{I_0 \cdot \left[\mathrm{e}^{-(\mu+\mu_{\mathrm{XMCD}})d} + \mathrm{e}^{-(\mu-\mu_{\mathrm{XMCD}})d}\right]} = -\tanh\left(\mu_{\mathrm{XMCD}} \cdot d\right). \tag{2.40}$$

2.2 Diffraction

Diffraction is a phenomenon that occurs when a wave passes an obstacle and is most pronounced when its wavelength is comparable to the size of the obstacle. A vivid representation of the physical process was given by Christiaan Huygens [93] and Augustin-Jean Fresnel [68, 69] stating that every transparent point of the obstacle becomes a point source of a spherical wave being able to interfere with each other.

2.2.1 Diffraction gratings

In this work several diffractive elements in zone-plate lenses or spectrographs are used. All gratings rely on the principle of a light field being modified by a periodic structure that transmits or reflects the beam only partially. The periodicity of the modulation is quantified by the grating constant d. For monochromatic light this leads to positive interference of the light field if the path difference Δ equals to integer multiples of the wavelength $n \cdot \lambda$. This condition is fulfilled at deflection angles φ in equation 2.41:

$$\Delta = n \cdot \lambda = d \cdot \sin(\varphi) \qquad \forall \qquad n \in \mathbb{Z}. \tag{2.41}$$

Those kinds of gratings are commonly used in spectrographs, as diffractive lenses or as dispersive elements in laser systems e.g. for frequency stabilization, laser pulse stretching or compression. When using diffraction gratings in a spectrograph the resolving power

$$\frac{\lambda}{\Delta\lambda} = nN \tag{2.42}$$

is of interest which includes the spectral resolution $\Delta\lambda$ and depends on the number of illuminated line-pairs N and the diffraction order n. Combining a transmission grating with a slit of width D perpendicular to the grating lines leads to a compact spectrograph [217]. In this case also a geometrical resolution limit

$$\Delta\lambda_g = d \cdot \left[\frac{D+q}{g} + \frac{D}{b}\right] \tag{2.43}$$

has to be taken into account because the shadow image of the slit is diffracted by the grating with period d. The spots of two adjacent wavelengths can only be separated if their slit shadows projected by a source of size q at distance g do not coincide on the detector at distance b (compare also figure 5.6).

2.2.2 Diffraction limited resolution

In general the resolution of an optical instrument with a focal length f operating at a certain wavelength λ is said to be diffraction limited if the *calculated* spot size by geometrical optics is below the Airy disc size determining the diffraction pattern of a single point at a circular aperture of diameter $D = 2a$. The properties of an optical system are commonly summarized by the f-number $N = f/D$ (sometimes written in form of the entrance pupil $f/\#$) described by the focal length f divided by aperture diameter D. In case of a circular aperture (i.e. circular shaped optics) the Airy pattern is the point spread function (PSF) of the optical system describing the impulse response of an optical assembly. This means that in the image plane every infinitesimally sharp point of an object gets convoluted with the Airy disc intensity distribution

$$I(\theta) = I_0 \left[\frac{2J_1(ka\sin(\theta))}{ka\sin(\theta)}\right]^2 = I_0 \left[\frac{2J_1\left(\pi\frac{q}{\lambda N}\right)}{\pi\frac{q}{\lambda N}}\right]^2 \qquad \text{with} \qquad k = \frac{2\pi}{\lambda} \tag{2.44}$$

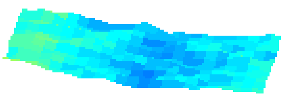

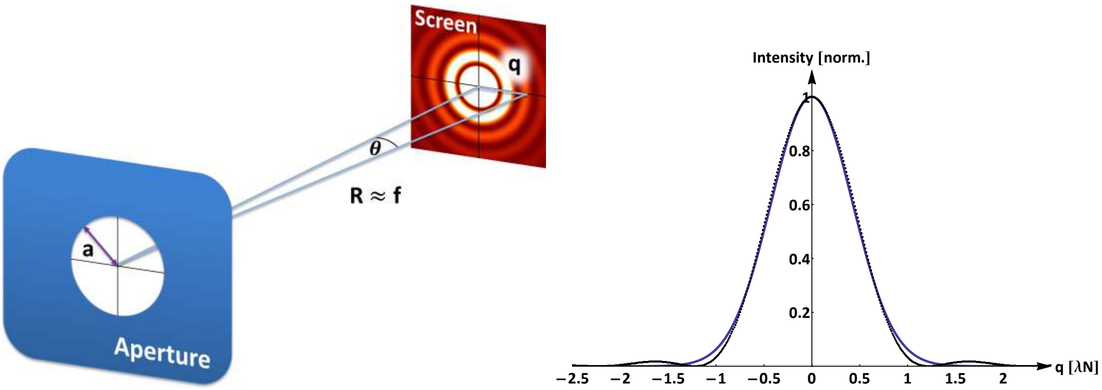

(a) Intensity of the Airy pattern $I(\theta)$ generated by an aperture of diameter $D = 2a$ at a distance $R \approx f$. q is the radial coordinate on the screen and relates to the diffraction angle θ like $\sin(\theta) = q/R$.

(b) Intensity of Airy function (black dashed line) with respect to the radial coordinate $I(q)$ in units of λN and best fit of Gauss function (blue solid line) with $\sigma \approx 0.43\lambda N$.

Figure 2.15: Generation of the Airy pattern by diffraction at a circular aperture and approximation of the Airy function by a Gaussian.

with respect to the diffraction angle θ. Here, J_1 is the Bessel function (of the first kind) of order 1 and q the radial distance from the center (compare figure 2.15a). Equation 2.44 can be obtained by calculating the squared modulus of the Fourier transform of a circular aperture with radius a at a distance R.

Now, according to Rayleigh's criterion commonly used in microscopy, a feature is said to be resolved if the maximum of the Airy disc of one point in the image coincides with the first diffraction minimum of the neighboring point. For this purpose, the first root of equation 2.44 has to be found. Knowing that the first zeros of the Bessel function $J_1(x_0) = 0$ are $x_0 \approx 0, 3.8317, \ldots$ it is sufficient to compare these numbers with the argument of J_1 in equation 2.44. This argument $ka\sin(\theta) = \frac{2\pi a}{\lambda}\frac{q}{R} = \frac{\pi q}{\lambda N}$ may be rewritten with respect to the radial coordinate q assuming $f \approx R$ and using the definition of the f-number $N = f/D$. A comparison with x_0 directly leads to the diffraction limited resolution $\Delta l = q_{\text{Rayleigh}}$ determined by equation 2.45 expressed here for optics with a numerical aperture $NA = n\sin(\theta)$ specifying the maximum half angle θ under which light may reach the optics:

$$\Delta l = 1.22 \cdot \lambda N = 1.22 \cdot \frac{\lambda f}{D} = 1.22 \cdot \frac{\lambda}{2 \cdot NA}. \tag{2.45}$$

However, this only applies to an Airy disc PSF and varies for other impulse response functions. For example, dealing with a Gaussian PSF defined like

$$I(q) = I_0 \exp\left(\frac{-q^2}{2\sigma^2}\right) \tag{2.46}$$

with respect to the radial distance q, means that we have to adjust the width σ of the function in a way that it fits best the form of the Airy pattern in order to use the resolution limit given by equation 2.45. The best least squares fit is obtained for $\sigma \approx 0.43\lambda N$ and demonstrated in figure 2.15b. So, the diffraction limited resolution for a Gaussian PSF of width

$$\sigma \approx 0.43 \cdot \lambda N \qquad \Rightarrow \qquad \sigma = 0.43 \cdot \frac{\lambda}{2 \cdot NA} \tag{2.47}$$

is equivalent to a resolution Δl determined by the Rayleigh criterion given by equation 2.45. In order to determine the resolution or the width of the PSF of an optical system, an infinitesimally sharp edge with a transition much smaller than the resolution of the system can be imaged. In the image the edge described by a step function would be convoluted with a Gaussian PSF. This convolution

$$I(x) = I_0 + \frac{A}{\sqrt{2\pi} \cdot \sigma} \cdot \mathrm{erf}\left(\frac{x - x_0}{\sqrt{2} \cdot \sigma}\right) \qquad \text{with} \qquad \mathrm{erf}(x) := \frac{2}{\sqrt{\pi}} \int_0^x \mathrm{e}^{-t^2}\, \mathrm{d}t \tag{2.48}$$

is known as error function. If, for example, the width σ of a Gaussian PSF in the error function of equation 2.48 is fitted to a dataset in order to obtain the resolution of a system, the resulting width has to be multiplied by a factor of $1.22/0.43 = 2.84$ to be comparable with the resolution defined by Rayleigh's criterion for an Airy disc PSF.

Lastly, it should be noted that the Rayleigh criterion is only applicable for incoherent light. When dealing with coherent illumination, the discernibility of two points is influenced by the phase distribution associated with the object and may increase or decrease dependent on the relative phase between the points [75]. Another resolution criterion readily generalizable to coherent illumination [85] is the sparrow criterion

$$\Delta l = 0.94 \cdot \frac{\lambda}{2 \cdot NA} \tag{2.49}$$

stating the distance between two points where the imaged contrast vanishes completely.

2.2.3 Zone plates

Since in the soft X-ray regime refractive optics are hard to build due to the high absorption in nearly every material, reflective or diffractive optics are commonly used. Circular diffraction patterns named zone plates act as optical elements with a fixed focal length f for a given wavelength λ. The calculation of zone radii r_n appeared fist in literature by

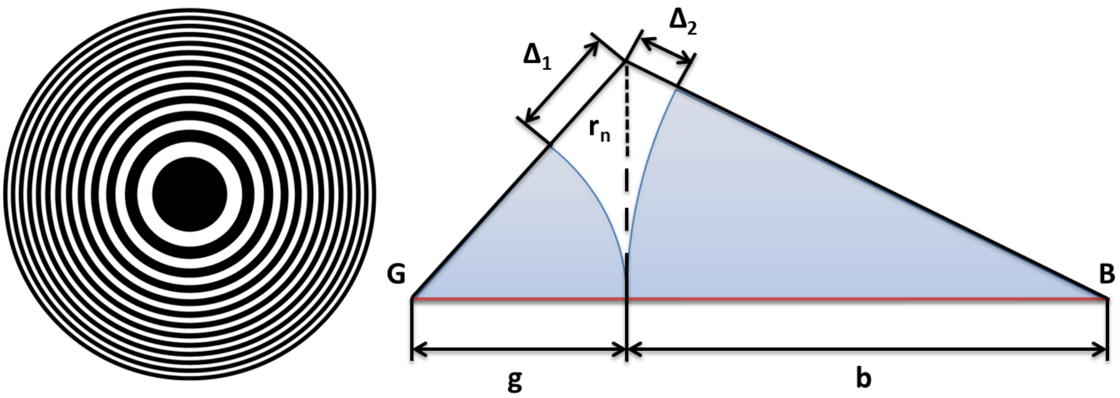

Figure 2.16: Calculated image of a zone plate and construction of the path difference $\Delta = \Delta_1 + \Delta_2$ at a certain zone radius r_n with respect to object and image distance g and b.

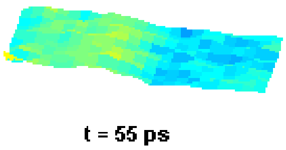

Soret in 1875 [183] and follows the approach in equation 2.51 where the path difference Δ is calculated with respect to object and image distance g and b, respectively. Figure 2.16 illustrates the construction of the path difference.

$$\Delta_1 = \sqrt{g^2 + r_n^2} - g \qquad \Delta_2 = \sqrt{b^2 + r_n^2} - b \tag{2.50}$$

$$\Delta = \Delta_1 + \Delta_2 = \sqrt{g^2 + r_n^2} + \sqrt{b^2 + r_n^2} - b - g \overset{!}{=} n\frac{\lambda}{2} \tag{2.51}$$

Every boundary between opaque and transparent areas and vice versa counts a zone. The optical path difference Δ has to be equal to $n \cdot \frac{\lambda}{2}$. If now every second zone is absorbing the radiation, the diffracted photons of the object constructively interfere (path difference $n \cdot \lambda$) at the image distance b of the zone plate and for every diffraction order n another image appears. In order to calculate the focal length f of the zone plate, one has to use the lens equation

$$\frac{1}{f} = \frac{1}{g} + \frac{1}{b} \tag{2.52}$$

and resolve equation 2.51 to r_n^2. Terms of higher order than $n^2\lambda^2$ are neglected because λ in general is small compared to the distances b and g. The calculation is carried out in detail in appendix A.3 and leads to

$$r_n^2 \approx nf\lambda + \frac{n^2\lambda^2}{4} \qquad \forall \qquad n \in \mathbb{N} \quad \wedge \quad n\lambda \ll g + b. \tag{2.53}$$

The circular diffraction pattern of the zone plate according to this equation shown in figure 2.16 basically resembles the diffraction pattern of a singular point, so every point in the sample plane is imaged by the zone plate into the image plane. By neglecting the second term in equation 2.53 we can calculate the derivative of the approximated zone radius with respect to n

$$\frac{\mathrm{d}r_n}{\mathrm{d}n} = \frac{f\lambda}{2\sqrt{nf\lambda}} = \frac{\sqrt{nf\lambda}}{2n} = \frac{r_n}{2n} \qquad \Rightarrow \qquad \Delta r_n = \frac{r_n}{2n} \tag{2.54}$$

and obtain the width Δr_n of one zone for $\mathrm{d}n = 1$. This enables the calculation of the numerical aperture

$$NA \approx \frac{r_N}{f} = \frac{\lambda}{2 \cdot \Delta r_N} \qquad \text{with} \qquad f = \frac{2r_n\Delta r_n}{\lambda}. \tag{2.55}$$

for a zone plate with a diameter of $D = 2r_N$ where N is the total number of zones and r_N the radius of the outermost zone. In the calculation a combination of equation 2.53 and 2.54 has been used to replace the focal distance f. It turns out that the numerical aperture only depends on the wavelength and the outermost zone width $\Delta r_N = r_N - r_{N-1}$. Despite the short wavelength available in the soft and hard X-ray regime corresponding theoretically to a spatial resolution in the order of λ, the actual resolution is usually limited by the optics i.e. the zone plate and reads in this case (compare also equation 2.45 from the previous chapter)

$$\Delta l = 1.22 \cdot \frac{\lambda}{2 \cdot NA} = 1.22 \cdot \Delta r_N. \tag{2.56}$$

Note that the resolution is only determined by the outermost zone width depending on the fabrication capabilities of the zone plate manufacturer and is physically a measure of the highest transferable spatial frequency through the optics. The depth of field (DOF) of a zone plate is given by

$$DOF = \pm \frac{\lambda}{2 \cdot (NA)^2}. \tag{2.57}$$

measuring the distance in front of and behind the focus where objects appear acceptably sharp.

The last discussed feature of a zone plate is the efficiency. For absorbing zone plates, ideally $1/\pi^2 \approx 10\,\%$ of the incident power is distributed into the first diffraction order while 50 % is absorbed by the opaque zones, 25 % transmitted in zero order, 12.5 % diffracted into negative orders and 2.5 % to higher positive orders [195].

2.3 Photocathodes

For the excitation of a magnetic system, a short magnetic field pulse has to be generated out of a current pulse of certain amplitude. Photocathodes can be used for this purpose and are based on the photoelectric effect that describes the emission of electrons from a solid surface on illumination with light of a certain wavelength. The correct theoretical description of the photoionization of solids was first described in 1905 by ALBERT EINSTEIN in his Nobel prize awarded work on the photo-effect [51] by introducing a quantized nature of light. He found that photoionization only occurs if the energy E of the incident light, connected to its frequency ν via $E_{\text{ph}} = h\nu$, exceeds the work function W of the material which is the energy needed to release an electron into the vacuum continuum. The kinetic energy of the electron

$$E_{\text{kin}} = h\nu - W \tag{2.58}$$

is then solely dependent on the photon energy. Later, in 1915 ROBERT ANDREWS MILLIKAN experimentally verified the proportionality factor $h = 2\pi\hbar = 6.626 \cdot 10^{-34}\,\text{J s}$ as the Planck constant [149, 163]. Up to then this was a contradiction to classical electrodynamics where the intensity should be responsible for the kinetic energy of the electron. However, in the correct description the number of released electrons is determined by the intensity. One parameter measuring the performance of the photocathode is given by the quantum efficiency

$$QE = \frac{N_{\text{e}}}{N_{\text{ph}}} \tag{2.59}$$

which is the ratio of generated electrons N_{e} per incident photons N_{ph} hitting the cathode. The number of electrons is given by the released charge q divided by the charge of one electron e and relates in a pulsed operation to a current with a peak amplitude of $I_0 \approx q/\tau$ when τ specifies the pulse duration. The number of corresponding photons in a laser pulse can be estimated by

$$N_{\text{ph}} = \frac{E_{\text{pulse}}}{E_{\text{ph}}} \quad \text{with} \quad E_{\text{pulse}} = \frac{P}{f} \quad \text{and} \quad E_{\text{ph}} = \frac{hc}{\lambda} \tag{2.60}$$

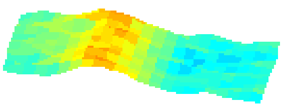

where E_{ph} is the energy of one photon and E_{pulse} the laser pulse energy determined by the average laser power P and the repetition rate f. In high electric fields E supplied by an anode the quantum efficiency

$$QE = A\,(h\nu - W)^2 \qquad \text{with} \qquad W = W_0 - \sqrt{\frac{e^3}{4\pi\varepsilon_0}} \cdot \sqrt{\beta E} \tag{2.61}$$

can be increased due to a lowering of the work function [221, 151] which is referred to as the Schottky effect. In equation 2.61 A is a constant depending on the material properties (absorption coefficient, density of states) as well as the polarization and angle of the incident light [184], W_0 is the work function at zero field and β is an empirical field enhancement parameter dependent on the surface quality of the cathode. A perfectly polished flat cathode surface corresponds to $\beta = 1$ and the factor increases with the surface roughness [76] leading to a bigger local electric field amplitude at surface spikes thus boosting the QE. However, care has to be taken when applying a high bias field because those spikes might lead to electric discharge sparks from the cathode to the anode.

When working with ultrashort and intense laser pulses, a lot of electrons will be released simultaneously screening the cathode surface from the electric field applied to remove the electrons. This dense cloud of electrons additionally experiences a strong repelling force due to the negative charge of each particle and is often referred to as space charge. The space charge limited current of an anode is determined by the Langmuir-Child law [32, 131]

$$I_a = j \cdot S = \frac{4\varepsilon_0}{9}\sqrt{\frac{2e}{m_e}} \cdot \frac{S U_a^{3/2}}{d^2} \tag{2.62}$$

and for an anode surface area S at an anode to cathode distance d this current is proportional to $U_a^{3/2}$ when U_a refers to the extraction voltage applied to the anode. The confinement of the released electron bunch is an important parameter when using photocathodes as electron source for particle accelerators because for instance in synchrotron radiation facilities it determines the maximum reachable brilliance of the storage ring. The degree of confinement is further characterized by a parameter called emittance which is not discussed here due to its irrelevance to this work where the cathode is only used as a pulsed current source and where the electron bunch is terminated directly at the anode surface.

2.4 Coplanar waveguides

The defined pulses created for example by the photocathode have to be delivered into the interaction region without distortion. Because the exciting pulse is quite short it is composed of high frequency (HF) components in the microwave (MW) to terahertz (THz) range and care has to be taken considering the transport of the pulse. A matched impedance regarding pulse insertion and termination is mandatory for the waveguide and losses as well as dispersion have to be avoided as far as possible.

In the microwave regime there are several possibilities to design such a waveguide for example a microstrip line, a slotline or a coplanar waveguide (CPW) that is used in this work. The CPW was first suggested by Wen in 1969 [212] and can be imagined

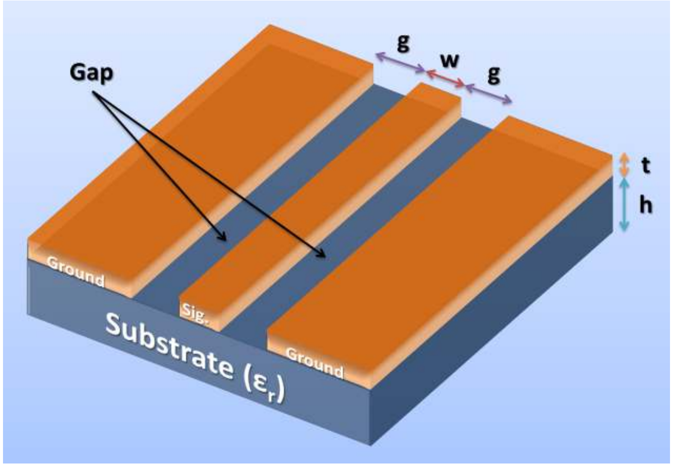

Figure 2.17: Metallic coplanar waveguide (CPW) of thickness t on a substrate of thickness h. The signal conductor (width w) is separated from two ground planes by a gap of width g.

as coaxial HF-cable projected onto a surface. Figure 2.17 shows a central conductor of width w surrounded by two ground planes in a distance g on a substrate of thickness h. By making use of conformal mappings (angle conserving transformations), the capacity can be calculated by taking into account the curved structure of the electric flux lines on the air/vacuum ($\varepsilon \approx \varepsilon_0$) side of the substrate and the field lines through the substrate with dielectric constant $\varepsilon = \varepsilon_0 \cdot \varepsilon_r$ and thickness h.

Starting with an infinitely thick substrate, the capacity per unit length of every half-space measures

$$C_{1/2} = 2 \cdot \varepsilon_0 \cdot \varepsilon_r \cdot \frac{K(k_1)}{K'(k_1)} \qquad \text{with} \qquad k_1 = \frac{w}{w+2g} \tag{2.63}$$

which includes the waveguide geometry in the constant k_1 and uses the complete elliptic integral of the first kind $K(k_1)$ and it's complement $K'(k_1)$. By adding both capacities of the air/vacuum and substrate half-spaces, the total line capacity C with an effective permittivity $\varepsilon_{\text{eff}} = (\varepsilon_r + 1)/2$ can be obtained. The characteristic impedance of the waveguide is then given by

$$Z = \frac{30\pi}{\sqrt{\varepsilon_{\text{eff}}}} \cdot \frac{K'(k_1)}{K(k_1)}. \tag{2.64}$$

Taking into account the finite substrate thickness h, the effective dielectric constant changes to

$$\varepsilon_{\text{eff}} = 1 + \frac{\varepsilon_r - 1}{2} \cdot \frac{K(k_2)}{K'(k_2)} \cdot \frac{K'(k_1)}{K(k_1)} \qquad \text{with} \qquad k_2 = \frac{\sinh\left(\frac{\pi w}{4h}\right)}{\sinh\left(\frac{\pi(w+2g)}{4h}\right)} \tag{2.65}$$

Furthermore, the effects of finite metalization thicknesses of signal and ground conductors can be included into the model as well. To do this, gap and conductor width as well as k_1 and ε_{eff} are modified to effective values with a correction factor

$$\Delta = \frac{1.25 \cdot t}{\pi} \cdot \left[1 + \ln\left(\frac{4\pi w}{t}\right)\right] \tag{2.66}$$

which is dependent on the metal thickness t. The waveguide parameters then transform to the effective values

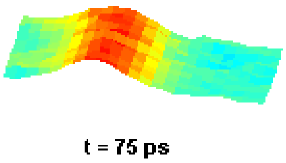

$$\begin{aligned}
w \Rightarrow w_e &= w + \Delta, && (2.67)\\
g \Rightarrow g_e &= g - \Delta, && (2.68)\\
k_1 \Rightarrow k_e &= \frac{w_e}{w_e + 2g_e}, && (2.69)\\
\varepsilon_{\text{eff}} \Rightarrow \varepsilon_{\text{eff}}^t &= \varepsilon_{\text{eff}} - \frac{0.7 \cdot (\varepsilon_{\text{eff}} - 1) \cdot \frac{t}{g}}{\frac{K(k_1)}{K'(k_1)} + 0.7 \cdot \frac{t}{g}}. && (2.70)
\end{aligned}$$

With the equations given above the geometry of the waveguide can be calculated for a given impedance Z and vice versa. An analytical model also is available for multilayer substrates [16, 31, 25].

The transmission losses in a waveguide are composed of ohmic contributions by the conductor, dielectric contributions from the substrate and losses due to radiation or surface waves and higher order modes [97]. The dielectric losses are described by

$$\alpha_d = \frac{\varepsilon_r}{\sqrt{\varepsilon_{\text{eff}}}} \cdot \frac{\varepsilon_{\text{eff}} - 1}{\varepsilon_r - 1} \cdot \frac{\pi}{\lambda} \cdot \tan(\delta) \tag{2.71}$$

and are negligible for a loss tangent of $\tan(\delta) < 10^{-3}$ [97] which is the case for all used materials except FR4 (see chapter 4 and appendix B). The ohmic conductor losses can be obtained by conformal mappings of the current density and were first reported in [158] and applied to a CPW in [71]

$$\begin{aligned}
\alpha_c = \frac{R_s \cdot \sqrt{\varepsilon_{\text{eff}}}}{480\pi \cdot K(k_1)K'(k_1) \cdot \left(1 - k_1^2\right)} & \left(\frac{2}{w}\left[\pi + \ln\left(\frac{4\pi w\,(1-k_1)}{t\,(1+k_1)}\right)\right]\right.\\
& \left. + \frac{2}{w+2g} \cdot \left[\pi + \ln\left(\frac{4\pi\,(w+2g)\,(1-k_1)}{t\,(1+k_1)}\right)\right]\right) \qquad (2.72)
\end{aligned}$$

for all $t > 3\delta$, $t \ll w$ and $t \ll g$. Notable is that the ohmic losses in equation 2.72 increase with surface resistivity R_s and decrease with conductor width w and metallic layer thickness t. As a rough estimate for the highest transmittable frequency through a CPW, the cut-off frequency

$$f_c = \frac{c}{4h \cdot \sqrt{\varepsilon_r - 1}} \tag{2.73}$$

of the TE_0 mode can be used [65, 70] and it becomes obvious that thin substrates with a high relative permittivity support high frequencies. Furthermore, the transmission of HF-signals leads to the skin effect stating that almost the whole charge transfer takes place at the surface of the conductor. The current density j at a high frequency f decreases exponentially from the surface with a certain skin depth δ depending also on the conductivity σ and magnetic permeability $\mu = \mu_0 \cdot \mu_r$.

$$j = j_s \cdot \exp\left(-\frac{d}{\delta}\right) \qquad \text{with} \qquad \delta = \frac{1}{\sqrt{\pi f \sigma \mu_0 \mu_r}} \tag{2.74}$$

The transversal external magnetic field amplitude h_x can be calculated with help of equation 2.75 by using Stokes' theorem and the Maxwell equations. It depends only on the current I and waveguide width w if higher order terms of the waveguide thickness t are neglected:

$$I = \iint_S \vec{j}\,\mathrm{d}\vec{s} = \iint_S \vec{\nabla} \times \vec{h}\,\mathrm{d}\vec{s} = \oint_{\partial S} \vec{h}\,\mathrm{d}\vec{l} = 2wh_x + \mathcal{O}\left(t\right). \tag{2.75}$$

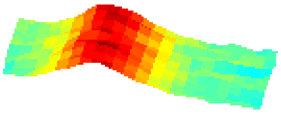

Chapter 3

Simulations

This chapter summarizes simulations that were carried out both before the experiments to improve the design of the setup and the sample system and afterwards to further improve the analysis of the measured data. Some additional simulations and calculations e.g. on magnetic fields of the waveguide and the reset coil in the experimental design and setup chapter are presented later since it is more convenient to show the computed output in line with the sketch of the experimental surroundings.

3.1 XMCD signal to noise ratio

The quality of the XMCD data depends on the converted electrons in the charge-coupled device (CCD) detector emerging from the collected photons and is subject to four major noise sources. First, a photon is absorbed in the CCD silicon depletion layer with a probability given by the quantum efficiency QE and generates $N_e = E_{\mathrm{ph}}/3.65\,\mathrm{eV}$ electrons depending on its photon energy E_{ph} and the threshold for electron-hole pair creation in silicon of 3.65 eV [146, 8, 9, 164]. The number of produced electrons is subject to fluctuation and varies with $\sigma = \sqrt{F \cdot N_e}$ where F denotes the Fano factor [57] that measures $F = 0.115$ for silicon [4]. The mean number of N generated electrons in the CCD chip contributing to the image information is governed by photon shot noise described by a Poisson distribution and scales with $\sigma = \sqrt{N}$ which means the signal to noise ratio (SNR) is proportional to $N/\sqrt{N} = \sqrt{N}$. Read out noise originates from transferring the electrons out of the CCD chip with subsequent amplification and scales with the number of electrons N_r generating the read noise. This factor can be minimized by keeping the read out rate small, which, however, means more time is necessary to acquire an image. The last contribution results from a dark current I_d measured in electrons pixel^{-1} s^{-1} and scales with $I_d \cdot t$ given the integration time t. Chip cooling prevents this effect to dominate. Overall, the signal to noise ratio reads [7, 166]

$$SNR = \frac{N}{\sqrt{N + F \cdot N_e + I_d t + N_r^2}} \quad \text{with} \quad N = I_{\mathrm{ph}} t \cdot QE \cdot N_e \quad \text{and} \quad N_e = \frac{E_{\mathrm{ph}}}{3.65\,\mathrm{eV}} \tag{3.1}$$

for an incident photon flux I_{ph} in units of photons pixel^{-1} s^{-1}. The expected digital counts C in the detector acquired by the camera software are predictable by dividing the number of generated electrons N by the gain factor which quantifies the necessary

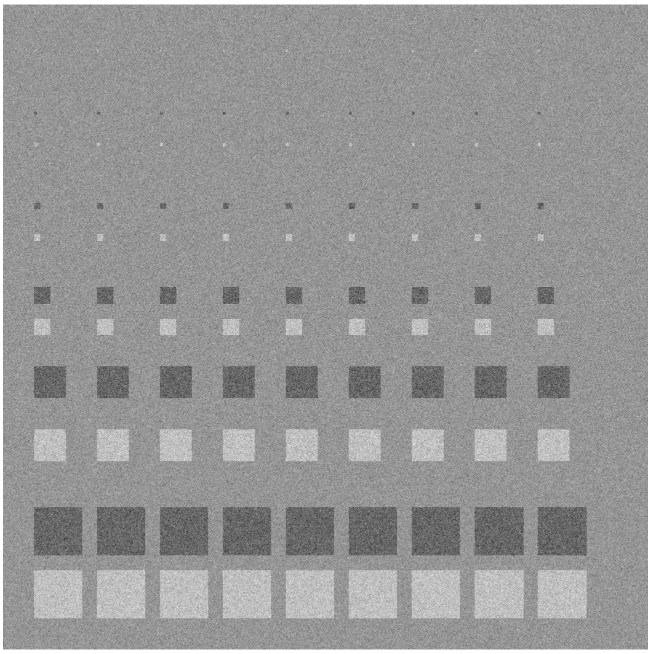

Figure 3.1: Simulation of the XMCD signal $(I^{+}-I^{-})/(I^{+}+I^{-})$ on a 1024 pixel × 1024 pixel detector generated by patterned 10 nm thin permalloy rows with alternating magnetization direction tilted at $\vartheta = 70°$. The calculated image at the nickel L_3 edge after 1 s exposure for each helicity includes optics and sample transmission, detector QE, photon to electron conversion, Fano noise, photon shot noise, dark current as well as readout noise.

electrons to create an analog-to-digital unit (ADU). An estimation of the counts and the noise level on a detector in an X-ray microscope is possible starting with the photon flux (here $8.75 \cdot 10^{10}$ photons/s at the operating photon energies[1] [45]) and taking into account the transmission through condenser, zone plate (typically 10 % diffraction efficiency for each optical element as reported in section 2.2.3) and sample. The sample absorption is modeled by equation 2.38 using the cross sections given in figure 2.14b and the attenuation coefficient for the silicon nitride membrane [195, 87] serving as soft X-ray transparent substrate material in the sample preparation process. Furthermore, the noise characteristics (N_r, I_d) and quantum efficiency of the detectors [6, 165] as well as the photon energy has to be known to estimate the generated electrons per photon.

For the calculation of the expected contrast, parts from the experimental setup and geometry described in chapter 4 are anticipated. In particular, a tilt of the sample at $\vartheta = 70°$ with respect to the photon beam direction is considered (figure 4.17). This tilt is necessary to be able to measure the in-plane component of the magnetization with a reduced signal of $\cos(\vartheta) = 0.34$ compared to a magnetization vector aligned in parallel to the photon direction. In an alloy like permalloy consisting of two magnetic elements, the XMCD measurements can be carried out at both elementary absorption edges with a diverse signal quality. The intensity difference for two magnetization directions leading to the XMCD contrast according to equation 2.40 computes to 1.5 % at the nickel L_3 edge behind a 10 nm thin permalloy sample tilted at $\vartheta = 70°$. The nickel edge was chosen in the experiment because for the same sample the contrast would be reduced to 1 % at the iron L_3 edge. In principle the XMCD signal corresponding to the cross section difference is higher for iron but the permalloy sample consist of only 20 % iron and 80 % nickel so that the measured effect in total is strongest at the nickel edge. Additionally, the efficiency of the phosphor screen used in the gateable detector (section 4.7.1) in the setup increases with higher photon energies [11]. For a 30 nm thin permalloy sample the

---

[1] In fact, the beamline delivers $3.5 \cdot 10^{12}$ photons/s but only 1/40 of the flux is usable for a time-resolved detection in the current setup as we will see later.

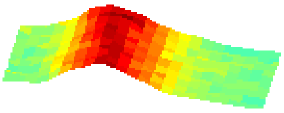

intensity difference measures 4.4 % at the nickel and 2.8 % at the iron edge scaling almost linear with the sample thickness in this regime.

Figure 3.1 shows the resulting XMCD contrast of permalloy elements arranged in rows with alternating magnetization direction taking into account Fano noise, photon shot noise, dark current as well as readout noise of the detector. An exposure time of 1 s for each photon helicity leads to the presented $(I^+ - I^-)/(I^+ + I^-)$ XMCD contrast. Overexposure of the camera sets in when the full well capacity is exceeded stating the number of electrons a pixel can collect before blooming occurs due to charge overflow to adjacent pixels (here typically 100 000 electrons/pixel [6, 165]).

3.2 Landau-Lifshitz-Gilbert solver

The dynamic response of the magnetization $\vec{M}(t)$ of a system in a static external bias field $\vec{H}_{\text{ext}}$ to an arbitrary excitation pulse form and pattern $\vec{h}(t)$ can be calculated by discretely solving the Landau-Lifshitz-Gilbert equation (see equation 2.14) and computing the change on the magnetization vector $\mathrm{d}\vec{M}$ during a short time interval $\mathrm{d}t$. The simulation written in *MATLAB*[2] for this purpose based on the code shown in appendix D numerically solves the LLG equation in an effective field $\vec{H}_{\text{eff}}(t)$ composed of external, excitation and demagnetization field

$$\vec{H}_{\text{eff}}(t) = \begin{pmatrix} h_x(t) - N_x M_x(t) \\ H_{\text{ext}} - N_y M_y(t) \\ h_z(t) - N_z M_z(t) \end{pmatrix} \qquad \text{with} \qquad \vec{M}(t=0) = \begin{pmatrix} 0 \\ M_s \\ 0 \end{pmatrix} \tag{3.2}$$

for a permalloy slab initially homogeneously magnetized in y direction with its saturation magnetization M_s similar to the arrangement explored in the Kerr microscope built in this work. The components of the demagnetization tensor were calculated with equation 2.22 using the fact that the trace equals unity (equation 2.9) and the N_x component vanishes in the thin film limit. The effective slab width w_{eff} was taken from equation 2.27 and the pulse form was modeled by a Gaussian envelope

$$h_x(t) = h_0 \cdot \exp\left(-\frac{(t-t_0)^2}{2\cdot\tau^2}\right) \qquad \text{and} \qquad h_z(t) = -\frac{1}{4}\cdot h_x(t) \tag{3.3}$$

where the relative amplitudes of the x and z components at the edge of the waveguide were extracted out of a *Finite Element Method Magnetics (femm)*[3] simulation (section 4.1.1). The permalloy element of $w = 10\,\mu\text{m}$ width and $t = 30\,\text{nm}$ thickness was modeled with the parameters $\mu_0 M_s = 1.040\,\text{T}$ and $\alpha = 0.008$ in an external field of $\mu_0 H_{\text{ext}} = 60\,\text{mT}$.

The computed reaction of the magnetization z-component $M_z(t)$ to a field pulse of $\mu_0 h_0 = 15\,\text{mT}$ amplitude (estimated by equation 2.75) and different pulse durations τ is plotted in figure 3.2. If the pulse is short enough, the system basically reacts with a damped oscillation at its FMR frequency (figure 3.2a). However, if the pulse duration increases, the oscillation is influenced by the magnetic field of the pulse still present after initiating the dynamics and the response differs from a pure damped oscillation.

---

[2] MathWorks MATLAB, mathworks.com

[3] Finite Element Method Magnetics (femm), femm.info

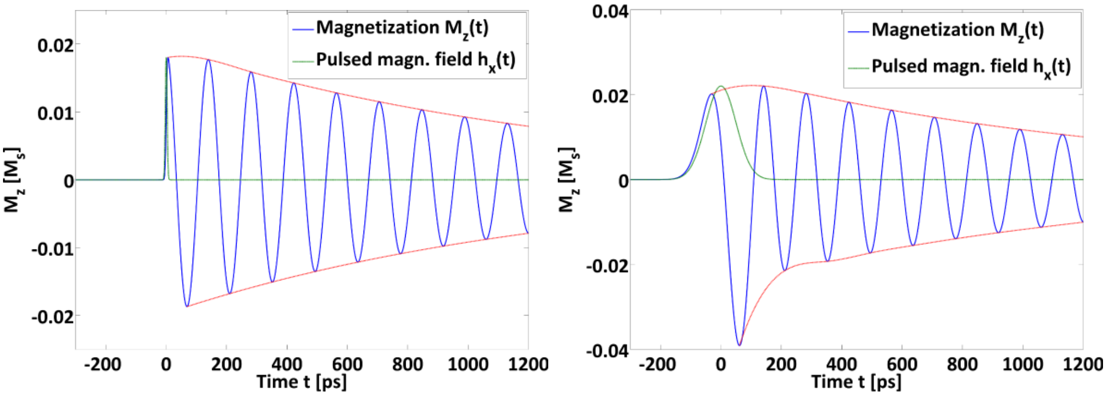

(a) Dynamic response of $M_z(t)$ to a pulse of $\tau = 3\,\mathrm{ps}$ duration.

(b) Dynamic response of $M_z(t)$ to a pulse of $\tau = 50\,\mathrm{ps}$ duration.

Figure 3.2: Simulated response $M_z(t)$ of a magnetic permalloy film (blue curve) of $w = 10\,\mu\mathrm{m}$ width and $t = 30\,\mathrm{nm}$ thickness to a pulsed excitation via $\vec{h}(t)$ (green curve) according to the LLG equation. The traces are calculated given an external field of $\mu_0 H_{\mathrm{ext}} = 60\,\mathrm{mT}$.

3.3 Micromagnetic simulations

Whenever it becomes necessary to simulate the time-evolution of a magnetic system, solving the Landau-Lifshitz-Gilbert equation (see equation 2.13) is essential. In the previous section this has been done in a discrete numerical approach for structureless samples where the magnetization is described by a single, spatially independent vector. For this case the numerical integration of the LLG equation works well and can deal with arbitrarily shaped external static and dynamic magnetic fields. However, in order to simulate real-world extended finite samples, an additional spatial discretization is unavoidable and the LLG equation has to be solved on a grid of finite elements carefully taking into account all the interactions between the individual cells. Long-range interactions mostly are modeled via dipolar coupling and short-range interplay is generally dominated by the exchange coupling. Thus, for obtaining reasonable results, the unit cell size has to be chosen in the order of the exchange length given by equation 2.11 corresponding to approximately 5 nm for permalloy systems. Due to computational limitations the maximum cell size is here set to 25 nm which is a reasonable approximation for permalloy due to the dominating demagnetization energy compared to the exchange energy [206]. All the aforementioned tasks can be carried out by available micromagnetic simulation software packages like the commonly used *Object Oriented MicroMagnetic Framework (OOMMF)*[4]. However, in this work another software package named *Nmag*[5] [61, 56] is operated which provides easy parallelizability to multiple computing units through the *Message Passing Interface (MPI)*[6] in order to minimize the computation time. Moreover, the output is written into a *Visualization Toolkit (VTK)* vector file format readable by sophisticated data analysis and visualization software like the here employed program

---

[4] OOMMF, NIST, math.nist.gov/oommf [50]

[5] Nmag, University of Southampton, nmag.soton.ac.uk/nmag [61, 56]

[6] Message Passing Interface (MPI), mcs.anl.gov/research/projects/mpi

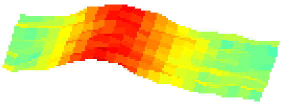

ParaView[7]. Additionally, the simulation problem is defined in *Python*[8] code providing great flexibility on including arbitrary functions and routines for example when defining pulsed fields.

To start a simulation, first the geometry of the sample is defined in a file and discretized by the mesh generator *NETGEN*[9] into small tetrahedral elements used as simulation cells by *Nmag*. Afterwards, a *Python* script similar to the code presented in appendix D is executed creating and controlling the `nmag` simulation object. First, the sample material is defined by providing saturation magnetization $\mu_0 M_s = 1.005\,\mathrm{T}$, exchange constant $A = 13 \cdot 10^{-12}\,\mathrm{J/m}$ and damping parameter $\alpha = 0.01$ for permalloy taken here from [205] for a comparable system. In the script two simulation objects are created, one modeling the real system called `sim` and an additional object `simHD` with an unusually high damping constant of $\alpha = 0.5$ to minimize the computation time when relaxing the system initially to its ground state. Next, the mesh is imported and assigned to these objects with a magnetization pattern close to the ground state and a static external field is defined. Loading the initial pattern is done in favor of saving computing time again; if only one unique ground state exists, relaxing from a random magnetization distribution would end up in the ground state pattern as well after some simulation time. Then, the highly damped system is relaxed to equilibrium by running the `simHD.relax` routine which computes the change on the magnetization by the effective field including all energetic contributions like for example demagnetization field, external fields etc. This is done until the change of the magnetization vector is negligible correlating to a stable pattern. Subsequently, this pattern is transferred into the `sim` object with the physically correct damping constant and the relaxation procedure is repeated. Once the system is in its equilibrium state, the reaction to an external stimulus can be modeled. Therefore, a spatially and temporally confined magnetic field is applied modeled by the rectangular function $\mathrm{rect}(x) = \Pi(x)$ in space and a Gaussian in time

$$h_x(t) = h_0 \cdot \Pi\left(\frac{x - \frac{\sigma_x}{2}}{\sigma_x}\right) \cdot \Pi\left(\frac{y - \frac{\sigma_y}{2}}{\sigma_y}\right) \cdot \Pi\left(\frac{z - \frac{\sigma_z}{2}}{\sigma_z}\right) \cdot \exp\left(-\frac{(t - t_0)^2}{2 \cdot \tau^2}\right) \tag{3.4}$$

including the spatial dimensions σ_x, σ_y and σ_z as well as the pulse duration τ. The relax algorithm is called after applying the field amplitude at each time step and the magnetization vectors on the grid are saved after customizable time steps. For more information on using *Nmag*, the manual [56] shall be considered providing examples with spatially and temporally confined fields on which the simulation code here is based on.

All calculations were carried out parallelized through *MPI* on four cores included in a 64 bit Intel® Core™ i5-2500 central processing unit (CPU) running at 3.30 GHz and equipped with 8 GB RAM in an *Ubuntu*[10] 12.04.3 LTS Linux operating system environment.

3.3.1 Vortex dynamics

The transmission X-ray microscope built in this work was able to unravel the dynamic behavior of rectangular and circular permalloy structures reacting to a strong and short

---

[7] ParaView, paraview.org

[8] Python programming language, python.org

[9] NETGEN, www.hpfem.jku.at/netgen

[10] Ubuntu, Canonical Ltd., ubuntu.com

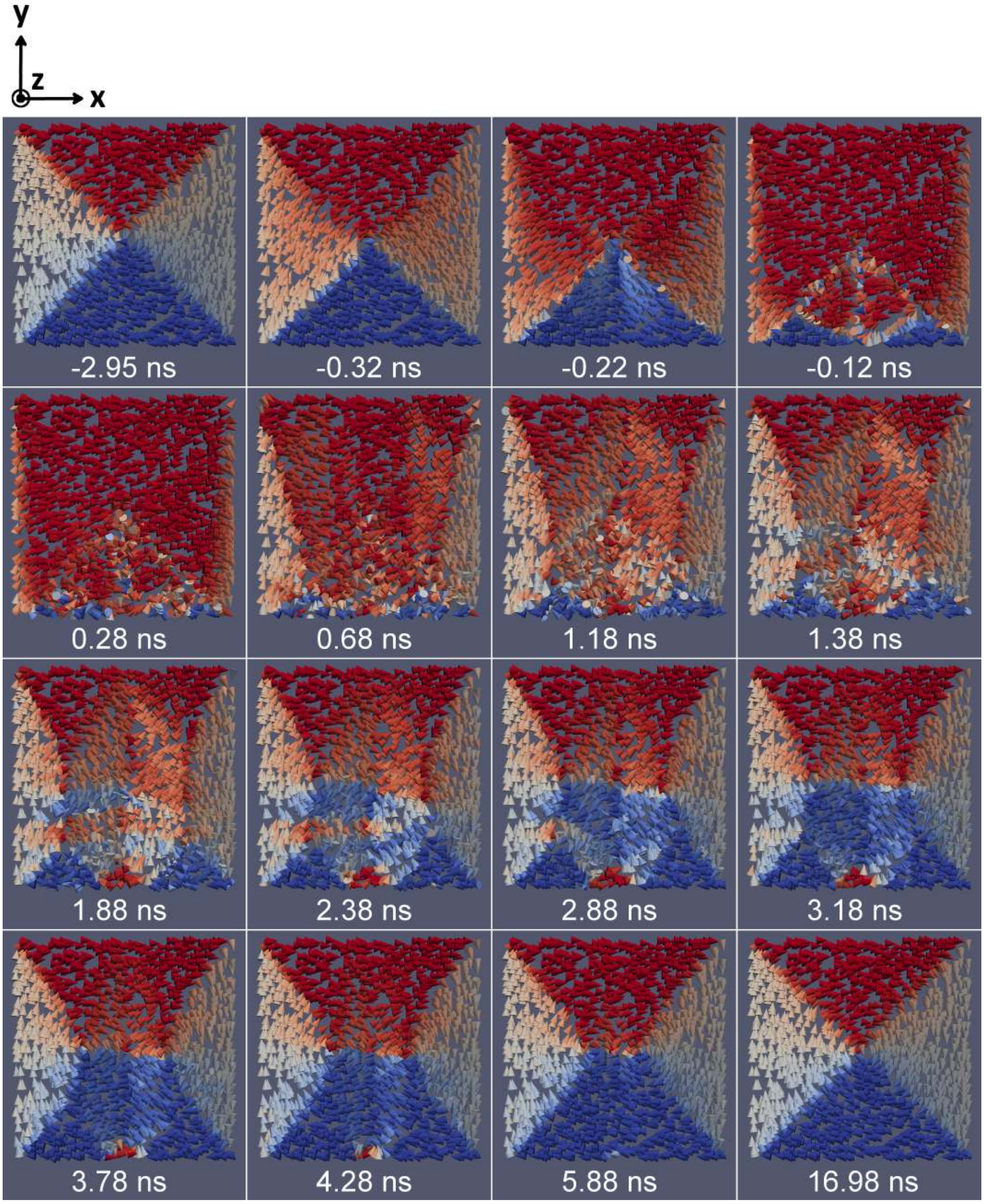

Figure 3.3: Dynamic simulation of the magnetization in a 2 µm × 2 µm permalloy square of 30 nm thickness with an initial Landau flux closure domain pattern excited into positive x direction by a short field pulse of $\tau = 210$ ps duration and $\mu_0 h_0 = 88$ mT peak amplitude at $t_0 = 0$ ns. After destruction of the initial domain pattern, a recovery takes place. Each cone represents a magnetization vector averaged over several grid units color coded by its x component (red: positive, blue: negative).

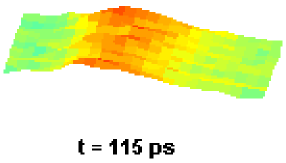

magnetic field pulse of $\mu_0 h_0 = 88\,\mathrm{mT}$ field strength at $t_0 = 0\,\mathrm{ns}$ and $\tau = 210\,\mathrm{ps}$ duration. To reproduce the measured data and gain a better understanding of the involved processes, a micromagnetic simulation was carried out with the parameters available in the experiment. Initially, the equilibrium magnetization distribution of the patterns was calculated by *Nmag* and for a $2\,\mu\mathrm{m} \times 2\,\mu\mathrm{m}$ square or a $2\,\mu\mathrm{m}$ diameter circle of $30\,\mathrm{nm}$ thickness we obtain a vector field curled around a central vortex core. In the circle the variation happens continuously whereas the square features four domains separated by domain walls along the diagonals of the square as it is visible in the first image of figure 3.3. The cones in the image represent a discretized magnetization vector averaged over several grid units because displaying every simulated vector on the mesh would derogate their visibility. Furthermore, the cones are color coded with their individual x component where red corresponds to maximal positive and blue to maximal negative values. The vortex flux closure patterns are the most efficient configuration for the given geometries in terms of minimizing all energetic contributions discussed in chapter 2 including for instance an energy demanding stray field outside the material. A core of a few nanometer radius is nucleated in the center of each vortex [181, 209] where the magnetization is forced to point along the z direction either out of or into the sample plane. The direction of the core (up or down) defines its *polarity* while the sense of rotation (clockwise or counterclockwise) defines the *chirality* of the vortex.

The dynamics presented in figure 3.3 is based on creating a highly out-of-equilibrium state by aligning 85 % of the magnetization into positive x direction via the applied field pulse with its peak amplitude at $t_0 = 0\,\mathrm{ns}$. Besides the left and right particle boundaries, the top, left and right domain almost switch completely 220 ps before the pulse maximum. The boundaries experience a strong demagnetization field leading to a rapid reorientation in these areas by creation of two domain walls which later propagate toward the center. The bottom domain initially aligned antiparallel to the excitation field is hard to switch due to the small torque in this configuration. Subsequently, the domain configuration of the square is split vertically and two vortices emerge on the left and right and eventually combine to a single one in the center. A small domain in the bottom pointing into positive x direction survives for several nanoseconds but aligns with the major domain direction when the vortex pattern is recovered after roughly 17 ns. The simulated spatially averaged magnetization component M_x is plotted together with the measurement in figure 6.22a and several decay slopes are discernible corresponding to the fast decay due to the demagnetization field on the left and right borders and the time-consuming reorientation of the magnetization afterwards. Comparison between simulation and experiment is elaborated in the results chapter in section 6.2. The simulated data of the circular structure is presented in figure C.11 in appendix C and not discussed here explicitly owing to a similar behavior besides a faster decay. The M_x component is shown along with the measured data in figure 6.22b and discussed there.

3.3.2 Non-reversible permalloy chain

As we have seen above, the vortices relax into their initial state automatically after an excitation out of equilibrium. In the introduction the importance of investigating non-reversible systems in need of an active reset was pointed out. For instance, a chain of small rectangular permalloy elements of $1.3\,\mu\mathrm{m} \times 0.3\,\mu\mathrm{m}$ size and $10\,\mathrm{nm}$ thickness separated by a gap of $30\,\mathrm{nm}$ in an external bias field shows such kind of behavior. In the simulation presented in figure 3.4 this chain of five elements was aligned in negative x

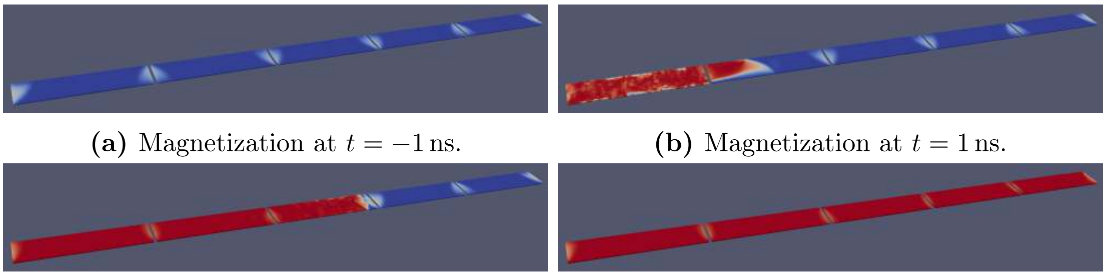

(a) Magnetization at $t = -1\,\mathrm{ns}$. **(b)** Magnetization at $t = 1\,\mathrm{ns}$.

(c) Magnetization at $t = 5\,\mathrm{ns}$. **(d)** Magnetization at $t = 12\,\mathrm{ns}$.

Figure 3.4: Simulation of a permalloy chain consisting of five $1.3\,\mu\mathrm{m} \times 0.3\,\mu\mathrm{m}$ rectangular elements with a magnetization initially aligned to the left (blue color code) in an external opposing field of $\mu_0 H_{\mathrm{ext}} = 11.3\,\mathrm{mT}$ pointing along the chain to the right. If the first element is switched by a short and defined pulse at $t = 0\,\mathrm{s}$, a chain reaction is initiated until all elements are aligned along the bias field direction (red color code).

direction (blue color code) and relaxed in an external static bias field of $\mu_0 H_{\mathrm{ext}} = 11.3\,\mathrm{mT}$ pointing along the positive x direction. The resulting vector field is presented in figure 3.4a and shows that the opposing field already manages to align the magnetization out of the $-x$ direction at the boundaries between the elements. Now, at $t = 0\,\mathrm{s}$ the first element is switched by an external field pulse of $\mu_0 h_0 = 88\,\mathrm{mT}$ amplitude and $\tau = 220\,\mathrm{ps}$ duration and aligns its magnetization along the positive x direction (red color code). The stray field near the gap to the next element is a sufficient stimulus for switching it along the bias field direction and thus one element after another reverses its magnetization (figure 3.4b - 3.4c) until the whole chain is aligned (figure 3.4d). For a new measurement the entire system needs to be reset to its initial state by an external torque. Figure 3.4b indicates that the switching is mediated by a domain wall motion inside a single element.

Figure 3.5 shows the spatially averaged magnetization components in units of the saturation magnetization M_s where a value of $-M_s$ corresponds to a complete alignment in $-x$ direction and $+M_s$ indicates maximal alignment along $+x$ direction. Switching one element by a pulse gives a change in M_x of $0.4M_s$ because five elements are distributed between the accessible range of $2M_s$. The first element excited by the external stimulus reverses its magnetization fast compared to the induced reversal of the remaining rectangles which consumes a bit more than $2\,\mathrm{ns}$ per element. In total, the process takes roughly $10\,\mathrm{ns}$ and should therefore be easily observable in an experiment. The fact that we do not start with a fully aligned chain at $-M_s$ is explained by the rearrangement of the magnetization at the gaps after relaxing. However, we end up at $+M_s$ due to the bias field pointing into the final magnetization direction.

A critical parameter in this experiment is the amplitude of the opposing field because it is adjusted in a way that a small external stimulus is sufficient for launching the chain reaction. If the field is too weak on the one hand, nothing happens after turning one element. On the other hand, an excessively powerful field already aligns the whole chain to $M_x = +M_s$ before the pulse. By varying the amplitude of the external field, the stability range was investigated in the simulation and a dynamic behavior is expected for amplitudes in the range of $\mu_0 H_{\mathrm{ext}} = 10\,\mathrm{mT}$ to $15\,\mathrm{mT}$. However, the switching speed is modified by the field amplitude; so for a reproducible measurement the stability of this quantity is an issue.

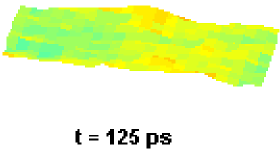

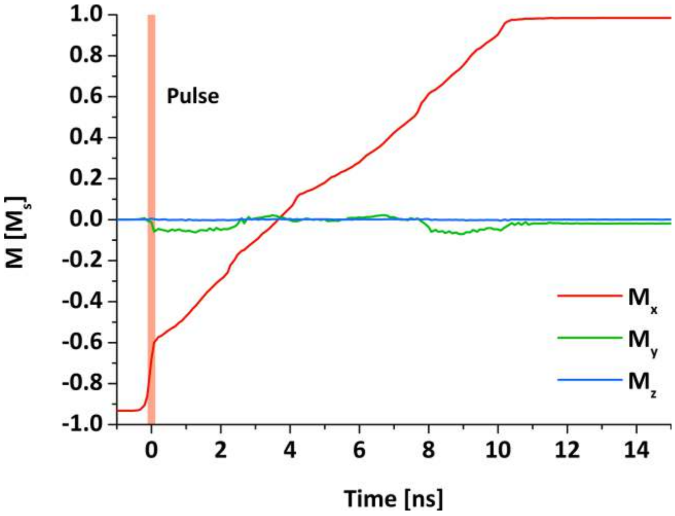

Figure 3.5: Time evolution of the spatially averaged magnetization components in units of the saturation magnetization M_s of the permalloy chain switched by a $\tau = 220\,\mathrm{ps}$ pulse in an external bias field of $\mu_0 H_{\mathrm{ext}} = 11.3\,\mathrm{mT}$. Turning over one element corresponds to a change of $\Delta M_x = 0.4 M_s$ on the ordinate.

A comparable system of smaller single domain $100\,\mathrm{nm} \times 75\,\mathrm{nm} \times 10\,\mathrm{nm}$ permalloy rectangles separated by 25 nm in an opposing field of $\mu_0 H_{\mathrm{ext}} = 35\,\mathrm{mT}$ was calculated by Benjamin Krüger in the theory group of Prof. Dr. Daniela Pfannkuche [126]. Switching one element here consumes 240 ps leading to a propagation velocity of 525 m/s. These values could be reproduced in a simulation with the *Nmag* code but only when a stronger bias field of 78 mT was applied. The discrepancy originates probably from a non-uniform magnetization distribution after relaxing the *Nmag* chain particles while the theoretical calculation relies on single domain particles. Moreover, the calculation was carried out for a chain of 500 elements while the *Nmag* assembly only contained five rectangles due to computational limitations in RAM size and number of CPU cores.

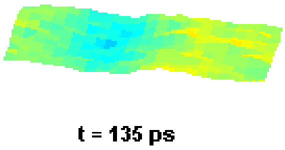
t = 135 ps

Chapter 4

Experimental design and setup

4.1 Samples

This chapter summarizes sample design and preparation. All samples have been created in a clean room facility on 14 mm × 7 mm sized substrates.

4.1.1 Coplanar waveguide design

In order to excite the magnetic system and study its dynamical behavior, a magnetic field pulse has to be transported to the nanostructured sample. This pulse emerges out of a current pulse propagating along a coplanar waveguide since current carrying wires exhibit a vortex magnetic field curled around the wire (compare also figure 2.7). Because the excitation pulses in general are short in the sense of 5 ps to 250 ps, care has to be taken about the dispersion of the pulse and the electrical characteristics (e.g. impedance matching) of the waveguide. Coplanar waveguides (CPW) are well suited and commonly used for high frequency applications in the microwave region of the electromagnetic spectrum and offer the additional advantage of having a nonmetallic gap between conductor and ground electrodes (figure 2.17) providing space for the magnetic sample preparation. The typical outline of the waveguide is presented in the insets of figure 4.1. In this work, the waveguides have an impedance of 100 Ω being rather uncommon in high frequency electronics normally adjusted to 50 Ω but advantageous for larger arrays of nanostructures because the gap between the electrodes increases with the impedance.

The layout of the waveguide has to provide one macroscopic interface to inject the current pulse and another one to terminate it in high frequency RF resistors with low parasitic inductance and capacitance to prevent signal reflections and oscillations for accurate pulse termination. The SMD resistors chosen here[1] for this purpose support a bandwidth of 50 GHz at voltage levels up to 37 V and an average power of 50 mW. In order to distribute the voltage drop and the terminated power, two 50 Ω resistors with a footprint of 1 mm × 0.6 mm are connected in series to provide the termination of the 100 Ω impedance waveguide. Corresponding SMD mounting pads to connect the resistors are foreseen in the layout.

For the current pulse injection, two different options were chosen. In one approach, the photocathode is manufactured directly on top of one end of the waveguide while the other design provides connection pads to another coplanar waveguide for flexible

---

[1] Vishay Sfernice CH0402-50RGF

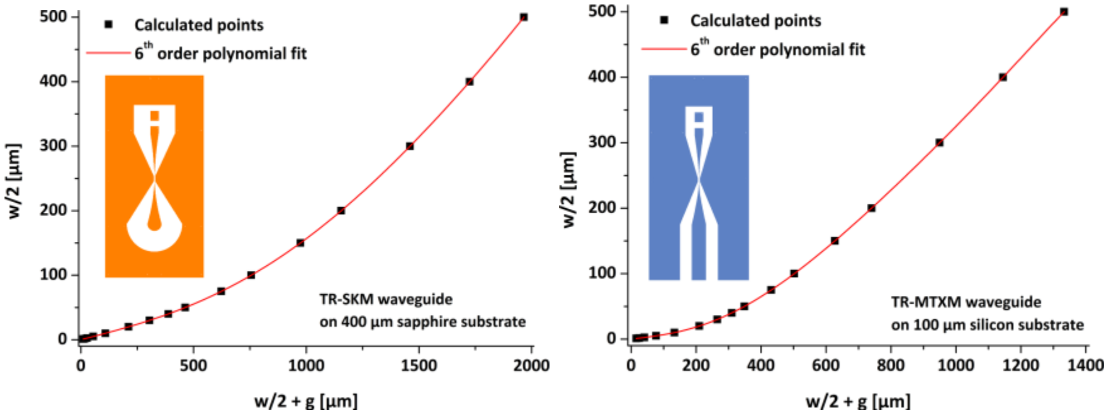

(a) TR-SKM waveguide on sapphire substrate of 400 µm thickness.

(b) TR-MTXM waveguide on silicon substrate of 100 µm thickness.

Figure 4.1: Data points of half conductor width $w/2$ vs. ground plane coordinate $w/2 + g$ obtained with *TX-Line* and polynomial fit of 6^{th} order according to equation B.1 with coefficients listed in table B.1.

mounting of additional electrical interfaces like an insertion circuit launching transient signals from a pulse generator into the waveguide. In both layouts, the width of the inner conductor at the connection point was chosen to be 1 mm being on the one hand big enough to handle the connection to further waveguides at the connection pads as well as providing enough space for a big photocathode in order to minimize space charge effects. On the other hand, the inner conductor should not exceed this width substantially because together with the gap size the substrate dimensions needed for the whole sample would become too large to be handled in the micro- and nanostructuring devices (spin-coater, mask-aligner, electron beam lithography, . . .). Additionally, with larger samples the tilt angle needed for XMCD measurements and thus the XMCD signal amplitude itself would have to be reduced due to collision with the micro zone plate at increased elongation of the sample width in the TR-MTXM (compare also figure 4.17).

The width of the inner conductor is tapered down from 1 mm to 10 µm to increase the current density and thus the magnetic field in the sample region conforming to equation 2.75. The gap size has to be adjusted accordingly to keep the impedance of the waveguide constant (see insets of figure 4.1 and confer equation 2.64). A size of 10 µm in the interaction region was chosen because this width is easily producible by photolithography, provides a gap big enough for the magnetic system at 100 Ω impedance and non-critical ohmic losses (equation 2.72). Furthermore, it is small enough to ensure sufficient current densities but not too small to be thermally destroyed by the pulse power. Subsequently, the width of conductor and gap increases again to 600 µm matching the width of the termination resistors.

The samples for the TR-SKM were created on a 400 µm thick sapphire substrate[2] which was chosen because the substrate material has to be either transparent in the visible electromagnetic spectral range and has to provide a good surface quality for the magnetic structures. Additionally, sapphire provides advantageous electric properties like high insulation, low dielectric losses, a uniform dielectric constant ε_r and good thermal

---

[2] R-lab 2" A-plane sapphire wafer, (400 ± 20) µm thickness, double side EPI polished ($R_a \leq 0.5$ nm)

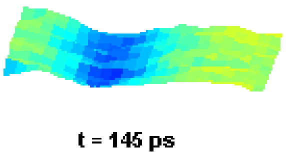

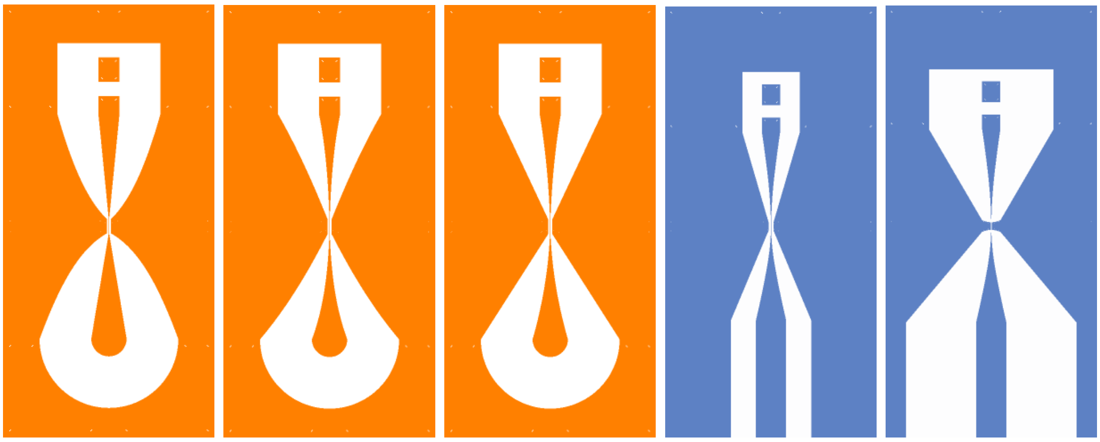

(a) Linear taper of the conductor width w.

(b) Linear taper of gap width g.

(c) Linear taper of sum $w/2 + g$.

(d) $Z_0 = 100\,\Omega$ without accounting for the membrane thickness.

(e) $Z_0 = 150\,\Omega$ with adjusted taper at the membrane.

Figure 4.2: CPWs for TR-SKM on sapphire substrates (orange) and TR-MTXM on silicon substrates (blue). The source with photocathode (orange) or current pulse injection (blue) is located at the bottom, the interaction region with magnetic samples in the middle and the pads for pulse termination in RF-resistors at the top. Colored areas represent the metallic layer while white areas correspond to substrate material. Different approaches of the taper layout are presented as discussed in the text.

conductivity. Since sapphire wafers can be EPI (epitaxy-ready) polished to a surface roughness down to $R_a \leq 0.3\,\text{nm}$ and are routinely used in semiconductor industry, it is an ideal and also cheap material for this purpose. The samples for the TR-MTXM were fabricated on a 100 µm silicon frame with a 200 nm thick silicon enriched nitride (SiRN) window of 250 µm × 250 µm size[3]. Silicon nitride substrates provide the ability to feature a thin window in the nanometer range etched into the sample that is mandatory for the transmission of the soft X-ray photons.

As metallic waveguide layer material 300 nm copper with a cap layer of 5 nm gold to prevent oxidation was chosen. Copper has the advantage of combining a good electric conductivity with a rather good soft X-ray transmission at the L absorption edges of the magnetic $3d$ transition metal elements used in this work. Increasing the thickness of the layer results in lower losses (equation 2.72) and thus less thermal load at high current densities preventing possible damage of the waveguide in the thinnest regions. However, the thickness can not be increased arbitrarily because thick metallic layers complicate the lift-off in the preparation process dramatically (see section 4.1.2) and, additionally, decrease the soft X-ray transmission.

The freeware program *TX-Line*[4] can calculate the width of the gap g for a given conductor size w, substrate thickness h and material, metalization thickness t and impedance Z_0 according to the theory presented in section 2.4. Because the conductor width is reduced over two orders of magnitude, the geometry of the waveguide does not transform smoothly from macroscopic to microscopic sizes by just a linear modification of

---

[3] Silson 14 mm × 7 mm Si frame, thickness 100 µm; 250 µm × 250 µm SiRN window, 200 nm thickness

[4] AWR TX-Line, awrcorp.com/products/optional-products/tx-line-transmission-line-calculator

the conductor or gap size. Decreasing the conductor width linearly and modifying the gap accordingly, results in the waveguide presented in figure 4.2a whereas a linear gap reduction results in the outline in figure 4.2b. However, a rather smooth transition can be achieved by reducing the sum of half the conductor width and the gap size $w/2 + g$ linearly and adjusting the half width of the conductor $w/2$ respectively (see figure 4.2c) due to the natural dependence of the waveguide impedance Z_0 on the ratio $k_1 = w/(w + 2g) = (w/2)/(w/2 + g)$ demonstrated in equation 2.64.

The geometry of the waveguide is calculated for some values of $w/2+g$ by the program *TX-Line* and all points in between are interpolated by a polynomial fit of 6^{th} order (confer figure 4.1 and equation B.1 with coefficients in table B.1 listed in appendix B). The TR-MTXM silicon substrates feature a 200 nm thin silicon nitride window and the waveguide impedance might be adjusted to the thin substrate window thickness over the etching cone. Unfavorably, this would result in a very small gap of 3.3 µm at 10 µm conductor width which is lithographically difficult to manufacture and provides hardly space for larger structures without short-circuiting conductor and ground plane[5]. Thus, the only possibility to do this is to further increase the impedance to $Z_0 = 150\,\Omega$ (see figure 4.2e) resulting in a gap of 11.8 µm in the interaction zone. In order to make the $150\,\Omega$ impedance waveguide still fit the maximum sample size of 14 mm × 7 mm at the input and termination devices, the substrate thickness of 100 µm was chosen as thin as possible and additionally thin substrates provide better HF characteristics since the cutoff frequency depends inversely on the substrate thickness (compare equation 2.73). However, thinner substrates would not be reasonably manageable through all processing steps in the sample preparation. The adjusted taper for the membrane window was actually never used in an experiment in this work (but still successfully manufactured) and the adjustment was neglected over the short 250 µm × 250 µm sized membrane resulting in the $Z_0 = 100\,\Omega$ impedance waveguide layout in 4.2d. The waveguide geometry for the silicon frame applied to the thin silicon nitride membrane results in an impedance of $Z_m = 240\,\Omega$ and leads to a reflected voltage amplitude U_r compared to the incident voltage peak U_0 at the boundary with a ratio given by the reflection coefficient [22]

$$\Gamma = \frac{U_r}{U_0} = \frac{Z_m - Z_0}{Z_m + Z_0} = 0.412. \tag{4.1}$$

The effectively reflected amplitude is expected to be much smaller because the impedance mismatch does not occur abrupt in the sense of a discrete change but continuous via the etching cone of the membrane window where the substrate thickness decreases smoothly.

Using the fit from figure 4.1, the final layout of the waveguides is coded into a binary GDSII file commonly used in semiconductor industry and readable by electron beam lithography facilities. This file consists of a collection of polygons and is generated by a *Python* script with help of the open source package *gdspy*[6]. The geometry included in this file is transformed into a chrome blank lithography mask on a quartz substrate with opaque and transparent areas by the company *compugraphics Jena* and is used as a reticle in the further sample preparation procedure.

Finally, a simulation of the current and magnetic field distribution at the interaction region was carried out using the software *femm*. For the simulation, a current of 0.5 A

---

[5] This problem could be overcome by using for example an insulating hydrogen silsesquioxane (HSQ) layer between magnetic sample and waveguide which would complicate the preparation process by additional steps and is avoided for this reason.

[6] gdspy, gdspy.sourceforge.net

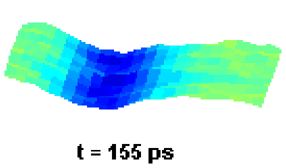

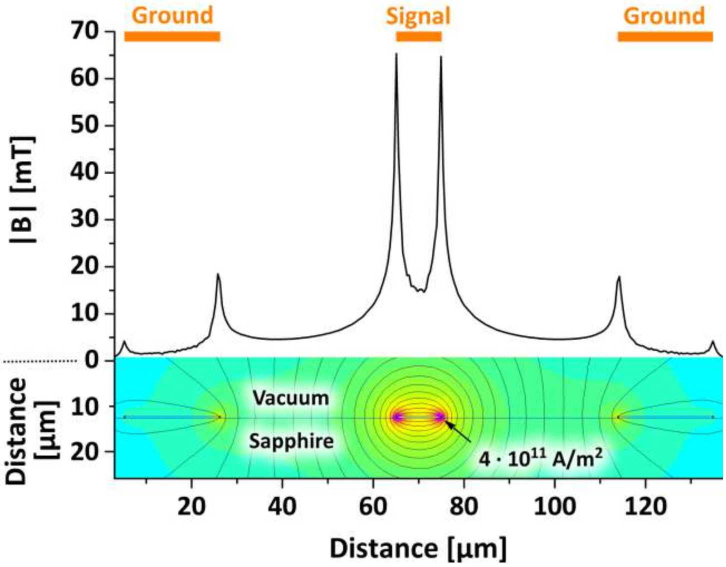

Figure 4.3: *femm* simulation of the magnetic field configuration and amplitude generated by the waveguide on a sapphire substrate. A peak current of 0.5 A generates a field of up to 65 mT which is maximal at the surface of the waveguide due to the skin effect that leads to high current densities of $4 \cdot 10^{11}$ A/m^2 at the borders of the conductor. The color code resembles the magnitude of the $|\vec{B}|$ field where purple corresponds to high and blue to low amplitudes.

corresponding to the peak current of the photocathode test setup (see section 5.1) was launched into the waveguide of $w = 10\,\mu\text{m}$ width and $t = 300\,\text{nm}$ copper thickness of impedance $Z_0 = 100\,\Omega$. The simulation is carried out for a signal frequency of 30 GHz corresponding to the highest frequency in a 15 ps FWHM pulse when the Fourier limited time bandwidth product of a Gaussian pulse $\Delta t \cdot \Delta f \geq 0.44$ applies. Owing to the short pulse duration, the duty cycle composed of pulse duration and repetition rate is small which leads to a continuous power dissipation in the µW range at the thinnest part of the waveguide conductor. The magnetic field distribution is presented in figure 4.3. Notable is the high current density of $4 \cdot 10^{11}$ A/m^2 at the edges of the conductor due to the skin effect (equation 2.74) present at the high frequencies included in the short pulses. The magnetic field amplitude at the surface of the substrate is also plotted along the cross-section of the waveguide and amplitudes of 65 mT can be reached directly at the highest current densities.

4.1.2 Preparation

All samples have been created in the class 100/1000 clean room of the University of Hamburg by lithographic techniques and the exact processing parameters are collected in detail in appendix B. The preparation is divided into two sub-processes, namely the fabrication of the (nano)magnetic system and the manufacturing of the waveguide needed for the excitation of the system. In general, first the magnetic layers are deposited since their properties depend on the quality of the substrate and a preceding waveguide deposition might corrupt the surface quality during the processing steps and leave remnants on the substrate. The whole preparation process is outlined in figure 4.4 and discussed in the following subsections.

Sample preparation

The structure of the magnetic sample system is inscribed into an electron-beam resist by electron-beam lithography (EBL). For this purpose the substrate is first coated with

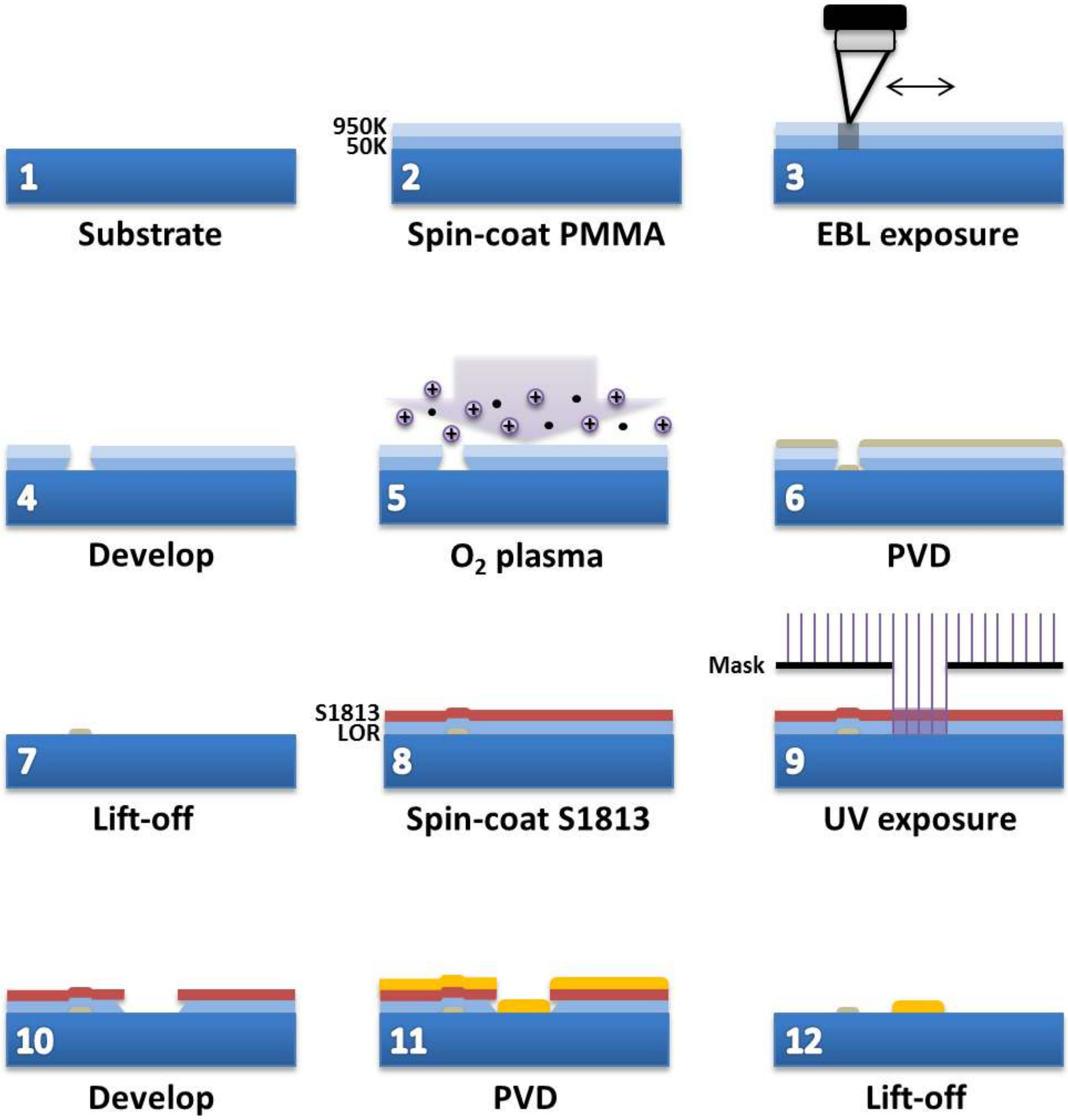

Figure 4.4: Outline of the sample preparation process. The substrate (1) gets spin-coated with a double layer of PMMA-50K and PMMA-950K electron beam resist (2) which is exposed during EBL in an SEM (3) that writes the structure pattern. Developing removes the exposed areas (4) with an undercut profile due to the double layer system. After cleaning in an oxygen plasma (5), the magnetic sample material is deposited by physical vapor deposition out of a heated boat (6). A lift-off process in acetone (7) removes the unwanted material on the resist. For the preparation of the waveguide on the same sample, a double layer consisting of lift-off resist (LOR) and photoresist (S1813) is spin-coated onto the substrate (8). Exposure to UV light through the chrome blank in a mask aligner leads to the structure transfer onto the sample (9) carried out by developing the resist layers (10) with an undercut profile advantageous for the lift-off. Deposition of the material is done in another PVD step (11) out of a boat and an electron beam evaporator. Eventually, the remaining resist together with the spare metal is removed in a final lift-off process (12).

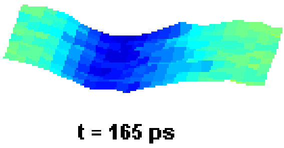

a double layer of poly(methyl methacrylate) (PMMA) resist with different molecular weights (50K and 950K) resulting in an undercut profile for a reliable lift-off process later in the preparation process. First, the PMMA-50K resist with a higher sensitivity ($\approx 20\,\%$ more sensitive compared to PMMA-950K) is spin-coated onto the substrate by injecting the resist onto the sample that is ramped afterwards to a defined rotational speed with an adjustable ramp and rotation duration resulting in a homogeneous layer of predictable thickness. The deposited layer is pre-baked on top of a hotplate to harden the layer, spin-coated with the less sensitive PMMA-950K electron-beam resist and finally the whole system is baked-out on the hotplate to reach the glass transition of the PMMA.

The resist-coated substrate is now ready for exposure and can be transferred into the EBL chamber where the electron beam writes programmed patterns specified in a GDSII polygon file (also generated with *gdspy*) with a defined dose into the PMMA resist. The samples are installed on conductive adhesive tapes to prevent charging of the substrate and thus a distortion of the written pattern. Next, the sample has to be aligned and positioned correctly and the electron beam has to be focused onto the sample by monitoring dirt or scratches during focusing in the imaging mode of the scanning electron microscope (SEM). Additionally, a small spot can be burnt into the resist by exposing a single position of the sample to the beam for $\approx 30\,\mathrm{s}$ which should provide a small structure to focus onto more precisely afterwards. Depending on the substrate (in this case silicon nitride membranes or sapphire wafers), back-scattering of the electrons in the substrate has to be taken into account leading to an exposure of neighboring areas. This so called proximity effect causes for example the merging of two adjacent structures separated by a small distance and in general reduces the contrast of the written patterns. In the 200 nm thin silicon nitride membranes the proximity effect is expected to be small because the membrane is rather transparent to the 10 keV electron beam but for the sapphire substrate it has to be considered. For this reason a GDSII file with a test pattern has been created and written into a PMMA double layer coated sapphire substrate with different exposure doses ranging from $50\,\mathrm{\mu C/cm^2}$ to $150\,\mathrm{\mu C/cm^2}$; the best results were obtained at a dose of $80\,\mathrm{\mu C/cm^2}$ to $90\,\mathrm{\mu C/cm^2}$. For all samples an aperture in the electron beam of $10\,\mathrm{\mu m}$ and a write field of $600\,\mathrm{\mu m} \times 600\,\mathrm{\mu m}$ is used. The large write field is necessary because together with the magnetic system, also alignment structures have been written into the sample to enable an accurate overlap with the waveguide mask later in the preparation schedule.

After the patterning by scanning the electron beam over the resist, the substrate is developed and areas exposed by the electron beam are removed since PMMA is a positive photoresist and the electron beam cuts the polymer chains during exposure. The chemically modified environment of the patterned areas is now sensitive to a developer and the material is removed by dipping the sample into the developer solution for a defined time. This process is stopped subsequently by bathing the sample in isopropyl alcohol (IPA).

With EBL small structures of only a few nm can be written which is necessary for the TR-MTXM samples. However, for the TR-SKM samples the structure sizes are big enough that there is no need for EBL (which is of course possible as well) and this step can be replaced by photolithography with a suitable mask similar to the fabrication of the waveguides (see next subsection).

Now that the structure has been transferred into the resist, the sample material can be applied. Before deposition the sample is cleaned in an oxygen (O_2) plasma chamber to remove dirt and resist remnants from the substrate surface resulting in a better contact and adhesion of the material on the substrate. Afterwards, the magnetic permalloy ($Ni_{80}Fe_{20}$) material is evaporated out of a heated tungsten boat by physical vapor deposition (PVD) inside a vacuum chamber with a cold trap to maintain a good base pressure of $1 \cdot 10^{-8}$ mbar to $1 \cdot 10^{-7}$ mbar despite short pumping times. The evaporation process is monitored by a quartz crystal located near the sample providing information about deposition rate and deposited film thickness. When finished, the whole sample is covered with a permalloy layer and in the next step the metal on the PMMA resist has to be removed to finalize the structure transfer.

This last step is called lift-off and is carried out in a bath of acetone that dissolves the PMMA layers and frees the metal from the substrate except of course where it is directly in contact with it. In this step the use of the PMMA 50K/950K double resist layer pays off because it generates an undercut in the profile (figure 4.4) so that the acetone can attack the PMMA due to a non-continuous metal layer. After several hours in the acetone bath, the process is complete and the pre-defined structure in the GDSII polygon file is transported into a patterned thin metallic layer onto the substrate. If the lift-off fails to remove some areas, carefully wiping over the sample with a soft swab or ultrasonic cleaning might help though the latter is not possible for the silicon nitride membrane substrates because the thin membrane can not withstand the ultrasonic vibrations. Anyway, by using the double layer system this is in general not required.

Waveguide preparation

The previously described preparation of the magnetic sample system is now complete and followed by the manufacturing of the waveguide. The substrate including the magnetic structures again is spin-coated with an ultraviolet (UV) sensitive double layer photoresist system to generate an undercut profile for a reliable lift-off. The first layer is a special lift-off resist (MicroChem LOR 5A and MicroChem G Thinner in a mixture of 50:50) baked out on a hotplate on top of which the Shipley S1813 photoresist is spin-coated and baked out accordingly. The sample is now ready for exposure.

The design of the waveguide calculated and explained in section 4.1.1 was defined in a GDSII file and transferred onto a chrome mask on a quartz substrate by a company (see above). This reticle is either transparent (no chrome deposited) or opaque (chrome deposited onto quartz substrate) on the predefined areas in the GDSII file and loaded into a mask aligner[7] for the lithography process together with the magnetic system on the sample substrate. Using an optical microscope included in the mask aligner, the sample is positioned under the chrome blank by translation via micrometer screws. For this purpose several alignment markers are imprinted into the waveguide design and into the magnetic sample pattern. They are overlapped in the mask aligner to ensure that the conductor of the waveguide is located at its dedicated position in order to excite the intended fractions of the system. When proper alignment is achieved, the sample is lifted up toward the lithography mask and brought into soft contact with the mask. The exposure can begin and the mask aligner automatically replaces the microscope with a UV lamp to expose the photoresist through the mask for a preset time controlled by a shutter (see figure 4.4).

Developing the exposed substrate leads to the removal of the illuminated areas be-

---

[7] SÜSS MicroTec MJB4 mask aligner

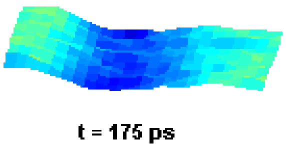

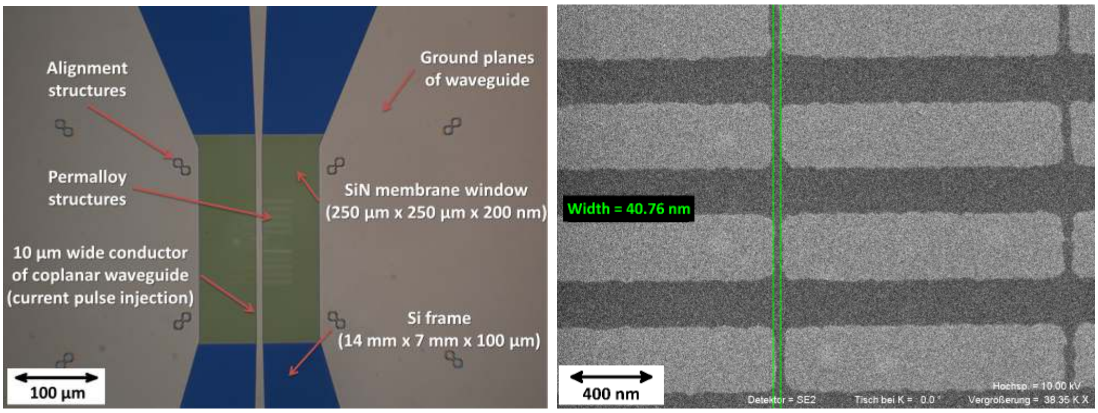

(a) Microscope image of the finished sample's central part.

(b) SEM image of permalloy elements in an array separated by ≈ 40 nm.

Figure 4.5: TR-MTXM sample including of permalloy structures and a coplanar waveguide on a silicon substrate with silicon nitride membrane.

cause polymer bonds have been broken by the UV light. In this case, the developing process is stopped in deionized (DI) water. Cleaning with an oxygen plasma is omitted here due to the risk of oxidization of the present magnetic layer.

Subsequently, PVD is carried out inside a vacuum chamber where thermally evaporated metal condenses either directly at the substrate where the resist was removed by the developer or on top of the remaining photoresist. Here, 300 nm copper (Cu) is evaporated out of a tungsten boat that is protected against oxidation by depositing 3 nm gold (Au) out of an electron-beam evaporator installed in the same vacuum chamber. Some test waveguides on sapphire substrates were manufactured without the lift-off resist but with a bottom 5 nm chromium (Cr) layer deposited out of the electron-beam evaporator as adhesion promoter. The chromium layer was omitted for the samples with magnetic material because if oxidization occurs, the resulting chromium oxide may influence the magnetic response of the system [204].

During the lift-off process, the remaining resist below the metallic layer is removed in a bath of acetone and lastly, the structure of the waveguide remains on the substrate in form of metallic areas representing conductor, ground planes etc. In the areas where magnetic structure and waveguide coincide, the magnetic layer is now buried under the waveguide material.

A section of a completed TR-MTXM sample is presented in figure 4.5 where the microscope image shows the central part of the sample around the silicon nitride membrane with the waveguide and the permalloy structures. In the SEM image a zoom-in to the permalloy structures is visible with an array of elements featuring a small gap of only 41 nm.

Additional steps

In order to terminate the current pulse at the end of the waveguide, the tiny resistors mentioned in section 4.1.1 fitting the CPW design have to be fixed to the dedicated mounting pads defined in the waveguide layout. They are glued onto the waveguide with help of tweezers and needles under a microscope using conductive epoxy adhesive which is

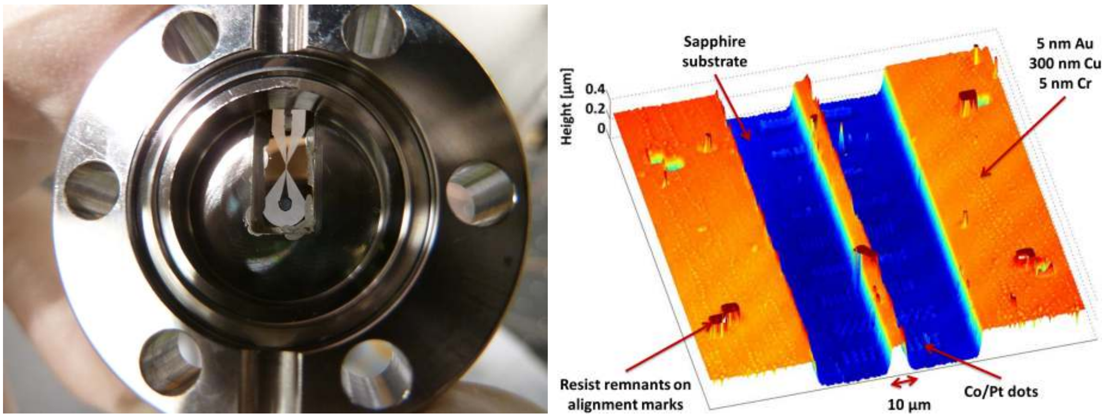

(a) Photo of the complete TR-SKM sample flange (CF16) with resistors and Mg photocathode.

(b) Interference microscope image providing depth information of the inner part of a waveguide with Co/Pt structures in the vicinity of the conductor.

Figure 4.6: TR-SKM sample flange with interferometric image of the interaction zone height profile.

cured by heating the sample on a hotplate for 10 min at 80 °C to ensure a low-resistance contact. SMD soldering paste is not feasible for fixation because it destroys the thin metallic layer during bake-out.

All TR-SKM samples additionally need the photocathode that is deposited onto the dedicated area by PVD of magnesium (Mg) grains out of a tungsten wire in a custom-built evaporation device at a base pressure of $1 \cdot 10^{-6}$ mbar to $2 \cdot 10^{-5}$ mbar. The macroscopic mask in this case is produced by milling a hole into a polyethylene sheet covering the sample besides the cathode area. To ensure proper shielding of the whole substrate this step has to be done before gluing of the resistors.

After deposition of the Mg photocathode and mounting of the termination resistors, the TR-SKM samples are ready for assembly into the experimental setup. Because the cathode has to be located inside the vacuum, the sapphire substrate is installed into a slot of a special CF16 adapter flange (see figure 4.6). By applying a UV curable adhesive[8] the sample is coupled to the flange and vacuum sealed. Finally, the ground planes of the CPW need to be connected electrically to the metal of the CF16 flange on the vacuum side by conductive silver to ensure proper grounding.

Concerning the TR-MTXM samples the photocathode is not attached directly onto the substrate due to space constraints in the X-ray microscope but contacts are available for the connection to either an external cathode or an electrical pulse generator. Owing to the high bandwidth of the pulses, the connection has to be established by high frequency components as well. For this purpose two printed circuit boards (PCBs) with additional coplanar waveguides were designed. The production of the circuit boards was outsourced to a commercial PCB service by handing in the layout files defining the geometry of the substrate and the copper layer. In this case a standard epoxy FR4 substrate ($\varepsilon_r = 4.8$) of 1 mm thickness and a footprint of 20 mm × 7 mm was used with a 35 µm copper (Cu) layer on top since these boards are commonly used in electronics providing a cheap solution.

---

[8] Dymax OP-29-Gel

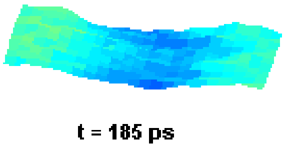

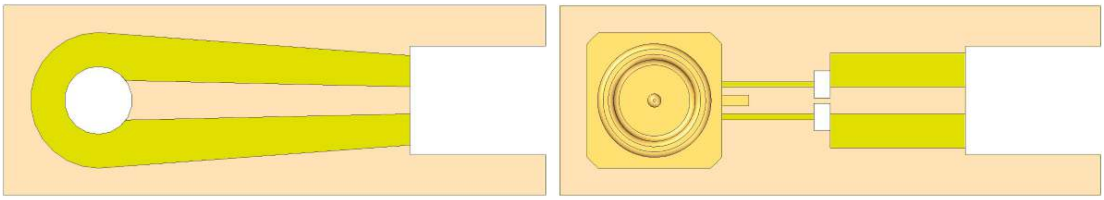

(a) Adapter PCB for laser setup with Mg photocathode and waveguide of 100 Ω impedance.

(b) Adapter PCB for pulser setup with SMP plug and two 200 Ω RF resistors for impedance matching from 50 Ω to 100 Ω.

Figure 4.7: PCB adapters of footprint 20 mm × 7 mm with a cutaway of 5 mm × 4 mm size. Parameters in table B.7

The use of solder resist was omitted because of possible outgassing under vacuum and electroless nickel immersion gold (ENIG) was chosen as a surface plating.

At the interface to the sample contacts the waveguide has to hold an impedance of 100 Ω with an inner conductor size of 1 mm. The connection is established via the flip-chip technique by turning the sample upside-down (figure 4.8a) so that the copper connectors of the two circuits face each other and then brought into contact with conductive silver between the connecting tracks for a reliable contact and for fixation. The waveguide of the photocathode PCB has a constant impedance of 100 Ω with a pad of 1.5 mm for magnesium deposition which is tapered down linearly to an inner conductor size of 1 mm compatible with the contact size of the sample (see figure 4.7a). The parameters are collected in table B.7 given in appendix B.

For the adapter PCB to connect the electric pulser, however, a constant impedance of 100 Ω for the CPW is not applicable because the picosecond pulse generator[9] expects a 50 Ω connection with an appropriate termination as almost all high frequency devices. This means the impedance has to be adapted from a 50 Ω device to a 100 Ω system. The transition region corresponds to a network where a 50 Ω transmission line branches into two 100 Ω waveguides connected in parallel and each terminated by 100 Ω resistors. Practically, one of the two lines is the waveguide to the sample and the other one solely consists of two 200 Ω RF resistors directly in the transition zone connected in parallel from the conductor to the ground planes for a symmetric termination (see figure 4.7b). Behind this point the geometry of the waveguide (in this case the gap size) changes since it is now a 100 Ω CPW and half of the input current amplitude is lost due to the 200 Ω impedance matching resistors. Since the output port of the pulse generator is an SMA flange, the signal is transported through a high quality 18 GHz SMA cable[10] and feedthrough[11] with 50 Ω impedance into the vacuum where it passes an SMA to SMP adapter because the connection to the CPW on the PCB adapter is established by an SMP PCB connector[12] glued onto the circuit board by conductive epoxy adhesive. SMP is chosen here over SMA because the plug has not to be tightened by screwing which can be dangerous due to the torque acting on the glued connection and onto the sample. The high frequency properties of SMP are comparable or even superior to SMA.

Lastly, the reset coil (see section 4.2) with an iron yoke is added to the TR-MTXM

---

[9] FID GmbH FPG 02-200PM, 50 V to 200 V, 220 ps to 250 ps pulse duration, 200 kHz repetition rate

[10] Rosenberger 32S-RTK-Flex 405-32S and 32S-RTK162-32S, 18 GHz

[11] allectra 242-SMAD18G-C16, 18 GHz

[12] Rosenberger 19S101-40ML5, 26.5 GHz

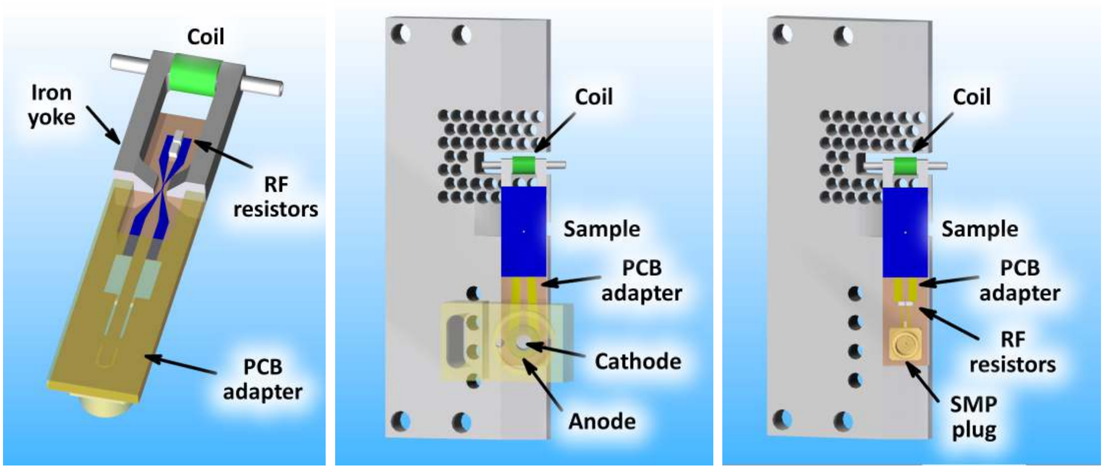

(a) Flip-chip mounting of the sample to the adapter PCB. **(b)** TR-MTXM sample with photocathode setup. **(c)** TR-MTXM sample for use with the picosecond pulse generator.

Figure 4.8: CAD image of the complete TR-MTXM sample consisting of the silicon frame including the magnetic sample on the membrane, waveguide and RF-resistors as well as reset coil with iron yoke and the PCB adapters. All parts are mounted onto a titanium sample holder.

samples. Eventually, the whole sample system shown in figure 4.8a is attached to a sample holder made out of titanium (Ti) due to its small thermal expansion coefficient which is important because the coil transfers heat into the system resulting in drifts of the sample in the X-ray microscope. The heat transfer is reduced by skeletonization of the sample holder around the coil. In the photocathode setup (figure 4.8b) a PEEK part holding the aluminum anode (see section 4.3) is connected to the Ti holder. Notable in figure 4.8 (or even more prominent in figure 4.16) is also that the sample is already positioned under a certain angle of 20° with respect to the normal plane of the photon beam to be sensitive to the in-plane magnetization component via XMCD.

4.2 Reset coils

A non-reversible magnetic system needs an active external stimulus in order to reset it into a defined state before a new pump-probe cycle can begin (compare also figure 1.1). In this experiment this pulse is generated by a small coil. Because the sample is pumped at 130.1 kHz repetition rate equal to the revolution frequency of the storage ring either by the synchronized laser or by the picosecond pulse generator, the reset pulse has to be applied at the same rate. The coils are in principle suitable for both, the TR-SKM and TR-MTXM experiments and are ready to use in a vacuum environment.

To be able to switch thin-film structures magnetized in the sample plane as well as out-of-plane magnetized perpendicular magnetic anisotropy (PMA) systems, two different coil designs have been developed and tested. One coil generates a field pulse along the substrate plane using an iron yoke. Another air core coil that is placed on top of the sample produces field pulses directed perpendicular to the substrate plane. Both layouts with the simulated magnetic field distribution (*femm*) are shown in figure 4.9.

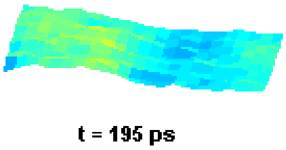

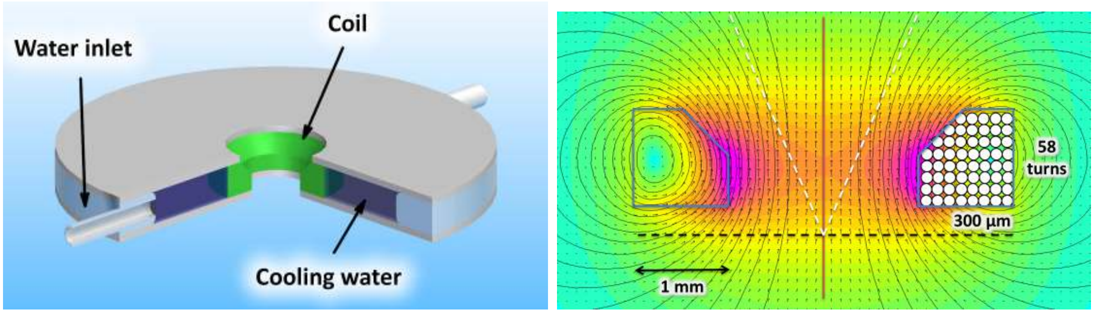

(a) CAD image of coil assembly for switching PMA systems.

(b) Simulation of the magnetic field of the air-core coil.

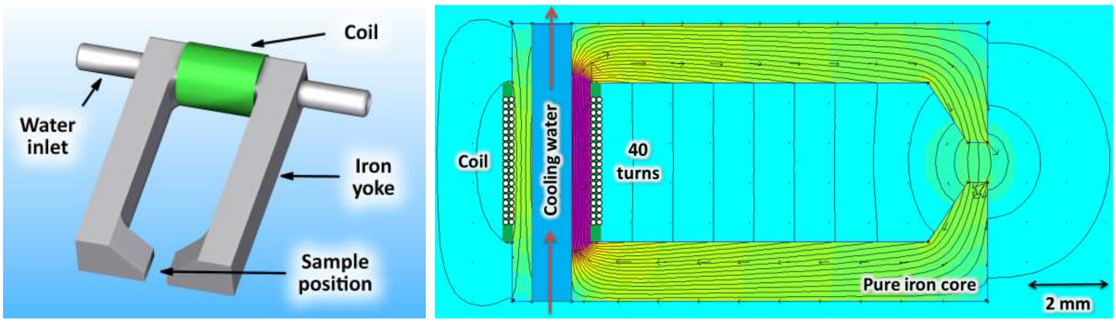

(c) CAD image of coil for switching in-plane magnetized systems.

(d) Simulation of the magnetic field inside iron yoke and in the gap where the sample is located.

Figure 4.9: Water-cooled reset coil designs with simulated magnetic field distribution.

The lateral reset device is a 4 mm diameter air-core coil of $L = 10\,\mu\text{H}$ inductance and $R = 0.7\,\Omega$ ohmic resistance with a beveled edge to provide enough space to fit the aperture cone of the focusing objective ($NA = 0.4$) in the TR-SKM indicated by the white dashed line in figure 4.9. The coil is wound out of 48 turns of 150 µm diameter enameled copper wire. The black dashed line represents the sample position roughly 300 µm away from the coil where a magnetic field of up to $\approx 150\,\text{mT}$ is producible in the center of the coil at 7 A current pulse amplitude that can be reached with this design (see chapter 5.6).

The in-plane reset coil is wound out of 40 turns around an iron (Fe) yoke and resulting in $L = 14\,\mu\text{H}$ inductance and $R = 0.22\,\Omega$ ohmic resistance. The iron guides the magnetic field close to the sample position where an amplitude up to 120 mT is achievable at 7 A peak current. The iron yoke becomes necessary due to the substrate dimensions because air-core coils would have to be 3.5 mm away from the sample position which is too far to provide a field strong enough to reset the nanomagnets.

Both coils have to be water-cooled outside and inside a vacuum environment to dissipate the heat generated owing to the ohmic power loss of $\approx 10\,\text{W}$ (see equation 4.2) at the coils at 7 A current pulse amplitude and a typical pulse duration of 1.5 µs to 2 µs at 130.1 kHz repetition rate.

4.2.1 Reset coil driver

A custom built driver was designed and tested to deliver the required current pulses. The circuit diagram is depicted in figure E.1 in appendix E. Basically, it consists of two

IRF530 metal-oxide semiconductor field effect transistors (MOSFETs) in a half-bridge configuration operated by an NCP5111 MOSFET driver. Because of the high repetition rate, the gate resistors of the MOSFETs have to be adjusted very carefully for keeping the ohmic switching losses small. Otherwise, they experience a huge thermal load and may be destroyed. Additionally, the slopes of the switching pulse must not be to steep because this would result in ringing of the pulse and in unwanted electromagnetic pulses (EMPs) released from the circuit leading to interferences with other electronic devices. The gate resistor dimension is a trade-off between minimal switching losses and minimal EMP.

Allowing an operation at 130.1 kHz repetition rates needs a time constant $\tau = L/R$ in the microsecond regime for the coil driven by the MOSFET half-bridge. This means a low-inductive resistor[13] of $R = 10\,\Omega$ has to be used in series with the $L = 10\,\mu\text{H}$ to $15\,\mu\text{H}$ inductance of the coil because the ohmic coil resistance is not sufficient to reach this time constant. In consequence, the additional resistor experiences a huge thermal load of $\approx 130\,\text{W}$ due to the high voltage drop at 7 A current pulse amplitude. A power rating of 300 W was chosen to safely endure the power dissipation according to table 4.1. Cooling of the resistor has to be performed as effectively as possible and is implemented here by a combination of a passive cooler in good thermal contact together with a fan.

$$P = \underbrace{f \cdot \tau}_{\substack{\text{duty}\\ \text{cycle}}} \cdot \underbrace{R \cdot I}_{\text{voltage } U} \cdot I \tag{4.2}$$

Table 4.1: Power dissipation P of the coil as well as resistor and MOSFETs in the driver calculated by equation 4.2.

	Duty cycle $f \cdot \tau$	**Ohmic resistance R**	**Current I**	**Power P**
Coil	$130.1\,\text{kHz} \cdot 2\,\mu\text{s}$	$0.7\,\Omega$	7 A	**10 W**
Resistor	$130.1\,\text{kHz} \cdot 2\,\mu\text{s}$	$10\,\Omega$	7 A	**130 W**
MOSFET	$130.1\,\text{kHz} \cdot 1\,\mu\text{s}$	$0.16\,\Omega$	7 A	**1 W**

4.3 Photocathode

The outline of the photocathode setup for generation of the current pulses is sketched in figure 4.10. A magnesium (Mg) layer provides the source of the electrons generated by the photoelectric effect and extracted via a high voltage (HV) generated by a power supply[14]. Magnesium is chosen because its work function $W_0 = 3.66\,\text{eV}$ [184] is below the photon energy $E_{\text{ph}} = 4.8\,\text{eV}$ of the ultraviolet (UV) fourth harmonic of the available pulsed laser radiation at a wavelength of 258 nm. Additionally, Mg cathodes are in need of only moderate vacuum requirements (10^{-8} mbar to 10^{-7} mbar) at long lifetimes compared to other materials with a high quantum efficiency like Cs_2Te.

---

[13] Vishay Sfernice LPS 300H, $10\,\Omega$, 300 W at 85 °C, $L \leq 0.1\,\mu\text{H}$

[14] CAEN N1471B, 5.5 kV, $300\,\mu\text{A}$, 5 nA monitor resolution

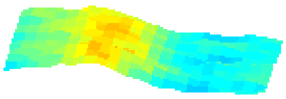

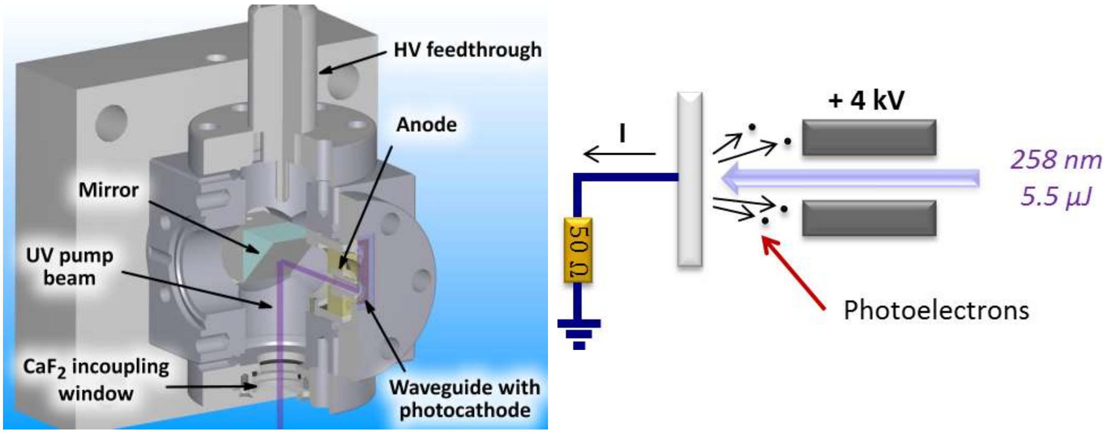

(a) Rendered CAD image of the photocathode in a CF16 cube vacuum chamber. The UV laser beam enters through a CaF_2 input coupling window and is redirected onto the photocathode by a prism mirror. The Mg layer is located on the sample substrate mounted into a CF16 flange opposite to the anode providing a static electric extraction field.

(b) Schematic setup of photocathode test setup. The UV pump beam of 258 nm enters through the cylindrical anode on a positive high voltage potential and extracts photoelectrons out of the cathode layer which results in a measurable positive voltage pulse on an impedance matched resistor.

Figure 4.10: Rendered and schematic setup of the magnesium photocathode.

After removing an oxygen layer from the Mg surface with a focused pulsed laser beam scanning the surface, the quantum efficiency can be increased from normally $2 \cdot 10^{-5}$ by up to two orders of magnitude to $2 \cdot 10^{-3}$. This technique is called laser cleaning [185, 151] and implemented in the setup by a lens on a linear stage for intensity adjustment and a motorized mirror mount to scan the surface. A good summary of the properties of Mg photocathodes also with comparison to other cathode materials can be found in [138].

For first tests, a Mg layer was deposited onto a semi-rigid SMA cable[15] by thermal evaporation in an in-house developed evaporation system based on a tungsten wire filament filled with magnesium grains at a base pressure $< 2 \cdot 10^{-5}$ mbar. The rather thick layer of a few micrometers has a rough surface structure which is advantageous for maximization of the extraction field at the surface (compare equation 2.61). The Mg surface of the SMA cable was then positioned in the vicinity of a cylindrically high voltage anode (figure 4.10) and illuminated with the pulsed laser radiation. By connecting a scope with sufficient bandwidth[16] the pulse profile is measurable at the other end of the SMA cable after an attenuator protecting the scope input. The TR-SKM sample with included photocathode is installed inside a vacuum system based on a CF16 cube with safe high-voltage (SHV) high voltage feedthrough for the positive anode voltage, a CaF_2 laser input coupling window for the UV pulses and flexible bellows to allow scanning of the sample in the TR-SKM (see section 4.5). Inside the chamber a prism mirror reflects the beam entering from below onto the photocathode surface on the sapphire substrate glued into the sample flange. The prism mirror avoids a direct visual axis to the laser input window which may suffer from debris contamination during the laser cleaning process otherwise. Opposite to the cathode a PEEK mount containing the cylindrical aluminum

---

[15] Huber+Suhner EZ_141_TP_M17, 33 GHz

[16] PicoScope 9211A sampling scope, 12 GHz bandwidth

anode on a positive high voltage up to 4 kV provides an extraction field of 8 kV/mm to 10 kV/mm for collection of the photoelectrons.

Evacuation of the vacuum camber is achieved through a turbo pump[17] connected to a diaphragm roughing pump. In order to prevent photocathode degradation and to get rid of vibrations from the pumps, evacuation is continued by an ion getter pump[18]. Turbo- and roughing pump can be switched off once reaching the operation pressure of the ion pump and are separated from the vacuum system by a butterfly valve[19]. The leakage rate of the system was tested with a helium leak tester and determined to be $< 3 \cdot 10^{-9}$ mbar · l/s. The throughput at the CF16 cube is mainly limited by the orifice of the CF16 bellows and leads to an effective throughput of 3.4 l/s for the turbo pump and 3.8 l/s for the ion pump. Working pressures $< 5 \cdot 10^{-8}$ mbar can be achieved routinely after bake-out of the system. The ion getter pump is installed in an orientation that the field at the sample is minimized and has an amplitude below the magnetic field of the earth. The field was measured without pump ($x = -12.5\,\mu\mathrm{T}$, $y = -17.8\,\mu\mathrm{T}$, $z = -11.5\,\mu\mathrm{T}$) and with pump ($x = 28.3\,\mu\mathrm{T}$, $y = -22.1\,\mu\mathrm{T}$, $z = 5.9\,\mu\mathrm{T}$); the coordinate system is chosen according to figure 2.7.

4.4 Femtosecond laser system

The laser pump TR-MTXM and laboratory-based TR-SKM measurements were performed with the commercial femtosecond solid-state laser system PHAROS[20] generating laser pulses of (1028 ± 5) nm wavelength in a diode-pumped ytterbium doped potassium-gadolinium tungstate (Yb:KGW) oscillator. The pulses of 290 fs FWHM duration are stretched, amplified and compressed again by making use of the chirped-pulse amplification (CPA) technique [192] and reach an average output power of 6 W [136]. The high repetition rate of 130 kHz matches the round trip frequency of the storage ring PETRA III to allow a synchronized operation of the two systems. This is achieved by piezo-motorization of one mirror in the oscillator cavity for gradual adjustment of the repetition rate through the cavity length controlled electronically by a phase-locked loop (PLL) to an external reference frequency. The jitter between laser and synchrotron pulses is then reduced to $\sigma < 5$ ps allowing pump-probe experiments only limited by the PETRA III pulse duration of 90 ps FWHM [178].

After leaving the compressor, the pulses can be converted to the second (515 nm at 3.5 W), third (343 nm at 2 W) or fourth (258 nm at 700 mW) harmonic in the HIRO module[21] using second-harmonic generation or sum frequency mixing in Beta-Barium-Borate (BBO) crystals in type I collinear interaction [135]. As another option, the laser pulses can be coupled into a collinear optical parametric amplifier (OPA) of white light continuum called ORPHEUS[22] to produce coherent photons in the wavelength range of 210 nm to 2900 nm with an output power depending on the selected wavelength [134].

The whole CPA laser system with harmonics generator and OPA fits onto a compact mobile laser table of 2.1 m × 0.9 m size for flexible usage inside the laboratory or at ex-

---

[17] Pfeiffer TurboDrag TPD 011, throughput 10 l/s, final pressure $< 5 \cdot 10^{-5}$ mbar

[18] Varian VacIon, throughput 8 l/s, final pressure $< 10^{-11}$ mbar

[19] VACOM 3BVM-25KF-VV-A, leak rate $< 10^{-9}$ mbar · l/s

[20] PHAROS-6W, Light Conversion Ltd.

[21] HIRO, Light Conversion Ltd.

[22] ORPHEUS, Light Conversion Ltd.

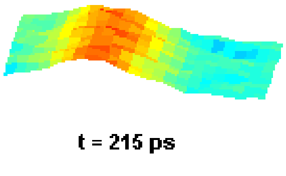

ternal facilities like PETRA III. For the latter case a portable laser safety hutch covering this table with all necessary interlocks and shields is available. Concerning details on the laser system and especially the in-house developed synchronization unit consult the PhD thesis of Moritz Schlie [178].

4.5 Time-resolved scanning Kerr microscope (TR-SKM)

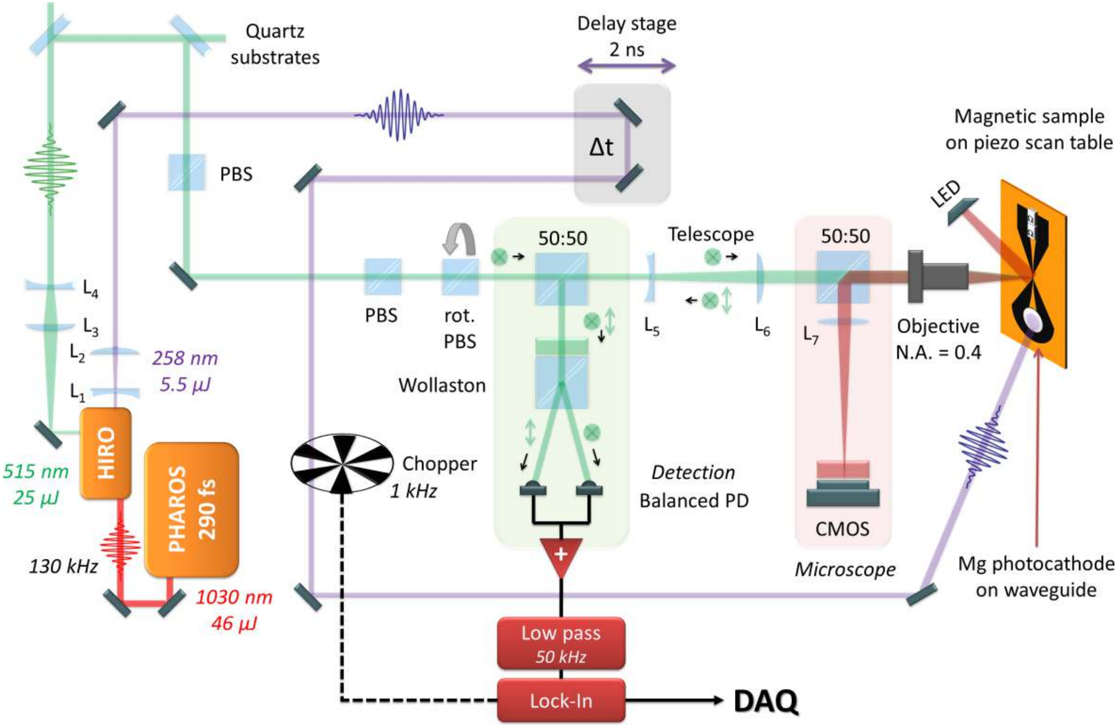

Figure 4.11: Setup of the time-resolved scanning Kerr microscope. The focal length of the lenses are $L_1 = -40\,\mathrm{mm}$, $L_2 = 150\,\mathrm{mm}$, $L_3 = 200\,\mathrm{mm}$, $L_4 = -75\,\mathrm{mm}$, $L_5 = -50\,\mathrm{mm}$, $L_6 = 250\,\mathrm{mm}$ and $L_7 = 200\,\mathrm{mm}$. Details are discussed in the text.

In oder to investigate the dynamics of small magnetic structures in the visible spectral range, a time-resolved scanning Kerr microscope (TR-SKM) has been set up. The Kerr microscope takes advantage of the magneto-optic Kerr effect (see chapter 2) in polar configuration (P-MOKE) by analyzing the polarization of the light reflected by the magnetic sample. It can either be operated with a 10 mW continuous-wave (CW) diode laser[23] at 532 nm wavelength for static measurements or with the PHAROS femtosecond CPA laser system at 515 nm for dynamic studies. A schematic overview of the setup is given in figure 4.11 that will be discussed in detail in this chapter.

The TR-SKM uses the fourth and second harmonic radiation of the PHAROS laser system generated in the HIRO module by frequency doubling in BBO crystals. The fourth harmonic UV pump pulses at 258 nm wavelength are created out of the frequency-doubled PHAROS pulses at 515 nm. Because this process does not convert all the photons, residual second harmonic pulses remain which are used as probe beam. Advantageously,

---

[23] Laser Components Flexpoint FP-53/10AF-AV-SD, laser class 3B

this means both pulses are inherently synchronized to each other and provide a jitter-free source of pump and probe pulses limiting the temporal resolution in principle to the laser pulse duration of 290 fs FWHM. Consequently, this also means that pump and probe beam energies are coupled in the way that maximal pulse energy in the UV pump beam of 5.5 µJ requires maximal pulse energy in the green probe beam of 25 µJ. For the TR-SKM experiments the laser amplifier runs at a repetition rate of 130 kHz similar to the synchrotron TR-MTXM experiments but, if needed, the repetition rate in the laboratory experiments can be chosen freely within the specifications of the laser amplifier [136].

The laser beams leaving the harmonics module are slightly divergent because they have to be focused into the BBO crystals for frequency conversion. That is why for both, pump and probe pulses, first a Galilei telescope is installed to collimate the beam and adjust the beam size. Due to the high intensities at the sample after eventually focusing the probe beam with a microscope objective, the second harmonic has to be attenuated by using the reflection of two quartz substrates and a polarizing beam splitter (PBS). Direct use of the PBS is avoided because the unattenuated pulses may destroy it. Afterwards, polarization filtering in the SKM takes place by two additional PBS of which the second one is rotatable to adjust the polarization plane in the Kerr microscope. The beam now passes two intensity beam splitters which retain the polarization and separate the light into two equal parts of 50 % input intensity. An expansion in a Galilei telescope takes care of fitting the input diameter of the 20X focusing microscope objective[24] with a numerical aperture of $NA = 0.4$. This allows for a minimal focal spot on the sample because only when fully illuminating the aperture, the maximal NA becomes available. The diffraction limited spot size of the focus and thus the achievable spatial resolution is given by the wavelength λ of the light and the NA of the objective. Here, the resolution is estimated to ≈ 785 nm for $\lambda = 515$ nm by the Rayleigh criterion given in equation 2.45 and corresponds to a Gaussian spot size of $d = 652$ nm FWHM according to equation 2.47 (see also section 2.2.2).

The sample can be scanned within the focal plane by two encoded piezo stages with 100 µm travel range and 25 nm positioning accuracy[25]. The reflected light is re-collected by the same microscope objective and partly reflected by one of the intensity beam splitters into a Wollaston prism[26] that separates the beam into two perpendicular polarization components each hitting a photodiode of a balanced detector[27]. A voltage signal proportional to the difference of the input intensities on the two photodiodes is generated by this detector featuring a bandwidth of 1 MHz and a transimpedance gain of $500 \cdot 10^3$ V/A. If the sample changes its magnetization and therefore the polarization of the light, one of those beams gains intensity at the expense of the other one. This change produces a measurable difference signal in the balanced photodetector being related to the intensity change and thus the Kerr rotation of the sample (cf. equation 4.3 and the theoretical background summarized in section 2.1.4 and appendix A.1 and A.2). An initially balanced intensity on the photodiodes leads to a vanishing difference signal which means the polarization is now tilted by 45° and has equal power in the s- and p-component. The measured output voltage U proportional to the intensity I of the incident light now reads $I_p = E^2 \cos^2(\pi/4)$ and $I_s = E^2 \sin^2(\pi/4)$, respectively. As depicted in figure 4.3,

---

[24] Thorlabs LMH-20X-532 high-power MicroSpot focusing objective

[25] Thorlabs PAZ100 and PAZ015 piezoelectric actuators with feedback and BPC203 controller

[26] Thorlabs WP10 Wollaston prim, 20° beam separation, 100 000:1 extinction ratio

[27] Thorlabs PDB210A/M large-area balanced Si photodetector

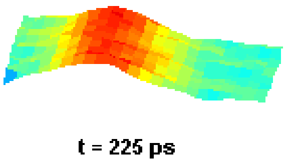

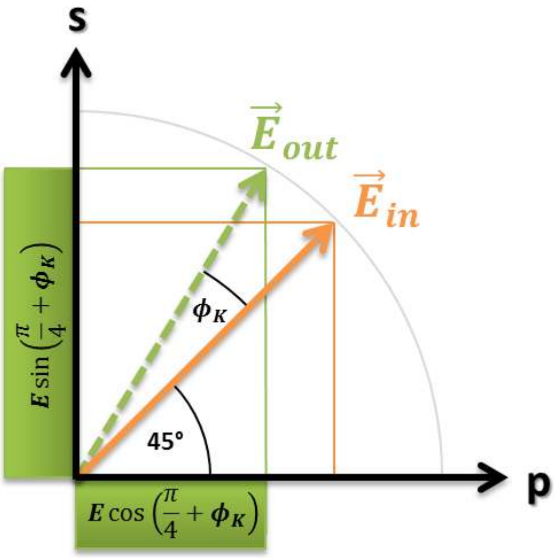

Figure 4.12: The TR-SKM detects the magnetization via the rotation of the polarization by the Kerr angle ϕ_K between the incident and reflected light fields $\vec{E}_{\text{in}}$ and $\vec{E}_{\text{out}}$. The balanced photodetector measures the *s*- and *p*-component of the polarized laser probe beam intensity and prior to a measurement the polarization of the incident beam $\vec{E}_{\text{in}}$ is adjusted to 45° such that the signal on the diodes is of equal intensity and vanishes. A Kerr rotation changes the intensity according to $I_p = E^2 \cdot \cos^2(\pi/4 + \phi_K)$ and $I_s = E^2 \cdot \sin^2(\pi/4 + \phi_K)$.

a Kerr rotation introduces an additional angle and modifies the intensities accordingly to $I_p = E^2 \cos^2(\pi/4 + \phi_K)$ and $I_s = E^2 \sin^2(\pi/4 + \phi_K)$. By measuring the difference signal normalized to the sum of both signals

$$\frac{U_p - U_s}{U_p + U_s} = \frac{I_p - I_s}{I_p + I_s} = \frac{E^2\left[\cos^2\left(\frac{\pi}{4}+\phi_K\right) - \sin^2\left(\frac{\pi}{4}+\phi_K\right)\right]}{E^2\left[\cos^2\left(\frac{\pi}{4}+\phi_K\right) + \sin^2\left(\frac{\pi}{4}+\phi_K\right)\right]} = \sin(2\phi_K) \approx 2\phi_K \tag{4.3}$$

the Kerr angle ϕ_K can be extracted. The data acquisition (DAQ) of the signal is done by an analog to digital (AD) converter[28] with 16 bit dynamic range and 250 kS/s bandwidth. Because the bandwidth of this device is not sufficient for the output pulses of the balanced photodetector, an analog low-pass with 50 kHz cutoff-frequency filters the signal first so that it is sufficient for the AD converter bandwidth and fast enough to identify the modulation by a 1 kHz chopper for lock-in detection. Despite the low cutoff-frequency compared to the laser repetition rate this approach is adequate because a single shot information is not essential in the pump-probe setup due to signal averaging over a lot of pump-probe cycles at a fixed time delay Δt.

Since the beam hits the sample perpendicular only the polar MOKE (P-MOKE) is detectable in this setup (see chapter 2) and thus solely the perpendicular magnetization out of the sample plane can be observed. Because of the NA of the objective, parts of the laser light hit the sample under a certain angle in principle allowing other detection geometries but due to a rotationally symmetric illumination cone, those components cancel out eventually and only the polar component is left. The advantage of the P-MOKE setup is that the focal spot is minimal in size compared to angular illumination allowing the highest spatial resolution compared to other MOKE configurations. Additionally, a strong Kerr signal with a negligible ellipticity is achieved (compare figure 2.13). The disadvantage of P-MOKE, however, is the inability to measure the in plane magnetization components which might be interesting especially in thin film structures.

The UV pump beam in the setup is able to excite the sample by the magnetic field of a short current pulse launched toward the magnetic system via a CPW on the sample

---

[28] National Instruments NI USB-6210

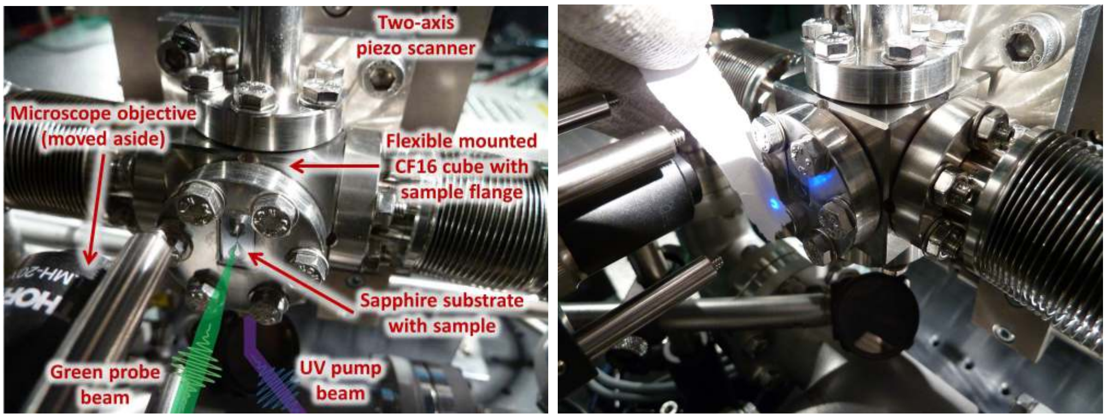

(a) Sample flange mounted onto the flexible vacuum chamber scannable with a two-axis piezo unit.

(b) Fluorescence of residual UV light hitting the cathode from the vacuum side is visible on a piece of paper.

Figure 4.13: TR-SKM sample flange installed into the vacuum system.

substrate (for details see section 4.1.1 and 4.1.2). The current pulse is generated via the photoeffect in a magnesium photocathode (section 4.3) and terminated in two RF-resistors matching the impedance of the CPW. A vacuum chamber containing sample and photocathode is mounted onto the piezo scanner unit and moved during image acquisition. Figure 4.13 provides photos of this part of the setup.

The delay Δt between pump and probe pulses can be tuned by an optical delay stage in the UV pulse beam path based on a motorized linear stage[29] with 300 mm travel range and a set of two mirrors covering a scan range of 2 ns with $\approx$ 1 fs accuracy.

In order to increase the detection sensitivity, the pump beam is modulated by a chopper running at 1 kHz frequency. The amplified difference signal of the balanced photodiodes is filtered in a lock-in amplifier[30] referenced to the chopper frequency. The installation of the chopper in the pump and not the probe beam has the advantage that the detection is only sensitive to signals originating from the excitation of the sample, so only transient responses of the pumped system are observable.

Supplementary, the SKM is equipped with a monochrome CMOS camera[31] to image the topology of the sample simultaneously with the same focusing objective used for scanning and an additional lens. The illumination is provided by a red high power light-emitting diode (LED) at a wavelength of 623 nm. To avoid disturbing effects from the laser to the camera and from the LED to the balanced photodetector, optical band-pass filters are installed in front of the detectors passing only the desired wavelength.

4.6 Soft X-ray beamline P04 at PETRA III

After the discovery of X-rays by Wilhelm Conrad Röntgen in 1895 [172, 173], the novel radiation lead insight into the structure of matter and was applicable in medicine and biology. In the early days, this radiation was only generated by radioactive ele-

---

[29] Feinmess Dresden PMT160-300-SM2-S10 with Oriental PK 245-02B stepper motor

[30] FEMTO LIA-MV-150

[31] Thorlabs DCC1545M monochrome CMOS camera, 1280 pixel × 1024 pixel of 5.2 µm × 5.2 µm size

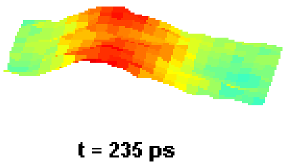

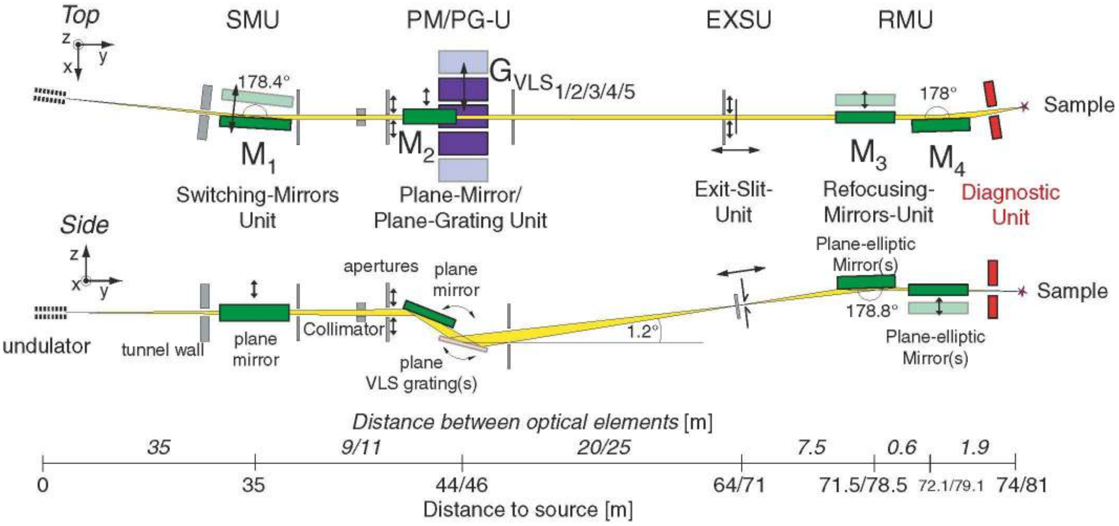

Figure 4.14: Layout of the P04 soft X-ray beamline at PETRA III [202, 45]. Details are discussed in the text.

ments and later X-ray tubes. Nowadays, highly brilliant X-ray light is available in third generation synchrotron sources like PETRA III[32].

PETRA III is a storage ring at DESY in Hamburg with a total circumference of 2304 m corresponding to a round trip frequency of 130.1 kHz. Since the year 2009 the facility is dedicated to the generation of synchrotron radiation and is up to now the most brilliant storage ring based X-ray source in the world. In normal operation mode the ring is filled with 960 packets of electrons called bunches but for time-resolved experiments also a 40 bunch mode with a separation of 192 ns between two light pulses generated out of the electron bunches is available as well. The ring stores an electron current of 100 mA in the top-up mode at 6 GeV electron energy.

The soft X-ray beamline P04 [202] at the synchrotron PETRA III delivers photons in the energy range of 250 eV to 3000 eV with variable polarization. The light is generated in a periodic magnetic structure called undulator inside the storage ring. This insertion device periodically modifies the electron trajectories due to the Lorentz force and this accelerated motion of charged particles leads to radiation of electromagnetic waves with a wavelength of [55]

$$\lambda = \frac{\lambda_u}{2n\gamma^2} \cdot \left(1 + \frac{K^2}{2} + \gamma^2\vartheta_x^2 + \gamma^2\vartheta_y^2\right) \quad \text{with} \quad K = \frac{eB\lambda_u}{2\pi m_e c} \quad \text{and} \quad \gamma = \frac{1}{\sqrt{1-\left(\frac{v}{c}\right)^2}} \tag{4.4}$$

that is determined by the Lorentz factor γ containing the velocity of the electrons, the undulator period λ_u of the magnetic structures, the observation angles ϑ_x and ϑ_y with respect to the undulator axis and the magnetic field B experienced by the charged particles in the storage ring. The dimensionless undulator parameter K by definition has to be smaller than unity for an undulator; otherwise the insertion device would be called

---

[32] PETRA (Positron Elektron Tandem Ring Anlage) was formerly used as a particle physics collider that discovered the exchange boson of the strong interaction known as gluon and is now in its third revision a dedicated synchrotron-radiation source.

a wiggler. In addition to the fundamental wavelength ($n = 1$) higher harmonic modes ($n = 3, 5, 7, \dots$) may radiate as well. Except for B all parameters in general are fixed by the geometry of the undulator and the storage ring operation parameters. Therefore, an adjustment of the gap between the bottom and top row of magnets tunes the field amplitude B and a change of the emitted wavelength can be achieved. The insertion device in the P04 beamline is an APPLE-II (advanced planar polarized light emitter) type undulator in the storage ring that generates a high photon flux in its first harmonic with linear, circular or elliptical polarization. The adjustment of the polarization is possible by tuning the undulator shift that modifies the magnetic field configuration and thus the electron trajectories in the undulator and enables for example the emission of right and left hand circular polarized photons needed for XMCD measurements. An overview of the P04 layout is presented in figure 4.14.

The emitted radiation can be directed into two identical beamline branches[33] by a switching-mirrors unit (SMU) to distribute the beam-time most efficiently between two experiments. The radiation gets spectrally separated by angular dispersion in a plane-mirror, plane-grating unit (PM/PG-U) with a 1200 lines/mm grating and is monochromatized in an exit-slit unit (EXSU) afterwards by selecting a particular bandwidth of the dispersed beam. The last optical elements are two sets of refocusing Kirkpatrick-Baez (KB) mirrors [116] in the refocusing-mirrors unit (RMU). One mirror set produces a 10 µm × 10 µm focus at the experimental platform behind the exit flange and the other set refocuses the beam to the permanently installed PIPE (photon-ion spectrometer at PETRA III) experiment meters behind the beamline platform. Trailing to the RMU a diagnostic unit is present for on-line monitoring of the beamline performance such as photon energy and flux, beam position, spectral resolution and polarization.

The P04 beamline was designed for high transmission and for this reason as few as possible only plane and plane-elliptical optical elements were used. Within the specifications a high photon flux $> 10^{12}$ photons/s is available at a resolving power $\lambda/\Delta\lambda$ of 10 000.

4.7 Time-resolved magnetic transmission X-ray microscope (TR-MTXM)

A full-field X-ray microscope, similar to an optical microscope, basically consists of a condenser optic for sample illumination and an objective lens to image the sample onto a suitable detector. However, as pointed out in chapter 2, in the soft X-ray spectral range it is advantageous to use diffractive optical elements as lenses. The general setup of the time-resolved magnetic transmission X-ray microscope (TR-MTXM) is illustrated in figure 4.15.

Beginning with the soft X-ray radiation delivered by the P04 undulator in the PETRA III storage ring and monochromatized by the PM/PG-U and EXSU, the beam enters the microscope through a grating condenser optic generating a 20 µm diameter illumination spot at its focal distance when operated at photon energies of the iron or nickel L absorption edge. Since the condenser takes care of focusing, the mirrors used for the PIPE experiment are moved into the RMU of the beamline as they only slightly

---

[33] During the beamtime shifts in this project all measurements were performed at the same beamline branch because the second branch was under construction at that time.

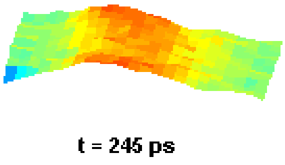

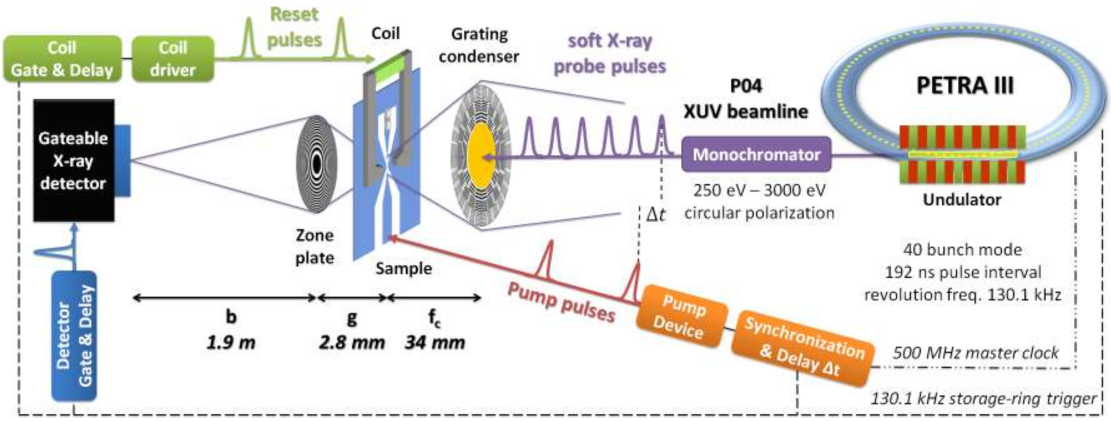

Figure 4.15: Setup of the time-resolved magnetic transmission X-ray microscope. Details are discussed in the text.

focus the beam on the platform. Table 4.2 gives an overview of the parameters of the soft X-ray optics and figure 5.10a shows an SEM image of the grating condenser designed as a concentric collection of diffraction gratings. The rays deflected by the gratings originate from different positions in the source and overlap in the focal plane of the condenser forming a flat-top illumination profile. This approach also reduces the spatial coherence of the radiation in the sample plane which would lead to artifacts and speckle patterns in the image. Further details on this optic including a ray-tracing can be found in [207]. The numerical aperture of the illumination optic is matched to the imaging optic aperture in order to provide maximal spatial resolution and, additionally, a central stop is included on the grating condenser to filter out the 0^{th} order of the direct beam since the microscope operates in the first diffraction order of the optical elements.

A micro zone plate (compare also section 2.2.3) with the parameters given in table 4.2 in combination with a suitable soft X-ray detector takes care of the imaging. Static measurements allow utilizing an in-vacuum back-thinned CCD detector[34], however, time-resolved dynamic studies have to be carried out with a special gateable soft X-ray detector (see chapter 5.5). Both detectors were cooled down to at least $-40\,°\text{C}$ to keep the noise level minimal. To ensure maximal spatial resolution in the microscope, the setup should be limited by the quality of the optic and not by parameters of the detector. For this purpose the magnification M has to be chosen in agreement with the Nyquist-Shannon sampling theorem. This means at least two pixel should correspond to the imaged resolution limit of the zone plate $\Delta l = 1.22\Delta r_N$ (equation 2.56). For both detectors the pixel size is $d_{\text{px}} = 13\,\mu\text{m}$ giving $M > 2d_{\text{px}}/\Delta l = 426$. Additionally, when the whole field of view (FOV) of $20\,\mu\text{m}$ generated by the condenser shall fit onto the camera chip ($13.3\,\text{mm} \times 13.3\,\text{mm}$), the magnification has to exceed $M > d_{\text{chip}}/FOV = 666$. A much larger number is not advantageous because it makes the setup more sensitive to mechanical vibrations and increases the overall dimension because for an optical element with a focal length f and a given magnification, the sample distance g and image distance b relate to

---

[34] Andor iKon-M 934 [DO], 1024 pixel × 1024 pixel of $13\,\mu\text{m} \times 13\,\mu\text{m}$ size

Table 4.2: Parameters of the TXM optics obtained from ZonePlates.com and created by Pambos Charalambous.

	Grating condenser	**Zone plate**
Number of zones **N**		400
Number of gratings	940	
Grating size	25 µm × 25 µm	
Diameter **D**	1 mm	80 µm
Outermost zone width Δr_N	50 nm	50 nm
Focal length **f**	34.3 mm at 851.5 eV	2.75 mm at 851.5 eV
Numerical aperture **NA**	0.0146 at 851.5 eV	0.0146 at 851.5 eV
Depth of field **DOF**		± 3.43 µm at 851.5 eV
Spot diameter **FOV**	20 µm	
Material	130 nm tungsten (W) on 100 nm Si_3N_4	130 nm tungsten (W) on 100 nm Si_3N_4
Central stop material	Gold (Au)	
Central stop diameter	500 µm	
Central stop thickness	500 nm	

$$g = \frac{1+M}{M} \cdot f = 2.754\,\text{mm} \qquad \text{and} \qquad b = (1+M) \cdot f = 1.928\,\text{m} \tag{4.5}$$

$$\text{with} \qquad M = \frac{b}{g} = 700 \tag{4.6}$$

by using the lens equation 2.52 for the zone plate specified in table 4.2. The chosen magnification of $M = 700$ allocates at least three detector pixel for sample features in the size of the zone plate resolution limit imaged onto the detector.

For pump-probe experiments an external stimulus (pump device in figure 4.15) is needed in order to excite the system reproducibly and is delivered here either by a synchronized femtosecond laser pulse converted in a photocathode or by an electric picosecond pulse generator (see also section 4.1). In the first case the PLL electronics of the laser synchronization needs the ≈ 500 MHz, 0 dBm sinusoidal reference frequency of the PETRA III master clock to lock the laser oscillator cavity to the synchrotron (compare section 4.4 and [178]). Additionally, the TTL storage-ring trigger available at the bunch clock provides the 130.1 kHz revolution frequency as Pockels cell trigger and is fed into the regenerative amplifier of the laser. This approach allows a synchronization with a jitter $\sigma < 5\,\text{ps}$ limiting the achievable time resolution to the PETRA III pulse duration of 90 ps with an electronic delay Δt adjustable by the synchronization unit [178].

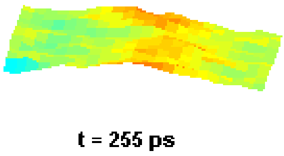

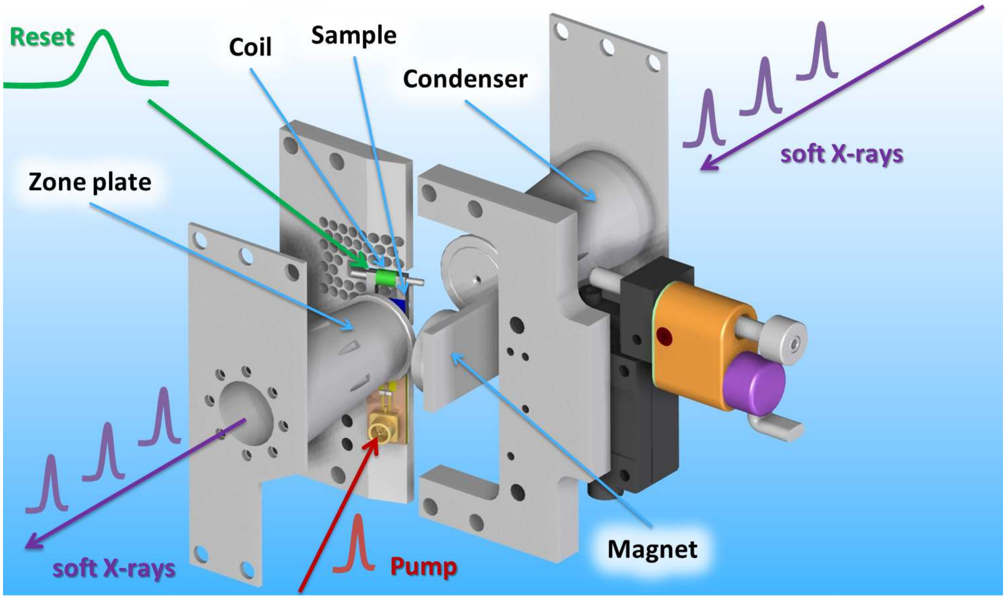

Figure 4.16: Rendered CAD image of the TR-MTXM assembly with suppressed parts of the piezo stages for better visibility. The soft X-ray beam enters through the condenser located on top of the upper right cone and gets focused onto the sample mounted at an angle of 70° with respect to the photon direction. The zone plate located on top of the lower left cone images the sample onto the detector (not shown). Excitation becomes possible via an adapter PCB by inserting electric current pulses or laser pulses hitting a photocathode. A motorized magnet and a coil provide bias and reset fields.

The second excitation solution makes use of the picosecond pulse generator delivering pulses of 50 V to 200 V amplitude at 220 ps to 250 ps pulse duration. A synchronization to the P04 light pulses is realized via a pulse and delay generator[35] allowing to set the delay with 5 ps resolution and a jitter < 25 ps RMS compared to the external TTL storage-ring trigger of the bunch clock. Because the delay generator offers additional channels, it is used likewise to trigger the driver of the reset coil as well as the gateable detector.

Both pump concepts only allow an operation at the revolution frequency of PETRA III limited either by the maximal repetition rate of the laser amplifier or the pulse generator. Additionally, the reset coil for dynamic studies of non-reversible systems is bound to this frequency as well. In order to identify the temporal overlap between pump and probe pulses, fast biased UV and an XUV photodiodes capable of detecting single shot signals can be moved into the laser or soft X-ray beam, respectively. In case of operating the pulse generator, the XUV photodiode is sufficient when carefully taking into account the delay accumulated by the cables.

A closer look into the essential TR-MTXM components is provided in figure 4.16 where the conical shaped mounts for the exchangeable soft X-ray optics are visible as well as the titanium sample holder containing the silicon frame with the magnetic system and the waveguide together with the pulse injection circuit and the reset coil (an unobscured view is provided in figure 4.8). Now it is obvious that the photocathode can not be directly manufactured onto the silicon frame for the TR-MTXM samples because it would simply

---

[35] Stanford Research Systems DG645 ultra-low jitter digital delay generator

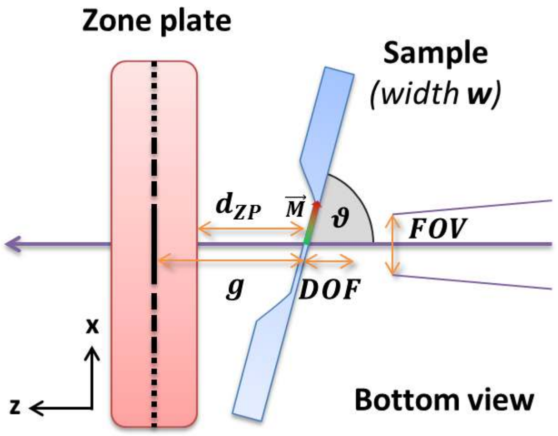

Figure 4.17: Influence of the sample tilt ϑ to the geometry (bottom view). The soft X-ray beam enters from the right through the condenser illuminating a spot of diameter FOV. The zone plate in its holder located at $d_{\mathrm{ZP}} < g$ images an area around $\pm DOF$ acceptably sharp onto the detector. The signal of the in-plane magnetization $\vec{M}$ is reduced by $\cos(\vartheta)$ because only the projection onto the beam axis is observable.

be blocked by the zone plate mount. Also prominent is the sample tilt of $\vartheta = 70°$ with respect to the photon beam propagation axis enabling an in-plane XMCD contrast and a movable permanent magnet located on a motorized linear stage. The angle is constrained by the sample width $w = 7\,\mathrm{mm}$ because contact to the zone plate located at a distance $d_{\mathrm{ZP}} = 1.75\,\mathrm{mm}$ smaller than the object distance g due to the zone plate holder has to be avoided. By claiming further that the sample tilt should not influence the resolution over the whole field of view we require

$$\vartheta > \arccos\left(\frac{2\cdot d_{\mathrm{ZP}}}{w}\right) = 60° \qquad \wedge \qquad \vartheta > \arctan\left(\frac{FOV}{2\cdot DOF}\right) = 71°. \tag{4.7}$$

The chosen tilt provides a reasonable compromise between an XMCD amplitude fraction of $\cos(70°) = 0.34$ and the spatial resolution.

The dominant magnetic offset field component B_x generated by the motorized permanent disk magnet of radius $R = 7.5\,\mathrm{mm}$ and thickness $L = 3\,\mathrm{mm}$ is described by

$$B_x(x) = \frac{B_r}{2}\left(\frac{L+x}{\sqrt{R^2+(L+x)^2}} - \frac{x}{\sqrt{R^2+x^2}}\right) \tag{4.8}$$

with the remanence $B_r = 1.35\,\mathrm{T}$ of the axially magnetized N45 NdFeB magnet. A plot over the accessible travel range is given in figure 4.18 and zero distance would correspond to a magnet position directly at the membrane. Due to the sample width and the distance

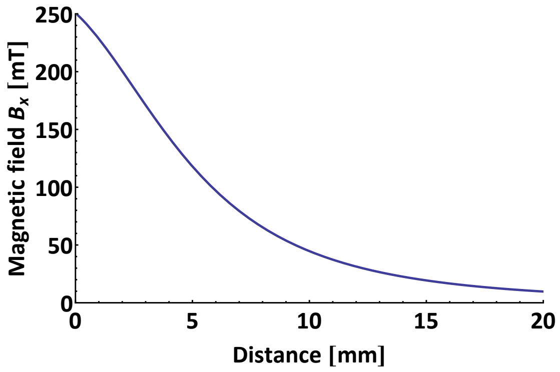

Figure 4.18: Magnetic field component B_x generated by the permanent magnet with respect to the sample distance according to equation 4.8.

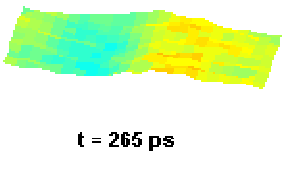

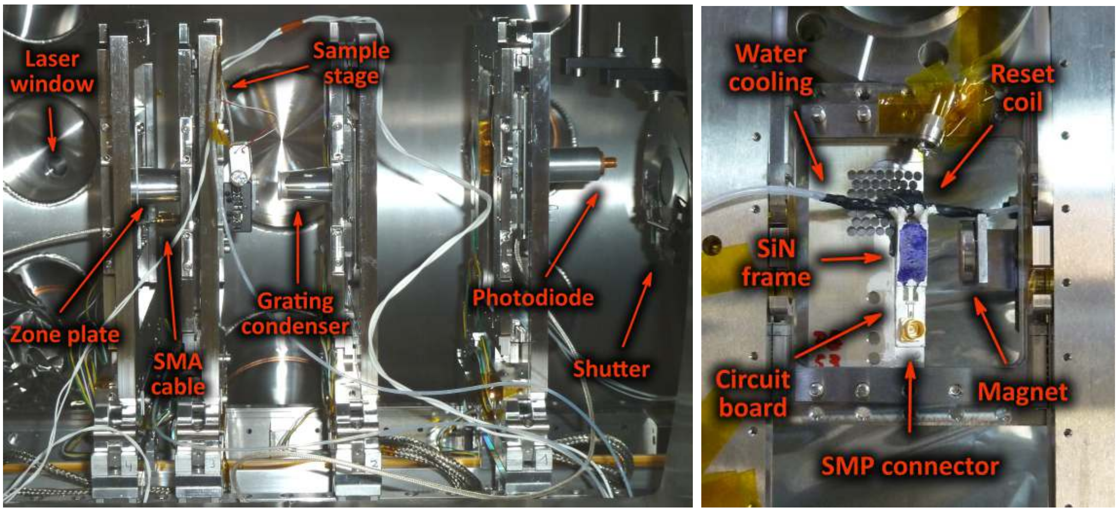

(a) Photo of the vacuum chamber interior with mounted components on the three-axis piezo stages. The beam enters from the right through a camera shutter. Arranged behind is a photodiode that can be moved into the beam for timing purposes followed by the TXM consisting of condenser, sample stage and micro zone plate. Visible in the back is a laser input coupling window for pumping with the femtosecond laser pulses.

(b) Photo of the sample stage containing the titanium sample holder with the silicon frame located on top of the water-cooled reset coil and the PCB for current pulse injection via the SMP connector. A motorized magnet provides an adjustable bias field.

Figure 4.19: Photos of the TR-MTXM installed into the vacuum chamber and the piezo stage with the sample.

of 3.5 mm to the silicon frame edge, the maximal field at the sample can not exceed 150 mT. A minimal field of 10 mT is always present which means that the magnet has to be removed for field free measurements.

Due to the high absorption of soft X-rays in air, the whole setup has to be placed into a vacuum environment. For this purpose a mobile and flexible endstation system is available with up to three vacuum chambers on a rail with a variety of viewports and large rectangular flanges for easy access of the inner components. The system can be adapted for several applications e.g. imaging, spectroscopy or non-linear physics experiments at synchrotrons, FELs or laboratory based HHG and laser sources. For the TR-MTXM one of the 500 mm diameter and 600 mm long chambers on a 3 m × 1 m support frame is sufficient. Evacuation is achieved by turbo pumps to a base pressure of $1 \cdot 10^{-7}$ mbar to $5 \cdot 10^{-5}$ mbar backed up by two preceding differential pumping stages to meet the requirements of the beamline vacuum interlock. This is mainly important when the large transparent acrylic glass flanges are installed due to outgassing of the material. The endstation features multiple in-house developed three-axis nanopositioning piezo stages designed for long travel ranges and high precision positioning which are easily customizable for mounting various components necessary in the experiment. In this case four to five stages have been used for photodiode, condenser, sample, zone plane and laser mirror (figure 4.19).

4.7.1 Fast gateable X-ray detector

In the time-resolved mode of PETRA III 40 bunches are circulating in the ring with a separation of $1/(40 \cdot 130.1\,\mathrm{kHz}) = 192\,\mathrm{ns}$. As mentioned before, the repetition rate of the laser amplifier and the picosecond pulse generator is adjusted to the round trip frequency of the synchrotron of 130.1 kHz; additionally, the reset pulse of the coil is not switchable at MHz repetition rates. In consequence, this means only every 40th bunch can be pumped. For the experiment it is counterproductive to detect all the other 39 bunches as well because they would result in a huge background signal not correlated with the dynamical behavior of the system under study. It is not possible to overcome the problem with an ordinary CCD camera because the readout of the chip takes a lot longer than 192 ns. Exactly for this purpose a fast X-ray chopper for single bunch extraction should be available at the P04 and P11 beamline [147]. Unfortunately, up to now the available chopper is not capable of extracting single bunches in the 40 bunch operation mode and is still in the development phase. This means another selection device had to be built and we decided to construct a fast gateable X-ray detector qualified of selecting one particular bunch in the storage ring for detection.

The general setup is outlined in figure 4.20 and starts with the image of the soft X-ray microscope being projected onto a P46 phosphor screen[36] of 3 µm thickness attached to an output window of the vacuum chamber. On incident high energy photons or particles this screen emits light in the visible yellow spectral range and has a decay constant of $\approx 200\,\mathrm{ns}$ so that most of the light already is emitted until the next bunch hits the phosphor.

The afterglow of the image on the screen is transferred by a large aperture 1:1 relay optic incorporating two 25 mm fast camera lenses[37] with an entrance pupil of $f/0.95$ onto a generation III GaAsP photocathode of an image intensifier tube[38] which is able to convert the incident light at $\lambda = 530\,\mathrm{nm}$ wavelength with a quantum efficiency of $QE = 0.5$ into electrons [3]. After absorbing a soft X-ray photon flash, the P46 phosphor emits a light pulse with a photon to photon conversion efficiency of $\approx 25\,\%$ [11]. The radiant intensity with respect to the observation angle ϑ relative to the surface normal is approximated to be proportional to $\cos(\vartheta)$ according to Lambert's cosine law [128, 91]. Although deviations from this directional characteristic are known for phosphor screens, the error is expected to be below 10 % for thin phosphor screens [72]. The relay-optic can only collect a fraction of this light due to the limited entrance pupil and its numerical aperture

$$NA = n \sin(\theta) = n \sin\left(\arctan\left(\frac{D}{2f}\right)\right) = 0.43 \qquad \Rightarrow \qquad \theta = 25.4°. \tag{4.9}$$

The collected photons in the solid angle compared to all emitted photons in forward and backward direction correspond to a transmission of

---

[36] ProxiVision P46, layer thickness 3 µm, finest grain size

[37] Voigtländer 25 mm / F 0.95 Nokton, MicroFourThirds (MFT)

[38] Hamamatsu V8070U-74-G160, resolution 50 line pairs/mm, min. gate pulse width 5 ns FWHM

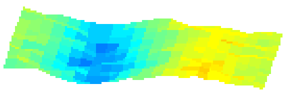

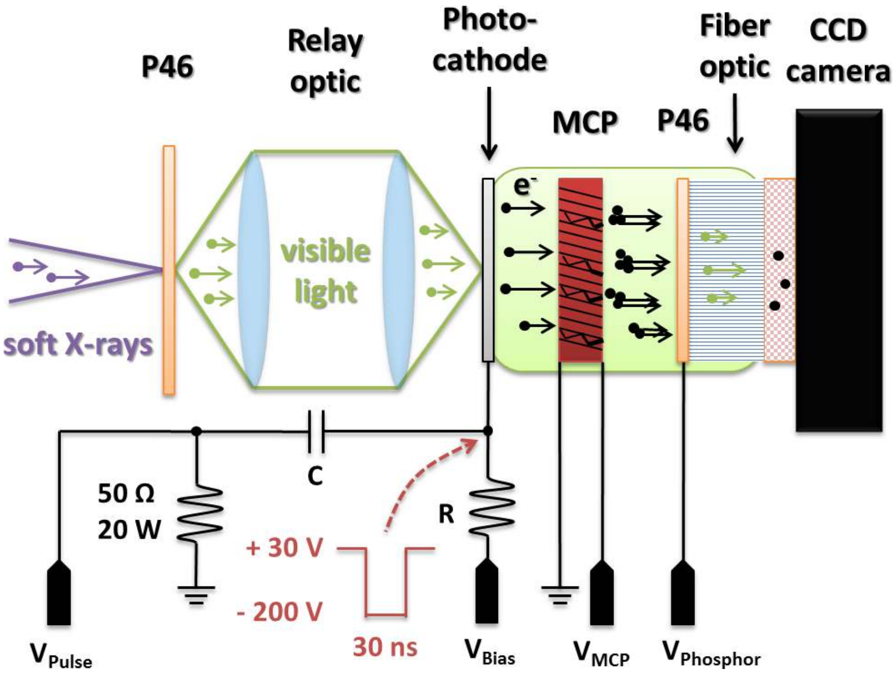

(a) Schematic setup of the fast gateable X-ray detector. A relay optic transports the X-ray microscope image appearing on a P46 phosphor screen onto an electronically gateable photocathode of an image intensifier tube in which signal amplification and transport onto a CCD camera takes place for image acquisition ($R = 1\,\mathrm{M}\Omega$, $C = 470\,\mathrm{pF}$).

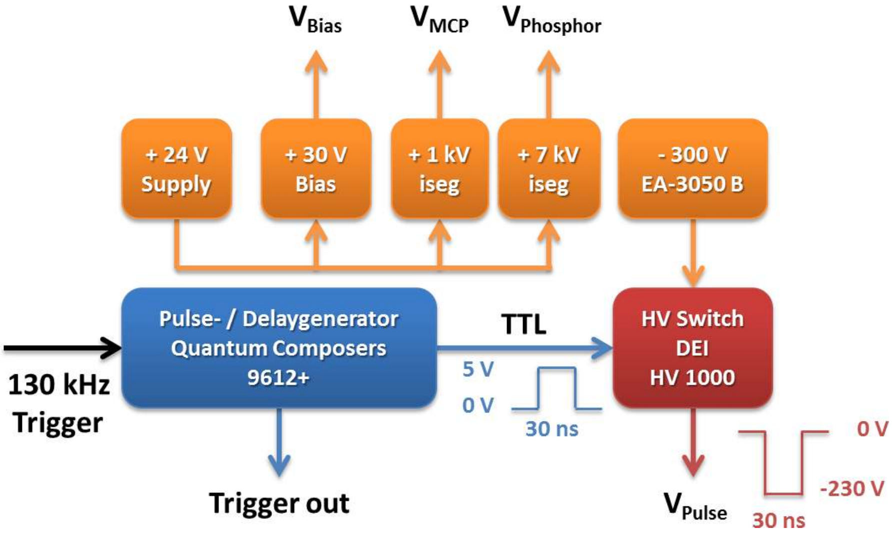

(b) Custom-built detector power supply providing the static high voltages needed for the MCP and phosphor screen and generating the positive cathode bias as well as the nanosecond high voltage pulse that can be delayed with 10 ns precision with respect to an external trigger by a pulse- / delaygenerator.

Figure 4.20: Fast gateable X-ray detector and power supply layout

$$T = \frac{\int_0^{2\pi}\int_0^{\theta}\cos(\vartheta)\sin(\vartheta)\,\mathrm{d}\vartheta\,\mathrm{d}\varphi}{2\cdot\int_0^{2\pi}\int_0^{\frac{\pi}{2}}\cos(\vartheta)\sin(\vartheta)\,\mathrm{d}\vartheta\,\mathrm{d}\varphi} = \frac{2\pi\left[\frac{-\cos^2(\vartheta)}{2}\right]_0^{\theta}}{4\pi\left[\frac{-\cos^2(\vartheta)}{2}\right]_0^{\frac{\pi}{2}}} = \frac{1-\cos^2(\theta)}{2\left[1-\cos^2\left(\frac{\pi}{2}\right)\right]} = 9.25\,\%. \tag{4.10}$$

The efficiency of the light collected by the relay optic may be improved by coating the phosphor with a thin aluminum layer so that it only emits into one half-plane. However, direct coating should be avoided because it may result in micro lenses due to the phosphor grains leading to a decreased spatial resolution. A planarization layer has to be applied first.

The cathode is normally biased through a $R = 1\,\mathrm{M\Omega}$ resistor with a positive voltage of $V_{\mathrm{Bias}} = 30\,\mathrm{V}$ preventing the electrons released due to the photoeffect from leaving the surface and passing on the image information. In this configuration the image is blocked and not visible on the CCD camera of the detector in the back.

By applying an electronic gate pulse of $V_{\mathrm{Pulse}} = -230\,\mathrm{V}$ amplitude and $\approx 40\,\mathrm{ns}$ pulse duration via the capacitor $C = 470\,\mathrm{pF}$ to the photocathode, the net voltage on the cathode will be $-200\,\mathrm{V}$ during the gate. Then, the photoelectrons of the cathode get accelerated onto the grounded surface of a micro-channel plate (MCP) where they are amplified by secondary electron emission in an avalanche effect owing to the positive potential at the MCP backside of up to $V_{\mathrm{MCP}} = 1\,\mathrm{kV}$. After leaving the MCP, the extracted amplified electronic image signal is accelerated onto another P46 phosphor screen at $V_{\mathrm{Phosphor}} = 6\,\mathrm{kV}$ where it is transformed back into photons. The amplification by the MCP at 600 V results in a luminous gain of $390\,\mathrm{lm/(m^2\,lx)}$ [3]. The photonic output screen signal is coupled out by a fiber taper fixed with an index matching fluid onto the fiber optic input of a cooled, low noise back-illuminated CCD camera[39] with $13\,\mathrm{\mu m} \times 13\,\mathrm{\mu m}$ pixel size. The CCD chip converts the light of the phosphor back into electrons with a quantum efficiency of 0.975 at $\lambda = 530\,\mathrm{nm}$ [165].

Because the detector uses multiple high voltages and needs an adjustable HV gate signal, a custom power supply schematically depicted in figure 4.20b has been built in cooperation with the electronic workshop of the University of Hamburg. A 24 V module generates a supply voltage for the electronic control circuits of the high voltage modules providing adjustable static MCP and phosphor voltages with sensitive current limiting on SHV and Kings 10 kV HV output ports, respectively as well as the +30 V bias for the photocathode on a BNC output port.

The HV gate pulse is generated by a high voltage switch[40] capable of switching up to 850 V in minimal 55 ns connected to a 300 V power supply[41] and triggered by a pulse- / delay-generator[42] that delivers a TTL output signal with alterable duration and delay at 10 ns timing resolution and a jitter $< 25\,\mathrm{ns}$ RMS with respect to an external trigger signal. The gate pulse is transported to the detector via a BNC cable and properly terminated on site by a water-cooled low-inductive $50\,\Omega$, 20 W resistor (see figure 4.20a). The cooled resistor guarantees safe operation at the synchrotron revolution frequency of $f = 130.1\,\mathrm{kHz}$ with up to $\tau = 150\,\mathrm{ns}$ gate pulse duration according to

---

[39] Princeton Instruments PIXIS-XF: 1024B, 1024 pixel × 1024 pixel of $13\,\mathrm{\mu m} \times 13\,\mathrm{\mu m}$ size

[40] IXYS Colorado DEI HV1000 negative polarity, 850 V, 17 A, min. 55 ns, jitter $< 100\,\mathrm{ps}$

[41] Elektro-Automatik EA-3050 B

[42] Quantum Composers 9612+

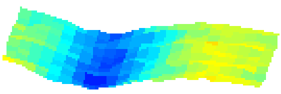

$$P_{\text{avg}} = \underbrace{f \cdot \tau}_{\substack{\text{duty}\\ \text{cycle}}} \cdot U \cdot \underbrace{\frac{U}{R}}_{\text{current } I} = 130.1\,\text{kHz} \cdot 150\,\text{ns} \cdot 230\,\text{V} \cdot \frac{230\,\text{V}}{50\,\Omega} \approx 20\,\text{W} \tag{4.11}$$

but is normally operated at a gate pulse duration of 40 ns. The pulse termination has to happen close to the detector unit in a shielded metallic enclosure to prevent the release of electromagnetic pulses (EMPs) potentially disturbing neighboring electronic devices.

The detector can also be operated in a permanently opened mode collecting the whole light generated by the synchrotron when no time information is needed. For this purpose the photocathode of the image intensifier is set to a constant negative potential by applying up to −230 V to the V_{Bias} input and no signal to the V_{Pulse} input (cf. figure 4.20). This reduces the necessary exposure time which is controlled by an additional in-vacuum shutter in front of the condenser.

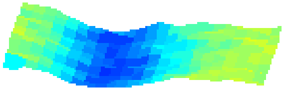

t = 295 ps

Chapter 5

Characterization

5.1 Photocathode

The characterization of the short electric pulses generated by the photocathode is not trivial since the coplanar waveguide in this experiment has an impedance of $100\,\Omega$ and all available high frequency measurement equipment is based on $50\,\Omega$ termination. A direct electrical measurement without disturbing the pulse shape due to impedance mismatch is impossible. Therefore, a test setup was built for pulse characterization consisting of a $\approx 1.8\,\mathrm{mm}^2$ magnesium coating evaporated onto the inner conductor of a semi-rigid $50\,\Omega$ SMA cable (see inset in figure 5.1a) located opposite to a cylindrical anode on a positive high voltage potential inside a vacuum chamber with a calcium fluoride (CaF_2) laser entrance window (figure 4.10).

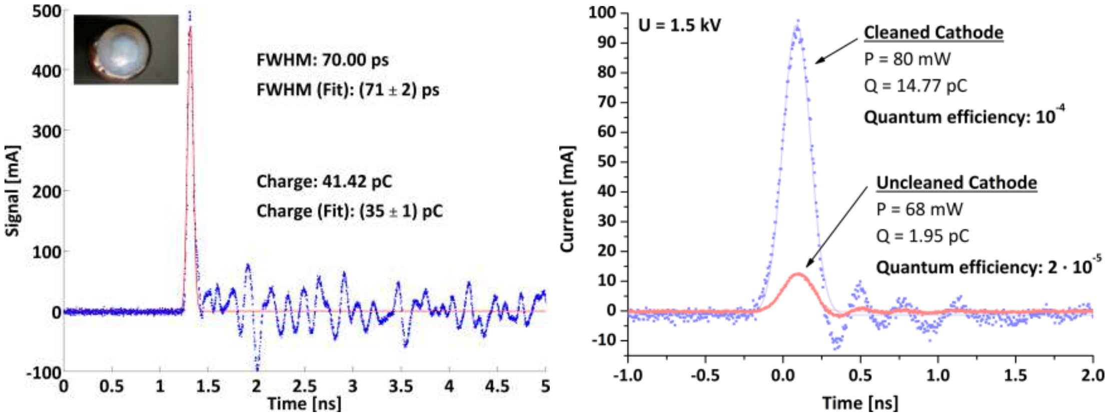

(a) Exemplary current pulse of $(35 \pm 1)\,\mathrm{pC}$ charge featuring $500\,\mathrm{mA}$ peak amplitude at $(71 \pm 2)\,\mathrm{ps}$ FWHM pulse duration in the magnesium photocathode test setup (measured with a $12\,\mathrm{GHz}$ sampling scope) at $250\,\mathrm{mW}$ laser power at the surface. The inset shows the SMA cable of $3.58\,\mathrm{mm}$ outer diameter with Mg layer coating.

(b) Pulse of an untreated photocathode compared to a laser scanned magnesium surface (measured with a $2\,\mathrm{GHz}$ scope) at an anode voltage of $1.5\,\mathrm{kV}$ and similar laser power around $70\,\mathrm{mW}$. The bunch charge increases from $1.95\,\mathrm{pC}$ to $14.77\,\mathrm{pC}$ corresponding to an enhancement in quantum efficiency from $2 \cdot 10^{-5}$ to $1 \cdot 10^{-4}$.

Figure 5.1: Pulses generated by the magnesium photocathode (inset) measured in the test setup and the effect of laser cleaning.

The electric pulses generated in this test setup were measured by a 12 GHz sampling scope with a rise time of 29.2 ps (10 % to 90 %). Figure 5.1a shows a typical pulse of (35 ± 1) pC charge with 500 mA peak amplitude and (71 ± 2) ps FWHM pulse duration at 250 mW laser power at the surface. The depicted data shows charge and pulse duration obtained by the fit and by integration over the trace or evaluating the width of the pulse at half peak amplitude, respectively. The measured duration is very close to the minimal supported value by the 12 GHz sampling scope thus it provides only an upper limit and it remains unclear if the actual pulse duration is even smaller. For a more precise measurement a broadband scope offering more bandwidth or a dedicated magneto-optical sampling pump-probe experiment using the Faraday effect as performed by Elezzabi et. al. [54] becomes necessary. Similar to MOKE, the Faraday effect describes a tilt of the polarization plane by an angle

$$\phi = V \cdot B \cdot L \qquad \text{with} \quad V(\lambda) = \frac{e\lambda}{2m_e c} \cdot \frac{\mathrm{d}n}{\mathrm{d}\lambda} \tag{5.1}$$

when an electromagnetic wave propagates through a crystal of refractive index n and length L along a magnetic field B in the same direction. This angle is proportional to the materials Verdet constant V. A time-resolved measurement of the rotation $\phi(t)$ would give insight into the dynamics of the magnetic field pulse $B(t)$. Cadmium-manganese-telluride (CdMnTe) crystals are promising candidates as Faraday rotators since the effect is fast [40] and the Verdet constant $V = 1658\,\mathrm{rad\,T^{-1}\,m^{-1}}$ at $\lambda = 635$ nm in $\mathrm{Cd_{0.5}Mn_{0.5}Te}$ is huge [95]. In principle the TR-SKM setup would be sufficient for measuring the pulse duration including the spatial distribution magneto-optically because it detects temporal- and spatial resolved polarization changes. Now that the present setup is limited to normal incidence, only out-of-plane components of the magnetic field are observable and a detection under a certain angle of incidence to obtain the in-plane components would need a dedicated analysis unit as well as a second microscope objective. However, a measurement of the out-of-plane component was attempted by placing an aluminum coated CdMnTe crystal on top of the waveguide and detecting the polarization rotation of the reflected light. Unfortunately, the measurement was not successful most probably due to an insufficient overlap between magnetic field and crystal placed in contact with the waveguide surface. A better position for the Faraday rotator would be the gap of the waveguide on the substrate directly adjacent to the conductor; but cutting, positioning and mounting of the small and very fragile pieces is challenging.

The quantum efficiency (equation 2.59) of magnesium photocathodes ranges typically around 10^{-5} but can be increased by several orders of magnitude when applying a laser cleaning technique [185] that removes oxygen cover layers located on top of the cathode. In the test setup, the effect of laser cleaning was investigated by monitoring the pulse with a 2 GHz scope[1] resulting in the data presented in figure 5.1b. The quantum efficiency of an untreated magnesium surface remains $2 \cdot 10^{-5}$ while a laser scanned surface enhances the QE about an order of magnitude to 10^{-4} at comparable laser input powers. Anyhow, the extracted bunch charge seems to be limited by space-charge effects because when the laser power was increased by a factor of 13, the extracted charge only rises by a factor of 3.5. In this scenario the released negatively charged electron cloud screens the extraction field between cathode and anode directly at the cathode surface and if a critical number of electrons is released, the field is completely compensated. Any additionally liberated

---

[1] LeCroy WaveRunner 204Xi, 2 GHz, 10 GS/s, rise time 225 ps

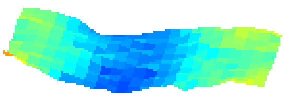

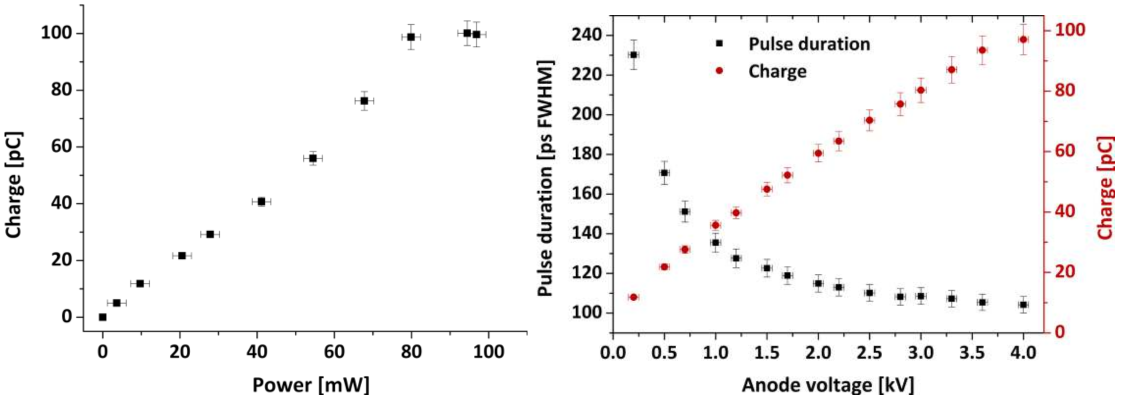

(a) Bunch charge vs. laser input power at 4 kV anode voltage.

(b) Bunch charge and pulse duration vs. anode voltage at 100 mW laser power.

Figure 5.2: Extracted bunch parameters of the photocathode vs. laser power and anode voltage measured in the test setup after increasing the magnesium area by applying a Mg cone to overcome space-charge effects.

electrons would be accelerated back to the magnesium layer and not be able to leave the surface for contributing to the current pulse.

To test this hypothesis the cathode area of the SMA cable's front size was increased by applying a cone of magnesium so that the illuminated area is now limited by the anode aperture of 2.2 mm diameter corresponding to an area of 3.8 mm^2. In figure 5.2 the extracted bunch charge vs. laser power and anode voltage is displayed for the magnesium cone attachment. Compared to figure 5.1 the charge has increased to values up to 100 pC corresponding to a peak amplitude of 1 A at the observable scope limited pulse duration. Although, the drawback of the increased power is the pulse form distortion resulting from increased ringing due to the impedance mismatch of the magnesium cone attachment. A saturation of the extracted charge beyond 80 mW laser power on the surface is an indication for still dominating space-charge effects. In figure 5.2b the bunch charge with respect to the extraction field is shown and with higher field amplitudes, more electrons become available. This is expected for space-charge limited cathodes (compare Langmuir-Child law in equation 2.62) because at a higher extraction field more electrons are necessary until the field is completely screened at the cathode surface. Fields generated by applying 4 kV correspond to an electric field of 8 kV/mm to 10 kV/mm and exceeding values already lead to discharge effects which should be avoided considering that the energy in a discharge flash might destroy the 10 µm thin conductor part in the waveguide. Applying low amplitude fields is not desirable either, owing to the reduced charge and the increasing pulse duration (figure 5.2b). In a future setup the extraction voltage could be pulsed to reduce discharge effects and provide strong extraction fields during the presence of the laser pulse.

5.2 Scanning Kerr microscope

In order to determine the spatial resolution of the scanning Kerr microscope, a structured magnetic sample was positioned at a fixed focal distance z away from the objective on the optical axis and an image was acquired by scanning the sample in x and y direction.

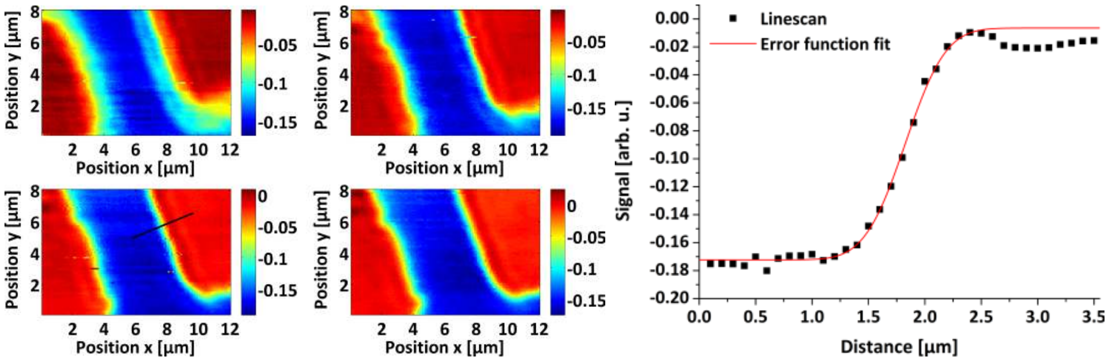

(a) SKM image of a sample with a Co/Pt grid. Each image was recorded at a slightly different focal distance along the z-axis. The black line denotes the profile plotted in figure 5.3b.

(b) Data points and error function fit with $\sigma = (284 \pm 13)\,\mathrm{nm}$ for the tagged profile in figure 5.3a.

Figure 5.3: Focus scan and profile of the transition boundary between Co/Pt multilayers and sapphire substrate supporting a sub micrometer diffraction limited resolution in the TR-SKM. The measured signal of the balanced photodetector corresponds to a polarization difference.

To locate the optimal focus position corresponding to the highest resolution, several images for each focal distance in z direction were obtained (figure 5.3a). These scans measure the polarization difference of the reflected laser beam that experiences different values for magnetic and substrate material due to the Kerr rotation and the ellipticity. A patterned Co/Pt grid was provided by Alexander Neumann by selectively removing previously created homogeneous Co/Pt multilayers on a sapphire substrate via argon ion sputtering through a mesh [153]. This sample features sharp edges smaller than the laser wavelength at the transition from Co/Pt layers to the substrate which was verified in an SEM analysis. The response when imaging the edge in the focal plane may be used to extract the optical resolution according to Rayleigh's criterion (equation 2.45) as discussed in section 2.2.2. A profile of the sharpest visible edge is presented in figure 5.3b. The error function fit (equation 2.48) returns a Gaussian width of $\sigma = (284 \pm 13)\,\mathrm{nm}$ in the convolution close to the theoretical limit (equation 2.47) of $\sigma = 286\,\mathrm{nm}$ at $\lambda = 532\,\mathrm{nm}$ (CW laser) with the $NA = 0.4$ objective. The measured value corresponds to a resolution of $\Delta l = (806 \pm 37)\,\mathrm{nm}$ and the good agreement with the theoretical limit is an indication for a diffraction limited SKM setup. In the Gaussian fit only the data points up to $2.5\,\mathrm{\mu m}$ are included because the drop of signal seems to be another feature of the transition boundary between Co/Pt and sapphire. Adding these points into the fit tends to underestimate the width σ of the Gaussian and thus the resolution.

Due to the shorter wavelength of $\lambda = 515\,\mathrm{nm}$ available with the femtosecond laser system the resolution slightly improves and is estimated to $\Delta l = 785\,\mathrm{nm}$ by the Rayleigh criterion and corresponds to a Gaussian spot of $w_0 = 553\,\mathrm{nm}$. Because of the small focal spot size, care has to be taken about the intensities at the sample. A much higher laser power than $P = 30\,\mathrm{\mu W}$ at $\tau_{\mathrm{FWHM}} = 290\,\mathrm{fs}$ pulse duration equivalent to a pulse energy of $E_{\mathrm{pulse}} = P/130\,\mathrm{kHz} = 230\,\mathrm{pJ}$ should be avoided at the sample because it already leads to peak intensities of

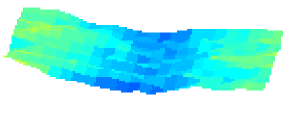

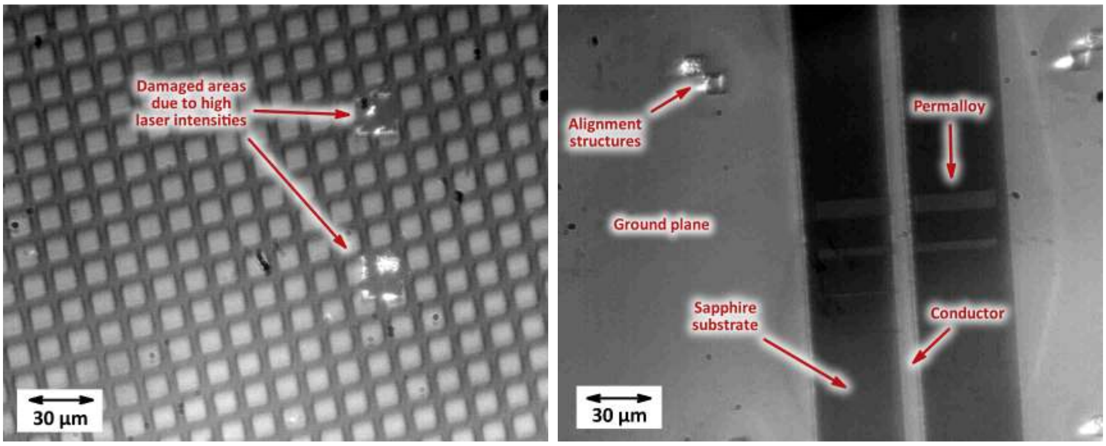

(a) Microscope image of a sample with Co/Pt islands damaged by the laser pulses.

(b) Microscope image of a coplanar waveguide with rectangular permalloy structures.

Figure 5.4: Images obtained with the in-situ microscope included into the SKM based on a CMOS camera to monitor the sample position.

$$I_0 = \frac{4\sqrt{\ln(2)}}{\sqrt{\pi}} \cdot \frac{E_{\text{pulse}}}{\pi w_0^2 \cdot \tau_{\text{FWHM}}} = 1.6 \cdot 10^{11}\,\text{W/cm}^2 \tag{5.2}$$

right below the damage threshold of the thin metallic layers on the substrate considering non-linear effects. An example of the result after scanning a sample with Co/Pt islands deposited through a mesh onto a sapphire substrate at laser intensities exceeding the damage threshold is visible in figure 5.4a. The image was obtained with the in situ sample microscope that magnifies the focal plane of the objective by a factor of 26 onto a CMOS camera when the sample is illuminated by a red high power LED. Besides this example of the Co/Pt grid for static measurements, a sample with rectangular permalloy structures and a coplanar waveguide for time-resolved measurements taken with the microscope is demonstrated in figure 5.4b.

The time-resolution available by tuning the arrival time of pump with respect to probe laser pulses in the TR-SKM is implemented by an optical delay stage (compare also figure 4.11) of $\Delta s = 300\,\text{mm}$ travel range driven by a stepper motor. Since the light travels this distance twice (back and forth), the maximal delay Δt corresponds to $\Delta t = 2\Delta s/c \approx 2\,\text{ns}$. In order to convert the driven µSteps of the stepper motor to actual time delays, a calibration of the stage has to be performed. This was carried out by installing a fast photodiode into the optical path of the pump pulse after the stage and monitoring the time delay with respect to a laser trigger signal for a series of µSteps sent to the stepper motor.

The result in figure 5.5 suggests a linear relationship since $s = c \cdot t$ and the distance s should be proportional to the number of steps of the motor. The calibration constant is extracted by fitting the slope m of the linear relationship $t = -m \cdot x$ and measures $m = (0.513 \pm 0.002)\,\text{fs/µStep}$ which means that the delay is adjustable with $\approx 1\,\text{fs}$ accuracy. This is short compared to the laser pulse duration of 290 fs and thus not limiting the time-resolution of the setup.

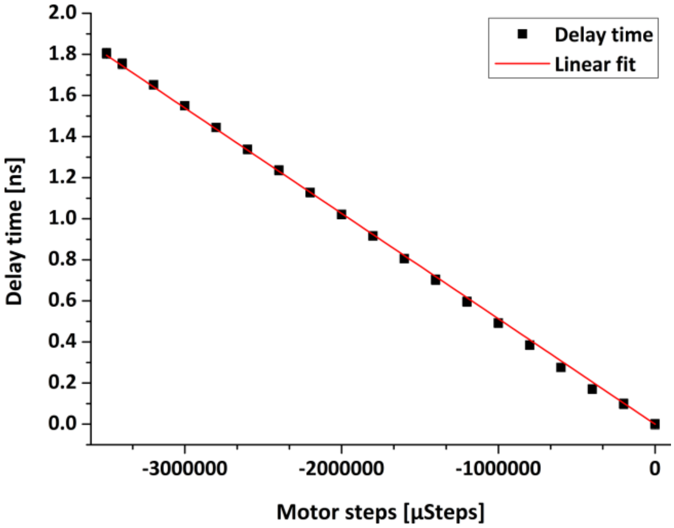

Figure 5.5: Calibration of the delay stage. The relative delay with respect to the number of µStep applied to the stepper motor was monitored with a photodiode and is well described by the linear fit $t = -m \cdot x$ using the constant $m = (0.513 \pm 0.002)\,\mathrm{fs/\mu Step}$. Error bars are included but too small to be visible.

5.3 Spectral characterization at P04

The first beamtime shifts with the TR-MTXM in June 2012 were performed in an early commissioning stage of the P04 beamline. Since the dedicated mirrors in the PM/PG-U and RMU were not available at that time, they were replaced by dummy aluminum mirrors with inferior surface quality compared to the intended ones. For a magnetic XMCD contrast it is mandatory to locate the L_3 absorption edge of the $3d$ transition metal elements investigated in the setup. After several Near Edge X-ray Absorption Fine Structure (NEXAFS) scans where the transmission of the material should drop significantly at the photon energy of the absorption edge, we were not able to locate the the edges. Therefore, a slit-grating spectrograph analogue to [217] was installed in order to measure the bandwidth of soft X-ray beam after passing the monochromator. This also enables an on-line optimization of the monochromator settings, namely exit slit size, mirror and grating position and tilt as well as the fixed-focus constant

$$c_{\mathrm{ff}} = \frac{\cos(\alpha)}{\cos(\beta)} \tag{5.3}$$

in which α and β describe the angles of incidence and diffraction, respectively. Operation of the monochromator is possible for different c_{ff} values that adjust the incident angle on the mirror and the grating but keep the output beam direction constant. The design value of $c_{\mathrm{ff}} = 2$ focuses the beam onto the exit slit for optimal spectral resolution.

The slit-grating spectrograph outlined in figure 5.6 consists of a grating with $d = 100\,\mathrm{nm}$ spacing and a support structure generating a perpendicular grating constant of $d_s = 1\,\mathrm{\mu m}$ combined with a $D = 52\,\mathrm{\mu m}$ slit. This approves a spectral resolution of up to $\lambda/\Delta\lambda = D/d = 520$ in the first diffraction order according to equation 2.42. The device is inserted directly into the soft X-ray beam and the diffracted light hits an articulated CCD detector movable in the perpendicular plane of the beam direction after a distance $b = 1968\,\mathrm{mm}$. Due to equation 2.43 this distance is needed in order to reach sufficient spectral resolution of $\lambda/\Delta\lambda_g = 435$ at $\lambda = 1.59\,\mathrm{nm}$ for a source size $q = 50\,\mathrm{\mu m}$ (exit slit size) at a distance of $g = 10\,\mathrm{m}$. Because the position of the first diffraction order exceeds the detector size, stitching over the whole spectrum by moving the camera in the diffraction plane of the grating is necessary. Two spectra representing different c_{ff}

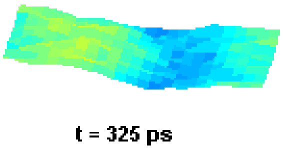

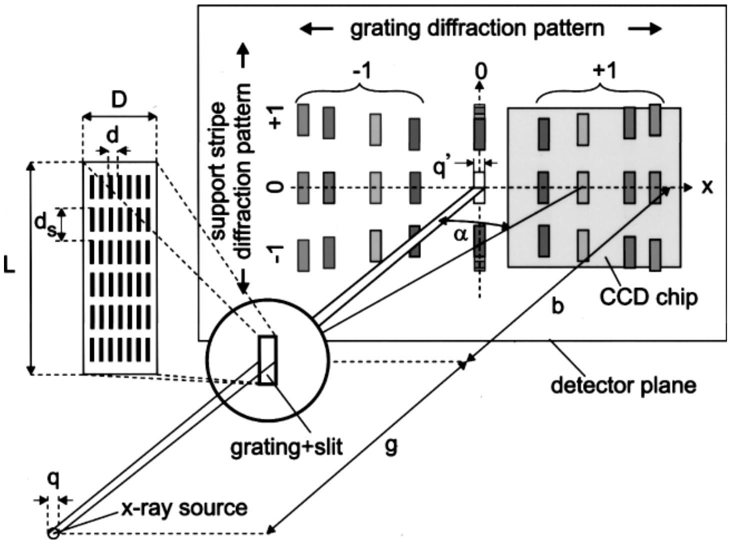

Figure 5.6: Geometry of the slit grating spectrograph setup [217] capable of analyzing the spectrum of a source (size q) located at distance g away from a grating (grating constant d, support structure grating constant d_s) combined with a slit (dimensions L x D) by diffraction onto a CCD detector at distance b.

values of the monochromator containing several images at overlapping camera positions are presented in figure 5.7.

In figure 5.7b the directly transmitted beam in the 0^{th} diffraction order as well as the diffracted beam in the first order of the 778 eV photon beam is visible while in figure 5.7a additionally the next harmonic generated by the undulator becomes observable. Conforming to equation 4.4 the wavelength peak of this harmonic ($n = 3$) is at one third of the fundamental ($n = 1$) but in the spectrum we also have to take into account the effect of the monochromator transmitting in its first diffraction order the fundamental wavelength and in its second order half of this wavelength in line with equation 2.41. Suppression of the higher undulator harmonics is possible by choosing smaller c_{ff} values matching steeper incident angles and thus lower reflectivity for higher energy photons.

Together with an energy calibration, the width of the first diffraction order in the spectrograph now is a measure of the soft X-ray bandwidth. Calibration can be achieved by tuning the photon energy while monitoring the pixel position on the detector and the resulting data in figure 5.8a is described nicely by a linear relationship $E = m \cdot x + b$ with a slope of $m = (-317 \pm 3)$ meV/pixel and an intercept of $b = (852.7 \pm 0.8)$ eV. A closer

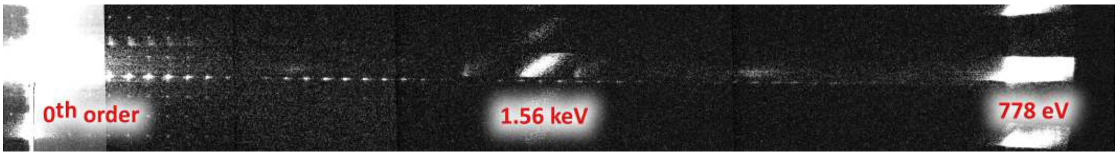

(a) Spectrum at $c_{\text{ff}} = 2$ with prominent next harmonic of the undulator.

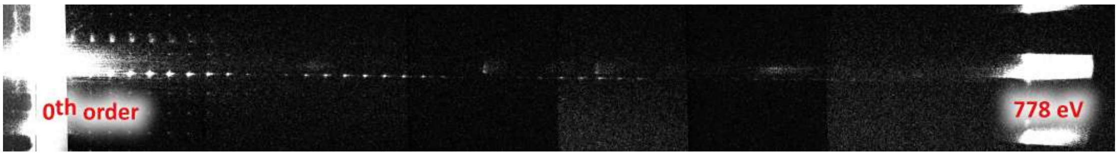

(b) Spectrum at $c_{\text{ff}} = 1.51$ with suppressed next harmonic of the undulator.

Figure 5.7: Stitched spectra at 778 eV photon energy and 90 µm exit slit size for two c_{ff} values.

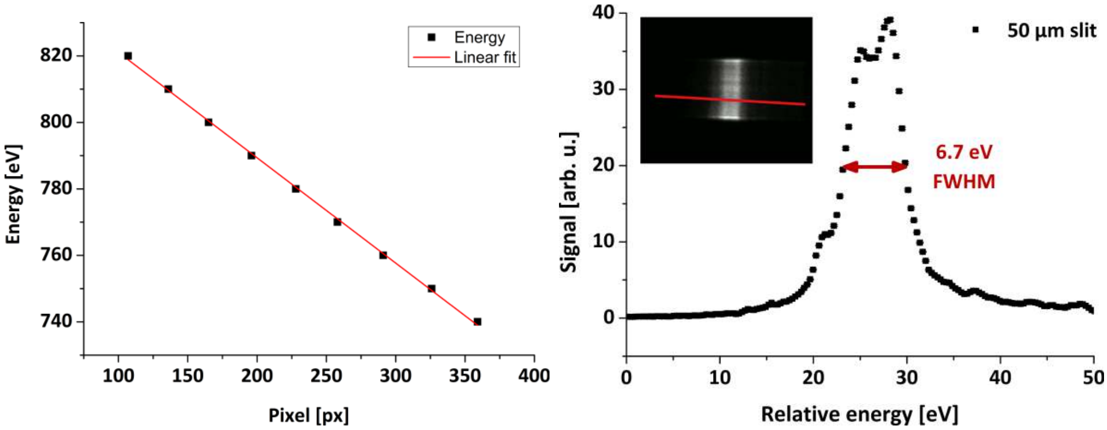

(a) Relative calibration of the spectrum. The energy with respect to the pixel position is well described by the linear fit $E = m \cdot x + b$ using the constants $m = (-317 \pm 3)\,\text{meV/pixel}$ and $b = (852.7 \pm 0.8)\,\text{eV}$.

(b) The bandwidth of the P04 beamline with the misoriented VLS grating at an exit slit opened 50 µm was determined to be 6.7 eV FWHM. The inset shows the original data on the camera and the profile position.

Figure 5.8: Calibration of the spectrograph and characterization of the P04 bandwidth with a misoriented VLS grating.

look into the first diffraction order of the spectrum in figure 5.7 is visible in the inset of figure 5.8b together with the profile of the spectrum obtained with the calibration in figure 5.8a. The data suggests a bandwidth of $\Delta E = 6.7\,\text{eV}$ FWHM at an exit slit of 50 µm corresponding to a resolving power of $\lambda/\Delta\lambda \approx 115$ at the cobalt L_3 edge which is not limited by the spectrograph resolution. The specified value at an exit slit opened 40 µm at the same energy should be $> 10\,000$ [45]. By looking at the first diffraction order it was also possible to tune the mirror position and angles. When hitting defects on the mirrors the shape on the detector gets distorted. All settings were optimized in a way that the bandwidth was as small and the spectrum as homogeneous as possible. Nevertheless, after the optimization process a smaller bandwidth than 6.7 eV FWHM could not be obtained and no absorption edge was measurable preventing the observation of magnetic XMCD contrast images in the first shifts. Later it turned out that the bad resolving power originated from a wrong oriented variable line spacing (VLS) grating installed inside the PM/PG-U of the P04 beamline. The incorrect orientation lead to a defocussing of the soft X-ray beam and smeared out the bandwidth. After turning over the VLS grating by the P04 staff in February 2013, instantaneously a resolving power of $\lambda/\Delta\lambda > 10\,000$ became available and NEXAFS scans as well as XMCD microscopy worked eventually in a successive shift in April 2013.

In order to measure the NEXAFS spectra in a subsequent beamtime, a 30 nm thick permalloy layer located on a < 1.5 µm thick PMMA layer on top of a 200 nm silicon nitride membrane (which is basically the precursor for the nanostructured samples without performing the lift-off) was inserted into the soft X-ray beam. The direct transmission of the photons was monitored on a phosphor screen imaged onto a CCD detector by recording the brightness of the cast shadow image of the membrane with respect to the photon energy of the beamline (figure 5.9).

After the orientation of the VLS grating was corrected inside the beamline, the spec-

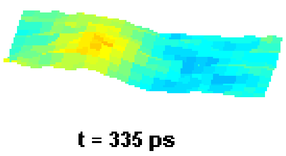

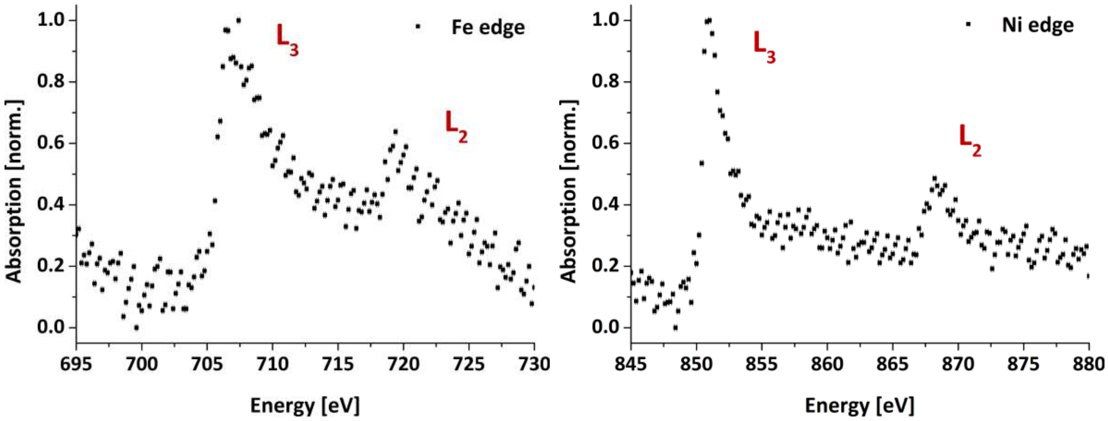

(a) Iron (Fe) L_2 and L_3 edges.

(b) Nickel (Ni) L_2 and L_3 edges.

Figure 5.9: NEXAFS spectra of a permalloy layer measured with monochromatized light behind an exit slit opened 38 µm after correcting the orientation of the VLS grating.

tral resolution was sufficient for detecting the fine structure components namely the L_2 and L_3 resonances. The high noise level in the data most probably originates from a defective contact inside the CCD camera that was present during these measurements and lead to fluctuating brightness levels.

5.4 Transmission X-ray microscope

Along with the characterization of the TXM also briefly the alignment procedure of the microscope at the beamline is sketched.

5.4.1 Alignment and grating condenser

The mobile soft X-ray microscopy endstation constructed in this work was set up and commissioned in the first beamtime shifts of this project in June 2012 only with a moderate resolving power of the beamline due to the misoriented VLS grating (see previous section). For pre-alignment of the microscope, the vacuum chambers were positioned on the optical axis with help of a leveler and two apertures at the front- and back flanges of the chamber while visible white light generated in the dipole bending magnet of the synchrotron served as a marker for the optical axis. Afterwards, the optical components are positioned into the beam one after another starting with the grating condenser pre-alignment. In order to verify the operation of the condenser and to fine-tune the alignment, first only the diffraction image of the condenser was projected onto the CCD detector.

Figure 5.10a shows an SEM image of the optic. In the far field of the condenser every grating diffracts the beam according to equation 2.41 and the spots of constructive interference for the first and second positive and negative diffraction orders n become visible on the detector. Spots corresponding to orders of different sign can be separated by moving a knife edge into the beam so that only one half of the condenser is illuminated because positive diffraction orders are convergent while negative ones diverge. The first and second order of the illuminated half of the condenser are then visible in one half-plane

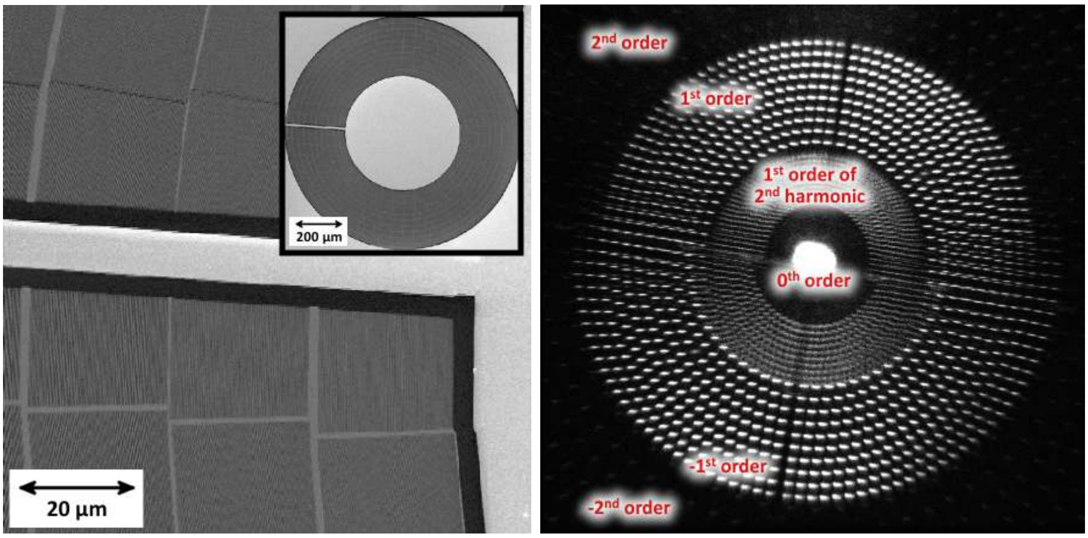

(a) SEM images [28] showing the 1 mm diameter grating condenser optic consisting of 940 diffraction gratings of 25 µm × 25 µm size with a gold central stop of 500 µm diameter (see also table 4.2).

(b) Diffraction pattern of the grating condenser with separated positive and negative diffraction orders obtained by blocking one half of the optic with a knife edge.

Figure 5.10: Real space and diffraction image of the grating condenser optic.

of the detector while the minus first and second one end up in the other half-plane. The result of such an acquisition is depicted in figure 5.10b showing also the bigger divergence of the $n = -1^{\mathrm{st}}$ diffraction order compared to the $+1^{\mathrm{st}}$ order. The diffraction pattern closer to the center can only be explained by higher harmonics from the undulator. In chapter 5.3 is discussed and demonstrated that the next harmonic of the undulator indeed can be present in the soft X-ray beam for certain values of the PM/PG-U fixed-focus constant c_{ff} explaining the inner diffraction pattern as the $\pm 1^{\mathrm{st}}$ diffraction order of the next harmonic radiation of the undulator. By a closer look into the peripheral region of figure 5.10b also the $\pm 2^{\mathrm{nd}}$ diffraction order is apparent. A homogeneous illumination of the whole optic with maximum photon flux is a criterion for a good alignment. This can either be checked by equal brightness of all diffraction spots or by the homogeneous illumination of the cast shadow image of the condenser in the 0^{th} diffraction order directly projected onto the detector.

The second step in setting up the microscope is the installation of the sample and the zone plate. Once the condenser is installed and aligned, the sample is placed into the focal plane of the condenser and pre-aligned with white light and leveler since the condenser optic still transmits enough light to be visible. Typically, the sample is a silicon frame with a silicon nitride membrane window of a few hundred micrometer size that has to be positioned onto the optical axis. Eventually, the micro zone plate has to be arranged onto the optical axis at its focal distance apart from the sample. In this stage the white light normally can not be seen through the leveler any more because it is attenuated too much by the soft X-ray optics and one has to rely on a good leveler pre-alignment and finish the positioning in the working microscope with light from the undulator.

Usually for the first images a small magnification of around $M \approx 300$ was chosen

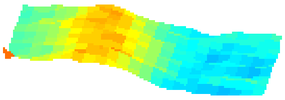

since the adjustment is easier compared to large magnifications. The change to higher values of $M \approx 700$ is not difficult to implement once the microscope is set up and well aligned because only the detector has to be moved further away to increase the image distance and the micro zone plate has to be refocused slightly to decrease the object distance (equation 4.5). If the real sample consists of only a few small objects it can be advantageous to install a mesh as first sample offering a periodic structure through the whole field of view that can be located more easily during alignment and focusing. However, an aperture should be installed as well near the object to get rid of stray light. For the $250\,\mu\text{m} \times 250\,\mu\text{m}$ silicon nitride membranes this was not necessary, the small membrane window itself acts as a sufficient stray light shield.

5.4.2 Spatial resolution

If the magnification of the X-ray microscope is high enough so that the spatial resolution is not limited by the detector (see also section 4.7), it is dominated by the quality of the optics i.e. the micro zone plate. The available zone plate with an outermost zone width of $\Delta r_N = 50\,\text{nm}$ allows a minimally observable distance of 61 nm according to equation 2.56. To check the achievable resolution, the pattern of a Siemens star was imprinted into the sample of Co/Pt structures as well. In an image of the star with n black and white spokes the resolution

$$\Delta l = \frac{\pi d}{n} \tag{5.4}$$

can be measured by determining the diameter d up to which the spokes are separated. A picture of a Siemens star with 50 spokes (i.e. $n = 100$) at $M = 700$ magnification recorded with the transmission X-ray microscope is depicted in figure 5.11a. The picture was corrected by subtracting a dark image obtained with closed camera shutter to remove artifacts originating from the camera. Additionally, the resulting data was divided by a dark image corrected flat-field picture acquired after moving the sample out of the field of view to correct for features formed by the illumination field. The inner part of the star is obscured by remnants of the lithography process and down to this 2.5 µm diameter area all spokes are discernible. This provides an upper limit for the resolution $\Delta l < 78\,\text{nm}$ conforming to equation 5.4.

To cross-check this value, a line profile of an image of Co/Pt nanostructures (visible in the inset of the graph) is plotted in figure 5.11b. The actual edge of the magnetic dot is assumed to be smaller than the resolution of the TXM because the focus of the electron microscope used for structuring in general limits the width since proximity effects can be neglected due to the lack of backscattering in the thin silicon nitride membrane. The pattern is free from remnants as well since the dots are more isolated structures compared to the dense line pattern of the Siemens star center. Similar to the TR-SKM data, a fit according to equation 2.48 is able to reconstruct the width σ of the Gaussian profile in the convolution. In this case it measures $\sigma = (22 \pm 3)\,\text{nm}$ corresponding to a resolution of $\Delta l = (62 \pm 8)\,\text{nm}$ in consonance with the Rayleigh criterion when mapping the Airy function (see section 2.2.2). The value agrees very well with the theoretical limit of $\Delta l = 61\,\text{nm}$ and suggests that the resolution is limited by the zone plate optic.

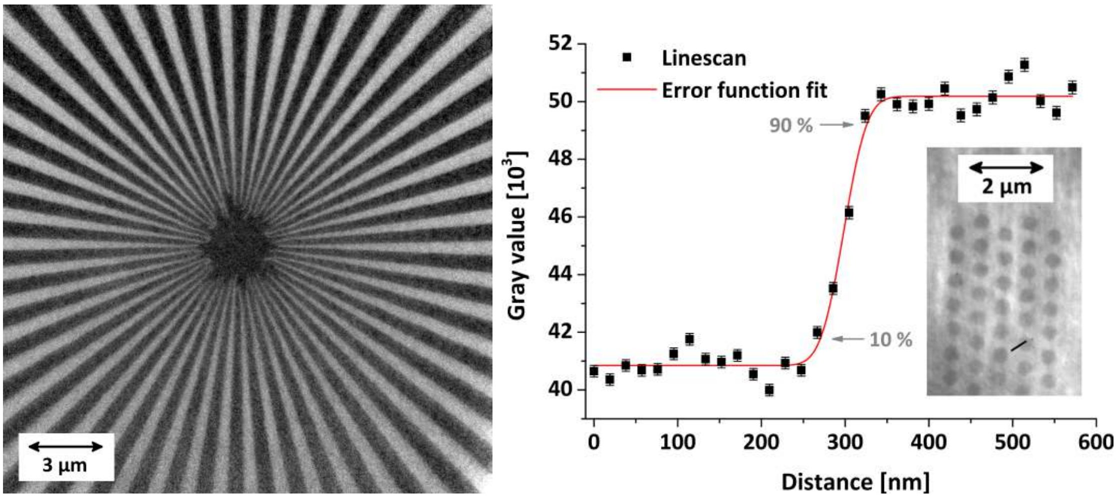

(a) Dark image and flat-field corrected TXM image of a Siemens star with 50 spokes. The inner part is obscured by remnants of the lithography process.

(b) Profile of the line in the inset image of a nanostructured magnetic Co/Pt multilayer system fitted by an error function with $\sigma = (22 \pm 3)\,\mathrm{nm}$. The signal increases from 10 % to 90 % in 57 nm.

Figure 5.11: Siemens star and line profile supporting a resolution limited by the zone plate optic. Each image was exposed for 300 ms.

5.4.3 Illumination field and spatial coherence

Due to the very small emittance of the PETRA III storage ring related to the small source size, the soft X-ray beam experiences a high degree of spatial coherence. When working at a small exit slit size in the P04 beamline corresponding to a high resolving power, the good monochromaticity additionally enhances the temporal coherence. For many applications and experiments this is very favorable but in a full-field microscope, however, the coherent beam interferes in the image plane generating a severe speckle pattern in the illumination field visible in the background of figure 5.12. For the construction of difference images needed for XMCD measurements this is troublesome because the speckle pattern also slightly changes for different photon helicities of the undulator and dominates any magnetic XMCD difference contrast.

This effect has also been observed in other full-field microscopes [207] and was resolved by inducing vibrations to the beam to destroy the spatial coherence. For this microscope different wobble mechanisms were tested and the best solution was installing a roughing pump on the hexapod of the last beamline refocusing mirror in the RMU to shake it with an amplitude larger than the speckle pattern period. Stirring the beam with the piezo actuators in the hexapod by applying an AC voltage did not work very well because the movement was too reproducible so that a structured background remained. Even randomizing the frequency of the AC signal did not resolve this problem and, additionally, the piezo controllers automatically switched off after some time stopping the movement. Another method was shaking the condenser optic itself. This, however, resulted in mechanical vibrations inside the vacuum chamber destroying the spatial resolution of the microscope and over time in damage of the piezo stage. Furthermore, the distance moved back and forth was not completely reproducible so that after some time the focus of the condenser shifts out of the field of view in the microscope. The homogeneous illumination

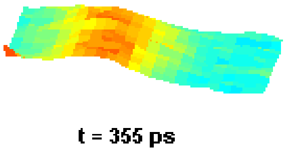

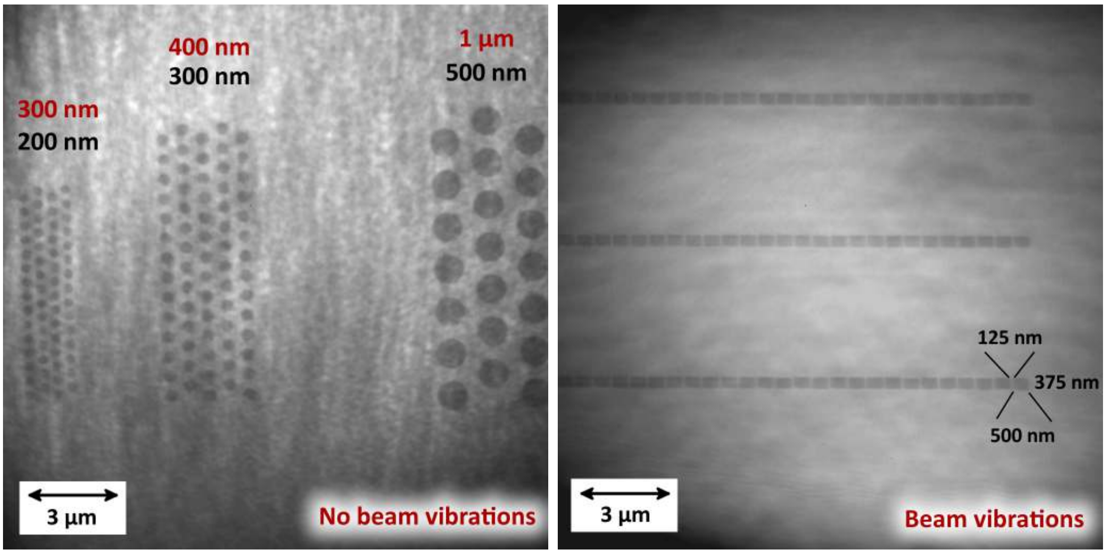

(a) Co/Pt multilayer system with a transmission of ≈ 75 % at the cobalt L_3 edge (778 eV). The red labels indicate the dot diameter while the black labels specify the minimum distance between two dots. The image shows the sum of 20 images taken at 250 ms exposure time at an exit slit of 1 mm.

(b) Chain of 500 nm × 375 nm permalloy rectangles separated by 125 nm with a transmission of ≈ 85 % at the iron L_3 edge (707 eV). Here, beam vibrations were induced to remove the speckle pattern in the illumination field. The image shows the sum of 30 images taken at 1 s exposure time.

Figure 5.12: TXM images of nanostructured magnetic materials. The data is only subtracted by a dark image and otherwise represents the raw output of the microscope.

field generated by the vibrations of the roughing pump can be seen in figure 5.12. Only a smoothed small speckle pattern remains that can be removed completely by correction with flat-field images (compare also figure 5.11a).

5.5 Fast gateable X-ray detector

The commissioning of the fast gateable X-ray detector was done without an X-ray microscope at the beamline by projecting the cast shadow of a permalloy layer on a silicon nitride membrane used for spectroscopy onto the first fluorescent screen. A crystalline Ce:YAG and a 3 µm thin P46 phosphor screen were tested as photon converters into the visible spectral range. By tuning the delay with respect to the storage ring trigger, the moment of the image snapshot is adjusted giving the opportunity to resolve the pulses of the synchrotron light due to the bunch structure inside the storage ring. These photon pulses of the beamline convoluted with the afterglow of the screens (≈ 200 ns) and the intensifier photocathode gate pulse duration of 40 ns become visible in figure 5.13. Here, the ring was filled with 40 bunches leading to a light pulse every 192 ns.

The amplitude between signal and background only ranges around two when using the Ce:YAG screen while the thin P46 achieves a suppression of approximately an order of magnitude to the permanent equilibrium background glowing level. Since the fluorescent material in both screens is the same, the thickness must be an explanation for the superior P46 screen. Only a small fraction of the Ce:YAG is exposed to the soft X-ray beam due

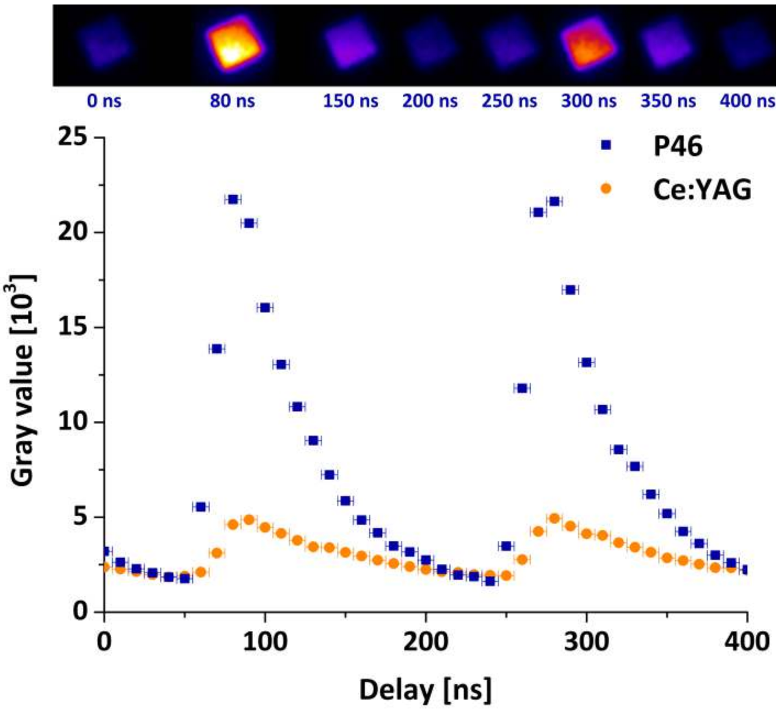

Figure 5.13: Brightness of a silicon nitride membrane shadow image (top) coated with a permalloy layer with respect to the detector gate pulse delay (bottom). The 192 ns separation of the 40 bunches in the storage ring convoluted with the gate pulse duration of 40 ns and the phosphor decay time is observable.

to the short penetration depth and a lot of fluorescent light might be reabsorbed by the crystal. The scattered light may lead to a higher background level.

Typically the detector is operated at 5.4 kV MCP to phosphor voltage, 600 V MCP and 170 V photocathode voltage. Higher MCP potentials resulting in more gain were avoided because they lead to bright spots in the output signal which are unfavorable in difference image calculation. Additionally, the gain at 600 V is sufficient yielding acceptable exposure times of the CCD camera. The pulse duration of 40 ns was chosen because it is short enough to select the signal from only one bunch and further increase does not result in considerably more counts in the camera. When setting up the detector, the output pulse duration should be checked manually with a HV probe because it depends on the trigger pulse duration and level.

During succeeding shifts at the P04 beamline, first the gateable detector was used for time-resolved XMCD measurements at the *nickel L* edge and then a direct X-ray CCD camera (Andor iKon-M) was installed for another TXM project on the investigation of clay mineral samples at the *iron L* edge. The acquired flat-field data allows an immediate comparison between the two detectors, because the samples were moved out of the the field of view. In case of the direct X-ray CCD, it has to be taken into account that one photon creates more than one electron when the photon energy exceeds the threshold of 3.65 eV for creating an electron-hole pair in the silicon layer of the CCD chip. The number of electrons N_e per photon is then given by the photon energy E_{ph} divided by 3.65 eV. With the knowledge of exposure time t and quantum efficiency QE describing here the probability of photon absorption in the depletion region, the photon flux

$$I_{\mathrm{ph}} = \frac{C \cdot \frac{e^-}{ADU}}{QE \cdot N_e \cdot t} \qquad \text{with} \qquad N_e = \frac{E_{\mathrm{ph}}}{3.65\,\mathrm{eV}} \tag{5.5}$$

on the CCD chip can be calculated. The counts C in an image relate to the electrons via

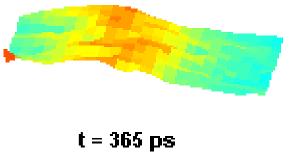

the conversion factor e^-/ADU specifying the number of electrons per analog-to-digital unit for the applied settings (in particular gain and readout rate). In case of detecting visible photons of the image intensifier phosphor output screen with the camera in the gateable detector, the N_e factor equals unity because the photon energy of visible light is below the threshold for creation of an electron-hole pair in the silicon layer of the CCD chip and one photon in average creates less than one electron (compare section 3.1). The CCD photon to electron conversion is then solely determined by the quantum efficiency of the CCD chip.

The Andor X-ray CCD camera exhibits a quantum efficiency of 0.82 to 0.9 [6] in the relevant photon energy range and experienced a photon flux of $(8.1 \pm 0.3) \cdot 10^8$ photons/s calculated by equation 5.5 and the counts in the flat-field images. This corresponds to $(8 \pm 2) \cdot 10^{10}$ photons/s emitted by the P04 beamline considering the diffraction efficiency of grating condenser and zone plate (each $\approx 10\,\%$) and is an order of magnitude lower than specified by the beamline parameters suggesting 10^{12} photons/s at the output flange [45]. The discrepancy is most probably explained by an imperfect condenser illumination because the beam size exceeds the condenser diameter of 1 mm at least in one direction due to a missing refocusing mirror in the RMU of the beamline. Furthermore, owing to the spectral resolution needed for the investigation of the clay mineral samples during these experiments, the exit slit was kept rather small.

At comparable conditions the CCD chip of the camera in the permanently opened gateable X-ray detector encountered a photon flux of $(1.00 \pm 0.02) \cdot 10^{10}$ visible photons/s generated by the output phosphor screen of the image intensifier. This means that the P46 phosphor plus relay optic plus image intensifier combination necessary for extracting time-resolved information amplifies the signal by a factor of approximately 12.3 ± 0.4 at the given operation conditions. Theoretically, given the photon to photon conversion efficiency of the phosphor (25 %), the transmission of the relay optic (9.25 %) and the luminous gain of the image intensifier ($390\,\mathrm{lm}/(\mathrm{m}^2\,\mathrm{lx})$) specified in section 4.7.1, an overall amplification of $0.25 \cdot 0.0925 \cdot 390 = 9$ is expected. The difference between the expected and measured value originates from the high uncertainty of the image intensifier gain due to the non-linear amplification characteristics of the included MCP and from different exit slit sizes applied in the compared measurements. In fact, the exit slit size was larger during the experiments with the gateable detector in consonance with the obtained higher amplification. In gated application (i.e. timing mode) the flux determined here is further reduced by a factor of 40 due to the limitation on the light generated by a single bunch.

5.6 Reset coil and driver

In the present configuration described in section 4.2 the water-cooled coil including the driver provides stable operation over several days at the full repetition rate of 130.1 kHz with 1.5 µs to 2 µs pulse duration inside a vacuum system at $1 \cdot 10^{-6}$ mbar base pressure. A collection of data characterizing the reset coil and its custom designed driver is presented in figure 5.14. Here, figure 5.14a shows a typical current pulse of 2 µs pulse duration with 7 A peak amplitude measured at the monitor port of the driver (see figure E.1 in appendix E) providing a 100 mV/A signal at a 0.1 Ω resistor in the coil current loop. At the switching moments of the MOSFETs electromagnetic pulses (EMPs) are released and occur in the visible signal as disturbances as well.

The figures 5.14b - 5.14d show a magneto-optic Kerr microscope measurement ob-

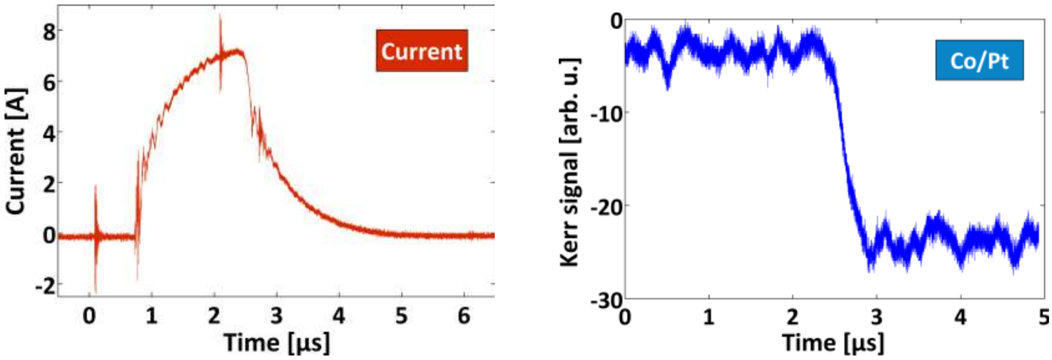

(a) Reset coil current pulse of 7 A amplitude and 2 µs duration measured at the monitor port of the coil driver.

(b) Kerr signal trace of a switching process in a Co/Pt multilayer system triggered by the magnetic field pulse of the coil.

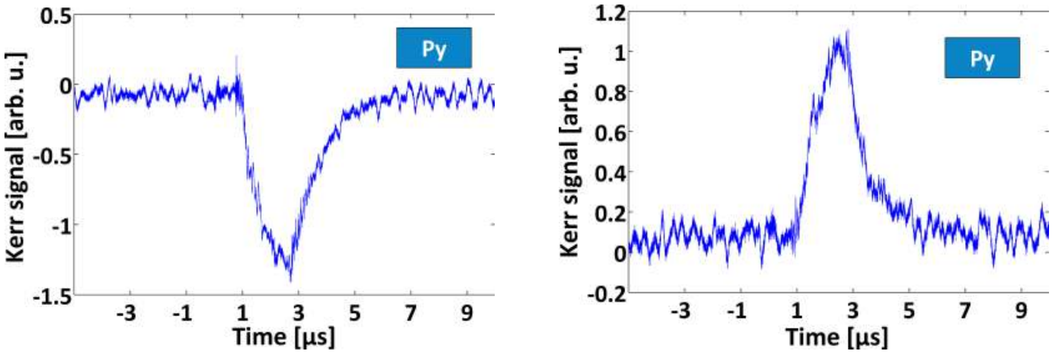

(c) Magnetic out-of-plane response of a thin permalloy film excited by the coil (EMP data subtracted).

(d) Magnetic out-of-plane response of a thin permalloy film excited by the coil (EMP data subtracted, field direction inverted).

Figure 5.14: Current pulse form and MOKE data for permalloy and Co/Pt layers switched by the air-core coil.

tained with a fast scope connected to the output of the balanced photodetector in the TR-SKM. A Co/Pt multilayer film positioned below the coil case demonstrates that these structures can be switched by a single magnetic field pulse of the coil (figure 5.14b) which is important for pump-probe and reset experiments. The magnetization of the Co/Pt multilayer remains in the direction of the pulsed field even after the amplitude has vanished due to the high coercivity. The same measurement has been repeated with a permalloy film in figures 5.14c and 5.14d for both directions of the coil field switchable by a relay. Usually, the thin film is magnetized in the sample plane but during the presence of the magnetic field pulse an out-of-plane component is observable that vanishes after the pulse is gone. A trace of the EMP obtained by acquiring the scope trace with the laser switched off (i.e. no Kerr signal) has been subtracted from the measured dataset. Generally, the magnetization profile resembles the current (and thus the field amplitude) profile which is expected because the displacement of the magnetization vector should happen adiabatically on the time scales of the long (µs) magnetic field pulse compared to the spin precession time (ps).

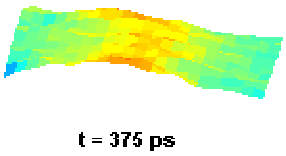

Chapter 6

Results and discussion

With the characterization of both magnetic microscopy setups, the performance of all important components (photocathode pulses, spectral resolution at P04, spatial resolution of SKM and TXM) could be verified to be sufficient for time-resolved experiments on the magnetization in micro- and nanostructures. The presented results in this chapter exclusively contain information on the nature of the magnetization in different samples imaged by the TR-SKM (section 6.1) and the TR-MTXM (section 6.2). Each section first reviews data obtained in static measurements and later on deals with the discussion and interpretation of the dynamic studies. Both experiments cover aspects of the collective action of coupled confined spin systems to a transient stimulus. The TR-SKM data treats the investigation of emerging spin-waves in continuous films while the TR-MTXM observes the dynamics in discrete elements excited out of their equilibrium magnetization patterns and aims toward research on coupled systems.

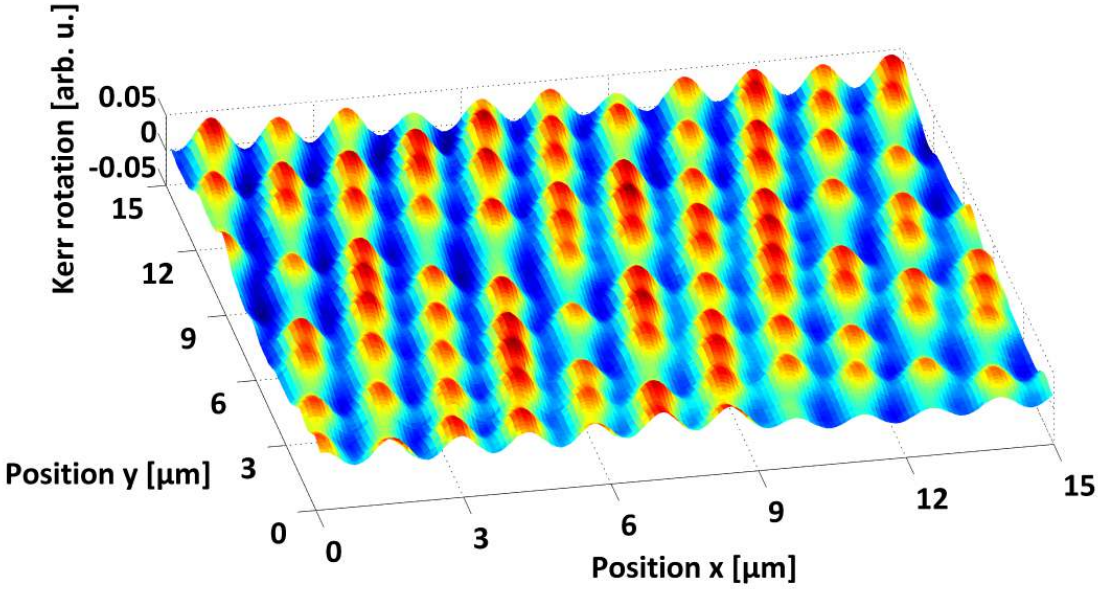

Figure 6.1: Kerr signal of a 15 µm × 15 µm area of a commercial MO-disk scanned in 100 nm steps. The bits representing the data stored on the device are clearly visible.

6.1 Time-resolved scanning Kerr microscopy

6.1.1 Static measurements

One of the first samples measured in the constructed scanning Kerr microscope was a commercial magneto-optical disk (MO-disk) because this storage medium relies on the balanced detection of the polarization rotated by the polar magneto-optic Kerr effect. Figure 6.1 shows a map of the magnetization in a 15 µm × 15 µm section scanned in 100 nm steps of a MO-disk previously filled with data. The magnetic bits of approximately 1 µm size represent the digital information in form of zeros and ones and are clearly visible in the tracks of the disc. This image demonstrates that the SKM works as expected for static measurements and can deal not only with artificially prepared samples but also flexibly with objects from everyday life.

An example of imaging and manipulating an artificially prepared sample is depicted in figure 6.2. The data shows the color-coded Kerr signal in degrees of a 50 µm × 50 µm area scanned in 250 nm steps of out-of-plane magnetized Co/Pt multilayer islands sputtered through a mesh onto a sapphire substrate [153]. The left image was taken after magnetizing the sample into one direction in the vicinity of a strong magnet while the right image was obtained after magnetizing the sample into the opposite direction by the other pole of the same magnet. So, in one image the magnetization points out of the sample plane while it points into the sample plane in the other dataset leading to a measurable Kerr angle of $\phi_K \approx 0.35°$ in good agreement with hysteresis measurements giving $\phi_K = 0.36°$ at another calibrated non-imaging MOKE setup [153]. This shows that the SKM is also able to extract quantitative information out of magnetized samples.

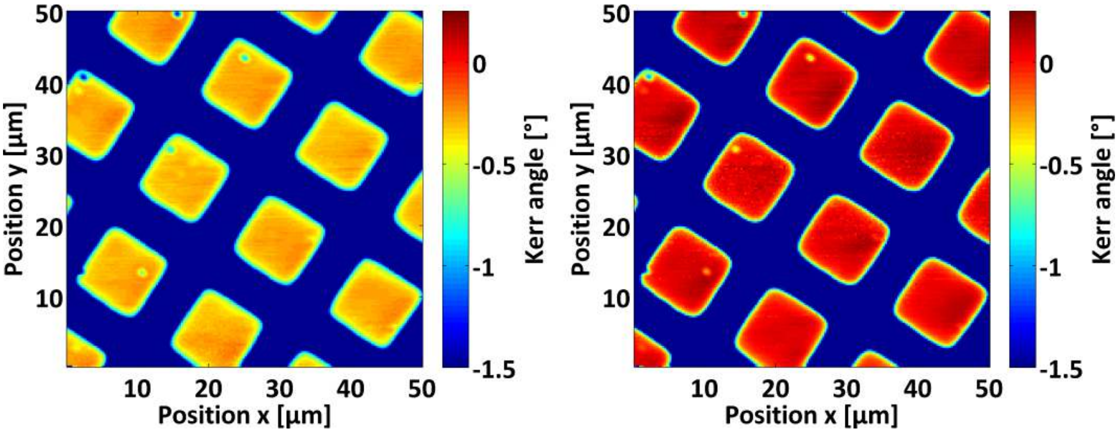

Figure 6.2: Kerr signal of a 50 µm × 50 µm area of an out-of-plane magnetized Co/Pt multilayer system scanned in 250 nm steps. The two images represent two magnetization configurations of the system and the color scale maps the Kerr rotation angle in degrees giving $\phi_K \approx 0.35°$ between both states presented in the images.

6.1.2 Temporally resolved spin-wave packets

Damon-Eshbach modes

A time-resolved measurement of a spin-wave packet in a permalloy slab in Damon-Eshbach (DE) configuration of 10 µm width, 35 µm length and 30 nm thickness was per-

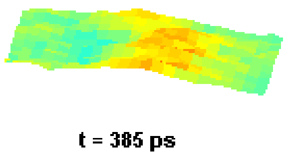

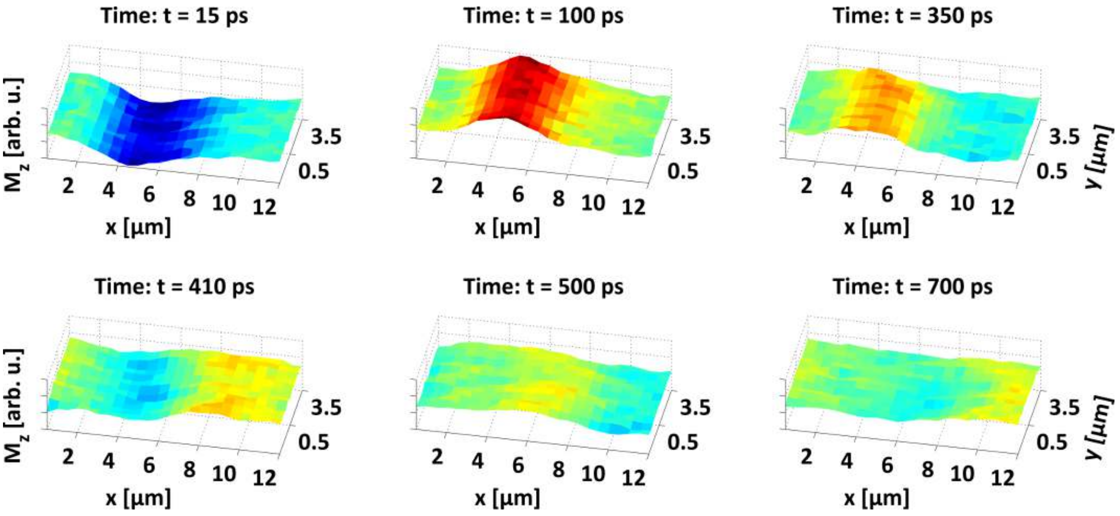

Figure 6.3: Selected frames of the acquired spin-wave packet movie illustrating the transient magnetization in a permalloy slab of 10 µm width at six delay settings.

formed with the TR-SKM. The spin-wave is launched into the slab at the overlapping region between waveguide and permalloy (figure 2.7) by the short excitation pulse generated in the photocathode. Figure 6.3 depicts six frames of the spin-wave movie[1] showing the M_z component of the magnetization measured by the TR-SKM at different delays after the excitation. The moment $t = 0\,\mathrm{s}$ indicates temporal overlap with the current pulse in the waveguide and the spatial overlap between waveguide and permalloy slab ends at $x = 5\,\mathrm{\mu m}$. The current pulse initiates spin precession with the eigenfrequency of the permalloy stripe in an external field of 60 mT (compare calculation in figure 2.8). Notable is that the excitation is maximal at the boundary of the waveguide which is explainable by the skin effect providing maximal current densities at the surface of the conductor for high frequencies (compare simulation in figure 4.3). The initially confined excitation starts to spread out into positive x direction after some time because neighboring spins not directly excited by the field of the pulse „see“ the initiated gyration and an energy transfer of the precessional motion takes place via dipolar and exchange coupling.

Each image was acquired by scanning a $\Delta x = 12\,\mathrm{\mu m}$ and $\Delta y = 6\,\mathrm{\mu m}$ area in 500 nm steps and measuring a trace of the balanced photodetector output of 50 kS length at a sample rate of 250 kS/s. This means the DAQ consumes 200 ms by averaging over ≈ 26 000 laser pulses (i.e. pump-probe cycles) per data point. In order to obtain temporal information, the delay Δt between the pump and probe pulses has to be varied. For this measurement a scan range of 1.5 ns was swept in 5 ps steps which means it consumes in total

$$T = \underbrace{200\,\mathrm{ms}}_{\substack{\text{DAQ time}\\ \text{per data point}}} \cdot \underbrace{\frac{12\,\mathrm{\mu m}}{500\,\mathrm{nm}}}_{\substack{\text{Pixel in}\\ x\text{ direction}}} \cdot \underbrace{\frac{6\,\mathrm{\mu m}}{500\,\mathrm{nm}}}_{\substack{\text{Pixel in}\\ y\text{ direction}}} \cdot \underbrace{\frac{1.5\,\mathrm{ns}}{5\,\mathrm{ps}}}_{\substack{\text{Number of}\\ \text{time steps}}} = 4.8\,\mathrm{h} \tag{6.1}$$

---

[1] Additional frames of this movie are available as flip-book film sequence in the bottom left corner of this thesis.

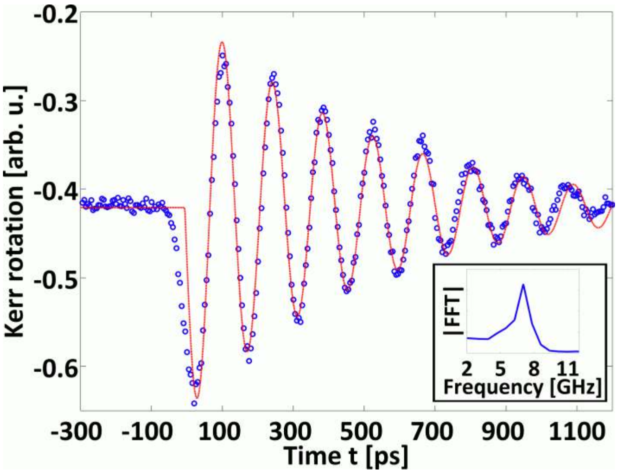

Figure 6.4: Magnetization component M_z with respect to time spatially averaged over an area of Δx = 5 µm to 10 µm and $\Delta y = -1.5$ µm to 3 µm excluding the boundaries and the overlap region in contact with the waveguide (blue curve). The fit according to equation 6.2 (red curve) returns an oscillation frequency of $f_r = (7.07 \pm 0.02)$ GHz and a damping constant of $\delta = (2.0 \pm 0.2)\,\mathrm{ns}^{-1}$. The inset shows a Fourier transform peaked at 7.03 GHz.

only considering the DAQ time and neglecting the piezo positioning time and the movement of the delay stage leading to 5.5 h total expenditure of time. Stable operation of all components is mandatory during this time because the pump-probe approach relies on the reproducibility of each measurement.

The lock-in amplifier was set to a sensitivity of 300 µV full-scale at low drift which represents maximal sensitivity without generating an overload error in the amplifier. The integration time-constant of 300 ms was chosen to be comparable to the time consumption of one data acquisition to minimize the overlap of the signal between adjacent data points[2]. For efficient filtering of low frequency noise, the chopper ran at 995 Hz close to its maximal frequency of 1 kHz.

The green probe laser power of ≈ 30 µW corresponding to 230 pJ pulse energy and $1.6 \cdot 10^{11}\,\mathrm{W/cm^2}$ peak intensity on the sample was set right below the damage threshold of the material to gain maximal signal per shot without destroying the metallic layers. The photocathode operated at an anode voltage of 3 kV resulting in an average current of 2 µA at 400 mW UV laser power measured before entering the vacuum chamber. Because during a TR-SKM experiment the parasitic measurement of the current pulses is impossible, the anode current is the only indicator for the extracted charge and was monitored to optimize the alignment of the UV beam onto the photocathode. Given the repetition rate of the laser, the charge of each bunch can be estimated to 15 pC. This is consistent with the quantum efficiency of the (uncleaned) cathode in the range of 10^{-5}. The pressure inside the chamber was kept at $1.7 \cdot 10^{-7}$ mbar with inserted laser beam.

Figure 6.4 shows the spatially averaged M_z oscillation amplitude over $\Delta x = 5$ µm to 10 µm and $\Delta y = -1.5$ µm to 3 µm by excluding the boundaries and the overlap region with the waveguide. The trace resembles a damped oscillation and a fit described by the model

$$M_z(t) = M_0 - M_A \cdot \Theta(t - t_0) \cdot \mathrm{e}^{-\delta(t-t_0)} \cdot \sin\left(\sqrt{\omega_0^2 - \delta^2} \cdot (t - t_0)\right) \tag{6.2}$$

---

[2] Technically, the DAQ time should exceed the lock-in integration time-constant to avoid any overlap between adjacent data points. Originally, the trace length was set to 125 kS corresponding to a DAQ time of 500 ms but unfortunately only 50 kS were taken at each scan point due to a software bug in the experimental control program that was discovered after the measurements.

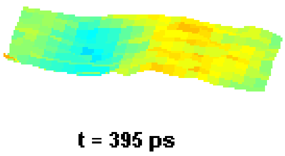

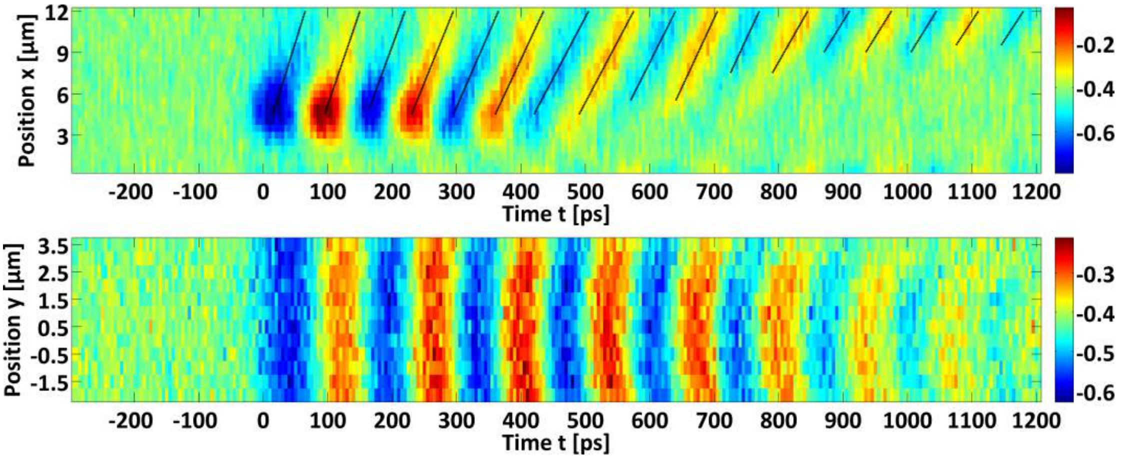

Figure 6.5: The top image shows the propagation of the spin-wave packet in x direction with respect to time at a fixed transversal position in the center of the slab ($y = 0\,\mu\text{m}$). The black lines are a measure of the propagation of the maxima and minima and correspond to the phase velocity v_{ph}. In the bottom image the spatial distribution of the transversal modes at a fixed longitudinal position at ($x = 8\,\mu\text{m}$) is displayed with respect to time.

was applied with $\Theta(t)$ describing the Heaviside step function, ω_0 the (undamped) eigenfrequency and δ the damping coefficient. M_0, M_A and t_0 are additional fit parameters to match the offset, amplitude and temporal overlap. The best agreement was achieved for a resonance frequency $f_r = \omega_0/(2\pi) = (7.07 \pm 0.02)\,\text{GHz}$ and $\delta = (2.0 \pm 0.2)\,\text{ns}^{-1}$. This oscillation frequency agrees with the maximum of the Fourier transform at 7.03 GHz presented in the inset of figure 6.4 within the accuracy of the fast Fourier transform (FFT) due to discretization. However, at time delays larger than 700 ps the data is not described very well by a single frequency oscillation and experiences a chirp toward higher frequencies. As we will see later this only seems to be the case in a spatially averaged evaluation and the gyration at one particular pixel position is well described by the single frequency model. Additionally, when comparing the data to the prediction obtained by discretely solving the LLG equation in figure 3.2a, it is conspicuous that the damping is much stronger than expected. Equation 2.33 relates the damping constant δ to the dimensionless damping parameter α and returns for the measured value $\alpha \approx 0.02$ more than a factor of two higher than $\alpha = 0.008$ for permalloy. An explanation for this effect is the limited area scanned by the Kerr microscope being smaller than the dimensions of the $10\,\mu\text{m} \times 35\,\mu\text{m}$ permalloy slab. Due to the coupled spin motion, energy is transferred through the system and eventually out of the scan window which makes the damping look stronger. An integration over the whole slab should give the correct decay of the oscillation amplitude described by the damping constant α of permalloy. Another feature connected to the current pulse duration can be explored by comparing the LLG simulation in figure 3.2 with the presented dynamics. Exciting the system with a rather long current pulse of 118 ps FWHM duration leads to an overshoot in the beginning of the damped oscillation during the presence of the pulse field. In an excitation with a 7 ps FWHM pulse shorter than the FMR gyration period this feature is not visible which indicates that the current pulses generated by the photocathode are shorter than 10 ps FWHM where the under- and overshoots vanish. The pulse duration measured in the

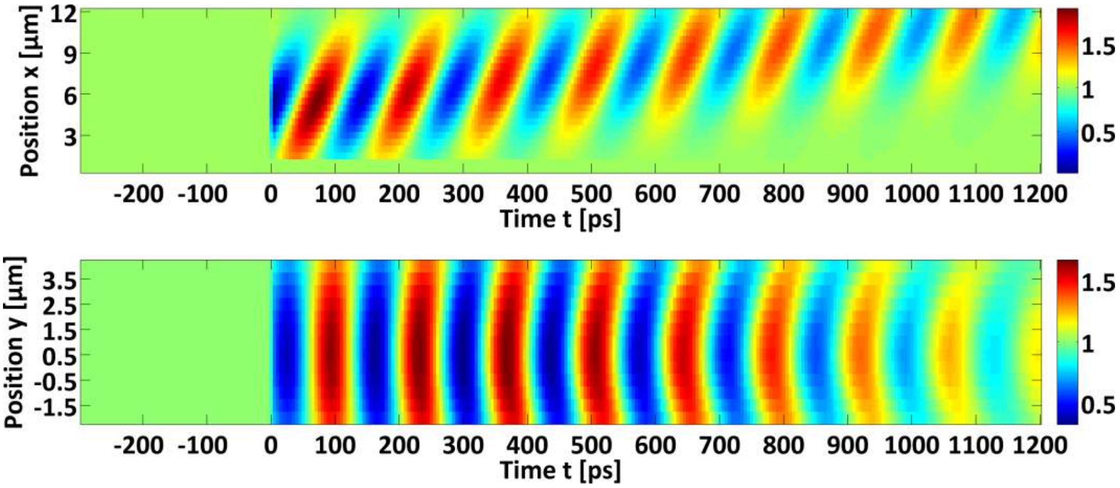

Figure 6.6: Calculated data of the spin-wave packet propagation in a 10 µm permalloy slab similar to figure 6.5 using equation 2.31 and a time dependent amplitude of the second transversal mode. The curvature in the bottom image agrees most with the measured profile by applying a phase shift of $\varphi = 40°$.

cathode test setup then must have been limited by the scope bandwidth.

So far, the spatially averaged data set was discussed. Gaining more insight is possible by investigating the TR-SKM measurement temporally and spatially resolved. Figure 6.5 presents the color-coded amplitude of the magnetization component M_z in propagation direction (x) at a fixed transversal position $y = 0$ µm in the center of the slab over time (top) as well as the magnetization distribution along the y axis at a fixed longitudinal position $x = 8$ µm over time (bottom).

The top image reflects the propagation of a spin-wave packet created by the field pulse along the x axis. By analyzing the maxima and minima positions with respect to time, the propagation speed of a particular extremum is traceable and relates to the phase velocity $v_{\text{ph}} = \omega/k$ via the slope measuring the propagated distance Δx in a time interval Δt. The trajectories are flagged by black lines and the extracted phase velocities are collected in figure 6.8a with the error bars representing the uncertainty of locating the extremum position due to the finite pixel size of 500 nm and 5 ps. An overall decrease of the phase velocity from (150 ± 25) km/s to (71 ± 25) km/s can be observed. However, in a region between 400 ps to 700 ps the velocity increases and drops afterwards to a constant level. Actually, the phase velocity is expected to increase for smaller wave vectors $|\vec{k}|$ according to the dispersion relation and the life time of a magnon scales reciprocal with the wave vectors [102]. Because of $|\vec{k}| = 2\pi/\lambda$ this means long-wave oscillations should survive in the end while short-wave oscillations are stronger attenuated. Consequently, a higher phase velocity is predicted along the propagation path [196]. Possibly, the magnetostatic conditions in the models do not apply for transient excitations in this experiment or the transition to higher phase velocities happens out of the scan window because it could be observed in a 15 µm wide stripe presented later.

The bottom image depicts areas of constant phase over the slab width and illustrates the transition from initially plane wave fronts to a curved structure. Due to limitations in data acquisition time only an area of $\Delta y = 6$ µm of the total 10 µm was scanned and not completely centered on the slab around position $y = 0$ µm. The emerging curvature can

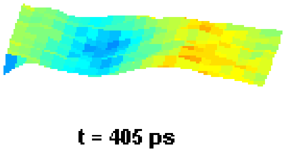

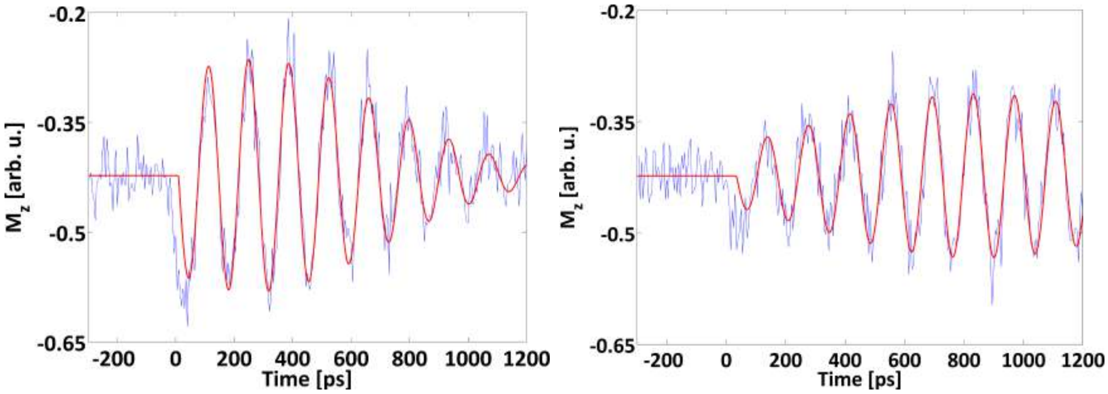

(a) Spin-wave packet data with fit at $x = 8\,\mu\text{m}$ and $y = 0\,\mu\text{m}$.

(b) Spin-wave packet data with fit at $x = 12\,\mu\text{m}$ and $y = 0\,\mu\text{m}$.

Figure 6.7: Spin-wave packets at two different positions. The blue curve represents the Kerr signal proportional to the magnetization component M_z and the red curve shows a fit to the data in line with equation 6.3.

be explained by interference of the first two quantized transversal modes k_{ny} with $n = 1, 3$ according to equation 2.26 due to the limited slab width where the spin-wave has to vanish at the boundaries. Remember that the relative amplitude of the $n = 3$ mode is reduced by a factor of three compared to the first one. This interference effect of quantized spin-wave modes is well known and has been observed before [123, 124, 142] by continuous-wave microwave excitation of the system at a single fixed frequency and allows observation of the steady-state mode distribution. Now, using a pulsed excitation of spin-wave packets in the present setup, the possibility arises to monitor the adjustment of the initial plane waves to the slab geometry and to see how the curvature emerges. Initially, the spin-wave does not “know” about the boundary conditions direct after creation and along the propagation effects of the nearby boundaries become prominent due to reflections on the edges when the wave packet “senses” the spatial limitations. Note that the pattern in figure 6.5 represents the spin-wave at $x = 8\,\mu\text{m}$ already behind the excitation region.

The structure of the data is reconstructible by superposition of the first two modes as stated in equation 2.31 with the result presented in figure 6.6 using the extracted group velocity v_g and wave packet duration τ obtained in the further analysis. The oscillation frequency ω and the $|\vec{k}|$ vector amplitude corresponding to the group velocity are extracted from the spin-wave dispersion relation. The phase shift φ is responsible for the curvature in the bottom image of figure 6.6 and the best agreement with the measured data is achieved for $\varphi = 40°$. Furthermore, a time-dependent increasing amplitude $a_3(t) = a_1/3 \cdot \left[1 - \exp\left(-\frac{t}{2\cdot\tau}\right)\right]$ of the second transversal mode including the duration of the wave-packet τ was included into the model to account for the transient response in the beginning of the oscillation dominated by the first transversal mode. The amplitude fulfills the mandatory boundary conditions $\lim\limits_{t\to 0} a_3(t) = 0$ and $\lim\limits_{t\to\infty} a_3(t) = a_1/3$. The reproduced data with equation 2.31, however, lacks a good agreement from 0 ps to 400 ps in the top image during the creation of the wave packet. A more sophisticated model describing not only the steady state motion but also the transient response directly after the pulse is needed and currently under development using micromagnetic simulations.

The fact that we deal with spin-wave packets is emphasized when plotting the mag-

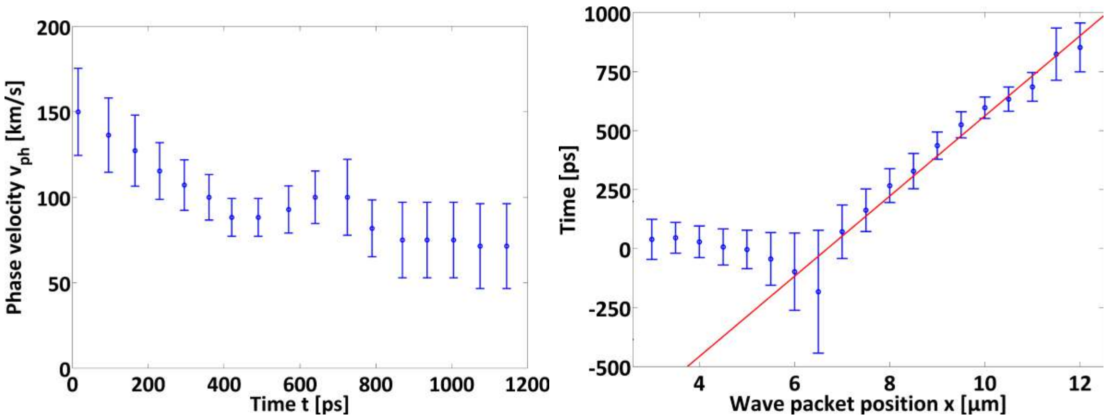

(a) Phase velocity of the spin-wave decreasing from $(150 \pm 25)\,\mathrm{km/s}$ to $(71 \pm 25)\,\mathrm{km/s}$ according to the traces marked in figure 6.5.

(b) Spin-wave packet position and time t_p relating to a group velocity of $(5.9 \pm 0.7)\,\mathrm{km/s}$ via a linear fit.

Figure 6.8: Phase velocities v_{ph} and group velocity v_g of the spin-wave packet in the $10\,\mu\mathrm{m}$ width permalloy slab.

netization amplitude of horizontal slices corresponding to different x positions in the top image of figure 6.5. Two examples of the spin-wave structure are given in figure 6.7 for the position $x = 8\,\mu\mathrm{m}$ and $12\,\mu\mathrm{m}$ at $y = 0\,\mu\mathrm{m}$ in the center of the slab. The plots distinctly demonstrate the structure of the wave-packets described by an oscillating term with a Gaussian envelope:

$$M_z(t) = M_0 - M_A \cdot \Theta(t - t_0) \cdot \exp\left(-\frac{(t - t_p)^2}{2 \cdot \tau^2}\right) \cdot \sin\left(\omega(t - t_0)\right). \tag{6.3}$$

It is clearly visible that the maximal amplitude decreases for larger x positions while the required time for the maximum to reach this positions increases. Furthermore, the spin wave-packet experiences a broadening due to dispersion as the pulse duration τ increases. As mentioned before, now it is obvious that the data for individual points is characterized by a single frequency oscillation without a chirp unlike to the spatially averaged data in figure 6.4. To explore the properties of the spin-wave packet, a fit in consonance with equation 6.3 was applied to each x position at a fixed $y = 0\,\mu\mathrm{m}$ coordinate in order to extract the oscillation frequency $f = \omega/(2\pi)$, wave-packet position t_p, pulse duration τ and peak amplitude M_A. The additional parameters M_0 and t_0 account for signal offset and excitation moment (i.e. arrival time of the pump pulse), respectively.

By relating the position of the maximal spin-wave amplitude in the center of the Gaussian envelope to the time t_p needed to get there, we are able to quantify the group velocity $v_g = \Delta x/\Delta t_p$ that describes the conveyor speed of the whole wave-packet. Figure 6.8b collects t_p from all fits for each x position with an error bar governed by a 95 % confidence interval. In the fit only locations $> x = 6\,\mu\mathrm{m}$ are taken into account because for smaller values no propagation is observed due to the local excitation around $x = 5\,\mu\mathrm{m}$ and the directed motion toward positive x positions for the DE modes. The data at $x < 3\,\mu\mathrm{m}$ is completely excluded and not shown due to lacking oscillation. The plot suggests a linear relationship and the application of the model $t = 1/v_g \cdot x + b$ gives a group velocity of $(5.9 \pm 0.7)\,\mathrm{km/s}$ close to the maximum of $v_g = 5.98\,\mathrm{km/s}$ in figure 2.10b extracted from the derivative of the dispersion relation. This group velocity corresponds

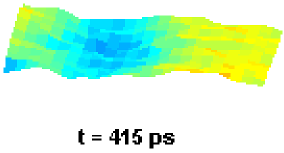

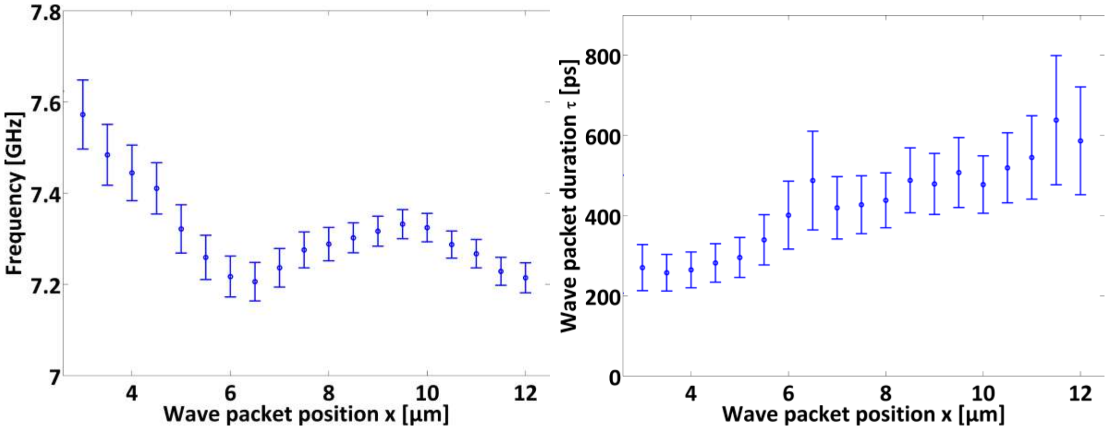

(a) Carrier frequency dependence on the wave packet position.

(b) Wave packet broadening due to an increasing pulse duration τ.

Figure 6.9: Spin-wave packet frequency and pulse duration with respect to the x position in propagation direction.

to a wave number of $k = 0.37\,\mu\text{m}^{-1}$. The agreement with the maximum of the calculated velocity curve is reasonable because this function has to be convoluted with the spectrum of the pulse given in figure 2.11b in order to obtain the excitation probability of the group velocities. The pulse spectrum only favors the stimulation of small $|\vec{k}|$ vectors due to the dominance of the spatial overlap between permalloy and waveguide.

An analysis of the wave-packet carrier frequency f at individual x positions results in the plot presented in figure 6.9a. Until the point where the wave packet is released (i.e. after the maximum position of the excitation in propagation direction), the frequency decreases linearly and then increases again for positions behind the origin of the wave-packet until a maximum at 9.5 µm is reached after which another drop in frequency sets in. The form of the carrier frequency with respect to time is remarkably similar to the form of the phase velocity with respect to the propagated distance. In fact, the traveled distance of the wave-packet is linearly related to the time via the group velocity which might be an indication that the phase velocity dependence $v_{\text{ph}} = \omega/k$ is dominated by the frequency change. As discussed before, the propagation of the wave packet starts at $x > 6\,\mu\text{m}$ (see figure 6.8b) which might be a hint that the aforementioned expected rising phase velocity is not observed here due to non steady-state conditions of the spin-wave packet.

The wave packet pulse duration τ in figure 6.9b expands over the whole propagation distance and the two examples given in figure 6.7 perfectly emphasize this effect. But there is also a difference in the broadening before and after the release point of the spin-wave packet as the duration rises exponentially until $x = 6.5\,\mu\text{m}$ and linearly afterwards. This can be understood considering the fact that the wave packet first has to form by escaping from the point of origin after pump pulse arrival. During this period the maximum of the Gaussian envelope is assumed to be at small x positions in front of the origin of the wave packet and in total two broadening mechanisms take place. Namely, the propagation of the wave-packet emerging out of the waveguide border leading to a larger observable part and the broadening due to dispersion and frequency dependent damping. Dispersion describes an unequal propagation velocity for individual frequency

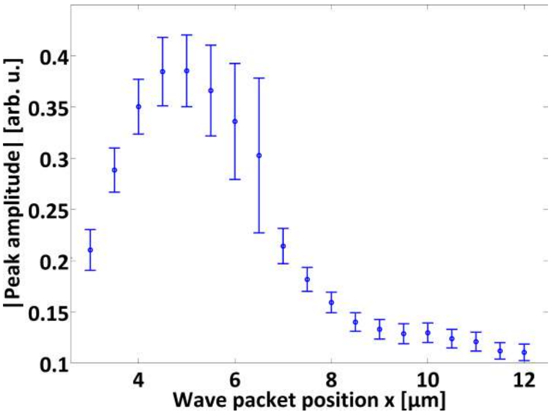

Figure 6.10: Spin-wave packet peak amplitude at fixed $y = 0\,\mu\mathrm{m}$ coordinate with respect to the x position in propagation direction. The amplitude of the wave packet first increases as is emerges out of the excitation zone and then decreases again due to damping and broadening of the wave packet.

components and leads to a diffusion of the wave packet observed in the linear slope of the pulse duration.

Owing to the temporal broadening of the wave packet, the related energy is distributed over an extended time interval. Figure 6.10 collects the peak amplitude of the wave packet with respect to the wave packet position x in propagation direction. During the creation of the spin-wave packet, the amplitude first increases until the localized wave is released out of the source region. A subsequent decrease in peak amplitude is evident due to damping of the spin precession via the material damping parameter α and due to the broadening of the wave packet. Possibly, an inelastic energy transfer between neighboring spins is subject to another spatially dependent damping term. It is not trivial do disentangle all contributions if the exact spatial and temporal dependence of the damping mechanisms is not known. Dedicated measurements have to be performed to characterize the individual factors.

Regarding the frequency dependent damping as one wave packet broadening mechanism, the spatially resolved Fourier transform obtained by applying the FFT algorithm to the data of figure 6.5 illustrates the spatial dependence of the frequency component amplitudes. The resulting pattern is given in figure 6.11. The Fourier transformed data relates the properties in the time domain to spectral information in the sense that an infinitely extended wave of a single frequency corresponds to an infinitely small spectrum of only one frequency component. A short pulse, on the other hand, needs a broad spectrum with sufficient superposed frequencies to achieve destructive interference out of its boundaries resulting in a confined oscillation.

In the left image of figure 6.11 showing the frequency components with respect to the propagation direction x we already see that a broad spectrum is present in the source region where the wave packet is created compared to the small spectrum around the resonance frequency peaking at 7.03 GHz for greater distances. With the two spin-wave examples in figure 6.7 this becomes more clear; the left packet is rather confined while the right packet after the arrival time of the pump pulse looks similar to a continuous-wave oscillation. In the source region up to $x = 5\,\mu\mathrm{m}$ the spectrum is extended to the low frequency region and the additional components rapidly die off toward higher x values. This is contradictory to the aforementioned fact that higher frequency components experience stronger damping (i.e. shorter magnon life times). However, after the release of the wave-packet at $x > 6\,\mu\mathrm{m}$ this behavior is confirmed because frequency components $> 7.03\,\mathrm{GHz}$ decrease along the propagation direction indicating increased

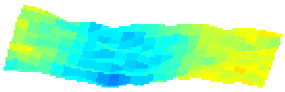

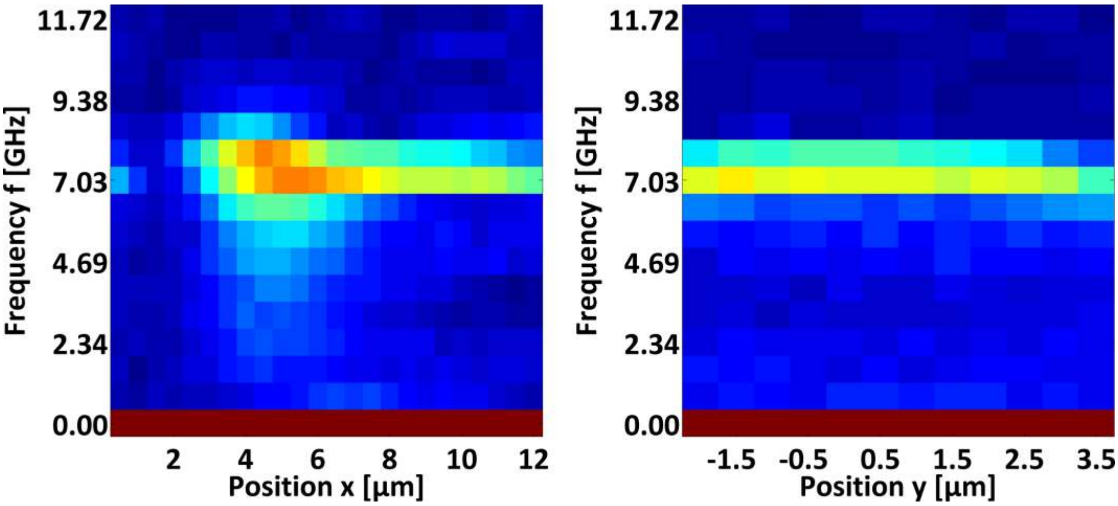

Figure 6.11: Spatially resolved fast Fourier transform of the data presented in figure 6.5 at the constant $y = 0\,\mu\text{m}$ (left) and $x = 8\,\mu\text{m}$ position (right).

frequency-dependent damping.

The right image shows the FFT along the transversal slab axis at the fixed position $x = 8\,\mu\text{m}$ with a more or less constant spectrum along the width of the permalloy stripe. In the center of the slab the spectrum is shifted and looks slightly broader compared to the boundaries. This could be explained by reflection of the wave fronts at the boundaries where frequency components might be annihilated. Because the FFT data is related to the real space plots in figure 6.5 where the transversal profile is shown after a few micrometers of propagation, additional frequency components already have vanished.

The previous analysis in this subsection was all based on one measurement observing the transient magnetic response of a 10 µm wide permalloy slab after excitation. Lastly, another data set acquired by monitoring the Kerr signal of a 15 µm wide permalloy slab will be shortly summarized. The parameters of the previous experiment apply apart from a higher anode current of 2.8 µA achieved here due to an improved laser alignment and a scan area of 17 µm × 17 µm in 500 nm steps. Overall, it shows the same aspects as described before (creation and propagation of the wave-packet and broadening) which will not be presented again.

Figure 6.12 collects the most important information extracted from this measurement and in the top image of figure 6.12a the decrease in phase velocity *over time* is visible in the decreasing slope of the extrema similar to the previous measurement. However, an additional curvature to the left present in the data points of fixed phase suggest that the phase velocity increases *along the propagation direction* as expected by the aforementioned model where long-wave magnons survive. This is confirmed by the analysis of the wave packet carrier frequency with respect to the x coordinate presented in figure 6.12b that shows a decrease of the frequency which is related to the phase velocity by $v_{\text{ph}} = 2\pi f/k$. The curvature of the phase fronts could also be reproduced in first OOMMF simulations by JAN-NIKLAS TÖDT [196]. The group velocity of $(5.8 \pm 0.5)\,\text{km/s}$ has not changed compared to the previous measurement on the 10 µm slab.

Supplementary, measurements with an inverted external field direction have been performed. The data will not be discussed here in detail but the relevant plots are

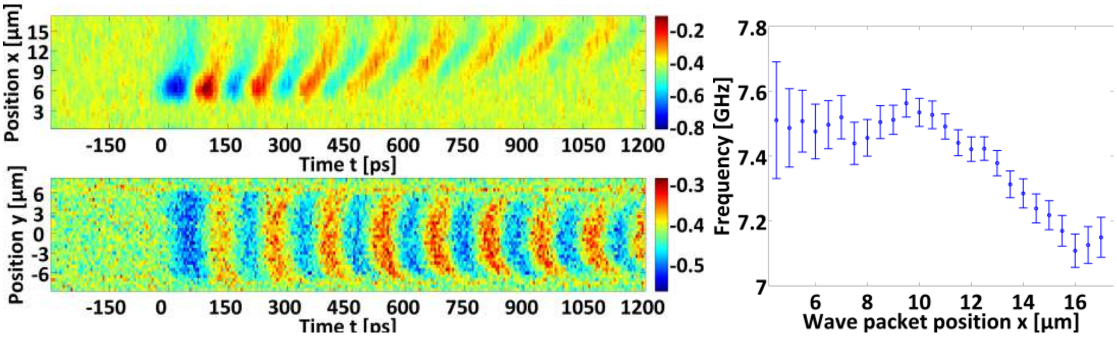

(a) Propagation in x direction at fixed $y = 0\,\mu\text{m}$ (top) and transversal modes at $x = 13.5\,\mu\text{m}$ (bottom) with respect to time.

(b) Carrier frequency with respect to the wave packet position.

Figure 6.12: Spin-wave packet propagation in a 15 µm wide permalloy slab.

shown in figure C.7 - C.10 in appendix C. In summary, the inversion of the field also reverses the propagation direction of the DE modes and due to the position of one stripe boundary close to the excitation region, also no propagation toward the preferred negative x direction is possible. During the first oscillation periods indeed no transfer of the wave fronts along the positive x direction is visible (zero phase velocity). However, later the maxima and minima are transferred along this axis most probably after reflection at the slab boundary which is approached after wave packet creation.

Backward volume modes

So far, only spin-waves in Damon-Eshbach (DE) geometry according to figure 2.7 with a wave-vector *perpendicular* to the external field have been discussed. To excite backward volume (BV) modes introduced in section 2.1 with a wave vector *parallel* to the bias field and a dispersion relation given in figure 2.10, the field direction has to be rotated by 90°. Due to repositioning of the permanent magnets generating the external field, the amplitude changed as well. Here, BV modes were excited in a 35 µm × 10 µm × 0.03 µm permalloy stripe and represent the first direct observation of backward volume modes in permalloy since such a measurement has not been reported in the literature so far. In general, the experimental conditions of the previous section apply except for the larger spatial scan area of 10 µm × 10 µm in 500 nm steps and the narrower temporal scan range of 1.4 ns in 5 ps steps. The slightly higher UV laser power of 450 mW driving the photocathode resulted in a comparable average anode current of 2.2 µA at 3.5 kV extraction voltage. The chopper for lock-in detection was operated at 1 kHz full speed.

Six selected frames of the movie are presented in figure 6.13. Similar to the Damon-Eshbach configuration, the magnetic dipole moments in overlap with the waveguide at small x values are excited out of their equilibrium state by the short magnetic field pulse generated in the photocathode. The resulting dynamics, however, is quite different because in this experiment the oscillation maxima and minima enter the scanned area from the right side (high x values) and do not emerge out of the excitation region. In the presented frames the blue color-coded minimum approaches the waveguide from the top right corner. Consulting the dispersion relation, the negative slope for small $\vec{k}$ vectors in the BV case presented in figure 2.10a leads to a counterpropagating group velocity

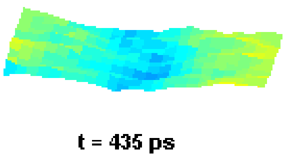

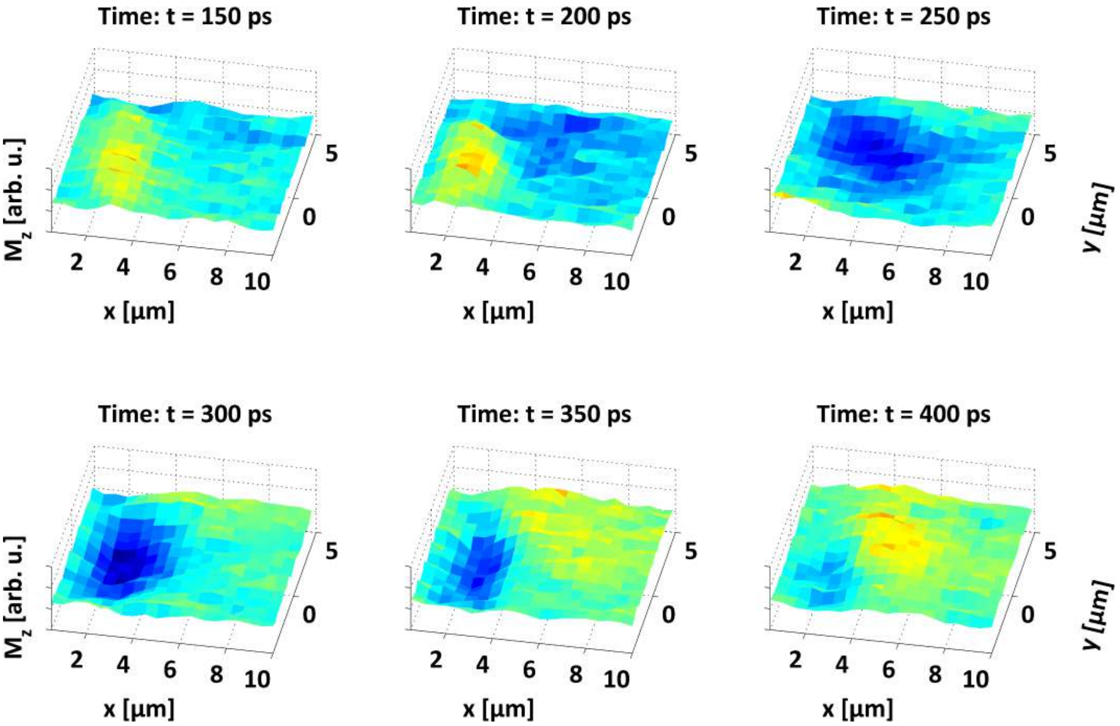

Figure 6.13: Selected frames of the acquired spin-wave movie of a backward volume mode illustrating the transient magnetization in a permalloy slab of 10 µm width at six delay settings.

with respect to the phase velocity. This is represented by a negative sign of $\vec{v}_g$ in figure 2.10b and can explain the observed characteristics. Unlike the DE modes, BV modes do not feature a preferred propagation direction and will propagate toward positive *and* negative x positions. Since the permalloy stripe terminates at the waveguide and is from there on elongated along the positive x direction, the only possible propagation path connected to the group velocity vector orientation points along this axis, too. In consequence, the phase velocity has to point into the opposite direction which explains the advancing oscillation wave fronts from positive x positions toward the waveguide. Despite the negative phase velocity represented by the wave fronts approaching the excitation region, the transportation direction of energy associated with the wave packet points along the group velocity away from the excitation point toward positive x values. A part of the wave packet initially launched along the negative x axis will be reflected on the left slab boundary and interfere with the wave packet launched into positive x direction (compare also the reflected DE modes with a reversed field direction in figure C.7 - C.10 in appendix C). Two examples of the wave packet at different x positions are given in figure 6.14 and emphasize the fact that the spin-wave spreads out toward positive x values. Due to the smaller frequency compared to the DE modes only a few oscillations are visible in the accessible time interval and it is hard to extract the envelope of the data. The wave packet also quickly broadens over the scanned time range. Moreover, the measured BV Kerr signal is weaker and thus noisier compared to the DE oscillations because the oscillation is mainly triggered via the out-of-plane (z) component of the driving field pulse so that only a fraction of the pulse energy is transferred to the magnetic system.

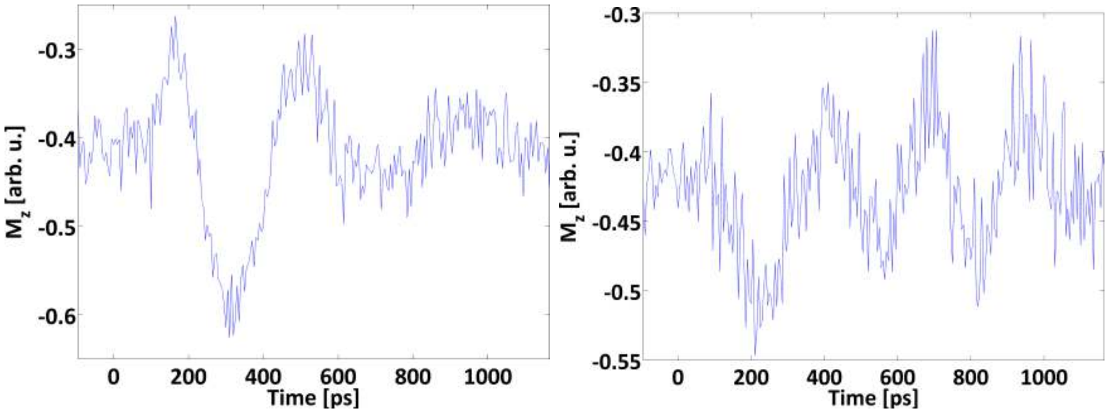

(a) Spin-wave packet data at $x = 3\,\mu\text{m}$ and $y = 0\,\mu\text{m}$.

(b) Spin-wave packet data at $x = 6\,\mu\text{m}$ and $y = 0\,\mu\text{m}$.

Figure 6.14: Spin-wave packets of the backward volume mode at two distinct positions of the slab with respect to time.

Similar to the DE spin-wave packets, a time-resolved overview of the data is given in figure 6.15 with respect to the propagation direction at a fixed $y = 0\,\mu\text{m}$ position in the center of the slab (top) and at a fixed $x = 7\,\mu\text{m}$ position for a variable y coordinate along the short slab elongation (bottom). The negative phase velocity is illustrated by the negative slopes of the maxima and minima in the top image. The oscillation frequency of 3.5 GHz relates via the dispersion relation (equation 2.28) to an external field of $\approx 3\,\text{mT}$ for BV modes with small $\vec{k}$ vectors. The applied bias field generated by two permanent magnets should be an order of magnitude higher but can not be measured directly at the sample position due to space constraints. The steel of the sample flange possibly modifies the field and may explain the deviation. Conspicuous

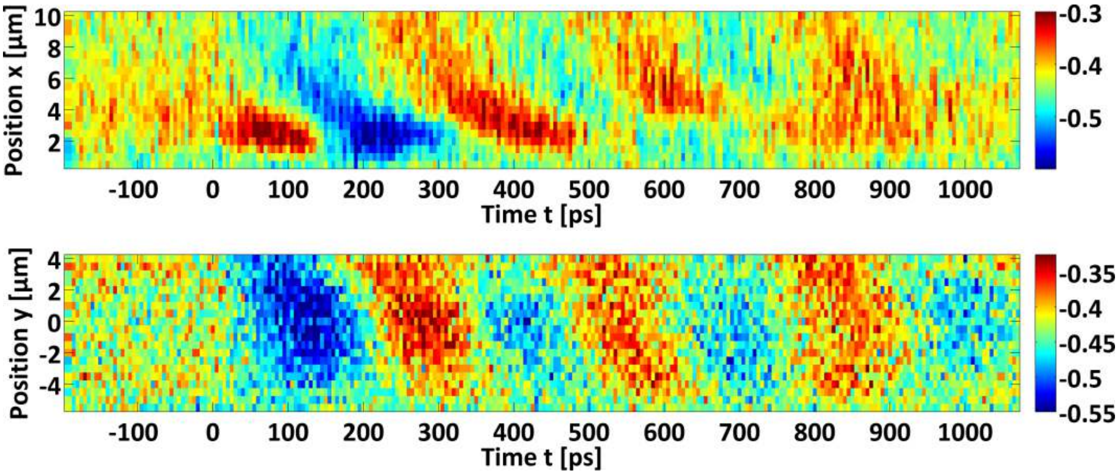

Figure 6.15: The top image shows the propagation of the backward volume spin-wave packet in $-x$ direction with respect to time at a fixed transversal position in the center of the slab ($y = 0\,\mu\text{m}$). In the bottom image the spatial distribution of the transversal modes at a fixed longitudinal position at ($x = 7\,\mu\text{m}$) is displayed with respect to time.

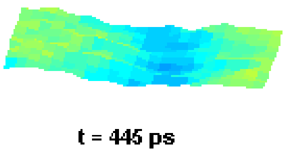

is that the propagation velocity vector does not point parallel to the elongated stripe direction as expected assuming a perfect collinear alignment of the external field with respect to the field pulses. The extrema enter the scan window from the top right corner in figure 6.13 corresponding to the tilted wavefronts in the bottom image of figure 6.15. This is explained by the sensitivity of the group velocity on the external field direction because a slight misalignment of the external field by 2° already tilts the group velocity vector by approximately 30° [196]. Note that a perfect collinear alignment results in a vanishing torque on the magnetic dipole moments by the h_x component of the dynamic field indicating that the dynamics is mainly driven by the h_z component.

Most of the hitherto observed dynamics is elegantly and consistently explained by the dispersion relation of magnetostatic waves.

Excitation without external field

The last presented TR-SKM measurement was performed without an artificial external field and the parameters of the previous experiment remain except for the removed magnets and a finer temporal scan step size of 2.5 ps. Due to pumping with isolated broadband pulses generated by the photocathode, the transient reaction of the magnetization to a short stimulus can be monitored in the permalloy slab. The commonly performed excitation with a single-frequency microwave signal done in other SKM setups only allows a time-resolved monitoring of the "steady-state" after several oscillation periods owing to the continuous signal injection.

Six selected frames of the acquired movie in a 10 µm wide permalloy stripe are depicted in figure 6.16. The pulsed dynamic field deflects the magnetic moments in overlap

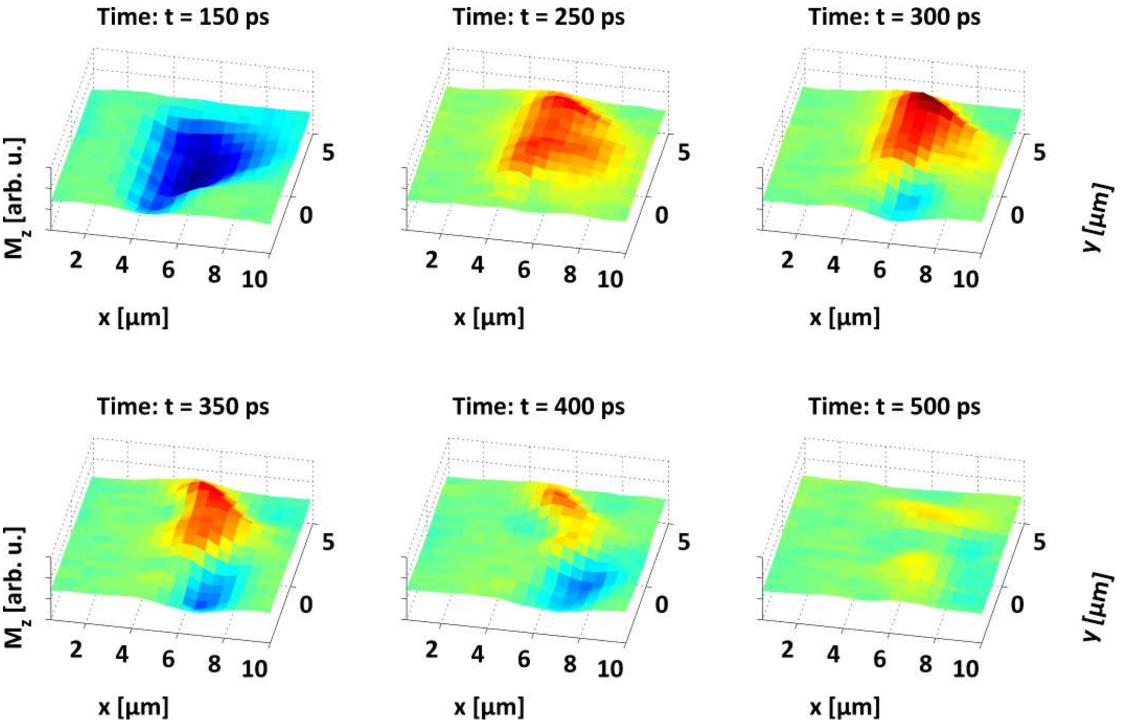

Figure 6.16: Selected frames of the acquired movie of the transient magnetization in an exited permalloy slab of 10 µm width without an external field at six delay settings.

with the waveguide ($t = 150\,\mathrm{ps}$) which gyrate within $100\,\mathrm{ps}$ into the opposite direction. Subsequently, the unfavorable alignment along the out of plane z direction decays via an "anti-ferromagnetic" state where the M_z magnetization component reverses over the slab width ($t = 300\,\mathrm{ps}$ to $400\,\mathrm{ps}$) until M_z vanishes completely.

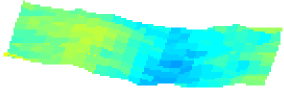

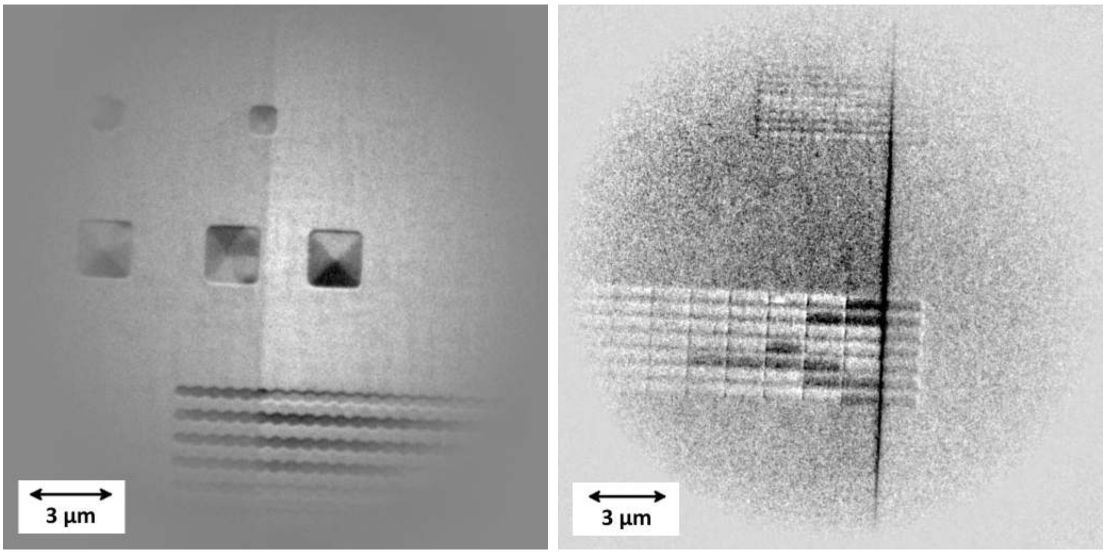

(a) Domain structure of 1 µm × 1 µm and 2 µm × 2 µm permalloy squares as well as a modulated nano-wire. The dark background in the left is a part of the 10 µm wide coplanar waveguide conductor. Displayed is the sum of 40 difference images exposed for 1 s at each photon helicity.

(b) Arrays of small permalloy bar magnets of 10 nm thickness with some elements (black) switched opposite to the array magnetization direction (white). The bottom array consists of 1.3 µm × 0.3 µm elements separated by ≈ 40 nm (SEM image in figure 4.5b). The waveguide is located on the right and overlaps with one array column.

Figure 6.17: Full-field XMCD images of patterned permalloy structures obtained by subtracting two images taken at different photon helicities. Black and white contrast corresponds to opposite magnetic orientations along the horizontal x axis.

6.2 Time-resolved magnetic transmission X-ray microscopy

After installing the transmission X-ray microscope and locating the nickel L_3 resonance (see chapter 5), the setup is ready to acquire XMCD images to trace the magnetization in thin magnetic films. Because the pump rate is limited to the revolution frequency of the synchrotron, time-resolved measurements require the fast gateable X-ray detector (section 4.7.1) to select light originating from one of the 40 bunches inside the storage ring to filter signal without dynamic information. Static XMCD images can be obtained using the whole light of the beamline to minimize the exposure time by permanently opening of the detector.

6.2.1 Static measurements

An example of a static XMCD image is given in figure 6.17a where the magnetization of patterned permalloy micro- and nano-structures in the vicinity of the CPW conductor is displayed. A part of the 10 µm wide conductor of the waveguide is visible as slightly darker background in the left half of the image. Located in the top and center are one 1 µm × 1 µm and three 2 µm × 2 µm squares while the bottom shows modulated nano-wires with 600 nm × 400 nm elements. All items are created out of a 30 nm thick permalloy layer. The XMCD image is based on two sets of images acquired at different

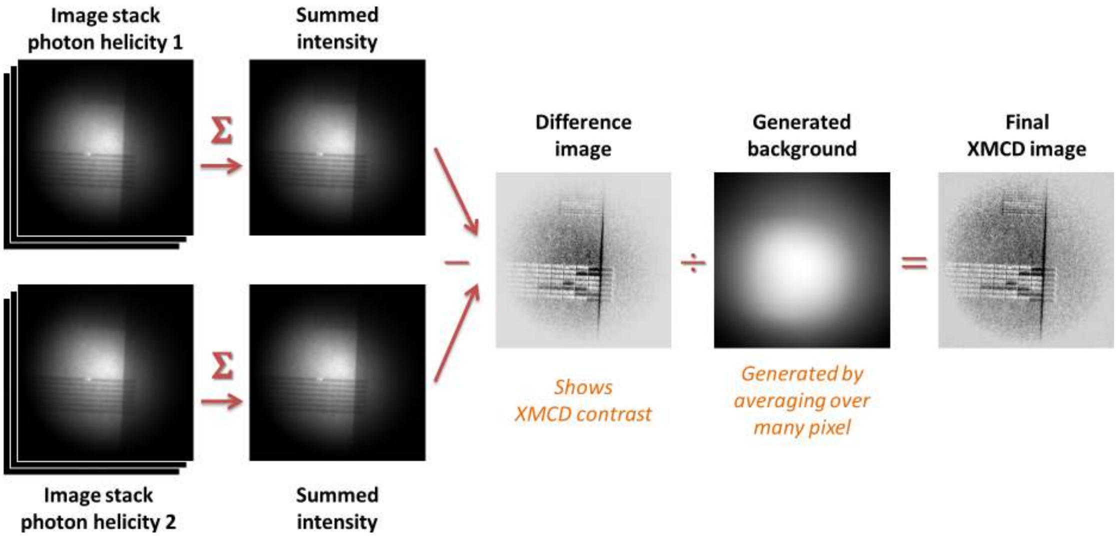

Figure 6.18: Image processing steps to create an XMCD magnetization map: First, the counts of every 16 bit camera picture acquired at the same photon helicity are stored in a stack of images. If dark and flat-field images are available, each file in the stack is subtracted by the dark image and divided by the flat-field data. Afterwards, all images in a stack are added up to generate one 32 bit file for each helicity. These two images are subtracted from each other to visualize the XMCD contrast. If no flat-field data is available, an artificial flat-field background is generated by averaging over a large pixel number to remove the structure information but keep the large scale illumination field. Lastly, the XMCD file is divided by the background to obtain the final image.

photon helicities (figure 6.18). In order to reach the excellent signal to noise ratio, 40 images of 1 s exposure time were captured at each helicity. Longer exposures are not feasible owing to overexposure of the CCD chip and blooming of the charge to neighboring pixels. To increase the total signal, more images have to be collected in a row. The pixel information of the image stack is added up to create one file for each photon helicity. These two files are subtracted from each other and the XMCD absorption difference remains corresponding to the magnetization vector direction projected onto the photon propagation path. Ideally, the structure of the non-magnetic waveguide should vanish after subtraction. The residual contrast originates most probably from slightly unequal brightness levels distributed over the beam profile and a small change of the beam position when switching the polarization by moving the undulator shift. Additionally, an artificial flat-field correction generated of out a smoothed averaged image was applied here. The editing was performed to correct for the intensity decay in the outer regions of the image present due to vignetting in the relay optic combined with the illumination profile of the condenser.

Attention should now be drawn to the substructure of the magnetic elements. The brightness difference maps the in-plane magnetization along the horizontal x direction. Facing the rightmost permalloy square we find three different shades of gray showing a pyramid-like flux closure Landau pattern consisting of four domains. According to the data the top and bottom domain point into opposite directions (left and right in the image) because they experience unequal absorption contrast while the left and right do-

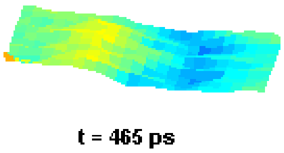

main experience a gray level in between. When comparing the pattern to the equilibrium state in the micromagnetic simulation (figure 3.3), we know that one of the remaining two domains points upward and the other one downward. These directions do not experience any overlap with the photon beam path due to the sample tilt angle which makes the setup insensitive to detect the magnetization along the vertical y axis, thus there is no detectable difference contrast comparing those domains. The Landau pattern is the most efficient way for the given structure to minimize all energetic contributions (compare section 2.1 and the simulation in section 3.3) and the four domain state with the magnetization curled around a vortex core in the center minimizes for example an energetically expensive stray field. Interestingly, the square to the left located on the edge of the waveguide experiences a more complicated domain pattern while all other quadratic structures resemble the flux closure vortex. Because this element is located directly at the border of the copper waveguide, it might be exposed to material strain that generates an anisotropy favoring the particular domain pattern [188]. Note that these systems were not exposed to magnetic fields other than the earth's field and any excitations were performed after taking this image.

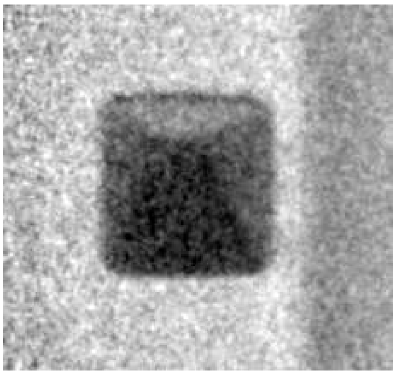

Figure 6.19: Flux closure arrangement of a 2 µm × 2 µm permalloy square modified by an external static field of the permanent magnet. The domain sizes adjust equivalent to the orientation to the magnetic flux lines and the vortex core is displaced accordingly.

When an external magnetic field is applied to the quadratic structure, the domain aligned along the field lines grows on cost of the other domains' size. After installing the permanent magnet, the modified pattern depicted in figure 6.19 could be observed with a displaced vortex core. Dynamic fields generated by AC currents can drive the flux-closure structure of the square into a gyrotropic eigenmode leading to periodic oscillations of the vortex core [34, 101, 205, 105] at a characteristic eigenfrequency [82] described by a harmonic oscillator model [125].

Another static image of 10 nm thick arrays of magnetic permalloy elements discussed in the simulations of section 3.3.2 is given in figure 6.17b. The presented data was part of a dynamic analysis where the detector was operated in gated mode implying that only 1/40 of the flux was present. For this acquisition five images of 30 s exposure time were taken. The lower array shows rectangular 1.3 µm × 0.3 µm elements separated by ≈ 40 nm conforming to the SEM image in figure 4.5b. The reset pulses of the coil aligned the array into one direction (white contrast) and oppositely directed pulses in the waveguide switched the elements in overlap to tackle the initiation of non-reversible dynamics already mentioned in the introduction. Here, a state during the alignment procedure is presented where some elements have switched (black contrast). Details on the pump, probe and reset procedure are elaborated later in section 6.2.3. The image demonstrates that features below the 61 nm resolution limit of the Rayleigh criterion are observable which is anticipated because this limit demands a contrast of 26 % and smaller features might be observed on cost of contrast. The Sparrow criterion defined by $\Delta l = 0.94 \cdot \Delta r_N = 47\,\text{nm}$ states the condition where individual details become indiscernible.

6.2.2 Reversible dynamical experiments

Laser-triggered measurements

The first experiment aiming to the initiation of reversible dynamics in magnetic structures without using permanent magnet and reset coil was performed with the photocathode switch triggered by the synchronized femtosecond laser system and the sample in figure 4.8b. For this purpose the Landau flux closure squares are ideal candidates because they normally relax to the vortex state automatically after excitation without any need of active reset. The first step in this experiment is to find the temporal overlap between pump, probe and detector gate pulses. In the case of laser excitation the synchronization between pump and probe pulse can be achieved with the help of an XUV photodiode that is moved into the soft X-ray beam and a UV diode collecting the leakage of the laser light through the last tilted mirror. Monitoring both pulses on a fast scope enables temporal shifting of the laser pulse with the synchronization electronics to accomplish a simultaneous arrival time of both pulses in the interaction zone. The correct timing of the gate pulse applied to the fast X-ray detector to select the pumped bunch can easily be checked with the stray-light of the laser pulse. Scattered photons of the UV pulse hit the detector when removing a 200 nm thick aluminum stray-light shield located between zone plate and phosphor screen providing a transmission of 90 % at the desired soft X-ray photon energy. Probing light generated by an unpumped bunch only leads to the X-ray microscope image visible on the detector. When setting the gate to the probe bunch coinciding with the pump pulse, additionally a dominant stray-light halo appears. This procedure assures that the soft X-ray pulse selected by the detector probes the system influenced by the laser pulse.

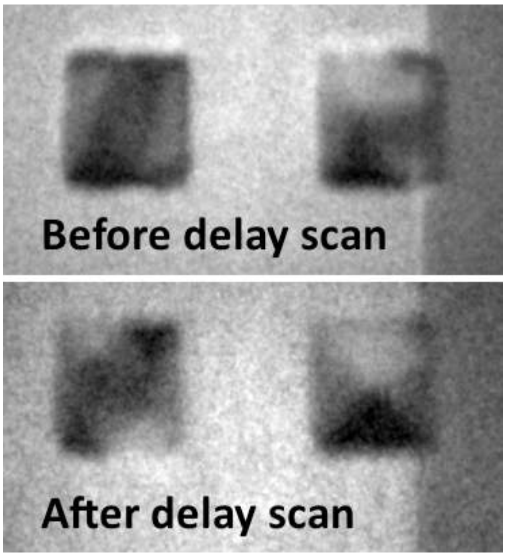

Figure 6.20: Magnetization pattern of 2 µm × 2 µm permalloy squares in the vicinity of the waveguide conductor (visible on the right of the image) before and after performing a delay scan to find the temporal overlap between laser pump and soft X-ray probe pulses. A net change of the magnetization pattern occurred but no signal correlated to the adjusted delay setting could be observed.

After the achievement of temporal overlap, a fine delay scan was performed monitoring the magnetization of the sample by taking XMCD images for various delay settings. The anode voltage was set to 1.5 kV leading to a current of 1.3 µA at 530 mW UV laser power in the laser hutch comparable to the laboratory TR-SKM experiments. Unfortunately, no dynamic signal correlated to the delay could be investigated. Anyway, as demonstrated in figure 6.20 a change of the initial magnetization pattern was observed after performing the delay scan indicating that the current pulses might have modified the system. Possibly, the pulses were not strong enough or too short to initiate any noticeable dynamics. Furthermore, the cathode current was not very stable during the

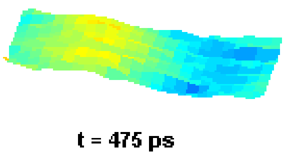

measurement and dropped over time. The FR4 substrate of the PCB adapter or the increased vacuum pressure of $5 \cdot 10^{-6}$ mbar compared to the TR-SKM setup could have led to fast degradation of the photocathode under UV illumination. Later, the timing was rechecked by the procedure described above and the sample contacts were tested to be operational as well after the laser pump-probe attempts to exclude timing and contact problems. The stability of the delay between pump and probe pulses was quantified by determining the fluctuation of the arrival time between laser and synchrotron pulses on the photodiodes and a jitter $< 17\,\mathrm{ps}$ likely limited by the amplitude to phase noise of the diodes indicated a synchronized operation.

Dynamics triggered by the picosecond pulse generator

The attempt to initiate dynamics with the femtosecond laser system was followed by replacing the photocathode with the picosecond pulse generator as pump device and the sample was modified according to figure 4.8c to allow connection and impedance matching of the waveguide. The time interval between pump and probe pulses is adjustable by a delay generator to an accuracy of $\sigma < 130\,\mathrm{ps}$ RMS[3] and was scanned to locate the temporal overlap. Using the electric pulse generator, the moment of overlap is estimated by carefully taking into account the signal transit time of all cables with respect to the XUV photodiode and can only be observed as a change in the XMCD data before and after excitation. XMCD images were acquired at varied delay settings which leads to a movie containing the frames presented in figure 6.21. One frame was captured by calculating difference images out of the sum of three images exposed for 60 s at each photon helicity. Because drifts of the sample and illumination field are very unfavorable when subtracting two added images stacks, the shift of the undulator was changed after every acquisition to minimize the time between two associated measurements. The movement of the undulator currently takes about 5 min including the time to wait for the beam quality to recover due to corrections on the electron orbit inside the storage ring near the insertion device. This means shooting one frame consumes roughly 12 min to 15 min including camera readout and delay operation time.

The right $2\,\mu\mathrm{m} \times 2\,\mu\mathrm{m}$ permalloy square in figure 6.21 is positioned in the gap of the CPW and the left two squares are located in overlap with the waveguide conductor and experience the in-plane component of the field curled around the $10\,\mu\mathrm{m}$ wide track. Additionally visible is a modulated nano-wire partly overlapping with the waveguide. A current pulse of 130 V peak amplitude launched into the $100\,\Omega$ waveguide corresponds to a field of

$$\mu_0 h_x = \mu_0 \cdot \frac{I}{2w} = \mu_0 \cdot \frac{\frac{130\,\mathrm{V}}{100\,\Omega}}{2 \cdot 10\,\mu\mathrm{m}} = \mu_0 \cdot \frac{1.3\,\mathrm{A}}{2 \cdot 10\,\mu\mathrm{m}} = 82\,\mathrm{mT} \tag{6.4}$$

on the conductor surface according to equation 2.75. This field is able to align the magnetization along its magnetic flux line in the temporal overlap and to destroy the four domain Landau pattern. Considering that the sample is flipped (figure 4.8c) and the camera looks at the back side, the squares located below the waveguide are forced into a single domain state with a net magnetization aligned along the x axis pointing

---

[3] The foreseen ultra-low jitter delay generator SRS DG645 providing synchronization down to 25 ps RMS jitter was not yet available during these beamtime shifts and was replaced by an SRS DG535 unit with measured residual jitter of $\sigma < 130\,\mathrm{ps}$.

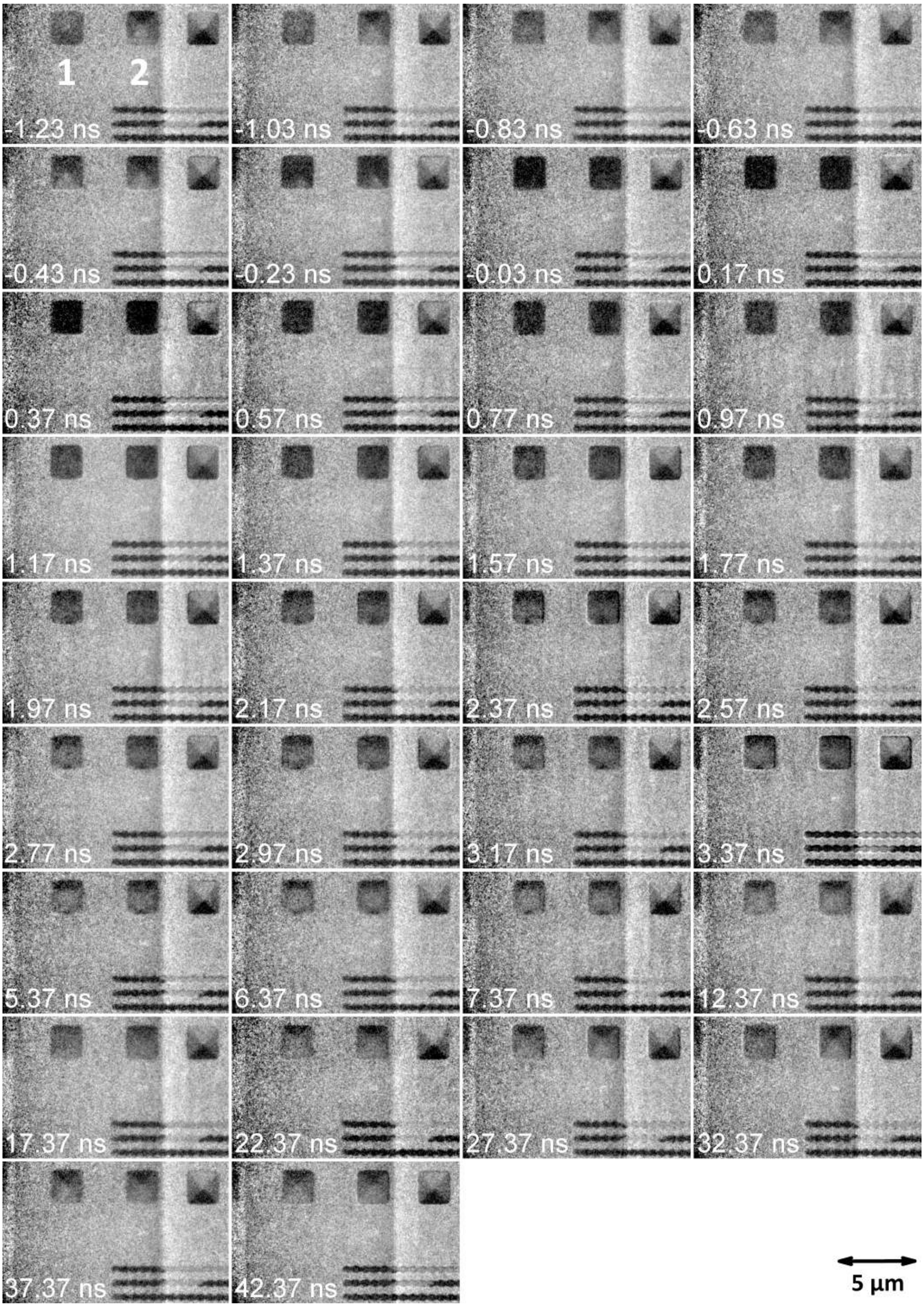

Figure 6.21: Domain pattern recovery of permalloy elements excited by the magnetic field of a current pulse which aligns the magnetization of the left two 2 µm × 2 µm squares (1 and 2) along the x direction. The domains of the right square in the CPW gap remain.

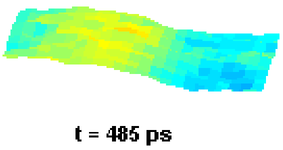

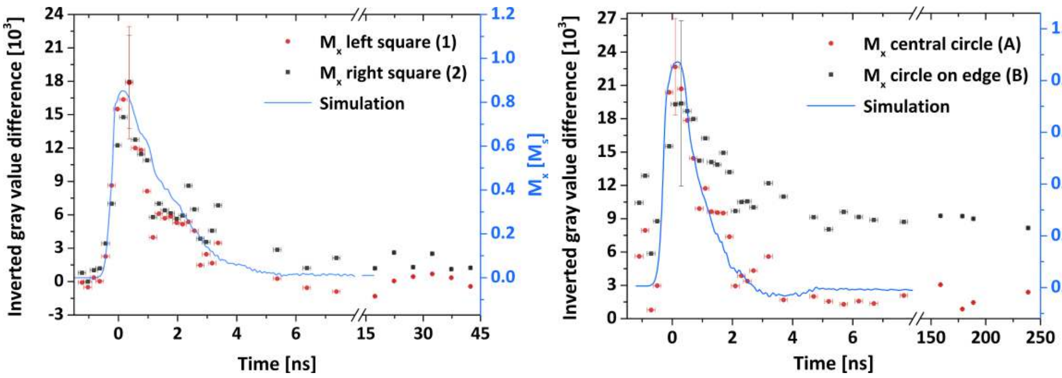

(a) Magnetization component M_x of both squares located on the waveguide.

(b) Magnetization component M_x of both circles located on the waveguide.

Figure 6.22: Gray value of the XMCD contrast images corresponding to the magnetization component M_x in the permalloy patterns on the CPW conductor investigated in the delay scans.

from left to right just like in figure 2.7. Because we deal with a positive voltage pulse generating a current of positive charges, the right hand rule applies. The brightness or gray levels thus shall from now on be addressed as a measure for the M_x magnetization component where low (dark) levels map a positive alignment together with high (bright) levels relating to negative M_x amplitudes.

The artificially created single domain state is energetically unfavorable due to the emerging stray field. Correspondingly, the large demagnetization field inside the material aligns the magnetic moments back to the flux closure ground state. This rearrangement happens on a pico- and nanosecond time scale and is probed by varying the delay of the pump pulse with the result given in figure 6.21. For a detailed analysis, the inverted brightness (gray level) of the permalloy square XMCD signal is plotted in figure 6.22a giving insight into the dynamics of the M_x component. It is not trivial to present accurate statistical error bars for this measurement because just showing the mean gray value with the standard deviation in the square is inappropriate due to multiple domains experiencing individual gray levels over the whole square. Spatially distributed magnetization components pointing in different directions would contribute to the standard deviation in addition to the shot noise of the detector. To provide an upper limit for the statistical fluctuations, one error bar representing the standard deviation in the most aligned state during the maximum of the pulse is given in the plot where the influence of unequally aligned magnetic components is minimized. The alignment along the current pulse field elapses on a fast time scale of roughly 500 ps whereas the decay back to a balanced magnetization distribution consumes more time in the order of 10 ns with a more drastic decay happening from 0.5 ns to 1 ns and a decrease with a moderate slope from 1 ns to 3 ns. Despite reaching gray levels comparable to values before the pump pulse after already 7 ns indicating a balanced magnetization, the domain pattern recovery to the Landau structure visible in figure 6.21 has not finished and consumes in total up to 40 ns for spatial rearrangement of the magnetization.

The micromagnetic simulation using *Nmag* presented in section 3.3 is able to generate a spatially averaged output for M_x as well which is plotted along with the data in figure 6.22a. The parameters of the dynamic $\vec{h}$ field were taken from the measured pulse profile and fine-tuned to maximal agreement with the measured data in the reasonable parameter space. The final values of $\mu_0 h_0 = 88\,\mathrm{mT}$ field strength and $\tau = 210\,\mathrm{ps}$ fit nicely the expected values according to equation 6.4 and the pulse duration extracted from a later measurement in figure 6.26. Moreover, these parameters consistently reproduce all the here presented dynamic measurements on permalloy squares with and without an external field as well as on permalloy circles. The computed trace reproduces the decay pattern with multiple slope sections qualitatively and almost quantitatively until the magnetization is balanced after 7 ns. By scaling the data to the simulation, we learn that the square is saturated to 85 % in x direction in the field pulse maximum. Also main features of the dynamic domain pattern are resembled. Figure 6.23 shows a direct comparison between the data in figure 6.21 and the simulation in figure 3.3. The zig-zag domains on the top and the small black domain in the bottom are reproduced well. However, the best match for the substructure in the measured and simulated data does not occur on the same moment in time. Despite the good temporal agreement of the averaged M_x component, the simulation does not satisfactory reproduce the realignment of the magnetization once the M_x amplitude is balanced. Reaching $M_x = 0$ in the simulation goes along with a Landau flux closure pattern which occurs yet later in the measurement. There, the four domain state is already prominent at 12.37 ns but the domain size still is imbalanced. The reason for this discrepancy most probably is a differing damping constant α and saturation magnetization M_s between simulation and experiment. Another explanation could be a less than 100 % reproducibility of the initiated dynamics needed for the pump-probe approach that relies on averaging over many sequences at a fixed delay.

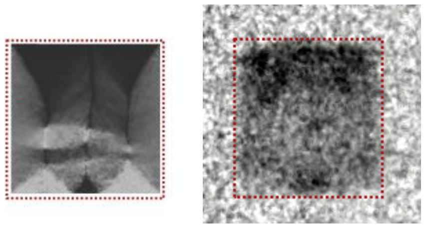

(a) Simulation at $t = 2.08\,\mathrm{ns}$. **(b)** Measurement at $t = 2.77\,\mathrm{ns}$.

Figure 6.23: Comparison between the simulated and the observed dynamic magnetization pattern of the $2\,\mu\mathrm{m} \times 2\,\mu\mathrm{m}$ permalloy square.

Focusing on the rising edge of the magnetization curve elucidates the destruction dynamics of the thermally stable vortex state. The characteristics of the vortex are described by its *chirality* defining the sense of rotation of the in-plane magnetization around the center and its *polarity* of the core located in the center of the squares pointing either upward or downward. As shown before in figure 6.19 this vortex core can be displaced from the center by applying an external field that increases the size of the domain aligned along the field direction. Furthermore, using low sinusoidal field amplitudes in the CPW, the vortex may be driven into oscillation at its gyrotropic eigenmode [205, 101, 21, 201] with the core on a circular trajectory at the corresponding eigenfrequency of several 100 MHz [82, 34, 81, 155, 132, 125]. The equations of motions of the rigid vortex core trajectory are described by the Thiele model [194] and the sense of gyration depends on the polarity. A slow, adiabatic increase of the field amplitude would lead to a growth of the domain in field direction until this domain dominates the whole pattern at the saturation magnetization M_s of the material. In this case, the vortex core would leave the square on a vertical trajectory. With strong fields featuring high gradients available in this setup, fast changes compared to the eigenfrequency of the system can be induced which enables the investigation of out-of-equilibrium dynamics presented in the XMCD images on the rising slope of the field

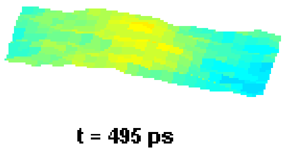

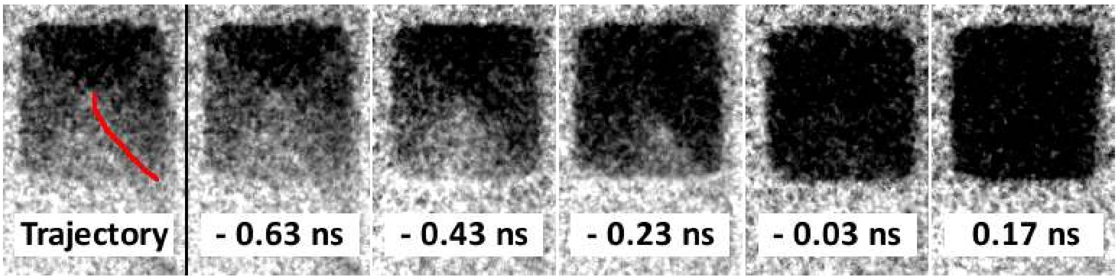

Figure 6.24: Magnetization dynamics of the 2 µm × 2 µm × 0.03 µm permalloy square on the rising edge of the magnetic field pulse revealing the trajectory during kick-out of the vortex core.

pulse (summarized in figure 6.24).

Here, the core is kicked out on a curved trajectory resembling the gyrotropic eigenmode of the system [211] which is expectable because the fast external stimulus corresponds to a broad spectrum triggering dynamics of modes with minimal losses most efficiently. The positions and velocities with respect to time are collected in table 6.1 and indicate unusual high domain wall velocities exceeding 1 km/s even when taking into account the confidence bounds given by the corresponding pixel dimension and the temporal jitter. By driving the vortex into oscillation and gradually increasing the oscillation amplitude (e.g. by resonant excitation or rising the alternating field amplitude), the fast motion should lead to switching of the core before destruction at velocities exceeding 300 m/s [133, 83, 211]. This behavior is not detected here and it should be stressed that the vortex chirality and polarity stay reproducibly constant because otherwise no trajectory would be observable in the pump-probe approach. The reason for a reproducible vortex configuration must be contained in the magnetic moments not completely aligned along the field pulse direction which have to be present due to $\max(M_x) < M_s$. According to the simulation only 85 % of the magnetization is pointing along the x direction (figure 6.22) and the simulated pattern in figure 3.3 suggests that during the maximum of the field pulse most unaligned magnetization vectors are found in the bottom domain originally directed along the $-x$ axis. Anyhow, in the simulation a kick-out of the core

Table 6.1: Positions and velocities of the vortex core in figure 6.24. The temporal uncertainty is dominated by the jitter of 130 ps and the spatial inaccuracy by the corresponding length of 40 nm (two pixel). The first core position defines the origin of the coordinate system.

Time t	**Position** x	**Position** y	**Velocity** v_x	**Velocity** $-v_y$
−630 ps	0 nm	0 nm	(0.1 ± 0.3) km/s	(1.1 ± 1.0) km/s
−430 ps	20 nm	−218 nm	(0.4 ± 0.2) km/s	(1.2 ± 0.6) km/s
−230 ps	178 nm	−475 nm	(1.8 ± 0.8) km/s	(2.1 ± 1.0) km/s
−30 ps	733 nm	−1069 nm	(1.7 ± 0.8) km/s	(1.7 ± 0.8) km/s
170 ps	581 nm	−1149 nm	(0.6 ± 0.6) km/s	(0.4 ± 0.5) km/s

could not be reproduced and only a symmetric destruction of the domain is evident. This might be explained by differing material parameters in simulation and experiment (see above) or by inhomogeneities of the pulsed field not included in the simulation. To verify this hypothesis, a dedicated measurement of M_s and α should be carried out on the sample together with a more realistic dynamic $\vec{h}$ field model in the simulation.

Besides the dynamics of permalloy squares, also circular patterns of 2 µm diameter were investigated resulting in the data given in figure 6.25. Just as the squares, these structures exhibit a vortex state but with a continuous change of the magnetization around a core in the center. Here, one circle is located next to the waveguide conductor, another one in complete overlap and a third one in partial overlap at the edge of the CPW conductor. The dark grains in the center located in the top and bottom part of each frame are (non-magnetic) dirt particles most likely from contamination with conductive silver fragments. An excitation with the same pulse parameters applied in the experiment shown before, leads to the displayed dynamical behavior. Similarly, the transient field aligns the majority of the magnetization into one direction (black contrast) and a time-resolved recovery of the vortex pattern is explorable.

Obviously, the two circular patterns in contact with the waveguide show a different recovery behavior. The magnetization of the specimen in complete overlap rapidly decays into a state with two domains in the top and bottom aligned in opposite direction to the central part which remains more or less stable for 10 ns. Afterwards, the disc appears homogeneously gray indicating a possible irreproducibility of the dynamics at large time delays. Also before the current pulse no distinct vortex state is observable referring to an indefinite final state. An equal probability for both final chiralities defining the sense of rotation of the vortex might explain the gray shape when the black contrast appears alternately in the top and in the bottom sector. The partly overlapping disc experiences a more complex substructure after excitation but ends up in a vortex with stable chirality after already 6 ns without the metastable state occurring in the neighboring circle. The different nature of the dynamics originates from the spatially dependent field configuration. A more homogeneous field in x direction perpendicular to the current flow is experienced by the central disk compared to the field with a strong out-of-plane component on the conductor boundary. Additionally, the x component only partly acts on the magnetization of the right disk owing to the limited overlap and the amplitude of the field may vary from the center to the edges due to the skin effect (compare figure 4.3 by bearing in mind that this simulation was performed for spectrally broader pulses available in the TR-SKM).

Furthermore, the dissimilar action to the encountered fields becomes also discernible when plotting the brightness of the two discs related to the spatially averaged M_x component of the magnetization in figure 6.22b. The decay behavior of the discs as well as the final brightness levels at large delay settings (150 ns to 250 ns) do not coincide. Outlined with the data is the simulation of the action on a disk by the same, spatially homogeneous current pulse employed when computing the dynamics of the square (figure 6.22a) which fits very well the data of the disk in the center of the waveguide that is exposed to the uniform part of the field. The dynamic magnetization output of the simulation is plotted in figure C.11 in appendix C. The fact that the simulation ends up in a vortex state while the measurement only shows a gray shade does not matter for the spatially averaged evaluation because in both cases the net magnetization is zero so that the computed result remains still valid if the final chirality is unstable and both

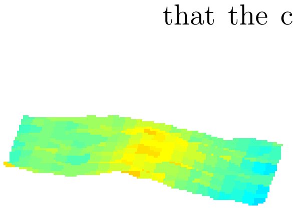

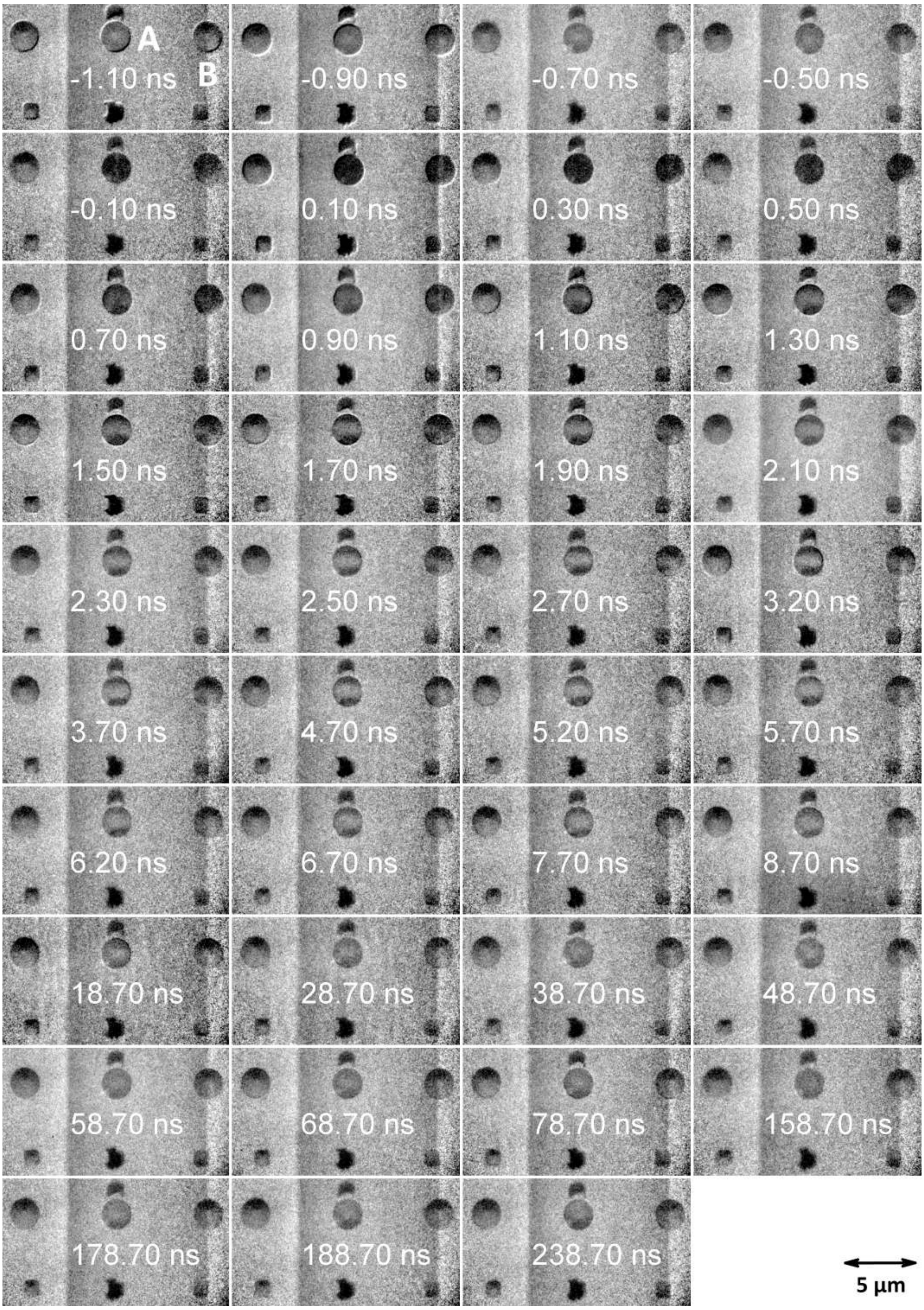

Figure 6.25: Domain pattern recovery of 2 µm diameter permalloy discs (A and B) excited by the magnetic field of a current pulse which aligns the magnetization of the specimens in overlap with the waveguide conductor along the x direction.

chiralities appear with an equal probability. However, a statistically imbalanced probability for the final chiralities may not explain the offset in the final brightness level in figure 6.22b for the circle located on the edge of the waveguide because both chiralities feature a vanishing spatially averaged M_x component. Similar to the permalloy squares, the simulation seems to underestimate the time needed for a complete recovery to the vortex state after 5 ns because in the measurement a gray state first occurs between 20 ns to 30 ns. In order to reproduce the domain pattern recovery of the partially overlapping disc, a dedicated simulation with the field seen by the right particle has to be performed.

Despite the mentioned issues concerning the simulation, the remarkable agreement between the decay shapes in figure 6.22 for the exact same pump pulse parameters should be stressed. The major contribution to the dynamics seems to originate from the geometry and shape of the structure and the imprinted magnetization pattern as remaining difference in computations as well as measurements between square and circle particles.

6.2.3 The pump-probe and reset approach

Toward the observation of the dynamics of non-reversible systems, an active reset to a defined initial state has to take place. For this purpose, the coil located at the sample was operated at the 130.1 kHz repetition rate synchronized to the storage ring. When first applying a current to the coil, the whole sample has to thermalize because heat is dissipated into the silicon substrate and the titanium sample holder despite water-cooling, minimized thermal contact and the implementation of materials with a small thermal expansion coefficient. The induced heating results in severe drifts of the sample position in the field of view of several micrometers over the next 4 h to 6 h. Taking difference images desired for XMCD contrast is not possible during this time owing to the rapid position change between two images. Minor drifts could also be observed during a few hours in the morning when the vacuum chambers were exposed to sunlight shining through the windows of the experimental hall. Once the whole setup is thermalized, a stable operation is possible when keeping the power dissipation in the coil at a constant level. Changing the voltage or the pulse duration introduces new drifts and should be avoided if a stable sample position is desired.

A first measurement with running coil after thermalization is presented in figure 6.26 where a reset pulse of 1.5 µs was applied after each pump-probe cycle roughly 1 µs after the pump pulse providing a time frame of this duration to observe any initiated dynamics. This pulse aligns all magnetic patterns on the silicon nitride membrane initially into $-x$ direction (white contrast) so that the pulser may induce an excitation through the $+x$ directed field (black contrast). During the temporal overlap with the pump pulse, a darkening of the squares and modulated nanowires on the conductor is obvious indeed. However, prior to the pulse no flux-closure domain pattern is visible in the permalloy squares and right after the excitation the black contrast is gone within 1 ns. This observation suggests the existence of a residual field at the sample originating most probably from the remanence of the iron core after the coil current has vanished. In principle this should not be a problem for the proposed measurements because this offset field ought to be compensable by the bias field of the permanent magnet necessary for the chain dynamics. Conspicuous in figure 6.26 is the evolution of the magnetization reversal of the left square starting at the vertical borders where the demagnetization field is maximal. Domain walls are generated and the outer domains enlarge while the central part starts

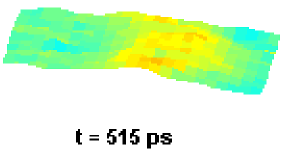

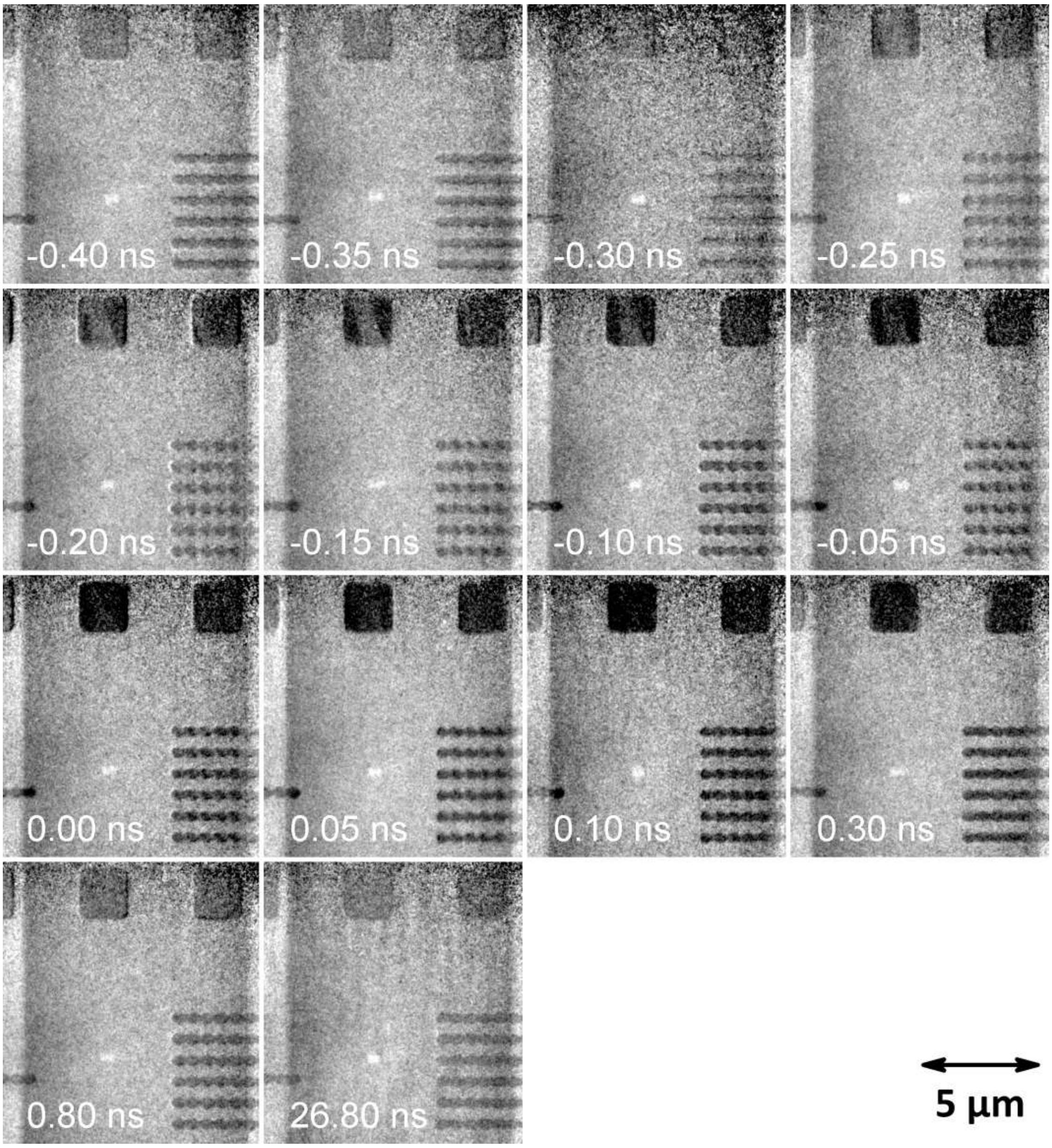

Figure 6.26: Dynamics of 2 µm × 2 µm permalloy squares and modulated nanowires featuring 600 nm × 400 nm elements excited by the short current pulse with activated reset coil. The coil initially aligns the magnetization into $-x$ direction (white contrast) and during the pump pulse a reorientation into $+x$ direction is observable (black contrast). The fast relaxation into the initial (white) state directly after the pump pulse suggests a static parasitic residual field generated due to the remanence of the iron core.

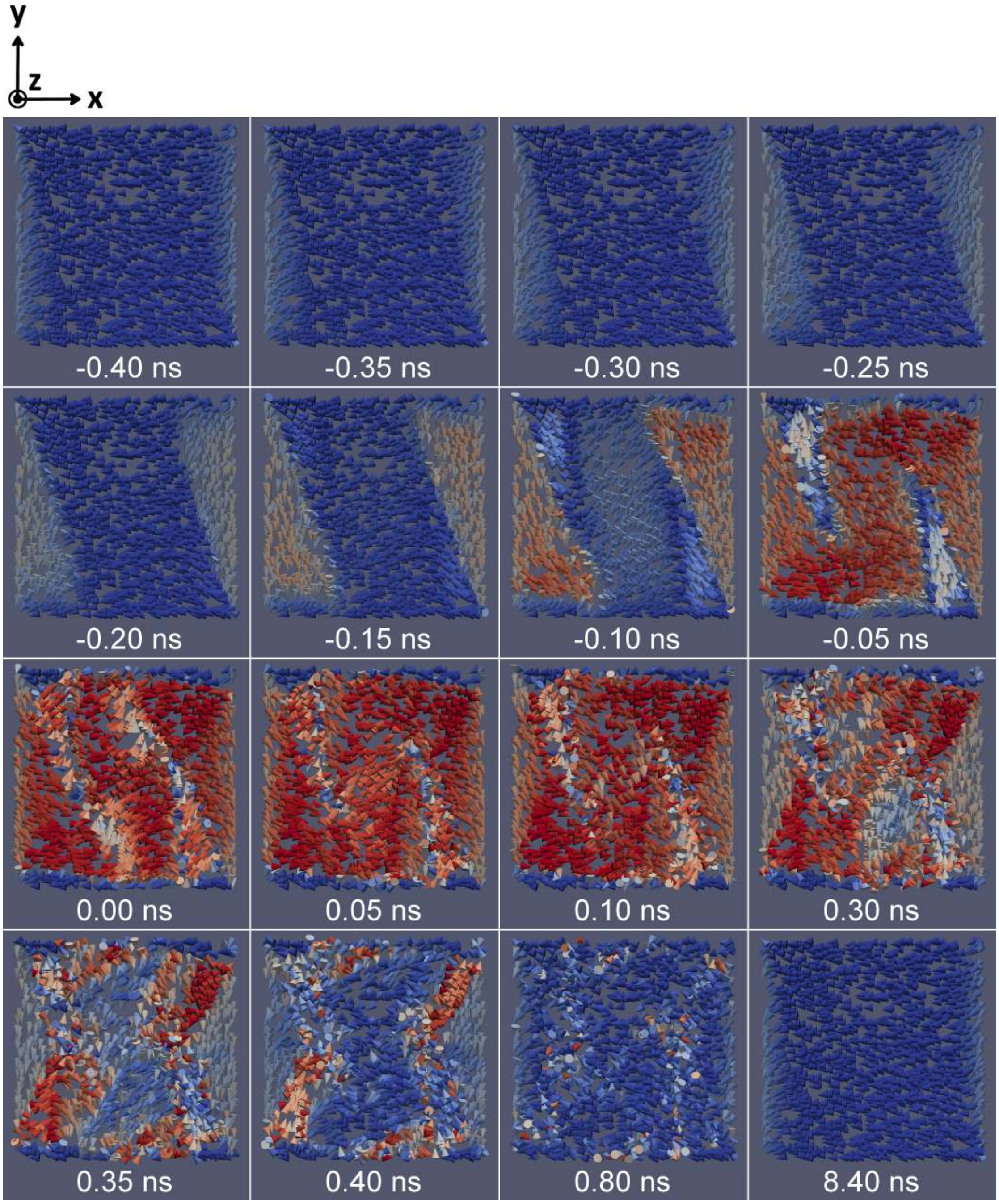

Figure 6.27: Simulation of the magnetization dynamics in the top left square related to the measurement presented in figure 6.26. A static opposing field of $\mu_0 H_{\text{ext}} = 38\,\text{mT}$ tilted at an angle of 5° was assumed. The excitation field of $\tau = 210\,\text{ps}$ duration and $\mu_0 h_0 = 88\,\text{mT}$ amplitude was not altered compared to all other simulations.

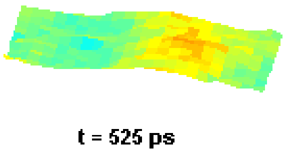

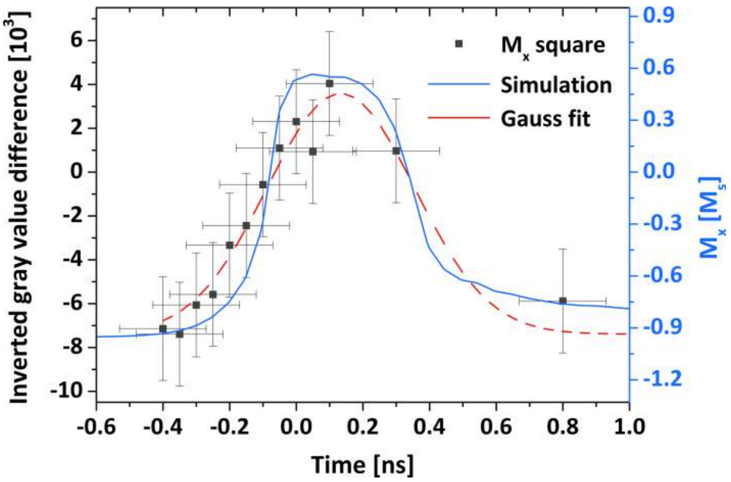

Figure 6.28: Spatially averaged magnetization component M_x of the left square on the conductor in the reset experiment with simulation output and a Gaussian fit suggesting a pulse duration of $\tau = (222 \pm 24)$ ps.

to reverse its magnetization at around −100 ps. The angle of the domain wall with respect to the particle boundary indicates a tilt of the iron core field direction with respect to the waveguide conductor perpendicular. A diverging action of the right square on the waveguide boundary may result from a varying field arrangement as already discussed above.

The dynamics of the of the left square was also simulated using *Nmag* and the result is depicted in figure 6.27. The dynamic parameters of the picosecond current pulse remain unaltered compared to the previous simulations in order to maintain consistency. Additionally, a static opposing field of $\mu_0 H_{\text{ext}} = 38\,\text{mT}$ tilted at an angle of 5° with respect to the waveguide conductor perpendicular was added to account for the remanence field of the iron yoke. The agreement between the measured and simulated patterns is quite remarkable and the simulation is capable of reproducing the dynamics initiated at the boundaries and the successive switching of the central part frame by frame. Note that in the simulation two additional frames between 0.3 ns and 0.8 ns are added to reveal the back-switching passage into the “white” state because no corresponding data is available for these delay settings.

Figure 6.28 shows the spatially averaged M_x magnetization component of the left square on the waveguide together with the data extracted from the simulation and a Gauss fit yielding a time constant of $\tau = (222 \pm 24)$ ps close to the current pulse duration of 210 ps used in the simulations to reproduce the data. The rising slope of the observed dynamics is smaller than suggested by the simulation which might be explained by the synchronization jitter of roughly 130 ps blurring the rapid increase of the M_x component. The dynamics of the this magnetization component is possibly governed by the pulse shape and jitter of the excitation pulse and the reorientation of the magnetization vectors follows the difference of dynamic pump field and the residual field that takes care of a fast realignment at positive delays.

Lastly, the observation of non-reversible magnetization dynamics in permalloy chains and arrays was tackled. As discovered by the simulation in chapter 3, the opposing field has to be adjusted carefully. For this purpose a delay setting for observation of a state after the pump pulse was chosen and the magnet was moved away from the sample so that all elements in the coupled system are aligned along $-x$ direction (white contrast). In this state the offset field is too weak to allow a switching chain reaction triggered by the short excitation pulse. Now, the magnet is gradually moved toward the sample to

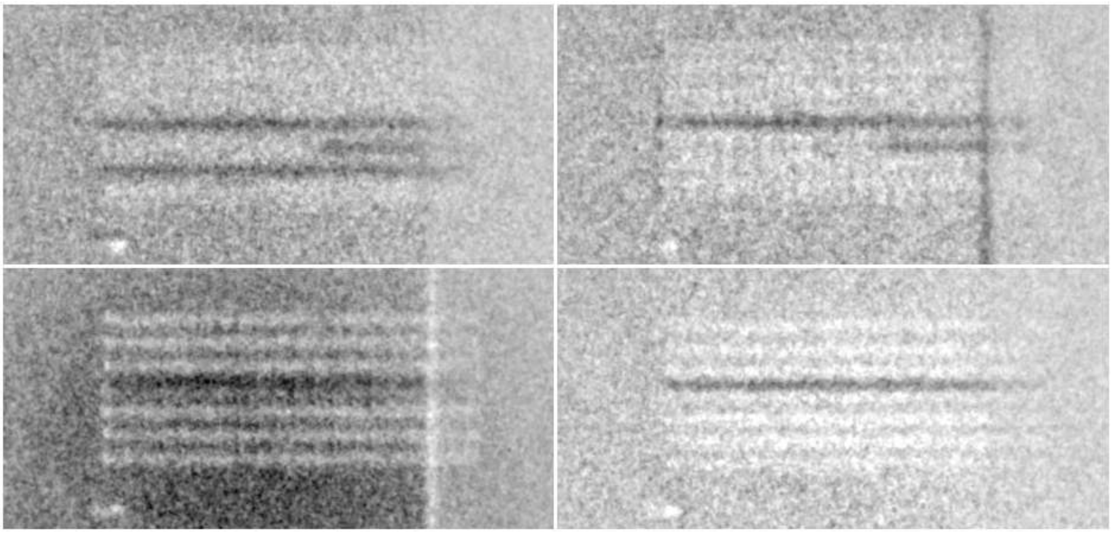

Figure 6.29: XMCD signal of a 7 µm × 3 µm array of permalloy nanostructures in partial overlap with the waveguide visible in the right. Each 400 nm × 100 nm element is separated by 50 nm horizontally and 250 nm vertically. The four images averaged over several pump-probe and reset cycles were taken consecutively at exactly the same dynamic settings (pump pulse amplitude, duration and delay; reset pulse current, duration and delay; magnet position) and the magnetization changes from image to image indicating a stochastic switching characteristic.

increase the field and the magnetization state is captured in an XMCD image after every step. At a position where some of the chains turn black, the field sufficient for switching should be found. Unfortunately, the measurement turned out to be not reproducible. Figure 6.29 shows four images averaged over several pump-probe and reset cycles at exactly the same settings (pump pulse amplitude, duration and delay; reset pulse current, duration and delay; magnet position) and the magnetization inside the array differs from frame to frame. Parts of the chains discretely switch after a random amount of time in the seconds to minutes range during data acquisition. Further reduction of the magnet distance allowed to align the array homogeneously to the $+x$ direction but at delays before the pump pulse no recovery to the initial "white" state was possible. Also arrays with larger elements (for example the one depicted in figure 6.17b) and isolated chains failed to switch reproducibly.

With the piezo motorized[4] linear stage of the magnet, a position accuracy $< 40\,\mu\text{m}$ is easily achievable. In the necessary field range around 10 mT to 50 mT according to equation 4.8 and figure 4.18, the B_x field component can be adjusted with an accurateness of $< 0.2\,\text{mT}/50\,\mu\text{m}$ which should be sufficient considering the requirement of a stable field between 10 mT to 15 mT according to the simulation in chapter 3.

It remains unclear why reliable switching could not be accomplished. A possible issue is the residual remanence field of the iron core after the reset pulse which, however, should be compensable by the permanent magnet. An unreproducible remanence field that has to relax on a long time scale over several microseconds could explain the behavior. Another concern is the inhomogeneity of the opposing field and the stray field components

---

[4] Newport vacuum picomotor 8353-V, #6-80 screw, 318 µm travel per revolution

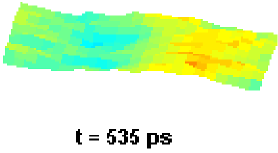

created by the magnet. In the simulation only a strong field in x direction was modeled with y and z components in the range of earth's magnetic field. Inhomogeneities in the elements and some not completely separated elements may add stochastic components to the dynamics. For future experiments improvements on reset and offset field should be introduced along with efforts in exploring a more stable sample geometry for dependable switching dynamics.

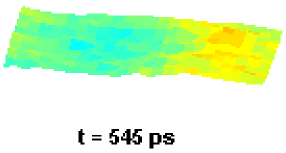
t = 545 ps

Chapter 7

Conclusion and outlook

For the spatial and temporal exploration of magnetic micro- and nanostructures, two new operational time-resolved imaging experiments have been set up in this work:

The laboratory based time-resolved scanning Kerr microscope (**TR-SKM**) implementing a femtosecond laser system with a temporal resolution down to **290 fs** FWHM if limited by the laser pulse duration and a spatial resolution of $w_0 = \mathbf{(553 \pm 26)\,nm}$ enables static and dynamic measurements on magnetic microstructures. The device has been used examining cobalt-platinum (Co/Pt) patterns and spin-wave packets in confined permalloy ($Ni_{80}Fe_{20}$) elements. A novel pump approach offers broadband, short and intense current pulses perfectly synchronized to the probe laser via a magnesium photocathode. The possibility of direct excitation and observation of Damon-Eshbach and backward volume spin-wave packets in space and time allows a global analysis of the wave packet parameters as suggested by Liu et. al. [137]. Moreover, the unique features of the pump pulse allowed direct observation of backward volume modes with counterpropagating phase and group velocities in permalloy layers for the first time. In cooperation with Jan-Niklas Tödt an OOMMF simulation is currently being set up and carried out to check if the simulated output is able to resemble all measured features [196].

The setup might further be improved by installing a prism stretcher in both the UV pump and the green probe beam path. An elongated pump pulse reduces space charge phenomena in the cathode and should increase the extracted bunch charge. Stretched probe pulses reduce the peak intensity on the sample allowing for more signal acquired in the photodiodes and thus a superior signal to noise ratio that minimizes the data acquisition time. The stretcher consisting of two fused silica prisms is already available and calculated to extend the UV pulse duration to 3 ps. First tests integrating the stretcher into the pump beam path indicate a slightly increased electron bunch extraction efficiency but systematic measurements have to be performed for reliable results. Another way to boost the bunch charge of the cathode is applying a higher anode voltage in a pulsed manner to raise the extraction field by simultaneously avoiding sparks. The optical resolution limit dictated by the probe wavelength can be overcome when using the UV pulses as pump *and* probe tool. The optical Kerr microscopy setup based on a reflective Schwarzschild objective is already available and assembled for enhancing the resolution up to a factor of two.

With the current setup research on logical units operating with spin-waves should be feasible and for example experiments proposed by Hertel et. al. [88] can be approached. The intense current pulses may also allow for switching of Co/Pt bits with perpendicular magnetic anisotropy by means of the magnetic out of plane component at the edge of the waveguide and could lead to an investigation of non-reversible dynamics in magnetic chains and arrays as pointed out in the introduction. Additionally, the setup is ready for research in the emerging field of all-optical switching of magnetic structures with laser pulses of arbitrary wavelength and polarization generated in an optical parametric amplifier (OPA) of the laser system with 290 fs temporal precision. Due to the additionally available synchronized pulses from the photocathode, coupling and interaction phenomena between spin-wave packets and electronic pulses can be studied to tailor future electro-magnetic interfaces.

The synchrotron radiation-based time-resolved magnetic transmission X-ray microscope (**TR-MTXM**) with a temporal resolution down to **90 ps** FWHM limited by the PETRA III soft X-ray pulse duration and a spatial resolution of $\mathbf{(62 \pm 8)\,nm}$ according to the Rayleigh criterion restricted by the micro zone plate optic allows performing static and dynamic measurements on magnetic nanostructures. The unique high pump field amplitude allows inducing highly out-of-equilibrium magnetization patterns in nanoscopic permalloy elements by aligning the majority of the magnetic moments into one direction. The time evolution during destruction and recovery of the domain patterns could be monitored and is backed up by micromagnetic simulations being able to reproduce key features of the dynamics. Furthermore, a stable vortex chirality and polarity could be maintained after recovery which is important thinking of a controlled manipulation of the vortices utilized as multi-bit memory cell. Depending on chirality and polarity, four distinguishable states may be stored in a single particle if deterministic writing and readout is achieved. During destruction of the vortex, also unusually high core velocities could be observed exceeding the threshold of 300 km/s where vortex switching is expected.

Toward the direction of investigating non-reversible switching processes, the reset mechanism should be improved by getting rid of the iron yoke that seems to generate residual fields after the current pulse has vanished. Also the control and adjustment of the opposing bias field could be done in a more sophisticated way. Furthermore, the full-field TXM may be transformed into a scanning X-ray microscope and benefit from the high degree of spatial coherence in the beamline rather than dealing with the speckle disturbances in the illumination field of the full-field setup. In order to image smaller samples, the micro zone plate should be replaced by an optic offering a reduced outermost zone width Δr_N. Zone plates fabricated by focused ion beam (FIB) have already been tested in this setup [157].

Considering the sample, promising candidates for non-reversible switching experiments are for example Co/Pt dot arrays or permalloy nanotubes like the ones manufactured in the group of KORNELIUS NIELSCH [154, 35, 148, 144, 150], both prepared on silicon nitride membranes. The nanotubes of a few hundred nanometer thickness would yield a huge XMCD contrast and feature a high aspect ratio being favorable for adjustable interactions through their stray field. Although the temporal resolution in the TR-MTXM setup is limited due to the synchrotron pulse duration, direct switching of magnetic nanostructures with the synchronized femtosecond laser pulses could be tackled. Presumably, the dynamics of one small element would elapse too fast to be reasonably resolved, but one could think of triggering large-scale dynamics in extended samples like chains, arrays or wires.

The constructed transmission X-ray microscope has also already proven its flexibility

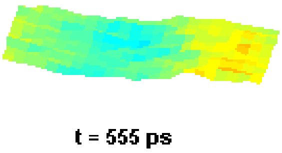

when it comes to the investigation of life-science samples apart from magnetic systems. Studies on the iron distribution in clay mineral samples were carried out by acquiring images at the iron absorption edge [1]. Moreover, biological samples were imaged at 530 eV and 1.3 keV photon energy and the dichroism of amino acids similar to the experiments by IZUMI et. al. [96] was investigated with the aim of providing additional imaging capabilities to examine non-artificial samples. The setup will be extended in the future into a mobile and flexible user endstation system with additional scanning, tomography and fluorescence imaging capabilities.

Thinking in bigger dimensions the experiments could be adapted to free-electron laser (FEL) sources to benefit from the short and intense pulses since techniques toward time-resolved single shot imaging at FELs are evolving [53, 78]. However, similar to other FELs, the FLASH facility in Hamburg would need a special soft X-ray polarizer [177] to be able to provide circular polarization when relying on XMCD measurements. A better understanding of the dynamics of magnetic systems might also become possible when combining the setups with terahertz (THz) radiation [170, 106] or high harmonic generation (HHG) sources [175, 203, 198, 127], both routinely available in nowadays laboratories equipped with femtosecond laser systems.

Eventually, after designing, setting up and characterizing the new instruments for time-resolved imaging of magnetic nanostructures, the experiments were able to gain novel insight considering the dynamics of small magnetic systems excited by now available uniquely strong and short defined magnetic field pulses. In comparison, the TR-MTXM features a better spatial resolution due to the short soft X-ray wavelength and is sensitive to the in-plane M_x and out-of-plane M_z magnetization component while the TR-SKM provides a superior temporal resolution due to the femtosecond laser system and is solely sensitive to the out-of-plane M_z component. The analyzed results of both experiments also demonstrate the flexibility and data quality of TR-SKM and TR-MTXM to explore forthcoming questions in magnetic research at its fundamental time- and length-scales.

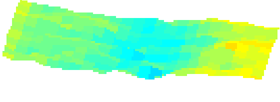

t = 565 ps

Appendix A

Calculations

A.1 Electromagnetic waves in magnetized matter

The approach in this section is to derive different refractive indices for circularly left- and right polarized light in magnetized matter. The calculation is based on the article by Z. Q. Qiu and S. D. Bader in [167]. The electrodynamics involved in this chapter is carried out in SI units and adapted from the text books of D. J. Griffiths [77] and W. Demtröder [44].

A.1.1 Maxwell equations

For a start we summarize Maxwell's equations in SI units [77]:

$$\vec{\nabla} \cdot \vec{E} = \frac{\rho}{\varepsilon_0} \tag{A.1}$$

$$\vec{\nabla} \cdot \vec{B} = 0 \tag{A.2}$$

$$\vec{\nabla} \times \vec{E} = -\frac{\partial \vec{B}}{\partial t} \tag{A.3}$$

$$\vec{\nabla} \times \vec{B} = \mu_0 \vec{j} + \mu_0 \varepsilon_0 \frac{\partial \vec{E}}{\partial t} \tag{A.4}$$

In magnetically and electrically polarized matter the equations can be adjusted by using the polarization $\vec{P}$ and the magnetization $\vec{M}$. It is then possible to split the contributions to the field in bound charges $\rho_b = -\vec{\nabla}\vec{P}$, bound currents $\vec{j}_b = \vec{\nabla} \times \vec{M}$ and polarization currents $\vec{j}_p = \frac{\partial \vec{P}}{\partial t}$ generated by the response of the material as well as external free charges ρ_f and free currents $\vec{j}_f$ summarized in $\rho = \rho_f + \rho_b$ and $\vec{j} = \vec{j}_f + \vec{j}_b + \vec{j}_p$:

$$\vec{\nabla} \cdot \vec{D} = \rho_f \tag{A.5}$$

$$\vec{\nabla} \cdot \vec{B} = 0 \tag{A.6}$$

$$\vec{\nabla} \times \vec{E} = -\frac{\partial \vec{B}}{\partial t} \tag{A.7}$$

$$\vec{\nabla} \times \vec{H} = \vec{j}_f + \frac{\partial \vec{D}}{\partial t} \tag{A.8}$$

with the definition of the auxiliary fields $\vec{D}$ and $\vec{H}$:

$$\vec{D} \equiv \varepsilon_0 \vec{E} + \vec{P} \tag{A.9}$$

$$\vec{H} \equiv \frac{1}{\mu_0} \vec{B} - \vec{M} \tag{A.10}$$

A.1.2 Magnetized linear media

By assuming a linear response of the material on the action of an external field given at low intensities, the auxiliary fields can be rewritten

$$\vec{P} = \varepsilon_0 \overset{\leftrightarrow}{\chi}_e \vec{E} \qquad \Rightarrow \qquad \vec{D} = \varepsilon_0 \underbrace{(\mathbb{1} + \overset{\leftrightarrow}{\chi}_e)}_{\overset{\leftrightarrow}{\varepsilon}_r} \vec{E} \tag{A.11}$$

$$\vec{M} = \overset{\leftrightarrow}{\chi}_m \vec{H} \qquad \Rightarrow \qquad \vec{B} = \mu_0 \underbrace{(\mathbb{1} + \overset{\leftrightarrow}{\chi}_m)}_{\overset{\leftrightarrow}{\mu}_r} \vec{H} \tag{A.12}$$

with the susceptibility $\overset{\leftrightarrow}{\chi}$ which is in general a tensor because an outer field may lead to a polarization not necessarily parallel to the field due to different crystal axis for example. The dielectric tensor for a magnetized medium can be expressed with the components of the Voigt vector $\vec{Q}$ and simplifies in the polar case (P-MOKE) to an expression only dependent on the Voigt constant $|\vec{Q}| = Q$ (confer [208, 130]).

$$\overset{\leftrightarrow}{\varepsilon}_r = \varepsilon_r \begin{pmatrix} 1 & iQ_z & -iQ_y \\ -iQ_z & 1 & iQ_x \\ iQ_y & -iQ_x & 1 \end{pmatrix}, \qquad \text{P-MOKE:} \quad \overset{\leftrightarrow}{\varepsilon}_r = \varepsilon_r \begin{pmatrix} 1 & iQ & 0 \\ -iQ & 1 & 0 \\ 0 & 0 & 1 \end{pmatrix} \tag{A.13}$$

When assuming $\overset{\leftrightarrow}{\mu}_r = \mu_r \mathbb{1}$ and using A.13, the equations A.11 and A.12 may be rewritten as

$$\vec{D} = \underbrace{\varepsilon_0 \varepsilon_r}_{\varepsilon} \left(\vec{E} + i\vec{E} \times \vec{Q} \right) \qquad \text{and} \qquad \vec{B} = \underbrace{\mu_0 \mu_r}_{\mu} \vec{H} \tag{A.14}$$

Maxwell's equations A.5 - A.8 combined with equation A.14 and the field ansatz $\vec{E} = \vec{E}_0 \cdot e^{i(\vec{k}\cdot\vec{x} - \omega t)}$ as well as $\vec{B} = \vec{B}_0 \cdot e^{i(\vec{k}\cdot\vec{x} - \omega t)}$ lead to:

$$\vec{k} \cdot \vec{E} + i\vec{k} \cdot \left(\vec{E} \times \vec{Q} \right) = 0 \tag{A.15}$$

$$\vec{k} \cdot \vec{H} = 0 \tag{A.16}$$

$$\vec{k} \times \vec{E} = \omega \mu_0 \mu_r \vec{H} \tag{A.17}$$

$$\vec{k} \times \vec{H} = -\omega \varepsilon_0 \varepsilon_r \left(\vec{E} + i\vec{E} \times \vec{Q} \right) \tag{A.18}$$

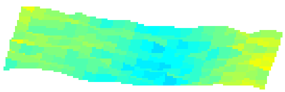

t = 575 ps

From A.15 - A.18 it is obvious that $\vec{k}$, $\vec{D}$ and $\vec{B}$ (as well as $\vec{H}$) are mutually perpendicular to each other. One can obtain the equations of motion (wave equation) and the amplitude of the electric field by applying the rotational operator $\left(\vec{\nabla}\times\right)$ again to equation A.7 to decouple the fields and then using equation A.8:

$$\vec{\nabla} \times \left(\vec{\nabla} \times \vec{E}\right) = -\frac{\partial}{\partial t}\left(\vec{\nabla} \times \vec{B}\right) \tag{A.19}$$

$$\Leftrightarrow \qquad \vec{\nabla}\left(\vec{\nabla} \cdot \vec{E}\right) - \Delta\vec{E} = -\mu_0\mu_r\frac{\partial}{\partial t}\left(\vec{\nabla} \times \vec{H}\right) \tag{A.20}$$

$$\Leftrightarrow \qquad i\vec{\nabla}\left(\vec{k} \cdot \vec{E}\right) + |\vec{k}|^2\vec{E} = -\mu_0\mu_r\frac{\partial^2\vec{D}}{\partial t^2} \tag{A.21}$$

$$\Leftrightarrow \qquad -\vec{k}\left(\vec{k} \cdot \vec{E}\right) + |\vec{k}|^2\vec{E} = -\mu_0\mu_r\varepsilon_0\varepsilon_r\frac{\partial^2}{\partial t^2}\left(\vec{E} + i\vec{E} \times \vec{Q}\right) \tag{A.22}$$

$$\Leftrightarrow \qquad -\vec{k}\left(\vec{k} \cdot \vec{E}\right) + |\vec{k}|^2\vec{E} = \frac{\omega^2\mu_r\varepsilon_r}{c^2}\left(\vec{E} + i\vec{E} \times \vec{Q}\right) \tag{A.23}$$

$$\Leftrightarrow \qquad \left(|\vec{k}|^2 - \frac{\omega^2\mu_r\varepsilon_r}{c^2}\right)\vec{E} = \vec{k}\left(\vec{k} \cdot \vec{E}\right) + \frac{i\omega^2\mu_r\varepsilon_r}{c^2}\vec{E} \times \vec{Q} \tag{A.24}$$

Splitting the electric field $\vec{E}$ propagating in $\vec{k}$ direction into s- and p- polarization components by inserting

$$\vec{E}_0 = \begin{pmatrix} E_s \\ E_p \\ E_k \end{pmatrix}, \qquad \vec{k} = \begin{pmatrix} 0 \\ 0 \\ k \end{pmatrix} \tag{A.25}$$

into A.24 simplifies the equations of motion. As a result the $\vec{E}$ field now is not any more purely transversal and has a component in $\vec{k}$ direction:

$$\left(\frac{\omega^2\mu_r\varepsilon_r}{c^2} - k^2\right)E_s = \frac{i\omega^2\mu_r\varepsilon_r}{c^2}\left(\vec{Q} \cdot \vec{e}_p E_k - \vec{Q} \cdot \vec{e}_k E_p\right) \tag{A.26}$$

$$\left(\frac{\omega^2\mu_r\varepsilon_r}{c^2} - k^2\right)E_p = \frac{i\omega^2\mu_r\varepsilon_r}{c^2}\left(\vec{Q} \cdot \vec{e}_k E_s - \vec{Q} \cdot \vec{e}_s E_k\right) \tag{A.27}$$

$$E_k = i\left(\vec{Q} \cdot \vec{e}_s E_p - \vec{Q} \cdot \vec{e}_p E_s\right) \tag{A.28}$$

For the field amplitude vector $\vec{E}_0$ in equation A.25 this means explicitly:

$$\vec{E}_0 = E_s\vec{e}_s + E_p\vec{e}_p + i\left(\vec{Q} \cdot \vec{e}_s E_p - \vec{Q} \cdot \vec{e}_p E_s\right)\vec{e}_k \tag{A.29}$$

By putting A.28 into A.26 and A.27 and neglecting terms quadratic in $\vec{Q}$, one obtains the equations of motion for E_s and E_p. This approximation is justified because Q is in the order of 10^{-2} to 10^{-1} ($|\vec{Q}| \ll 1$) for most magnetic materials. For the P-MOKE case even no approximation is needed, because there is only a Q_k component in the Voigt vector and Q_s as well as Q_p vanish. For a nontrivial solution where $E_s \neq 0$ and $E_p \neq 0$, the determinant of the approximated equations has to vanish which results in a different refractive index for the eigenvectors of the system.

$$\det \begin{pmatrix} 1 - \frac{c^2k^2}{\omega^2\mu_r\varepsilon_r} & -i\vec{Q}\cdot\vec{e}_k \\ i\vec{Q}\cdot\vec{e}_k & 1 - \frac{c^2k^2}{\omega^2\mu_r\varepsilon_r} \end{pmatrix} = 0 \tag{A.30}$$

$$\left(1 - \frac{c^2k^2}{\omega^2\mu_r\varepsilon_r}\right)^2 = \left(\vec{Q}\cdot\vec{e}_k\right)^2 \tag{A.31}$$

$$1 - \frac{c^2k^2}{\omega^2\mu_r\varepsilon_r} = \pm\vec{Q}\cdot\vec{e}_k \tag{A.32}$$

$$k^\pm = \underbrace{\frac{\omega}{c}\sqrt{\mu_r\varepsilon_r}}_{k}\sqrt{1 \mp \vec{Q}\cdot\vec{e}_k} \tag{A.33}$$

$$n^\pm \approx \underbrace{\sqrt{\mu_r\varepsilon_r}}_{n}\left(1 \mp \frac{1}{2}\vec{Q}\cdot\vec{e}_k\right) \tag{A.34}$$

By inserting the result of equation A.33 into the equations of motion, the eigenvectors turn out to be the circular polarized modes $\sigma^\pm$ of the electric field with $E_p = \pm iE_s$:

$$\sigma^+ \quad : \quad E_p = iE_s \quad \Rightarrow \quad \vec{E}_0^+ = E_0^+ \begin{pmatrix} 1 \\ i \\ 0 \end{pmatrix} \tag{A.35}$$

$$\sigma^- \quad : \quad E_p = -iE_s \quad \Rightarrow \quad \vec{E}_0^- = E_0^- \begin{pmatrix} 1 \\ -i \\ 0 \end{pmatrix} \tag{A.36}$$

Any linear combination is a solution as well, so in general we obtain $\vec{E} = \alpha\cdot\vec{E}^+ + \beta\cdot\vec{E}^-$. For $\alpha = \beta$ the field becomes linear polarized. Note that for oblique incidence without the approximation the modes are not completely circular polarized [67].

A.2 Magneto-optic Kerr effect (MOKE)

In this section the calculation of the Kerr rotation and ellipticity of an arbitrarily magnetized multilayer system is summarized following the universal approach published in [222, 223, 224, 167]. The approach relies on the calculations performed in appendix A.1.

For the theoretical calculation of the Kerr effect it is useful to describe an incoming, linearly polarized light beam with an electric field $\vec{E}$ as superposition of two circularly polarized waves $\vec{E}^+$ and $\vec{E}^-$ which we have identified as the eigenmodes of the equations of motion in magnetized matter (see equations A.35 and A.35 as well as the preceding calculations in appendix A.1):

$$\vec{E} = \vec{E}^+ + \vec{E}^- \qquad \text{with} \qquad \vec{E}^\pm = \frac{E_0}{2}\cdot\begin{pmatrix} 1 \\ \pm i \\ 0 \end{pmatrix}\cdot e^{i(\vec{k}\cdot\vec{x}-\omega t)} \tag{A.37}$$

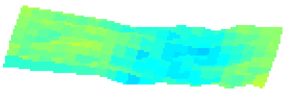

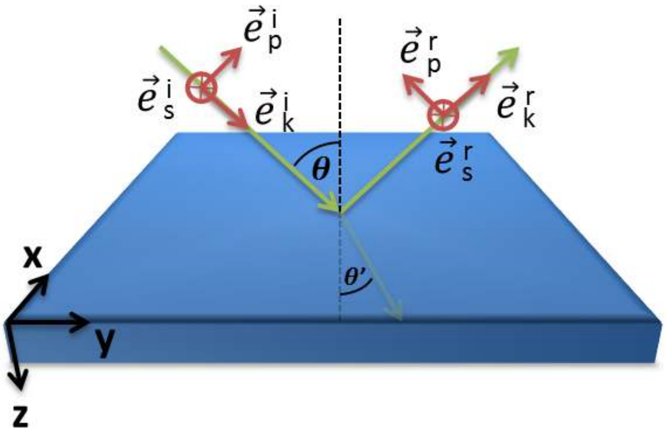

Figure A.1: Incident, reflected and refracted beam at a medium boundary and definition of the coordinate systems.

First, starting with a two layer system with one boundary represented by the xy plane. The vector $\vec{F}$ in equation A.38 contains the x and y components of the electromagnetic field while $\vec{P}$ contains the electric field components in the basis of the incident ($\vec{E}^i$) and reflected ($\vec{E}^r$) wave perpendicular (E_s) and parallel (E_p) to the plane of incidence (cf. figure A.1). We are now looking for the matrix A relating both representations to each other.

$$\vec{F} = A\vec{P} \qquad \text{with} \qquad \vec{F} = \begin{pmatrix} E_x \\ E_y \\ cB_x \\ cB_y \end{pmatrix}, \quad \vec{P} = \begin{pmatrix} E^i_s \\ E^i_p \\ E^r_s \\ E^r_p \end{pmatrix} \tag{A.38}$$

The x and y axis are in the film plane and perpendicular or parallel to the incident plane, respectively. With the k components taken from equation A.28 the basis transformation can be expressed as:

$$E_x = E^i_s + E^r_s \tag{A.39}$$

$$\begin{aligned} E_y = {} & E^{i+}_p \cos\theta^+ + E^{i-}_p \cos\theta^- + i\left(\vec{Q}\cdot\vec{e}^{\,i}_s E^i_p - \vec{Q}\cdot\vec{e}^{\,i}_p E^i_s\right)\cdot\sin\theta \\ & - E^{r+}_p \cos\theta^+ - E^{r-}_p \cos\theta^- + i\left(\vec{Q}\cdot\vec{e}^{\,r}_s E^r_p - \vec{Q}\cdot\vec{e}^{\,r}_p E^r_s\right)\cdot\sin\theta \end{aligned} \tag{A.40}$$

$$\begin{aligned} E_z = {} & -E^{i+}_p \sin\theta^+ - E^{i-}_p \sin\theta^- + i\left(\vec{Q}\cdot\vec{e}^{\,i}_s E^i_p - \vec{Q}\cdot\vec{e}^{\,i}_p E^i_s\right)\cdot\cos\theta \\ & - E^{r+}_p \sin\theta^+ - E^{r-}_p \sin\theta^- - i\left(\vec{Q}\cdot\vec{e}^{\,r}_s E^r_p - \vec{Q}\cdot\vec{e}^{\,r}_p E^r_s\right)\cdot\cos\theta \end{aligned} \tag{A.41}$$

using

$$E^+_p = +iE^+_s \tag{A.42}$$

$$E^-_p = -iE^-_s \tag{A.43}$$

$$n^+ \sin\theta^+ = n\sin\theta = n^- \sin\theta^- \tag{A.44}$$

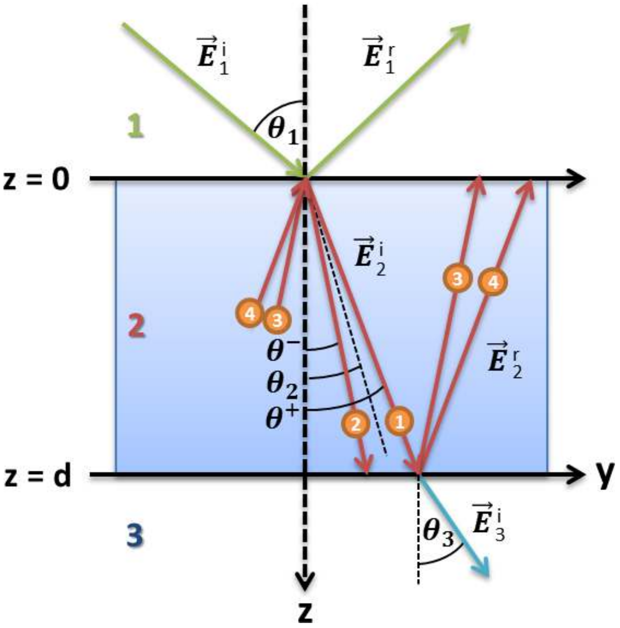

Figure A.2: Propagating beams inside a magnetic multilayer system. Because of the unequal indices of refraction $n^\pm$, different eigenmodes experience individual refraction angles $\theta^\pm$ (inspired by [222]).

from equations A.35 and A.36 and Snell's law (figure A.2) which means to first order in Q:

$$\sin\theta^+ = \frac{1}{\sqrt{1-\vec{Q}\cdot\vec{e}_k}}\sin\theta \approx \left(1+\frac{1}{2}\vec{Q}\cdot\vec{e}_k\right)\sin\theta \tag{A.45}$$

$$\sin\theta^- = \frac{1}{\sqrt{1+\vec{Q}\cdot\vec{e}_k}}\sin\theta \approx \left(1-\frac{1}{2}\vec{Q}\cdot\vec{e}_k\right)\sin\theta \tag{A.46}$$

$$\cos\theta^+ = \sqrt{1-\frac{\sin^2\theta}{1-\vec{Q}\cdot\vec{e}_k}} \approx \left(1-\frac{1}{2}\vec{Q}\cdot\vec{e}_k\tan^2\theta\right)\cos\theta \tag{A.47}$$

$$\cos\theta^- = \sqrt{1-\frac{\sin^2\theta}{1+\vec{Q}\cdot\vec{e}_k}} \approx \left(1+\frac{1}{2}\vec{Q}\cdot\vec{e}_k\tan^2\theta\right)\cos\theta \tag{A.48}$$

and

$$E_p = E_p^+ + E_p^- \tag{A.49}$$

$$E_s = E_s^+ + E_s^- = i\left(E_p^- - E_p^+\right) \tag{A.50}$$

obtained with A.43 and A.42 one gets

$$\begin{aligned} E_y = {} & \frac{i}{2}\left[Q_z\sin^2\theta - Q_y\tan\theta\left(1+\cos^2\theta\right)\right]E_s^i + \left(\cos\theta + iQ_x\sin\theta\right)E_p^i \\ & + \frac{i}{2}\left[Q_z\sin^2\theta + Q_y\tan\theta\left(1+\cos^2\theta\right)\right]E_s^r - \left(\cos\theta - iQ_x\sin\theta\right)E_p^r. \end{aligned} \tag{A.51}$$

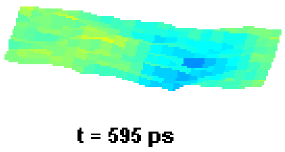

Now, we have already expressed E_x (equation A.39) and E_y (equation A.51) in the basis of E_s^i and E_p^i and we can do the same for B_x and B_y with $\vec{k} \times \vec{E} = \omega \vec{B}$ in the xyz basis by neglecting terms of $\mathcal{O}(Q^2)$:

$$\begin{aligned} B_x &= \frac{k_y}{\omega} E_z - \frac{k_z}{\omega} E_y && \text{(A.52)} \\ &= \frac{in}{2c}\left(Q_y \sin\theta + Q_z \cos\theta\right) E_s^i - \frac{n}{c} E_p^i + \frac{in}{2c}\left(Q_y \sin\theta - Q_z \cos\theta\right) E_s^r - \frac{n}{c} E_p^r && \text{(A.53)} \end{aligned}$$

$$\begin{aligned} B_y &= \frac{k_z}{\omega} E_x && \text{(A.54)} \\ &= \frac{n}{c} \cos\theta E_s^i + \frac{in}{2c}\left(Q_y \tan\theta + Q_z\right) E_p^i - \frac{n}{c} \cos\theta E_s^r - \frac{in}{2c}\left(Q_y \tan\theta - Q_z\right) E_p^r && \text{(A.55)} \end{aligned}$$

With this we have found the so called medium boundary matrix A between those two media. The problem for a single boundary can be solved by computing the four unknowns (E_{1s}^r, E_{1p}^r, E_{2s}^i, E_{2p}^i) in the set of four linear equations $A_1 \vec{P}_1 = A_2 \vec{P}_2$. When introducing the abbreviations $\alpha_y = \sin\theta$ and $\alpha_z = \cos\theta$ the matrix A reads:

$$A = \begin{pmatrix} 1 & 0 & 1 & 0 \\ \frac{i\alpha_y^2}{2}\left(Q_z - Q_y \frac{1+\alpha_z^2}{\alpha_y \alpha_z}\right) & iQ_x \alpha_y + \alpha_z & \frac{i\alpha_y^2}{2}\left(Q_z + Q_y \frac{1+\alpha_z^2}{\alpha_y \alpha_z}\right) & iQ_x \alpha_y - \alpha_z \\ \frac{in}{2}\left(Q_y \alpha_y + Q_z \alpha_z\right) & -n & \frac{in}{2}\left(Q_y \alpha_y - Q_z \alpha_z\right) & -n \\ n\alpha_z & \frac{in}{2}\left(Q_z + Q_y \frac{\alpha_y}{\alpha_z}\right) & -n\alpha_z & \frac{in}{2}\left(Q_z - Q_y \frac{\alpha_y}{\alpha_z}\right) \end{pmatrix} \tag{A.56}$$

This reduces in the polar case to:

$$\text{P-MOKE:} \qquad A_{\text{pol}} = \begin{pmatrix} 1 & 0 & 1 & 0 \\ \frac{i}{2}\alpha_y^2 Q & \alpha_z & \frac{i}{2}\alpha_y^2 Q & -\alpha_z \\ \frac{in}{2}\alpha_z Q & -n & -\frac{in}{2}\alpha_z Q & -n \\ n\alpha_z & \frac{in}{2} Q & -n\alpha_z & \frac{in}{2} Q \end{pmatrix} \tag{A.57}$$

In a multilayer system the propagation inside the medium is important, as well. That is why one also has to know another matrix D called medium propagation matrix to account for the accumulated phases during propagation. This matrix describes the evolution of $\vec{P}$ at any level z inside the medium and is defined by $\vec{P}(0) = D(z)\vec{P}(z)$. The components E_x^j of the electric field of the four rays inside the medium vary in phase as described by

$$\begin{pmatrix} E_s^i \\ E_p^i \\ E_s^r \\ E_p^r \end{pmatrix}_A = D \begin{pmatrix} E_s^i \\ E_p^i \\ E_s^r \\ E_p^r \end{pmatrix}_B \tag{A.58}$$

$$E_A^{i\pm}(0) = E_B^{i\pm}(z)\exp\left(-i\vec{k}^{\pm} z\vec{e}_z\right) = E_B^{i\pm}(d)\exp\left(-ik^{\pm} d\cos\theta^{\pm}\right) \tag{A.59}$$

$$E_A^{r\pm}(0) = E_B^{r\pm}(z)\exp\left(i\vec{k}^{\pm} z\vec{e}_z\right) = E_B^{r\pm}(d)\exp\left(ik^{\pm} d\cos\theta^{\pm}\right) \tag{A.60}$$

This leads to the medium propagation matrix D to first order in Q:

$$D = \begin{pmatrix} U\cos\delta_i & U\sin\delta_i & 0 & 0 \\ -U\sin\delta_i & U\cos\delta_i & 0 & 0 \\ 0 & 0 & U^{-1}\cos\delta_r & -U^{-1}\sin\delta_r \\ 0 & 0 & U^{-1}\sin\delta_r & U^{-1}\cos\delta_r \end{pmatrix} \tag{A.61}$$

$$\approx \begin{pmatrix} U & U\delta_i & 0 & 0 \\ -U\delta_i & U & 0 & 0 \\ 0 & 0 & U^{-1} & -U^{-1}\delta_r \\ 0 & 0 & U^{-1}\delta_r & U^{-1} \end{pmatrix} \tag{A.62}$$

with

$$U = \exp\left(-ikd\cos\theta\right) \tag{A.63}$$

$$\delta_i = \frac{kd}{2}\left(Q_y\tan\theta + Q_z\right) \tag{A.64}$$

$$\delta_r = \frac{kd}{2}\left(Q_y\tan\theta - Q_z\right) \tag{A.65}$$

For the extraction of the magneto-optic coefficients one first has to calculate the matrix M in $\vec{P}_i = M\vec{P}_f$ like

$$M = A_i^{-1}\prod_m A_m D_m A_m^{-1} A_f \equiv \begin{pmatrix} G & H \\ I & J \end{pmatrix} \tag{A.66}$$

Now one can show that this relates to the Fresnel transmission and reflection parameters [222]

$$\begin{pmatrix} t_{ss} & t_{sp} \\ t_{ps} & t_{pp} \end{pmatrix} = G^{-1} \tag{A.67}$$

$$\begin{pmatrix} r_{ss} & r_{sp} \\ r_{ps} & r_{pp} \end{pmatrix} = IG^{-1} \tag{A.68}$$

and from those parameters the complex Kerr angle for perpendicular (s) and parallel (p) polarized light with respect to the incident plane is computable immediately:

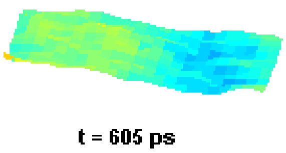

$$s\text{-polarization} : \phi_K = \phi_K^r + i\phi_K^e = \frac{r_{ps}}{r_{ss}} \tag{A.69}$$

$$p\text{-polarization} : \phi_K = -\phi_K^r + i\phi_K^e = \frac{r_{sp}}{r_{pp}} \tag{A.70}$$

A.3 Zone plates

The calculation of the rule for the zone radii r_n is performed in detail here. The path difference Δ of equation 2.51 illustrated in figure 2.16 has to be solved to r_n:

$$\Delta = \Delta_1 + \Delta_2 = \sqrt{g^2 + r_n^2} + \sqrt{b^2 + r_n^2} - b - g \overset{!}{=} n\frac{\lambda}{2} \tag{A.71}$$

$$\Rightarrow g^2 + r_n^2 + b^2 + r_n^2 + 2\sqrt{\left(g^2 + r_n^2\right)\left(b^2 + r_n^2\right)} = \left(n\frac{\lambda}{2} + b + g\right)^2 \tag{A.72}$$

$$\Rightarrow 4\left(g^2 + r_n^2\right)\left(b^2 + r_n^2\right) = \left[\left(n\frac{\lambda}{2} + b + g\right)^2 - g^2 - b^2 - 2r_n^2\right]^2 \tag{A.73}$$

$$\Leftrightarrow 4\left(g^2 + r_n^2\right)\left(b^2 + r_n^2\right) = \left[n^2\frac{\lambda^2}{4} + n\lambda(b+g) + 2bg - 2r_n^2\right]^2 \tag{A.74}$$

$$\Leftrightarrow 4\left[g^2b^2 + r_n^2\left(g^2 + b^2\right) + r_n^4\right] = n^4\frac{\lambda^4}{16} + n^3\frac{\lambda^3}{2}(b+g) + n^2\lambda^2 bg - n^2\lambda^2 r_n^2 \tag{A.75}$$

$$+ n^2\lambda^2(b+g)^2 + 4n\lambda(b+g)bg - 4n\lambda(b+g)r_n^2 + 4b^2g^2 - 8bgr_n^2 + 4r_n^4 \tag{A.76}$$

$$\Leftrightarrow 4r_n^2\left(g^2 + b^2\right) + n^2\lambda^2 r_n^2 + 4n\lambda(b+g)r_n^2 + 8bgr_n^2 = n^4\frac{\lambda^4}{16} + n^3\frac{\lambda^3}{2}(b+g) \tag{A.77}$$

$$+ n^2\lambda^2 bg + n^2\lambda^2(b+g)^2 + 4n\lambda(b+g)bg \tag{A.78}$$

$$\Leftrightarrow r_n^2 = \frac{n^4\frac{\lambda^4}{16} + n^3\frac{\lambda^3}{2}(b+g) + n^2\lambda^2\left[bg + (b+g)^2\right] + 4n\lambda(b+g)bg}{4\left(g^2 + b^2\right) + n^2\lambda^2 + 4n\lambda(b+g) + 8bg} \tag{A.79}$$

$$\Leftrightarrow r_n^2 = \frac{n\lambda(4g + n\lambda)(4b + n\lambda)(4(b+g) + n\lambda)}{16(2(b+g) + n\lambda)^2} \tag{A.80}$$

$$\Rightarrow r_n = \frac{\sqrt{n\lambda(4g + n\lambda)(4b + n\lambda)(4(b+g) + n\lambda)}}{4(2(b+g) + n\lambda)} \tag{A.81}$$

A Taylor series expansion of $r_n^2(\lambda)$ including the order λ^2 around $\lambda = 0$ is possible because in general $\lambda \ll b, g, f$ holds. Using the lens equation 2.52 ($1/f = 1/b + 1/g$) results in

$$r_n^2 \approx \frac{bgn\lambda}{b+g} + \frac{(b^2 - bg + g^2)n^2\lambda^2}{4(b+g)^2} \tag{A.82}$$

$$r_n^2 \approx nf\lambda + \frac{(b+g)^2 - 3bg}{4(b+g)^2} n^2\lambda^2 \tag{A.83}$$

$$r_n^2 \approx nf\lambda + \frac{n^2\lambda^2}{4} - \frac{3bgn^2\lambda^2}{\underbrace{4(b+g)^2}_{\to 0}} \tag{A.84}$$

$$r_n^2 \approx nf\lambda + \frac{n^2\lambda^2}{4} \tag{A.85}$$

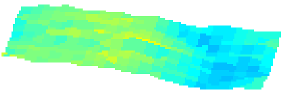

Appendix B

Preparation parameters

This chapter summarizes the design and processing parameters adopted during the sample preparation for TR-SKM and TR-MTXM samples. In general first the magnetic system was deposited and on top of it the coplanar waveguide. Concerning the waveguide design the 6th order polynomial fits of half conductor width $w/2$ vs. ground plane coordinate $y = w/2 + g$ shown in figure 4.1 according to

$$y\left(\frac{w}{2}\right) = \sum_{i=0}^{6} a_i \cdot \left(\frac{w}{2}\right)^i \qquad \text{with} \qquad y = \frac{w}{2} + g \tag{B.1}$$

were obtained with the coefficients listed in table B.1.

Table B.1: Coefficients for the 6th order polynomial fit according to equation B.1 of the copper (conductivity $\sigma = 5.88 \cdot 10^7\,\mathrm{S/m}$) waveguide on sapphire ($\varepsilon_r = 9.4$, $\tan(\delta) = 3 \cdot 10^{-5}$) or silicon ($\varepsilon_r = 11.9$, $\tan(\delta) = 10^{-3}$) substrates.

Coefficient	**TR-SKM (400 µm sapphire)**	**TR-MTXM (100 µm silicon)**
$a_0\ [\mathrm{\mu m}]$	$0.038\,66 \pm 0.017\,29$	$0.003\,33 \pm 0.068\,29$
$a_1\ [1]$	$0.090\,540\,000 \pm 0.000\,399\,457$	$0.061\,85 \pm 0.001\,95$
$a_2\ \left[\mathrm{\mu m}^{-1}\right]$	$(-0.960\,467 \pm 2.124\,620) \cdot 10^{-6}$	$(-6.320\,02 \pm 1.428\,76) \cdot 10^{-5}$
$a_3\ \left[\mathrm{\mu m}^{-2}\right]$	$(9.619\,240 \pm 0.447\,074) \cdot 10^{-8}$	$(1.449\,550\,0 \pm 0.043\,212\,2) \cdot 10^{-6}$
$a_4\ \left[\mathrm{\mu m}^{-3}\right]$	$(-2.786\,590 \pm 0.439\,385) \cdot 10^{-11}$	$(-2.141\,960\,0 \pm 0.062\,072\,1) \cdot 10^{-9}$
$a_5\ \left[\mathrm{\mu m}^{-4}\right]$	$(-2.884\,59 \pm 2.017\,21) \cdot 10^{-15}$	$(1.324\,620\,0 \pm 0.041\,950\,9) \cdot 10^{-12}$
$a_6\ \left[\mathrm{\mu m}^{-5}\right]$	$(1.658\,190 \pm 0.348\,853) \cdot 10^{-18}$	$(-3.058\,160 \pm 0.107\,121) \cdot 10^{-16}$

Table B.2: Processing parameters of **TR-SKM** coplanar waveguide preparation on a sapphire substrate without a magnetic system.

Substrate	400 µm A-plane sapphire (Al_2O_3)
Photoresist Spin coating Bake-out	Shipley S1813 5000 rpm, 60 s, Ramp 100 Hotplate 115 °C, 60 s
Exposure Develop Stop	22 mW/cm^2, 4 s MF-319, 40 s DI water
Plasma cleaning Material deposition Lift-off	1.3 mbar O_2 plasma, 30 s, 300 W 5 nm Cr, 300 nm Cu, 5 nm Au ca. 12 h acetone, ultrasonic cleaning

Table B.3: Processing parameters of **TR-SKM** magnetic structure preparation on a sapphire substrate.

Substrate	400 µm A-plane sapphire (Al_2O_3)
Electron-beam resist Spin coating Pre-bake Electron-beam resist Spin coating Bake-out	PMMA-50K 6000 rpm, 60 s, Ramp 30 Hotplate 160 °C, 30 s PMMA-950K 6000 rpm, 60 s, Ramp 30 Hotplate 160 °C, 120 s
Electron current Exposure Develop Stop	228 pA, 10 kV, 10 µm aperture 90 µC/cm^2 Allresist AR 600-56, 70 s Isopropyl alcohol, 30 s
Plasma cleaning Material deposition Lift-off	1.3 mbar O_2 plasma, 30 s, 300 W 50 nm permalloy ($Ni_{80}Fe_{20}$) ca. 12 h acetone

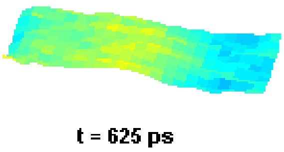

Table B.4: Processing parameters of **TR-SKM** coplanar waveguide preparation on a sapphire substrate on top of a magnetic sample.

Substrate	400 µm A-plane sapphire (Al_2O_3)
Lift-off resist	MicroChem LOR 5A + MicroChem G Thinner (50:50)
Spin coating	4500 rpm, 60 s, Ramp 250
Bake-out	Hotplate 160 °C, 300 s
Photoresist	Shipley S1813
Spin coating	6000 rpm, 60 s, Ramp 250
Bake-out	Hotplate 115 °C, 60 s
Exposure	22 mW/cm^2, 5 s
Develop	MF-319, 60 s
Stop	DI water
Material deposition	300 nm Cu, 3 nm Au
Lift-off	ca. 12 h acetone

Table B.5: Processing parameters of **TR-MTXM** magnetic structure preparation on a silicon nitride membrane.

Substrate	200 nm SiRN
Electron-beam resist	PMMA-50K
Spin coating	6000 rpm, 60 s, Ramp 30
Pre-bake	Hotplate 160 °C, 30 s
Electron-beam resist	PMMA-950K
Spin coating	6000 rpm, 60 s, Ramp 30
Bake-out	Hotplate 160 °C, 120 s
Electron current	177 pA, 10 kV, 10 µm aperture
Exposure	130 µC/cm^2 to 150 µC/cm^2
Develop	Allresist AR 600-56, 70 s
Stop	Isopropyl alcohol, 30 s
Plasma cleaning	1.3 mbar O_2 plasma, 30 s, 300 W
Material deposition	10 nm to 30 nm permalloy ($Ni_{80}Fe_{20}$)
Lift-off	ca. 12 h acetone

Table B.6: Processing parameters of **TR-MTXM** coplanar waveguide preparation on a silicon substrate on top of a magnetic sample.

Substrate	200 nm SiRN on 100 µm Si
Lift-off resist	MicroChem LOR 5A + MicroChem G Thinner (50:50)
Spin coating	4500 rpm, 60 s, Ramp 250
Bake-out	Hotplate 160 °C, 300 s
Photoresist	Shipley S1813
Spin coating	6000 rpm, 60 s, Ramp 250
Bake-out	Hotplate 115 °C, 60 s
Exposure	22 mW/cm^2, 5 s
Develop	MF-319, 60 s
Stop	DI water
Material deposition	300 nm Cu, 3 nm Au
Lift-off	ca. 12 h acetone

Table B.7: Coplanar copper (conductivity $\sigma = 5.88 \cdot 10^7\,\mathrm{S/m}$, 35 µm thickness) waveguides of the adapter PCBs for the **TR-MTXM** samples with a footprint of 20 mm × 7 mm and a cutaway of 5 mm × 4 mm size (compare figure 4.7) on 1 mm thick FR4 substrates ($\varepsilon_r = 4.8$, $\tan(\delta) = 1.8 \cdot 10^{-2}$). In the photocathode case conductor and gap are reduced linearly.

	Photocathode PCB (laser setup)	**SMP plug PCB (pulser setup)**
Source impedance	100 Ω	50 Ω
Conductor width	1500 µm	1000 µm
Gap size	1673 µm	166 µm
Interface impedance	100 Ω	100 Ω
Conductor width	1000 µm	1000 µm
Gap size	1310 µm	1310 µm

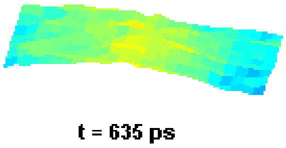

Appendix C

Additional data

C.1 Time-resolved scanning Kerr microscopy

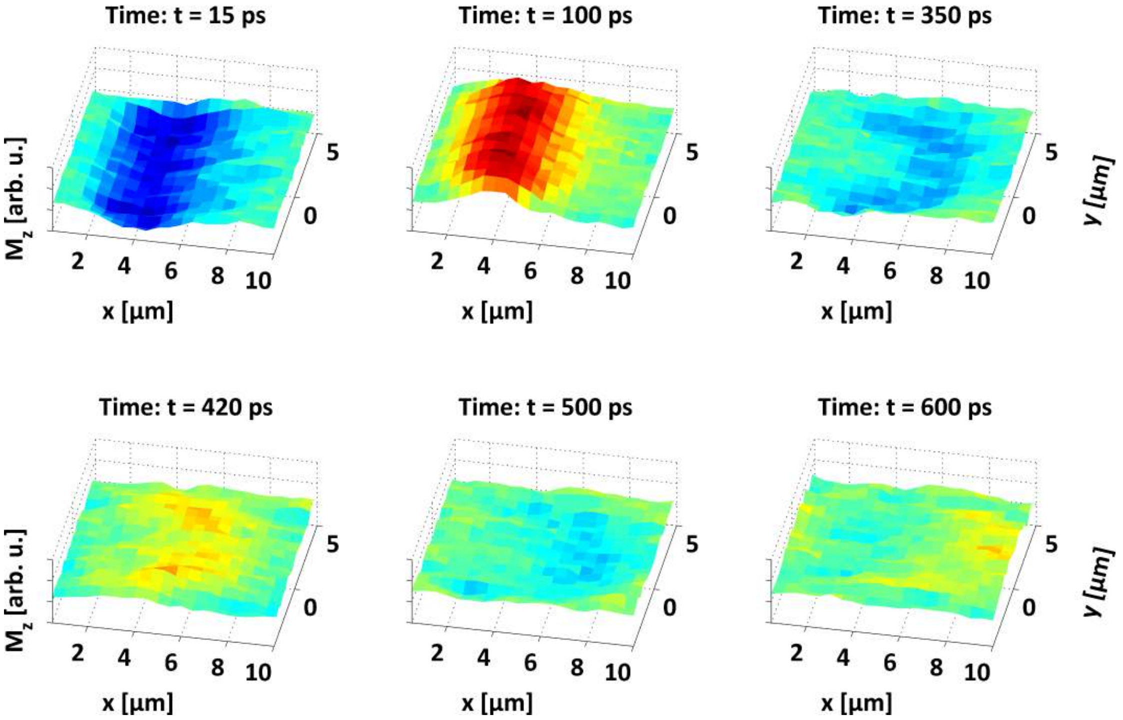

Figure C.1: Selected frames of another acquired spin-wave movie of a Damon-Eshbach mode illustrating the transient magnetization in a permalloy slab of 10 µm width at six delay settings.

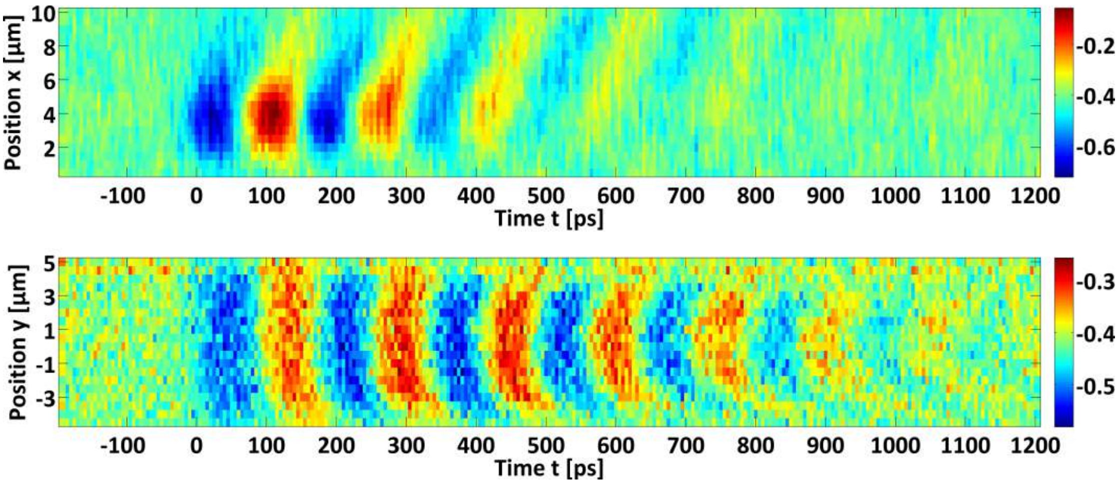

Figure C.2: Propagation in x direction at fixed $y = 0\,\mu\text{m}$ (top) and transversal modes at $x = 8\,\mu\text{m}$ (bottom) with respect to time in a $10\,\mu\text{m}$ slab in DE configuration.

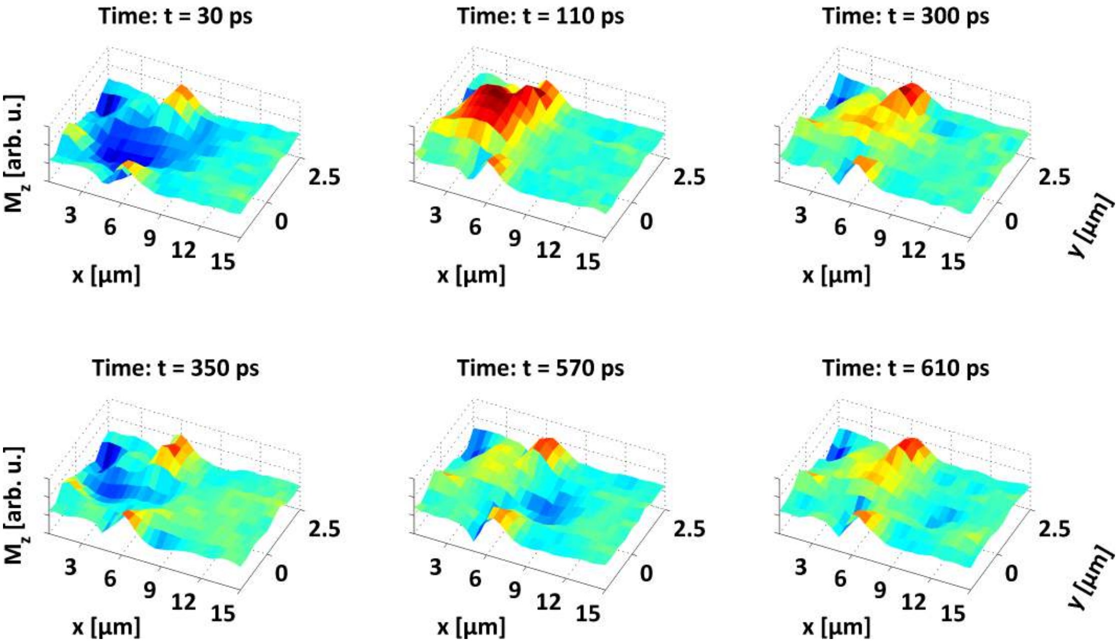

Figure C.3: Selected frames of another acquired spin-wave movie of a Damon-Eshbach mode illustrating the transient magnetization in a permalloy slab of $3\,\mu\text{m}$ width at six delay settings.

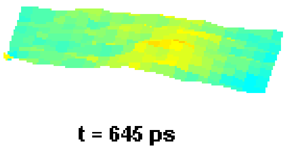

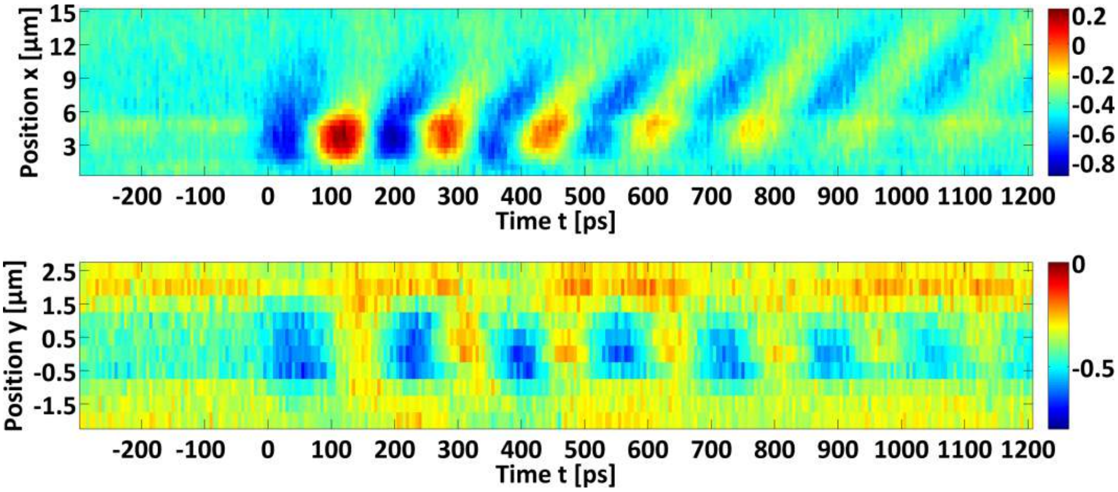

Figure C.4: Propagation in x direction at fixed $y = 0\,\mu\text{m}$ (top) and transversal modes at $x = 7.5\,\mu\text{m}$ (bottom) with respect to time in a $3\,\mu\text{m}$ slab in DE configuration.

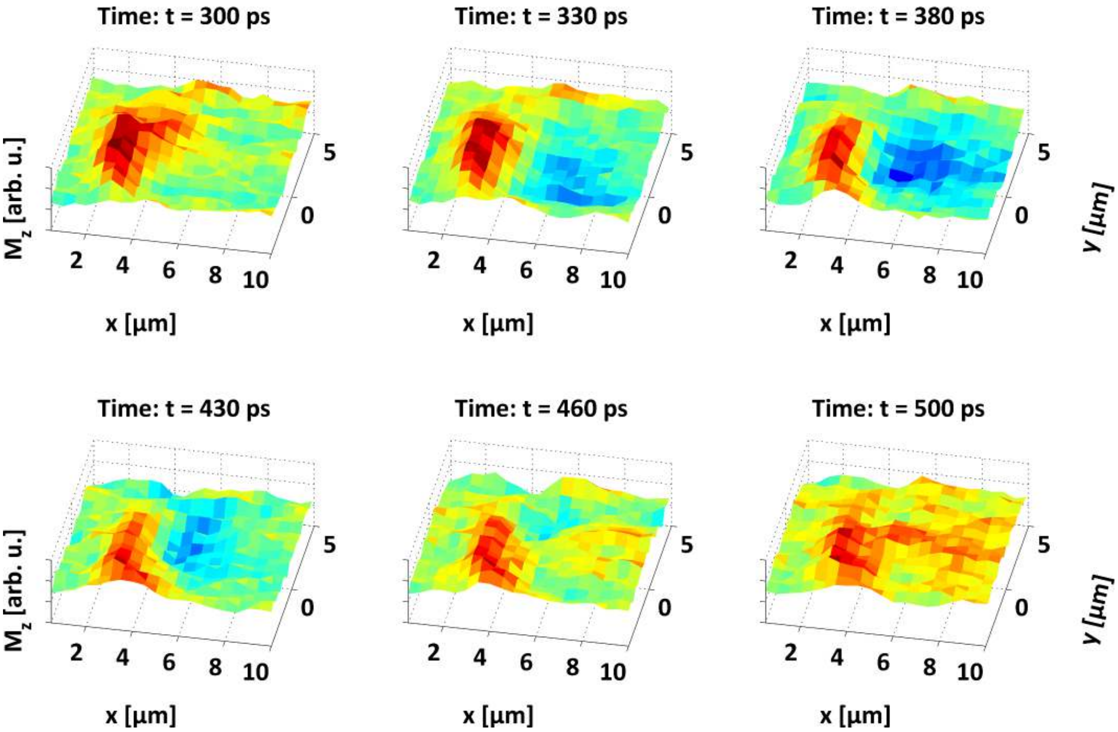

Figure C.5: Selected frames of another acquired spin-wave movie of a backward volume mode illustrating the transient magnetization in a permalloy slab of $10\,\mu\text{m}$ width at six delay settings.

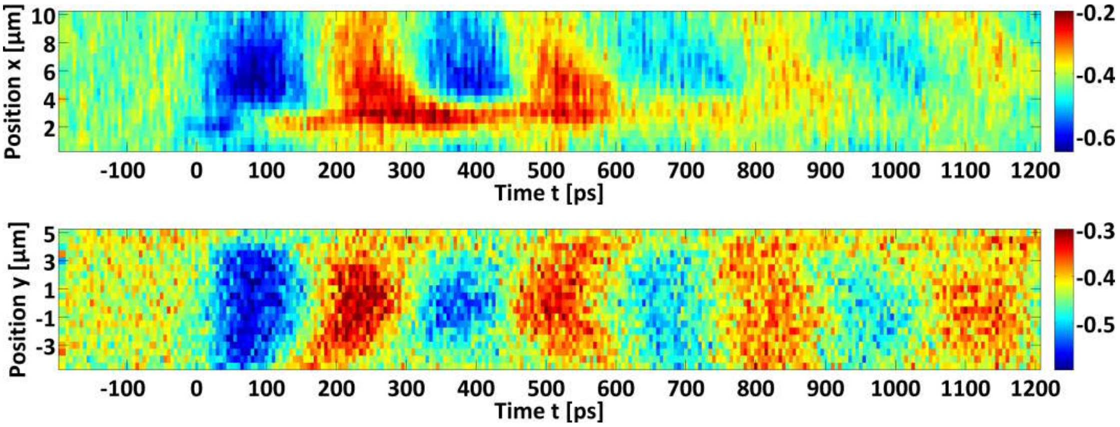

Figure C.6: The top image shows the propagation of the backward volume spin-wave packet with respect to time at a fixed transversal position in the center of the slab ($y = 0\,\mu\text{m}$). In the bottom image the spectrum of the transversal modes at a fixed longitudinal position at ($x = 8\,\mu\text{m}$) is displayed with respect to time.

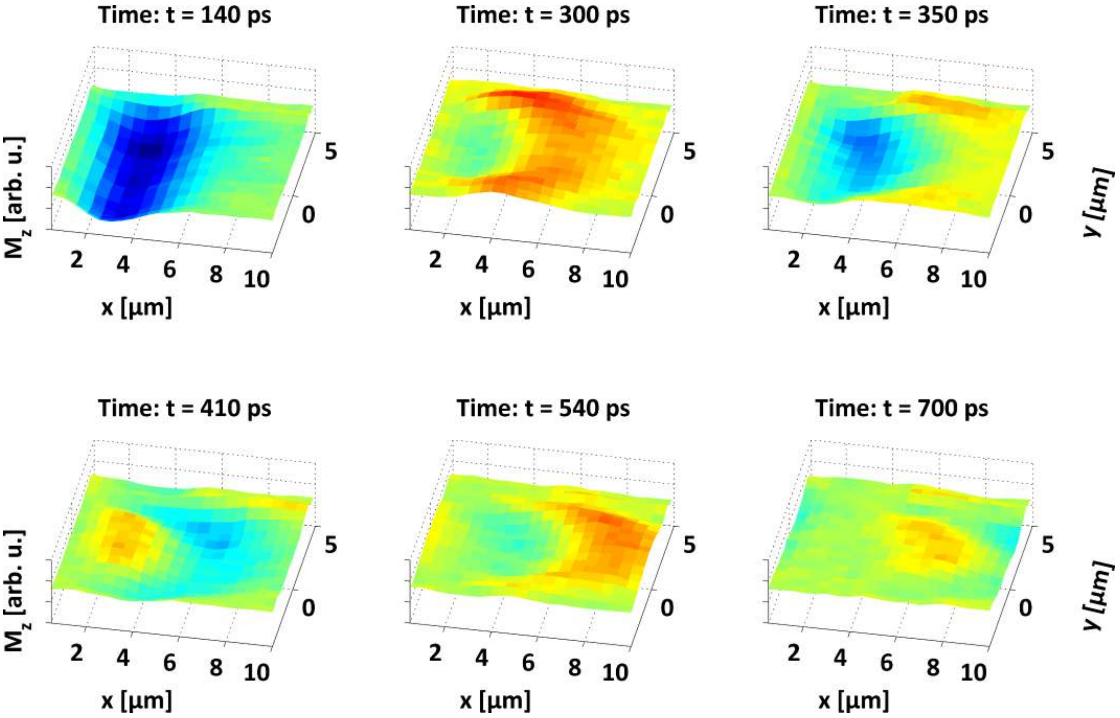

Figure C.7: Selected frames of another acquired spin-wave movie of a reverse Damon-Eshbach mode illustrating the transient magnetization in a permalloy slab of 10 µm width at six delay settings.

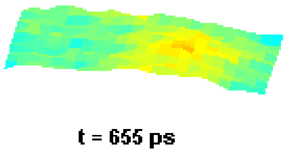

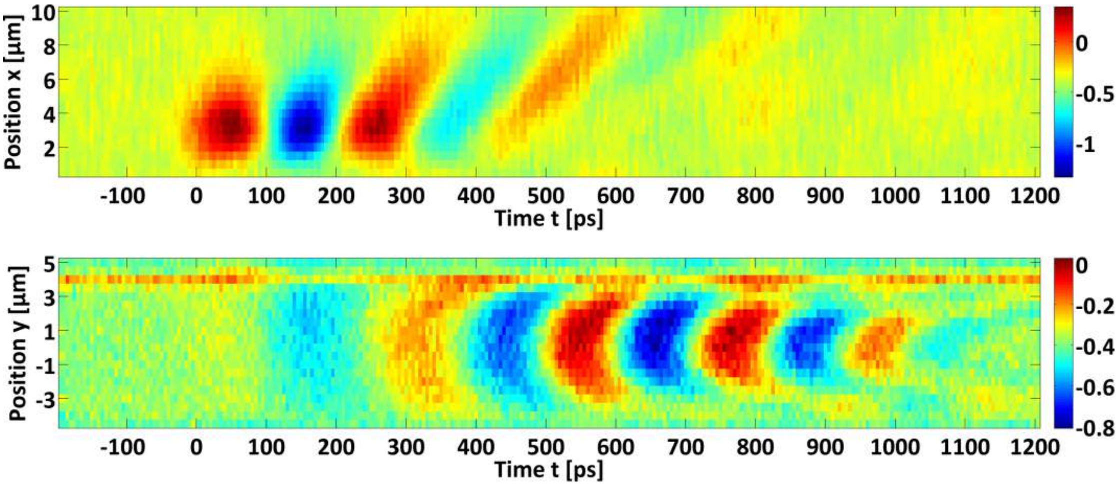

Figure C.8: Propagation in x direction at fixed $y = 0\,\mu\text{m}$ (top) and transversal modes at $x = 9\,\mu\text{m}$ (bottom) with respect to time in a 10 µm slab in reverse DE configuration.

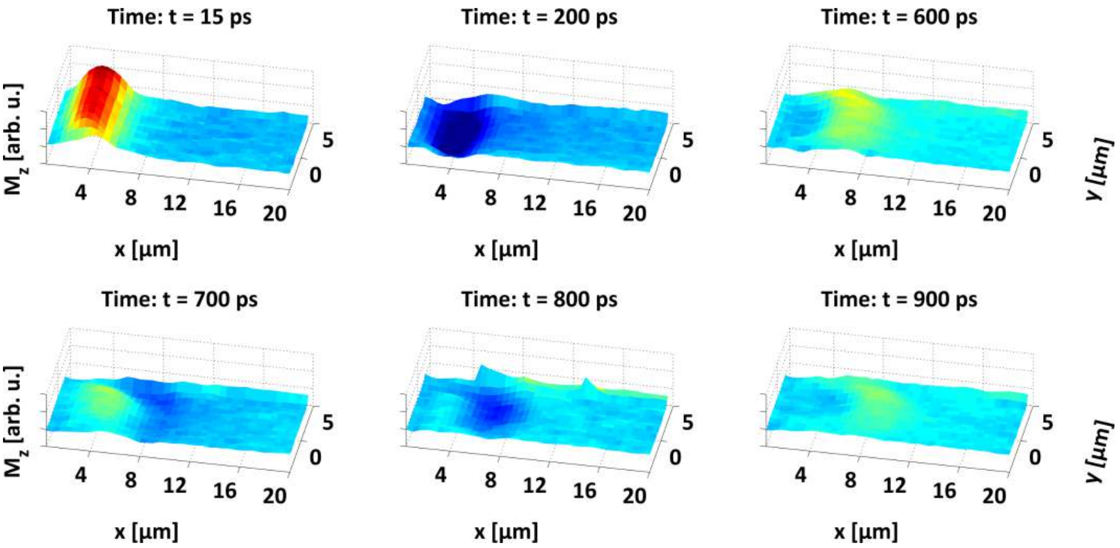

Figure C.9: Selected frames of another acquired spin-wave movie of a reverse Damon-Eshbach mode illustrating the transient magnetization in a permalloy slab of 10 µm width at six delay settings.

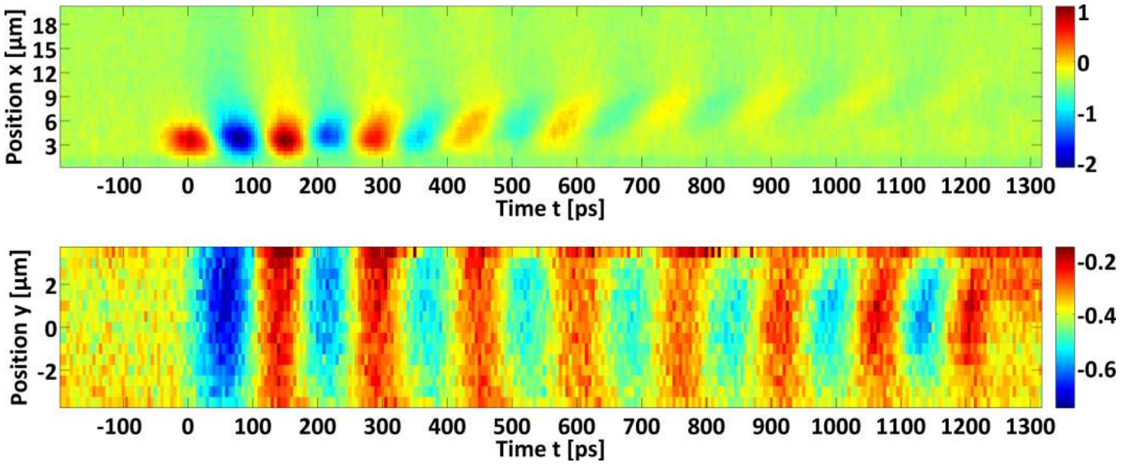

Figure C.10: Propagation in x direction at fixed $y = 0\,\mu\text{m}$ (top) and transversal modes at $x = 12\,\mu\text{m}$ (bottom) with respect to time in a $10\,\mu\text{m}$ slab in reverse DE configuration.

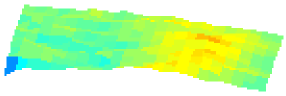

C.2 Time-resolved magnetic transmission X-ray microscopy

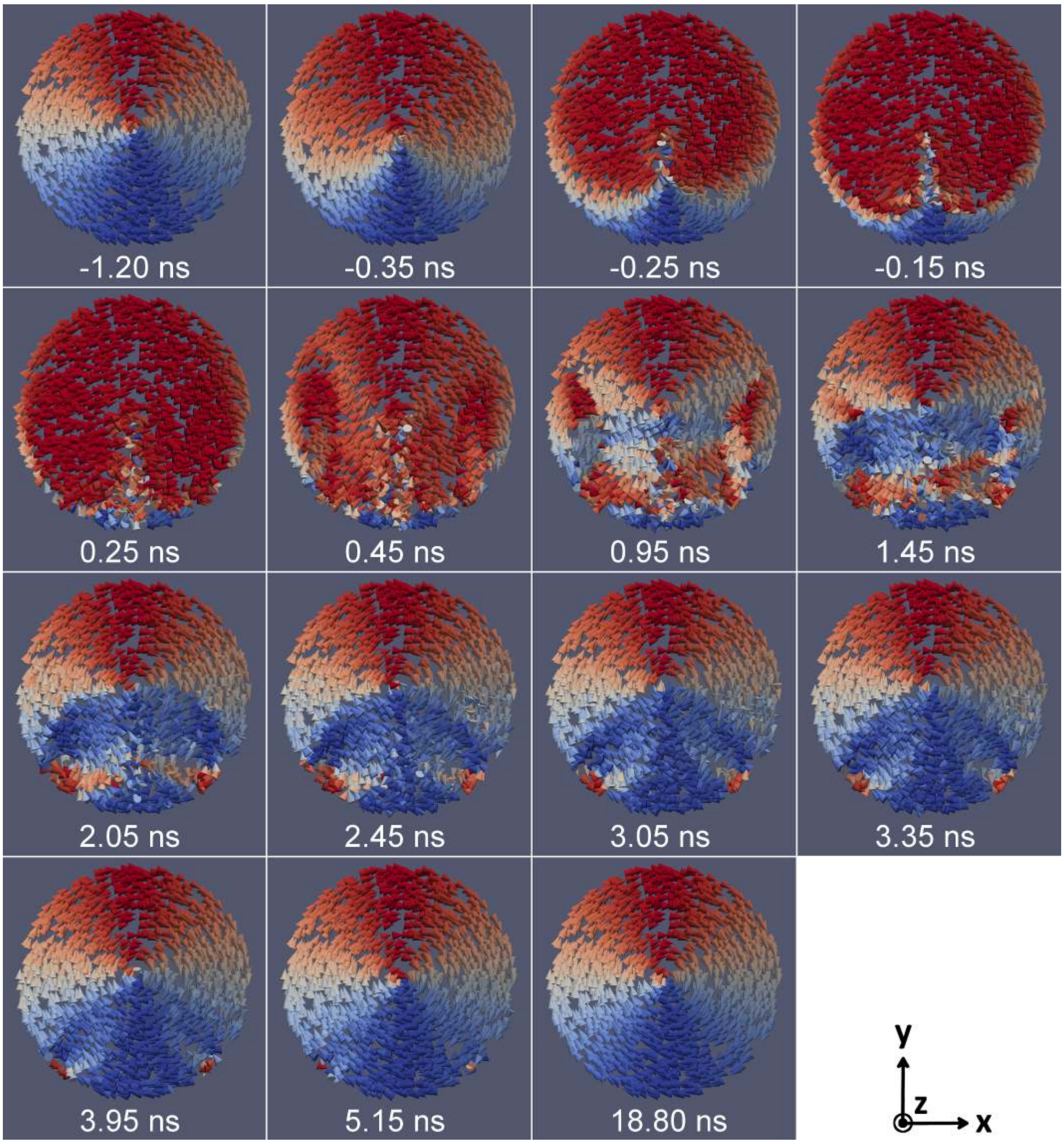

Figure C.11: Dynamic simulation of the magnetization in a 2 µm diameter permalloy circle of 30 nm thickness in an initial vortex state excited by a short field pulse of $\tau = 210\,\mathrm{ps}$ duration and $\mu_0 h_0 = 88\,\mathrm{mT}$ amplitude at $t_0 = 0\,\mathrm{ns}$ into positive x direction. After destruction of the domain pattern, a recovery takes place. Each cone represents a magnetization vector averaged over several grid units color coded by its x component (red: positive, blue: negative).

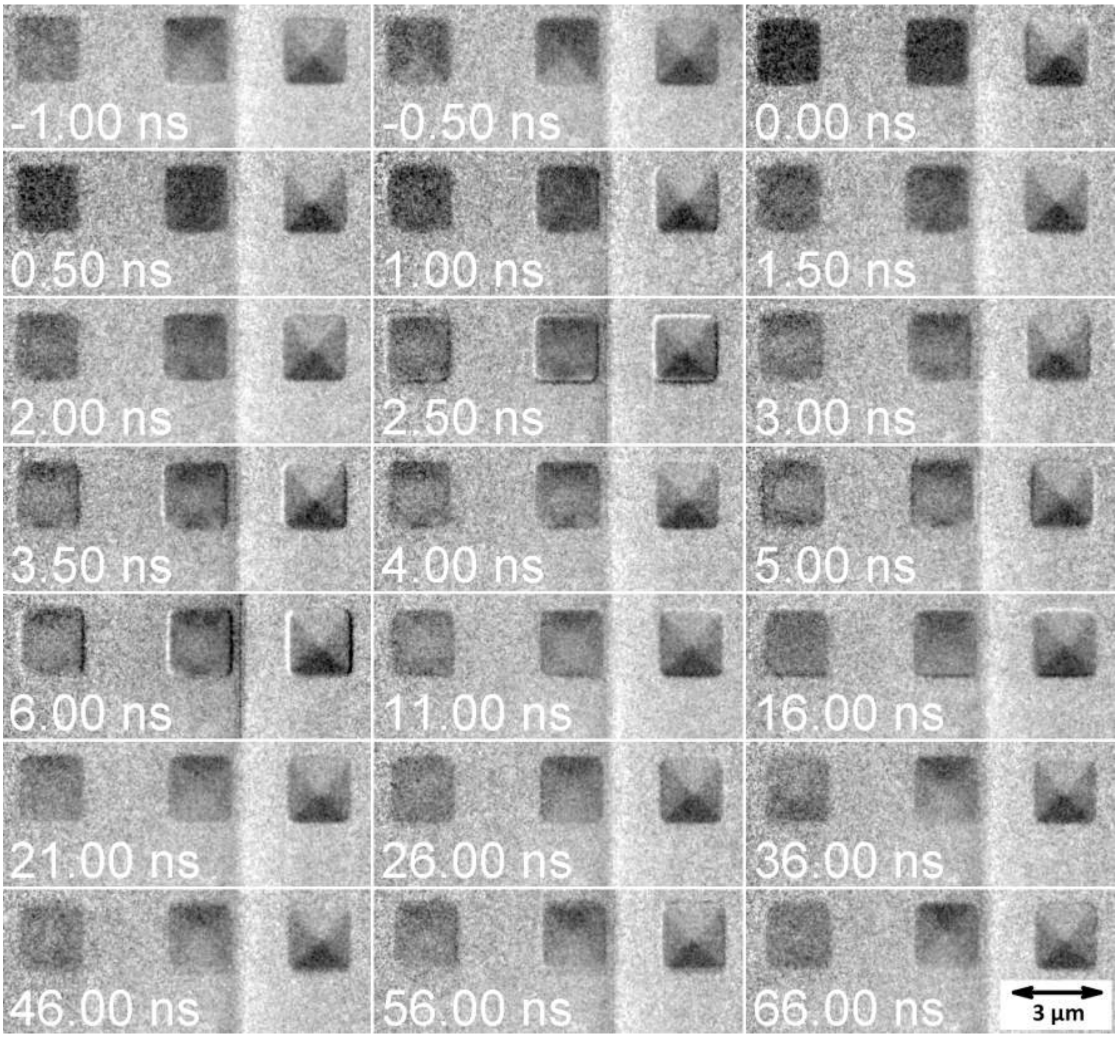

Figure C.12: Another scan of the domain pattern recovery of permalloy elements excited by the magnetic field of a current pulse which aligns the magnetization of the left two 2 µm × 2 µm squares along the x direction. The right square in the CPW gap keeps its four domain pattern.

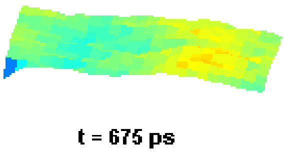

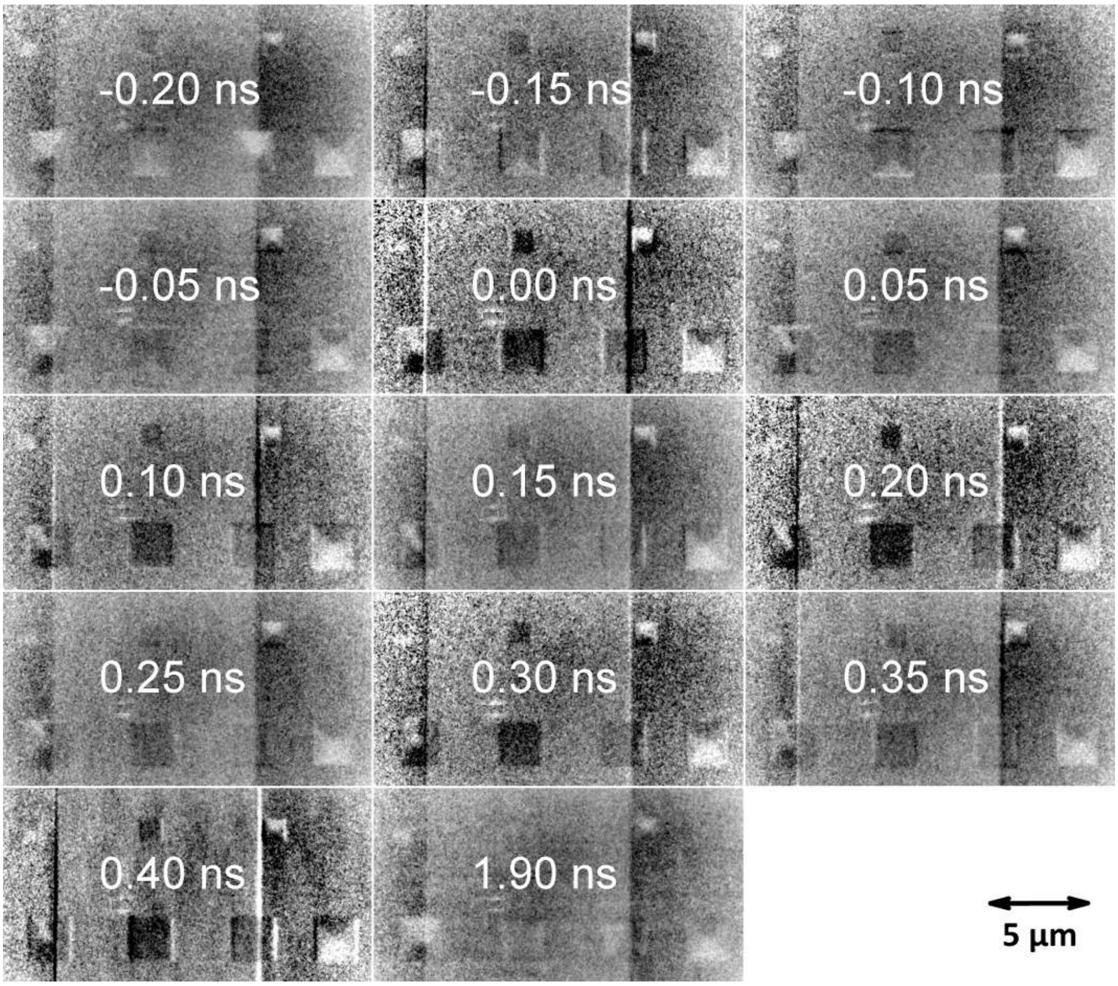

Figure C.13: Fine delay scan with low-jitter pulse generator of domain pattern recovery in permalloy elements excited by the magnetic field of a current pulse which aligns the magnetization of the elements in overlap with the waveguide along the x direction.

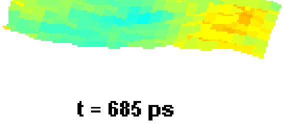

t = 685 ps

Appendix D

Simulation code

D.1 Landau-Lifshitz-Gilbert solver

MATLAB code used in chapter 3 to solve the Landau-Lifshitz-Gilbert equation numerically on discrete time intervals.

```
%% Landau-Lifshitz-Gilbert solver for thin film slabs
% This program solves the Landau-Lifshitz-Gilbert (LLG) equation
% for discrete time intervals dt and computes
% the time evolution of the magnetization vector _M(t)_
% for an arbitrary magnetic field pulse _h(t)_.
%
% All computations are carried out in SI units.

%% Constants
% Physical constants used in the calculation
c      = 299792458;       % Speed of light
e      = 1.602176487e-19; % Elementary charge
me     = 9.10938215e-31;  % Mass of the electron
h      = 6.62606896e-34;  % Planck’s constant
hbar   = h/(2*pi);
mu0    = 4*pi*1e-7;       % Vacuum permeability
eps0   = 1/(mu0*c^2);     % Dielectric constant
g      = 2.0023193048;    % Lande factor of an electron
gamma0 = g*e/(2*me);      % Gyromagnetic ratio

%% Simulation parameters
ti       = -0.300e-9;  % Start time
dt       = 50.000e-15; % Time step
simtime  =  1.500e-9;  % Total simulation time

%% Material parameters
% Here: Permalloy (Ni80Fe20)
A     = 13.0e-12;   % Exchange stiffness constant
Ms    =  1.040/mu0; % Saturation magnetization
alpha =  0.008;     % Damping constant
```

```
%% Experiment parameters
% Field properties and slab geometry
Hext     =   60.0e-3/mu0; % External DC bias field
h0       =   15.0e-3/mu0; % Pulsed field amplitude
tau      =    3.0e-12;    % Pulse duration
t0       =    0.0e-12;    % Pulse offset
w        =   10.0e-6;     % Slab width
T        =   30.0e-9;     % Slab thickness

%% Functions and constants used in the simulation

% Effective slab width weff
d     = @(w) 2*pi/(T/w * (1 - 2*log(T/w)));
weff  = w * d(w)/(d(w) - 2);

% External pulsed field
hx = @(t) h0*exp(-(t - t0)^2/(2*tau^2));
hz = @(t) -1/4*hx(t);

% Demagnetization tensor
N  = zeros(3,3);
Ny = 1/pi * (atan(T/weff) - atan(-T/weff));
N(1,1) = 0; N(2,2) = Ny; N(3,3) = 1 - Ny;

%% Simulation
% Do the actual work and discretely solve the LLGE

% Preallocate memory for simulation vectors
clear time; clear M; clear H; clear Heff;
n     = simtime/dt;              % Number of iterations
time  = zeros(1, n,   ’double’); % Time vector
M     = zeros([3, n], ’double’); % Magnetization vector
H     = zeros([3, n], ’double’); % External field (DC and pulsed)
Heff  = zeros([3, n], ’double’); % Effective field (H - Hdemag)

% Set initial condition
time(1)     = ti;
M(:,1)      = [0;             Ms;   0];
H(:,1)      = [hx(time(1));   Hext; hz(time(1))];
Heff(:,1)   = H(:,1) - N*M(:,1);

% Loop over simulation time in intervals of _dt_
% and carry out LLG computation.
for i = 2:1:n
    % Fill time vector
    time(i) = ti + i*dt;
```

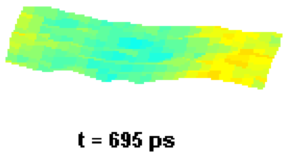

```
    % Calculate change of magnetization vector _dM_ according to
    % LLGE (dM/dt) on time interval _dt_
    dM = (-gamma0*mu0/(1 + alpha^2) * cross(M(:,i-1), Heff(:,i-1)) ...
        - alpha*gamma0*mu0/(norm(M(:,i-1))*(1 + alpha^2)) ...
        * cross(M(:,i-1), cross(M(:,i-1), Heff(:,i-1)))) * dt;
    M(:,i) = M(:,i-1) + dM;

    % Calculate evolution of H fields
    H(:,i) = [hx(time(i)); Hext; hz(time(i))];
    Heff(:,i) = H(:,i) - N*M(:,i);
end

% Rescale magnetization in units of saturation magnetization _Ms_
mx = M(1,:)/Ms;
my = M(2,:)/Ms;
mz = M(3,:)/Ms;

%% Display results

% Plot the magnetization and field pulse
p = plot(time*1e12, mz, '-', time*1e12, H(1,:)/h0*max(mz), '--');
leg = legend('Magnetization M_z(t)', 'Pulsed magn. field h_x(t)');

% Format the plot
set(p, 'LineWidth', 2)
set(gca, 'FontName', 'Calibri');
set(gca, 'FontSize', 30);
set(gca, 'FontWeight', 'bold');
set(gca, 'XDir', 'normal');
set(gca, 'YDir', 'normal');
set(gca, 'PlotBoxAspectRatio', [4 3 1]);
xlim([-300, 1200]);
ylim([-0.025, 0.025]);
xlabel('Time t [ps]');
ylabel('M_z [M_s]');
```

D.2 Nmag simulation

Example of Python code using the micromagnetic simulation package Nmag solving the response of a Landau flux closure structure in a 2 µm × 2 µm sized permalloy square. The results are presented in chapter 3.

```
import nmag
import math
from nmag import SI, every, at
from nmag.common import *

# Define SI unit abbreviations
ps = SI(1e-12, "s") # corresponds to one picosecond
ns = SI(1e-9,  "s") # corresponds to one nanosecond

# Define spatial rectangular pulse function
def rect(x):
    if abs(x) < 0.5:
        return 1.0
    elif abs(x) == 0.5:
        return 0.5
    elif abs(x) > 0.5:
        return 0.0

# Define Landau magnetization pattern
def landau((x, y, z)):
    x = x -  1e-6
    y = y -  1e-6
    z = z - 15e-9

    if y >= x and y >= -x and y <= 1e-6:
        mag = (1, 0, 0)
    elif y <= x and y >= -x and x <= 1e-6:
        mag = (0, -1, 0)
    elif y <= x and y <= -x and y >= -1e-6:
        mag = (-1, 0, 0)
    elif y >= x and y <= -x and x >= -1e-6:
        mag = (0, 1, 0)
    else:
        mag = (1, 1, 1)

    # return magnetisation vector for position (x, y, z)
    return mag

# Create simulation objects
simHD = nmag.Simulation("py_quadratHD")
sim   = nmag.Simulation("py_quadrat")
```

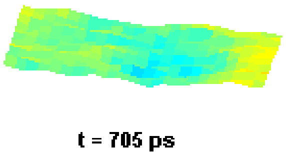

```
# Define magnetic material (permalloy) with high and low damping
PyHD = nmag.MagMaterial(name="PyHD",
                        Ms=SI(800.0e3, "A/m"),
                        exchange_coupling=SI(13.0e-12, "J/m"),
                        llg_damping=0.5)

Py = nmag.MagMaterial(name="Py",
                      Ms=SI(800.0e3, "A/m"),
                      exchange_coupling=SI(13.0e-12, "J/m"),
                      llg_damping=0.01)

# Load mesh with permalloy rectangles (high damping)
simHD.load_mesh("py_quadrat.nmesh.h5", [("quadrat", PyHD)],
                unit_length=SI(5e-9, "m"))

# Set initial magnetization pattern (Landau)
simHD.set_m(landau)

# Set magnetic field of the earth at the beamline
Hx = 14.0
Hy = 26.0
Hz = -15.0
simHD.set_H_ext([Hx, Hy, Hz], SI(1, "A/m"))

# Relax the system to initial state
simHD.relax(save = [('averages', every('time', 500*ps)),
                    ('fields',   every('time', 1*ns)  )])

# Extract the equilibrium magnetization pattern
# from the damped simulation object
myM = simHD.get_subfield("m_PyHD")

# Load mesh with permalloy rectangles (low damping)
sim.load_mesh("py_quadrat.nmesh.h5", [("quadrat", Py)],
              unit_length=SI(5e-9, "m"))
sim.set_m(myM) # Set the previously extracted pattern
sim.set_H_ext([Hx, Hy, Hz], SI(1, "A/m")) # Set external field
sim.relax(save = [('averages', every('time', 500*ps)),
                  ('fields',   every('time', 1*ns)  )])

# Rectangular transient external magnetic field pulse
t0 = [sim.time]
def set_H(sim):
    t = float((sim.time - t0[0])/ns) # get time in ns
    width_x = 2000.0 # nm
    width_y = 2000.0 # nm
    width_z = 30.0   # nm
```

```
    tau = 0.210      # ns
    H_amplitude = 7e4 * math.exp(-(t - 4*tau)**2/(2*tau**2)) # A/m
    print "Time [ns]:", t
    print "Pulsed field [A/m]:", H_amplitude
    def H(r):
        x, y, z = [i/1e-9 for i in r]
        factor = H_amplitude \
            * rect((x - width_x/2)/width_x) \
            * rect((y - width_y/2)/width_y) \
            * rect((z - width_z/2)/width_z)
        return [Hx + factor, Hy, Hz]

    sim.set_H_ext(H, unit=SI("A/m"))

set_H(sim)

# Do not stop automatically
sim.set_params(stopping_dm_dt=0*degrees_per_ns)

# Relax the system
sim.relax(save = [('averages', every('time', 50*ps)),
                  ('fields', every('time', 100*ps, first=t0[0]))],
            do = [(set_H, every('time', 10*ps, first=t0[0])),
                  ('exit', at('time', 20*ns))])
```

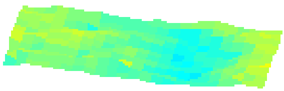

Appendix E

Circuits

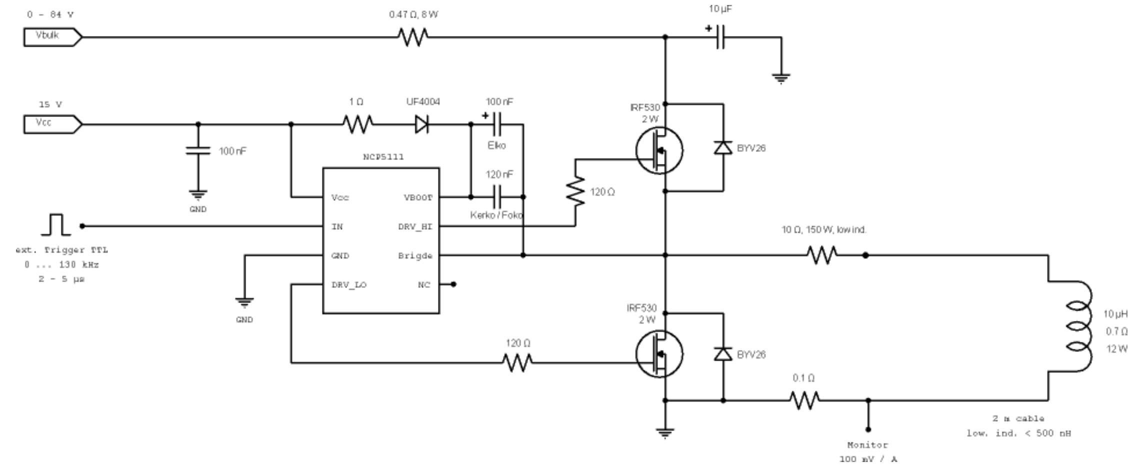

Figure E.1: Circuit diagram of the custom-built coil driver.

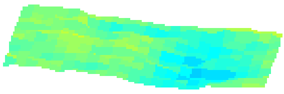

t = 725 ps

Appendix F

List of publications

- Ph. Wessels, J. Ewald, M. Wieland, T. Nisius, G. Abbati, S. Baumbach, J. Overbuschmann, A. Vogel, A. Neumann, J. Viefhaus, H. P. Oepen, G. Meier, T. Wilhein, and M. Drescher, *Time-resolved soft X-ray microscopy of magnetic nanostructures at the P04 beamline at PETRA III*, J. Phys.: Conf. Ser. **499**, 012009 (2014) [214].
- Ph. Wessels, M. Schlie, M. Wieland, J. Ewald, G. Abbati, S. Baumbach, J. Overbuschmann, T. Nisius, A. Vogel, A. Neumann, A. Meents, J. Viefhaus, H. P. Oepen, G. Meier, T. Wilhein, and M. Drescher, *XMCD microscopy with synchronized soft X-ray and laser pulses at PETRA III for time-resolved studies*, J. Phys.: Conf. Ser. **463**, 012023 (2013) [215].
- S. Yu, G. Santoro, K. Sarkar, B. Dicke, Ph. Wessels, S. Bommel, R. Döhrmann, J. Perlich, M. Kuhlmann, E. Metwalli, J. F. H. Risch, M. Schwartzkopf, M. Drescher, P. Müller-Buschbaum, and S. V. Roth, *Formation of Al Nanostructures on Alq3: An in Situ Grazing Incidence Small Angle X-ray Scattering Study during Radio Frequency Sputter Deposition*, J. Phys. Chem. Lett. **4**, 3170 (2013) [220].
- M. Krikunova, Th. Maltezopoulos, Ph. Wessels, M. Schlie, A. Azima, T. Gaumnitz, T. Gebert, M. Wieland, and M. Drescher, *Strong-field ionization of molecular iodine traced with XUV pulses from a free-electron laser*, Phys. Rev. A **86**, 043430 (2012) [121].
- M. Krikunova, Th. Maltezopoulos, Ph. Wessels, M. Schlie, A. Azima, M. Wieland, and M. Drescher, *Ultrafast photofragmentation dynamics of molecular iodine driven with timed XUV and near-infrared light pulses*, J. Chem. Phys. **134**, 024313 (2011) [122].

F.1 Conference contributions

- Ph. Wessels, J. Ewald, M. Wieland, T. Nisius, G. Abbati, S. Baumbach, J. Viefhaus, T. Wilhein, and M. Drescher, *Time-resolved soft X-ray microscopy of magnetic nanostructures at the P04 beamline at PETRA III*, DESY Photon Science Users' Meeting, January 2014, Hamburg, Germany.

- Ph. Wessels, J. Ewald, M. Wieland, T. Nisius, G. Abbati, S. Baumbach, J. Viefhaus, T. Wilhein, and M. Drescher, *Time-resolved soft X-ray microscopy of magnetic nanostructures at the P04 beamline at PETRA III*, 22nd International Congress on X-Ray Optics and Microanalysis (**ICXOM22**), September 2013, Hamburg, Germany.

- Ph. Wessels, M. Schlie, M. Wieland, J. Ewald, G. Abbati, S. Baumbach, J. Overbuschmann, T. Nisius, J. Viefhaus, T. Wilhein, and M. Drescher, *Setup for time-resolved soft X-ray microscopy studies of magnetic nanostructures at PETRA III*, DPG-Frühjahrstagung der Sektion Kondensierte Materie (**DPG SKM 2013**), March 2013, Regensburg, Germany.

- Ph. Wessels, M. Schlie, M. Wieland, J. Ewald, G. Abbati, S. Baumbach, J. Overbuschmann, T. Nisius, J. Viefhaus, T. Wilhein, and M. Drescher, *Setup for time-resolved soft X-ray microscopy studies of magnetic nanostructures at PETRA III*, DESY Photon Science Users' Meeting, January 2013, Hamburg, Germany.

- Ph. Wessels, M. Schlie, M. Wieland, J. Ewald, G. Abbati, S. Baumbach, J. Overbuschmann, T. Nisius, T. Wilhein, and M. Drescher, *XMCD microscopy with synchronized soft X-ray and laser pulses at PETRA III for time-resolved studies*, 11th International Conference on X-Ray Microscopy (**XRM2012**), August 2012, Shanghai, China.

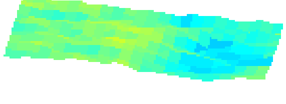

Appendix G

Declaration on oath

I hereby declare, on oath, that I have written the present dissertation by my own and have not used other than the acknowledged resources and aids.

Hamburg, 21st January 2014

\- Philipp K. G. Wessels -

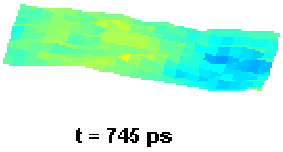
t = 745 ps

Appendix H

Acknowledgments

First, I want to thank Prof. Dr. Markus Drescher for the ability and confidence to carry out this fascinating project in his group and for providing competent supervision of the work including the possibility to approach him with questions and problems to receive expedient solution proposals. I am grateful to the whole *DynamiX* group for providing a convenient working environment and I want to emphasize the effort of Dr. Marek Wieland for always offering a sympathetic ear and a lot of time to discuss all kinds of problems occurring in the daily laboratory routine, for providing manpower during never-ending beamtime shifts and for reading the manuscript. The mobile, synchronized laser system was set up by Dr. Moritz Schlie and I thank him for transferring all the knowledge and dodges to be able to operate it. When it comes to technical issues, I want to acknowledge the great support consistently provided by Oliver Becker, even on short notice.

Additionally, I am very grateful to Prof. Dr. Thomas Wilhein for agreeing to evaluate this work as second referee, for all the encouragement along the way and for the outstanding support offered by his group. Especially, without the everlasting work of Johannes Ewald and Thomas Nisius regarding the vacuum system, piezo-motorization and laser-safety requirements, the shifts at the synchrotron would have been impossible. I strongly acknowledge the commitment of Johannes and Thomas as well as Gennaro Abbati, Stefan Baumbach and Johannes Overbuschmann to spend many days and nights together with PETRA.

Without the kind support I experienced from PD Dr. habil. Guido Meier, who also willingly agreed to examine the dissertation as a referee, and his group the creation of nanostructured samples would have been impossible. I am really grateful for providing uncomplicated access to the clean room and SEM facilities of the University of Hamburg and the confidence to supply all the necessary equipment. Notable is the generous engagement of Dr. Andreas Vogel who trained me in the work with all clean room devices and was a great help during SEM operation. Furthermore, I also like to thank Dr. Toru Matsuyama and Andrea Köppen for assistance concerning the mask aligner and the evaporation system.

I also like to express my gratitude to Prof. Dr. Hermann Dürr for the evaluation of this thesis as an additional referee.

I appreciate the cooperation with Prof. Dr. Hans Peter Oepen and Alexander Neumann for fabrication and characterization (SEM images and hysteresis measurements on a calibrated MOKE setup) of individual Co/Pt structures and nanodots. Furthermore, I would like to thank Jan-Niklas Tödt for his enthusiasm and expertise when discussing my spin-wave data and Dr. Sebastian Mansfeld for knowledge transfer concerning waveguide fabrication and SKM design.

During the beamtime shifts the lively interest and great flexibility of the whole P04 beamline crew was of key importance. I like to emphasize the outstanding support of Dr. Jens Viefhaus, Dr. Leif Glaser, Frank Scholz and Jörn Seltmann as well as the operators of PETRA III for providing a stable and brilliant source of soft X-ray radiation.

I want to offer many thanks to Dr. Pambos Charalambous (ZonePlates.com) for manufacturing of the zone plates and grating condenser and his continuing interest in this work.

Moreover, I acknowledge all the technical support provided by the University of Hamburg and DESY starting with the excellent work done in the mechanical workshop headed by Stephan Fleig and Frank Jonas who were able to find inspiring solutions when CAD design meets reality especially in the planning phase of the TXM and SKM mechanics. The same counts for the electrical workshop headed by Armin Spikofsky when assembling the custom power supply for the gateable X-ray detector. Additionally, I want to thank Manfred Spiewek for cutting the sapphire wafers into handy substrate pieces and Reinhard Mielck for technical support in the TR-SKM laboratory located in the Centre for Optical Quantum Technologies (ZOQ).

I gratefully thank the DFG Collaborative Research Centre 668 (SFB 668 - Magnetismus vom Einzelatom zur Nanostruktur) for financial support within the subproject B5 as well as the German Federal Ministry of Education and Research (BMBF - Bundesministerium für Bildung und Forschung) for financial support within the Nanofocus projects (05KS7GU4 and 05KS7UL1).

Lastly, I thank Federal Chancellor Dr. Angela Merkel, Frist Mayor of Hamburg Olaf Scholz and Nobel laureate Prof. Dr. Ada Yonath for signing the PHAROS laser system along with a visit of the PETRA III facility as well as Christina Staarmann for reading the manuscript and for all the encouragement. I want to thank my parents Kurt Wessels and Edith Wessels for all the support throughout the years.

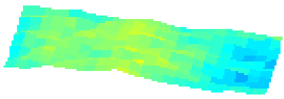

List of Figures

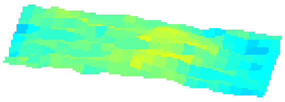
t = 765 ps

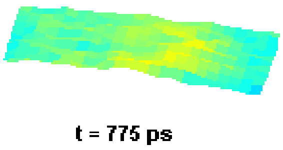
t = 775 ps

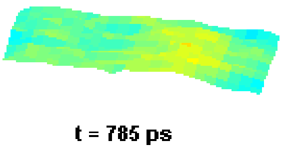
t = 785 ps

List of Tables

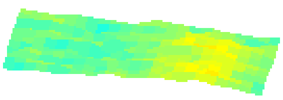

t = 795 ps

Bibliography

[1] G. Abbati, C. Seim, H. Legall, H. Stiel, N. Thomas, and T. Wilhein, *Preparation of clay mineral samples for high resolution x-ray imaging*, J. Phys.: Conf. Ser. **463**, 012051 (2013).

[2] D. W. Abraham and Y. Lu, *Observation of switching of magnetic particle arrays with weak dipole interaction field effects*, J. Appl. Phys. **98**, 023902 (2005).

[3] K. Akiyama and A. Onoda, *Image Intensifier V8070U-74-G160 Final Test Sheet*, Hamamatsu Photonics K.K., Electron Tube Division, 314-5, Shimokanzo, Iwata City, Shizuoka Pref., 438-0193, Japan, Dec 2012.

[4] R. C. Alig, S. Bloom, and C. W. Struck, *Scattering by ionization and phonon emission in semiconductors*, Phys. Rev. B **22**, 5565 (1980).

[5] D. A. Allwood, G. Xiong, M. D. Cooke, C. C. Faulkner, D. Atkinson, N. Vernier, and R. P. Cowburn, *Submicrometer Ferromagnetic NOT Gate and Shift Register*, Science **296**, 2003 (2002).

[6] Andor Technology, *iKon-M 934 [DO] Data Sheet*, Andor Technology, 7 Millennium Way, Springvale Business Park, Belfast BT12 7AL, UK, Aug 2008.

[7] ——, *CCD Signal to Noise Ratio.* andor.com/learning-academy/ccd-signal-to-noise-ratio-calculating-the-snr-of-a-ccd, Jan 2014.

[8] ——, *Direct Detection.* andor.com/learning-academy/direct-detection-understand-direct-detection-ccds, Jan 2014.

[9] Andor Technology and LOT-QuantumDesign, *X-Ray CCD Detectors - Course Notes.* lot-qd.de/files/downloads/andor/en/cc_notesxray_deen.pdf, Sep 2002.

[10] M. Arruebo, R. Fernández-Pacheco, M. R. Ibarra, and J. Santamaría, *Magnetic nanoparticles for drug delivery*, Nano Today **2**, 22 (2007).

[11] A. Baciero, K. J. McCarthy, M. A. Acedo, L. Rodriguez-Barquero, J. Avila, Y. Huttel, V. Perez Dieste, M. C. Asensio, and B. Zurro, *A study of the response of $Y_3Al_5O_12$:Ce phosphor powder screens in the vacuum ultraviolet and soft X-ray regions using synchrotron radiation*, J. Synchrotron Rad. **7**, 215 (2000).

[12] C. H. Back and D. Pescia, *Applied physics: Speed limit ahead*, Nature **428**, 808 (2004).

[13] M. Battiato, K. Carva, and P. M. Oppeneer, *Superdiffusive Spin Transport as a Mechanism of Ultrafast Demagnetization*, Phys. Rev. Lett. **105**, 027203 (2010).

[14] C. Bayer, J. Jorzick, B. Hillebrands, S. O. Demokritov, R. Kouba, R. Bozinoski, A. N. Slavin, K. Y. Guslienko, D. V. Berkov, N. L. Gorn, and M. P. Kostylev, *Spin-wave excitations in finite rectangular elements of* $Ni_{80}Fe_{20}$, Phys. Rev. B **72**, 064427 (2005).

[15] E. Beaurepaire, J.-C. Merle, A. Daunois, and J.-Y. Bigot, *Ultrafast Spin Dynamics in Ferromagnetic Nickel*, Phys. Rev. Lett. **76**, 4250 (1996). Figure 2.1 contains material from this article reprinted with kind permission from Eric Beaurepaire and Jean-Yves Bigot. Copyright ©1996 by the American Physical Society. Online abstract: link.aps.org/abstract/PRL/v76/p4250.

[16] E. Benevent, B. Viala, and J.-P. Michel, *Analytical Modeling of Multilayered Coplanar Waveguides Including Ferromagnetic Thin Films on Semiconductor Substrates*, IEEE T. Microw. Theory **58**, 645 (2010).

[17] C. C. Berry and A. S. G. Curtis, *Functionalisation of magnetic nanoparticles for applications in biomedicine*, J. Phys. D: Appl. Phys. **36**, R198 (2003).

[18] J.-Y. Bigot and M. Vomir, *Ultrafast magnetization dynamics of nanostructures*, Ann. Phys. (Berlin) **525**, 2 (2013).

[19] J.-Y. Bigot, M. Vomir, and E. Beaurepaire, *Coherent ultrafast magnetism induced by femtosecond laser pulses*, Nat. Phys. **5**, 515 (2009).

[20] R. P. Boardman, *Computer simulation studies of magnetic nanostructures*, PhD thesis, University of Southampton, School of Engineering Sciences, May 2005. Figure 2.1 contains material from this thesis reprinted with kind permission from Richard Boardman.

[21] L. Bocklage, B. Krüger, R. Eiselt, M. Bolte, P. Fischer, and G. Meier, *Time-resolved imaging of current-induced domain-wall oscillations*, Phys. Rev. B **78**, 180405 (2008).

[22] C. Bowick, J. Blyler, and C. Ajluni, *RF Circuit Design*, Newnes / Elsevier, 30 Corporate Drive, Suite 400, Burlington, MA 01803, USA, second ed., (2008).

[23] C. Brazel, *Magnetothermally-responsive Nanomaterials: Combining Magnetic Nanostructures and Thermally-Sensitive Polymers for Triggered Drug Release*, Pharm. Res. **26**, 644 (2009).

[24] L. Brundle and N. Freedman, *Magnetostatic surface waves on a y.i.g. slab*, Electron. Lett. **4**, 132 (1968).

[25] E. Carlsson and S. Gevorgian, *Conformal mapping of the field and charge distributions in multilayered substrate CPWs*, IEEE T. Microw. Theory **47**, 1544 (1999).

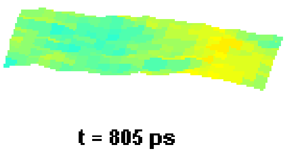

[26] W. Chao, B. D. Harteneck, J. A. Liddle, E. H. Anderson, and D. T. Attwood, *Soft X-ray microscopy at a spatial resolution better than 15 nm*, Nature **435**, 1210 (2005).

[27] C. Chappert, A. Fert, and F. N. Van Dau, *The emergence of spin electronics in data storage*, Nat. Mater. **6**, 813 (2007).

[28] P. Charalambous, *ZonePlates Ltd. website.* www.zoneplates.com, Sep 2013. Images in Figure 5.10a by courtesy of Pambos Charalambous.

[29] C. T. Chen, Y. U. Idzerda, H.-J. Lin, N. V. Smith, G. Meigs, E. Chaban, G. H. Ho, E. Pellegrin, and F. Sette, *Experimental Confirmation of the X-Ray Magnetic Circular Dichroism Sum Rules for Iron and Cobalt*, Phys. Rev. Lett. **75**, 152 (1995).

[30] C. T. Chen, N. V. Smith, and F. Sette, *Exchange, spin-orbit, and correlation effects in the soft-x-ray magnetic-circular-dichroism spectrum of nickel*, Phys. Rev. B **43**, 6785 (1991).

[31] E. Chen and S. Chou, *Characteristics of coplanar transmission lines on multilayer substrates: modeling and experiments*, IEEE T. Microw. Theory **45**, 939 (1997).

[32] C. D. Child, *Discharge From Hot CaO*, Phys. Rev. (Series I) **32**, 492 (1911).

[33] M. H. Cho, E. J. Lee, M. Son, J.-H. Lee, D. Yoo, J.-w. Kim, S. W. Park, J.-S. Shin, and J. Cheon, *A magnetic switch for the control of cell death signalling in in vitro and in vivo systems*, Nat. Mater. **11**, 1038 (2012).

[34] S.-B. Choe, Y. Acremann, A. Scholl, A. Bauer, A. Doran, J. Stöhr, and H. A. Padmore, *Vortex Core-Driven Magnetization Dynamics*, Science **304**, 420 (2004).

[35] Y. T. Chong, D. Görlitz, S. Martens, M. Y. E. Yau, S. Allende, J. Bachmann, and K. Nielsch, *Multilayered Core/Shell Nanowires Displaying Two Distinct Magnetic Switching Events*, Adv. Mater. **22**, 2435 (2010).

[36] R. Cowburn, *Magnetic nanodots for device applications*, J. Magn. Magn. Mater. **242 - 245, Part 1**, 505 (2002). Proceedings of the Joint European Magnetic Symposia (JEMS 01).

[37] R. P. Cowburn and M. E. Welland, *Room Temperature Magnetic Quantum Cellular Automata*, Science **287**, 1466 (2000).

[38] M. Creixell, A. C. Bohórquez, M. Torres-Lugo, and C. Rinaldi, *EGFR-Targeted Magnetic Nanoparticle Heaters Kill Cancer Cells without a Perceptible Temperature Rise*, ACS Nano **5**, 7124 (2011).

[39] R. Damon and J. Eshbach, *Magnetostatic modes of a ferromagnet slab*, J. Phys. Chem. Solids **19**, 308 (1961).

[40] R. R. de Castro, D. Wang, X. Zheng, A. Verevkin, R. Sobolewski, M. Mikulics, R. Adam, P. Kordoš, and A. Mycielski, *Subpicosecond Faraday effect in $Cd_{1-x}Mn_xTe$ and its application in magneto-optical sampling*, Appl. Phys. Lett. **85**, 3806 (2004).

[41] S. Demokritov, B. Hillebrands, and A. Slavin, *Brillouin light scattering studies of confined spin waves: linear and nonlinear confinement*, Phys. Rep. **348**, 441 (2001).

[42] S. O. Demokritov, V. E. Demidov, O. Dzyapko, G. A. Melkov, A. A. Serga, B. Hillebrands, and A. N. Slavin, *Bose-Einstein condensation of quasi-equilibrium magnons at room temperature under pumping*, Nature **443**, 430 (2006).

[43] S. O. Demokritov, A. A. Serga, A. André, V. E. Demidov, M. P. Kostylev, B. Hillebrands, and A. N. Slavin, *Tunneling of Dipolar Spin Waves through a Region of Inhomogeneous Magnetic Field*, Phys. Rev. Lett. **93**, 047201 (2004).

[44] W. Demtröder, *Experimentalphysik 2*, Springer, Berlin / Heidelberg / New York, third ed., (2004).

[45] Deutsches Elektronen-Synchrotron DESY, *P04 Beamline at DESY photon science website.* photon-science.desy.de, Sep 2013.

[46] P. A. M. Dirac, *The Quantum Theory of the Emission and Absorption of Radiation*, Proc. R. Soc. A **114**, 243 (1927).

[47] J. Dobson, *Magnetic nanoparticles for drug delivery*, Drug Dev. Res. **67**, 55 (2006).

[48] ——, *Remote control of cellular behaviour with magnetic nanoparticles*, Nat. Nanotechnol. **3**, 139 (2008).

[49] ——, *Cancer therapy: Death by magnetism*, Nat. Mater. **11**, 1006 (2012).

[50] M. Donahue and D. Porter, *OOMMF User's Guide, Version 1.0*, National Institute of Standards and Technology, Gaithersburg, MD, Sep 1999. Interagency Report NISTIR 6376.

[51] A. Einstein, *Über einen die Erzeugung und Verwandlung des Lichtes betreffenden heuristischen Gesichtspunkt*, Ann. Phys. (Berlin) **322**, 132 (1905).

[52] A. Einstein, *Zur Elektrodynamik bewegter Körper*, Ann. Phys. (Berlin) **322**, 891 (1905).

[53] S. Eisebitt, J. Lüning, W. F. Schlotter, M. Lörgen, O. Hellwig, W. Eberhardt, and J. Stöhr, *Lensless imaging of magnetic nanostructures by X-ray spectro-holography*, Nature **432**, 885 (2004).

[54] A. Y. Elezzabi and M. R. Freeman, *Ultrafast magneto-optic sampling of picosecond current pulses*, Appl. Phys. Lett. **68**, 3546 (1996).

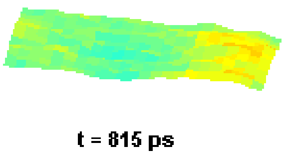

[55] J. Falta and T. Möller, eds., *Forschung mit Synchrotronstrahlung*, Vieweg+Teubner, Wiesbaden, first ed., (2010).

[56] H. Fangohr, T. Fischbacher, M. Franchin, G. Bordignon, J. Generowicz, A. Knittel, M. Walter, and M. Albert, *NMAG User Manual Documentation, Release 0.2.1*, University of Southampton, Highfield, Southampton SO17 1BJ, United Kingdom, Jan 2012.

[57] U. Fano, *Ionization Yield of Radiations. II. The Fluctuations of the Number of Ions*, Phys. Rev. **72**, 26 (1947).

[58] ——, *Spin Orientation of Photoelectrons Ejected by Circularly Polarized Light*, Phys. Rev. **178**, 131 (1969).

[59] ——, *Spin Orientation of Photoelectrons: Erratum and Addendum*, Phys. Rev. **184**, 250 (1969).

[60] E. Fermi, *Nuclear Physics: A Course Given by Enrico Fermi at the University of Chicago*, The University of Chicago Press, Chicago, London, (1949).

[61] T. Fischbacher, M. Franchin, G. Bordignon, and H. Fangohr, *A Systematic Approach to Multiphysics Extensions of Finite-Element-Based Micromagnetic Simulations: Nmag*, IEEE T. Magn. **43**, 2896 (2007).

[62] P. Fischer, *Exploring nanoscale magnetism in advanced materials with polarized X-rays*, Mater. Sci. Eng. R Rep. **72**, 81 (2011).

[63] P. Fischer, T. Eimüller, G. Schütz, G. Bayreuther, S. Tsunashima, N. Takagi, G. Denbeaux, and D. Attwood, *Magnetic domains in nanostructured media studied with M-TXM*, J. Synchrotron Rad. **8**, 325 (2001).

[64] P. Fischer, G. Schütz, G. Schmahl, P. Guttmann, and D. Raasch, *Imaging of magnetic domains with the X-ray microscope at BESSY using X-ray magnetic circular dichroism*, Z. Phys. B **101**, 313 (1996).

[65] M. Frankel, S. Gupta, J. Valdmanis, and G. Mourou, *Terahertz attenuation and dispersion characteristics of coplanar transmission lines*, IEEE T. Microw. Theory **39**, 910 (1991).

[66] M. R. Freeman, W. K. Hiebert, and A. Stankiewicz, *Time-resolved scanning Kerr microscopy of ferromagnetic structures (invited)*, J. Appl. Phys. **83**, 6217 (1998).

[67] M. Freiser, *A survey of magnetooptic effects*, IEEE T. Magn. **4**, 152 (1968).

[68] A.-J. Fresnel, *Mémoire sur la diffraction de la lumière*, Annales de la Chemie et de Physique **1**, 239 (1816).

[69] ——, *Mémoire sur la diffraction de la lumière*, Mémoires de l'Académie des Sciences **5**, 33 (1826).

[70] S. Gevorgian, T. Martinsson, A. Deleniv, E. Kollberg, and I. Vendik, *Simple and accurate dispersion expression for the effective dielectric constant of coplanar waveguides*, IEE Proc. Microw. Antennas Propag. **144**, 145 (1997).

[71] G. Ghione, *A CAD-oriented analytical model for the losses of general asymmetric coplanar lines in hybrid and monolithic MICs*, IEEE T. Microw. Theory **41**, 1499 (1993).

[72] G. E. Giakoumakis and D. M. Miliotis, *Light angular distribution of fluorescent screens excited by x-rays*, Phys. Med. Biol. **30**, 21 (1985).

[73] T. Gilbert, *A Lagrangian formulation of the gyromagnetic equation of the magnetic field*, Phys. Rev. **100**, 1243 (1955).

[74] ——, *A phenomenological theory of damping in ferromagnetic materials*, IEEE T. Magn. **40**, 3443 (2004).

[75] J. W. Goodman, *Introduction to Fourier Optics*, Roberts & Company, 4950 S. Yosemite Street, F2 #197, Greenwood Viallge, CO 80111, third ed., (2005).

[76] W. Graves, L. DiMauro, R. Heese, E. Johnson, J. Rose, J. Rudati, T. Shaftan, and B. Sheehy, *Measurement of thermal emittance for a copper photocathode*, Proceedings of the 2001 Particle Accelerator Conference (PAC 2001) **3**, 2227 (2001).

[77] D. J. Griffiths, *Introduction to Electrodynamics*, Pearson Benjamin Cummings, 1301 Sansome St., San Francisco, CA 94111, third ed., (2008).

[78] C. M. Günther, B. Pfau, R. Mitzner, B. Siemer, S. Roling, H. Zacharias, O. Kutz, I. Rudolph, D. Schondelmaier, R. Treusch, and S. Eisebitt, *Sequential femtosecond X-ray imaging*, Nat. Photon. **5**, 99 (2011).

[79] K. Y. Guslienko, R. W. Chantrell, and A. N. Slavin, *Dipolar localization of quantized spin-wave modes in thin rectangular magnetic elements*, Phys. Rev. B **68**, 024422 (2003).

[80] K. Y. Guslienko, S. O. Demokritov, B. Hillebrands, and A. N. Slavin, *Effective dipolar boundary conditions for dynamic magnetization in thin magnetic stripes*, Phys. Rev. B **66**, 132402 (2002).

[81] K. Y. Guslienko, X. F. Han, D. J. Keavney, R. Divan, and S. D. Bader, *Magnetic Vortex Core Dynamics in Cylindrical Ferromagnetic Dots*, Phys. Rev. Lett. **96**, 067205 (2006).

[82] K. Y. Guslienko, B. A. Ivanov, V. Novosad, Y. Otani, H. Shima, and K. Fukamichi, *Eigenfrequencies of vortex state excitations in magnetic submicron-size disks*, J. Appl. Phys. **91**, 8037 (2002).

[83] K. Y. Guslienko, K.-S. Lee, and S.-K. Kim, *Dynamic Origin of Vortex Core Switching in Soft Magnetic Nanodots*, Phys. Rev. Lett. **100**, 027203 (2008).

[84] M. Hayashi, L. Thomas, R. Moriya, C. Rettner, and S. S. P. Parkin, *Current-Controlled Magnetic Domain-Wall Nanowire Shift Register*, Science **320**, 209 (2008).

[85] E. Hecht, *Optics*, Addison Wesley, 1301 Sansome St., San Francisco, CA 94111, fourth ed., (2002).

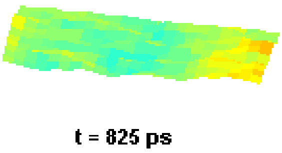

[86] W. Heisenberg, *Über den anschaulichen Inhalt der quantentheoretischen Kinematik und Mechanik*, Z. Phys. A **43**, 172 (1927).

[87] B. Henke, E. Gullikson, and J. Davis, *X-Ray Interactions: Photoabsorption, Scattering, Transmission, and Reflection at E = 50-30,000 eV, Z = 1-92*, At. Data Nucl. Data Tables **54**, 181 (1993).

[88] R. Hertel, W. Wulfhekel, and J. Kirschner, *Domain-Wall Induced Phase Shifts in Spin Waves*, Phys. Rev. Lett. **93**, 257202 (2004).

[89] B. Hillebrands and K. Ounadjela, eds., *Spin Dynamics in Confined Magnetic Structures II*, Springer, Berlin / Heidelberg / New York, first ed., (2003).

[90] ——, *Spin Dynamics in Confined Magnetic Structures III*, Springer, Berlin / Heidelberg / New York, first ed., (2006).

[91] M. Hornig, *Production and characterisation of ZnO:Ga and Gd_2O_2S:Tb phosphor screens*, bachelor thesis, University of Hamburg, (2012).

[92] H. Huang, S. Delikanli, H. Zeng, D. M. Ferkey, and A. Pralle, *Remote control of ion channels and neurons through magnetic-field heating of nanoparticles*, Nat. Nanotechnol. **5**, 602 (2010).

[93] C. Huygens, *Traité de la lumière*, Pieter van der Aa, Leiden, Netherlands, (1690).

[94] S. Ingvarsson, L. Ritchie, X. Y. Liu, G. Xiao, J. C. Slonczewski, P. L. Trouilloud, and R. H. Koch, *Role of electron scattering in the magnetization relaxation of thin $Ni_{81}Fe_{19}$ films*, Phys. Rev. B **66**, 214416 (2002).

[95] International Crystal Laboratories, *CdMnTe - Verdet Constant Brochure*, Oct 2013.

[96] Y. Izumi, M. Tanabe, A. Imazu, A. Mimoto, M. Tanaka, A. Agui, T. Muro, and K. Nakagawa, *Characteristic oxygen K-edge circular dichroism spectra of amino acid films by improved measurement technique*, J. Chem. Phys. **138**, 074305 (2013).

[97] S. Jahn, M. Margraf, V. Habchi, and R. Jacob, *Qucs - Technical Papers.* qucs.sourceforge.net, (2007).

[98] M. Jamali, J. H. Kwon, S.-M. Seo, K.-J. Lee, and H. Yang, *Spin wave nonreciprocity for logic device applications*, Sci. Rep. **3**, 3160 (2013).

[99] A. V. Jausovec, G. Xiong, and R. P. Cowburn, *Stability of magnetization states in submicron Permalloy disks*, J. Appl. Phys. **99**, 08B103 (2006).

[100] R. I. Joseph and E. Schlömann, *Demagnetizing Field in Nonellipsoidal Bodies*, J. Appl. Phys. **36**, 1579 (1965).

[101] H. Jung, Y.-S. Yu, K.-S. Lee, M.-Y. Im, P. Fischer, L. Bocklage, A. Vogel, M. Bolte, G. Meier, and S.-K. Kim, *Observation of coupled vortex gyrations by 70-ps-time- and 20-nm-space-resolved full-field magnetic transmission soft x-ray microscopy*, Appl. Phys. Lett. **97**, 222502 (2010).

[102] M. I. Kaganov, N. B. Pustyl'nik, and T. I. Shalaeva, *Magnons, magnetic polaritons, magnetostatic waves*, Physics-Uspekhi **40**, 181 (1997).

[103] A. Kaidatzis and J. M. García-Martín, *Torsional resonance mode magnetic force microscopy: enabling higher lateral resolution magnetic imaging without topography-related effects*, Nanotechnology **24**, 165704 (2013). Figure 2.1 contains material from this article reprinted with kind permission from Andreas Kaidatzis. Copyright ©IOP Publishing. Reproduced with permission. All rights reserved. Online article: dx.doi.org/10.1088/0957-4484/24/16/165704.

[104] B. A. Kalinikos and A. N. Slavin, *Theory of dipole-exchange spin wave spectrum for ferromagnetic films with mixed exchange boundary conditions*, J. Phys. C: Solid State Phys. **19**, 7013 (1986).

[105] T. Kamionka, M. Martens, K. W. Chou, M. Curcic, A. Drews, G. Schütz, T. Tyliszczak, H. Stoll, B. Van Waeyenberge, and G. Meier, *Magnetic Antivortex-Core Reversal by Circular-Rotational Spin Currents*, Phys. Rev. Lett. **105**, 137204 (2010).

[106] T. Kampfrath, M. Battiato, P. Maldonado, G. Eilers, J. Nötzold, S. Mährlein, V. Zbarsky, F. Freimuth, Y. Mokrousov, S. Blügel, M. Wolf, I. Radu, P. M. Oppeneer, and M. Münzenberg, *Terahertz spin current pulses controlled by magnetic heterostructures*, Nat. Nanotechnol. **8**, 256 (2013).

[107] T. Kampfrath, R. G. Ulbrich, F. Leuenberger, M. Münzenberg, B. Sass, and W. Felsch, *Ultrafast magneto-optical response of iron thin films*, Phys. Rev. B **65**, 104429 (2002).

[108] J. Kerr, *XLIII. On rotation of the plane of polarization by reflection from the pole of a magnet*, Philos. Mag. Series 5 **3**, 321 (1877).

[109] ——, *XXIV. On reflection of polarized light from the equatorial surface of a magnet*, Philos. Mag. Series 5 **5**, 161 (1878).

[110] A. A. Khajetoorians, J. Wiebe, B. Chilian, and R. Wiesendanger, *Realizing All-Spin-Based Logic Operations Atom by Atom*, Science **332**, 1062 (2011).

[111] A. Khitun, M. Bao, J.-Y. Kim, A. Hong, A. P. Jacob, and K. Wang, *Logic Devices with Spin Wave Buses: Potential Advantages and Shortcoming*, Device Research Conference 2008, 159 (2008).

[112] A. Khitun, M. Bao, Y. Wu, J.-Y. Kim, A. Hong, A. P. Jacob, K. Galatsis, and K. L. Wang, *Logic Devices with Spin Wave Buses - an Approach to Scalable Magneto-Electric Circuitry*, MRS Online Proceedings Library **1067** (2008).

[113] D.-H. Kim, E. A. Rozhkova, I. V. Ulasov, S. D. Bader, T. Rajh, M. S. Lesniak, and V. Novosad, *Biofunctionalized magnetic-vortex microdiscs for targeted cancer-cell destruction*, Nat. Mater. **9**, 165 (2010).

[114] A. V. Kimel, A. Kirilyuk, P. A. Usachev, R. V. Pisarev, A. M. Balbashov, and T. Rasing, *Ultrafast non-thermal control of magnetization by instantaneous photomagnetic pulses*, Nature **435**, 655 (2005).

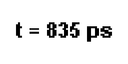

[115] A. Kirilyuk, A. V. Kimel, and T. Rasing, *Ultrafast optical manipulation of magnetic order*, Rev. Mod. Phys. **82**, 2731 (2010).

[116] P. Kirkpatrick and A. V. Baez, *Formation of Optical Images by X-Rays*, J. Opt. Soc. Am. **38**, 766 (1948).

[117] C. Kittel, *On the Theory of Ferromagnetic Resonance Absorption*, Phys. Rev. **73**, 155 (1948).

[118] C. Kittel, *Excitation of Spin Waves in a Ferromagnet by a Uniform rf Field*, Phys. Rev. **110**, 1295 (1958).

[119] T. Korn, *Time-resolved magnetization measurements on ferromagnetic films and microstructures*, PhD thesis, University of Hamburg, May 2004.

[120] M. P. Kostylev, A. A. Serga, T. Schneider, B. Leven, and B. Hillebrands, *Spin-wave logical gates*, Appl. Phys. Lett. **87**, 153501 (2005).

[121] M. Krikunova, T. Maltezopoulos, P. Wessels, M. Schlie, A. Azima, T. Gaumnitz, T. Gebert, M. Wieland, and M. Drescher, *Strong-field ionization of molecular iodine traced with XUV pulses from a free-electron laser*, Phys. Rev. A **86**, 043430 (2012).

[122] M. Krikunova, T. Maltezopoulos, P. Wessels, M. Schlie, A. Azima, M. Wieland, and M. Drescher, *Ultrafast photofragmentation dynamics of molecular iodine driven with timed XUV and near-infrared light pulses*, J. Chem. Phys. **134**, 024313 (2011).

[123] A. Krohn, *Spin-wave interference in ferromagnetic stripes and rolls*, PhD thesis, University of Hamburg, Jan 2010.

[124] A. Krohn, S. Mansfeld, J. Podbielski, J. Topp, W. Hansen, D. Heitmann, and S. Mendach, *Observation of spin-wave propagation in permalloy microstripes*. arXiv:0905.2172, (2009).

[125] B. Krüger, A. Drews, M. Bolte, U. Merkt, D. Pfannkuche, and G. Meier, *Harmonic oscillator model for current- and field-driven magnetic vortices*, Phys. Rev. B **76**, 224426 (2007).

[126] B. Krüger and D. Pfannkuche. Private communication, (2012).

[127] C. La-O-Vorakiat, E. Turgut, C. A. Teale, H. C. Kapteyn, M. M. Murnane, S. Mathias, M. Aeschlimann, C. M. Schneider, J. M. Shaw, H. T. Nembach, and T. J. Silva, *Ultrafast Demagnetization Measurements Using Extreme Ultraviolet Light: Comparison of Electronic and Magnetic Contributions*, Phys. Rev. X **2**, 011005 (2012).

[128] J. H. Lambert and E. Anding, *Lambert's Photometrie*, Lamberts Photometrie: Photometria, sive De mensura et gradibus luminus, colorum et umbrae, W. Engelmann, Leipzig, (1892).

[129] L. D. Landau and E. Lifshitz, *On the theory of the dispersion of magnetic permeability in ferromagnetic bodies*, Phys. Z. Sowjetunion **8**, 153 (1935).

[130] L. D. Landau and E. M. Lifshitz, *Electrodynamics Of Continuous Media*, Pergamon Press, Oxford / New York / Beijing / Frankfurt, second ed., (1984).

[131] I. Langmuir, *The Effect of Space Charge and Residual Gases on Thermionic Currents in High Vacuum*, Phys. Rev. **2**, 450 (1913).

[132] K.-S. Lee and S.-K. Kim, *Gyrotropic linear and nonlinear motions of a magnetic vortex in soft magnetic nanodots*, Appl. Phys. Lett. **91**, 132511 (2007).

[133] K.-S. Lee, S.-K. Kim, Y.-S. Yu, Y.-S. Choi, K. Y. Guslienko, H. Jung, and P. Fischer, *Universal Criterion and Phase Diagram for Switching a Magnetic Vortex Core in Soft Magnetic Nanodots*, Phys. Rev. Lett. **101**, 267206 (2008).

[134] Light Conversion Ltd., *ORPHEUS User's manual*, Light Conversion Ltd., Saulėtekio av. 10; LT-10223 Vilnius, Lithuania.

[135] ——, *HIRO User's manual*, Light Conversion Ltd., Saulėtekio av. 10; LT-10223 Vilnius, Lithuania, Apr 2009.

[136] ——, *PHAROS User's manual*, Light Conversion Ltd., Saulėtekio av. 10; LT-10223 Vilnius, Lithuania, Jun 2009.

[137] Z. Liu, F. Giesen, X. Zhu, R. D. Sydora, and M. R. Freeman, *Spin Wave Dynamics and the Determination of Intrinsic Damping in Locally Excited Permalloy Thin Films*, Phys. Rev. Lett. **98**, 087201 (2007).

[138] R. A. Loch, *Cesium-Telluride and Magnesium for high quality photocathodes - Preparation and diagnostics*, master's thesis, University of Twente, Jun 2005.

[139] S. Loth, S. Baumann, C. P. Lutz, D. M. Eigler, and A. J. Heinrich, *Bistability in Atomic-Scale Antiferromagnets*, Science **335**, 196 (2012).

[140] V. Magero, *Magnetic storage webpage.* bellevuecollege.edu/distance/cs110rh/IT215/week_06/6_magnetic.htm, (2003).

[141] R. J. Mannix, S. Kumar, F. Cassiola, M. Montoya-Zavala, E. Feinstein, M. Prentiss, and D. E. Ingber, *Nanomagnetic actuation of receptor-mediated signal transduction*, Nat. Nanotechnol. **3**, 36 (2008).

[142] S. Mansfeld, *Zeitaufgelöste Kerr-Mikroskopie an zweidimensionalen Mikrostrukturen bei dynamischer Anregung mit hochfrequenten Wechselströmen*, master's thesis, University of Hamburg, Jan 2008.

[143] S. Mansfeld, J. Topp, K. Martens, J. N. Toedt, W. Hansen, D. Heitmann, and S. Mendach, *Spin Wave Diffraction and Perfect Imaging of a Grating*, Phys. Rev. Lett. **108**, 047204 (2012).

[144] S. Martens, O. Albrecht, K. Nielsch, and D. Görlitz, *Local modes and two magnon scattering in ordered permalloy antidot arrays*, J. Appl. Phys. **105**, 07C113 (2009).

[145] J. C. Maxwell, *A Dynamical Theory of the Electromagnetic Field*, Philos. Trans. Roy. Soc. London **155**, 459 (1865).

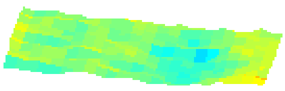

[146] M. Mazziotta, *Electron-hole pair creation energy and Fano factor temperature dependence in silicon*, Nucl. Instrum. Methods Phys. Res., Sect. A **584**, 436 (2008).

[147] A. Meents, B. Reime, M. Kaiser, X.-Y. Wang, R. Abela, E. Weckert, and C. Schulze-Briese, *A fast X-ray chopper for single-bunch extraction at synchrotron sources*, J. Appl. Crystallogr. **42**, 901 (2009).

[148] S. Melle, J. L. Menéndez, G. Armelles, D. Navas, M. Vázquez, K. Nielsch, R. B. Wehrspohn, and U. Gösele, *Magneto-optical properties of nickel nanowire arrays*, Appl. Phys. Lett. **83**, 4547 (2003).

[149] R. A. Millikan, *A Direct Photoelectric Determination of Planck's h*, Phys. Rev. **7**, 355 (1916).

[150] G. M. Müller, G. Eilers, Z. Wang, M. Scherff, R. Ji, K. Nielsch, C. A. Ross, and M. Münzenberg, *Magnetization dynamics in optically excited nanostructured nickel films*, New J. Phys. **10**, 123004 (2008).

[151] T. Nakajyo, J. Yang, F. Sakai, and Y. Aoki, *Quantum Efficiencies of Mg Photocathode under Illumination with 3rd and 4th Harmonics Nd:LiYF$_4$ Laser Light in RF Gun*, Jpn. J. Appl. Phys. **42**, 1470 (2003).

[152] G. Neuber, R. Rauer, J. Kunze, T. Korn, C. Pels, G. Meier, U. Merkt, J. Bäckström, and M. Rübhausen, *Temperature-dependent spectral generalized magneto-optical ellipsometry*, Appl. Phys. Lett. **83**, 4509 (2003).

[153] A. Neumann. Private communication, (2010).

[154] K. Nielsch, *Hochgeordnete ferromagnetische Nano-Stabensembles: Elektrochemische Herstellung und magnetische Charakterisierung*, PhD thesis, Martin Luther University Halle-Wittenberg, Feb 2002.

[155] V. Novosad, F. Y. Fradin, P. E. Roy, K. S. Buchanan, K. Y. Guslienko, and S. D. Bader, *Magnetic vortex resonance in patterned ferromagnetic dots*, Phys. Rev. B **72**, 024455 (2005).

[156] T. Ostler, J. Barker, R. Evans, R. Chantrell, U. Atxitia, O. Chubykalo-Fesenko, S. El Moussaoui, L. Le Guyader, E. Mengotti, L. Heyderman, F. Nolting, A. Tsukamoto, A. Itoh, D. Afanasiev, B. Ivanov, A. Kalashnikova, K. Vahaplar, J. Mentink, A. Kirilyuk, T. Rasing, and A. Kimel, *Ultrafast heating as a sufficient stimulus for magnetization reversal in a ferrimagnet*, Nat. Commun. **3**, 666 (2012).

[157] J. Overbuschmann, J. Hengster, S. Irsen, and T. Wilhein, *Fabrication of Fresnel zone plates by ion-beam lithography and application as objective lenses in extreme ultraviolet microscopy at 13 nm wavelength*, Opt. Lett. **37**, 5100 (2012).

[158] G. H. Owyang and T. Wu, *The approximate parameters of slot lines and their complement*, IRE Trans. Antennas Propag. **6**, 49 (1958).

[159] Q. A. Pankhurst, N. T. K. Thanh, S. K. Jones, and J. Dobson, *Progress in applications of magnetic nanoparticles in biomedicine*, J. Phys. D: Appl. Phys. **42**, 224001 (2009).

[160] S. S. P. Parkin, M. Hayashi, and L. Thomas, *Magnetic Domain-Wall Racetrack Memory*, Science **320**, 190 (2008).

[161] K. Perzlmaier, G. Woltersdorf, and C. H. Back, *Observation of the propagation and interference of spin waves in ferromagnetic thin films*, Phys. Rev. B **77**, 054425 (2008).

[162] B. Pfau, S. Schaffert, L. Müller, C. Gutt, A. Al-Shemmary, F. Büttner, R. Delaunay, S. Düsterer, S. Flewett, R. Frömter, J. Geilhufe, E. Guehrs, C. Günther, R. Hawaldar, M. Hille, N. Jaouen, A. Kobs, K. Li, J. Mohanty, H. Redlin, W. Schlotter, D. Stickler, R. Treusch, B. Vodungbo, M. Kläui, H. Oepen, J. Lüning, G. Grübel, and S. Eisebitt, *Ultrafast optical demagnetization manipulates nanoscale spin structure in domain walls*, Nat. Commun. **3**, 1100 (2012).

[163] M. Planck, *Ueber das Gesetz der Energieverteilung im Normalspectrum*, Ann. Phys. (Berlin) **309**, 553 (1901).

[164] Princeton Instruments, *Direct detection of X-rays (30 eV to 20 keV) using detectors based on CCD technology*, Princeton Instruments, 3660 Quakerbridge Road, Trenton, NJ 08619 USA, technical note #1 ed., (2010).

[165] ——, *PIXIS-XF: 1024 Data Sheet*, Princeton Instruments, 3660 Quakerbridge Road, Trenton, NJ 08619 USA, (2010).

[166] ——, *Signal-to-Noise Ratio.* princetoninstruments.com/cms/index.php/ccd-primer/172-signal-to-noise-ratio, Dec 2011.

[167] Z. Q. Qiu and S. D. Bader, *Surface magneto-optic Kerr effect*, Rev. Sci. Instrum. **71**, 1243 (2000).

[168] I. Radu, K. Vahaplar, C. Stamm, T. Kachel, N. Pontius, H. A. Dürr, T. A. Ostler, J. Barker, R. F. L. Evans, R. W. Chantrell, A. Tsukamoto, A. Itoh, A. Kirilyuk, T. Rasing, and A. V. Kimel, *Transient ferromagnetic-like state mediating ultrafast reversal of antiferromagnetically coupled spins*, Nature **472**, 205 (2011).

[169] J. Åkerman, *Toward a Universal Memory*, Science **308**, 508 (2005).

[170] M. Rini, R. Tobey, N. Dean, J. Itatani, Y. Tomioka, Y. Tokura, R. W. Schoenlein, and A. Cavalleri, *Control of the electronic phase of a manganite by mode-selective vibrational excitation*, Nature **449**, 72 (2007).

[171] N. Romming, C. Hanneken, M. Menzel, J. E. Bickel, B. Wolter, K. von Bergmann, A. Kubetzka, and R. Wiesendanger, *Writing and Deleting Single Magnetic Skyrmions*, Science **341**, 636 (2013).

[172] W. C. Röntgen, *Über eine neue Art von Strahlen.* Sitzungsberichte der Würzburger Physik.-medic. Gesellschaft, Dec 1895.

[173] ——, *Über eine neue Art von Strahlen*, Ann. Phys. (Berlin) **300**, 1 (1898).

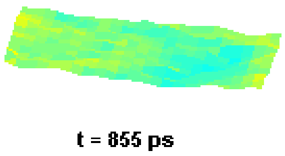

[174] C. Ross, *Patterned magnetic recording media*, Annu. Rev. Mater. Res. **31**, 203 (2001).

[175] D. Rudolf, C. La-O-Vorakiat, M. Battiato, R. Adam, J. M. Shaw, E. Turgut, P. Maldonado, S. Mathias, P. Grychtol, H. T. Nembach, T. J. Silva, M. Aeschlimann, H. C. Kapteyn, M. M. Murnane, C. M. Schneider, and P. M. Oppeneer, *Ultrafast magnetization enhancement in metallic multilayers driven by superdiffusive spin current*, Nat. Commun. **3**, 1037 (2012).

[176] R. Sbiaa and S. N. Piramanayagam, *Patterned Media Towards Nano-bit Magnetic Recording: Fabrication and Challenges*, Recent Patents on Nanotechnology **1**, 29 (2007).

[177] F. Schäfers, H.-C. Mertins, A. Gaupp, W. Gudat, M. Mertin, I. Packe, F. Schmolla, S. D. Fonzo, G. Soullié, W. Jark, R. Walker, X. L. Cann, R. Nyholm, and M. Eriksson, *Soft-X-Ray Polarimeter with Multilayer Optics: Complete Analysis of the Polarization State of Light*, Appl. Opt. **38**, 4074 (1999).

[178] M. Schlie, *Time-resolved Studies at PETRA III with a Highly Repetitive Synchronized Laser System*, PhD thesis, University of Hamburg, Sep 2013.

[179] E. Schlömann, *A Sum Rule Concerning the Inhomogeneous Demagnetizing Field in Nonellipsoidal Samples*, J. Appl. Phys. **33**, 2825 (1962).

[180] G. Schütz, W. Wagner, W. Wilhelm, P. Kienle, R. Zeller, R. Frahm, and G. Materlik, *Absorption of circularly polarized x rays in iron*, Phys. Rev. Lett. **58**, 737 (1987).

[181] T. Shinjo, T. Okuno, R. Hassdorf, K. Shigeto, and T. Ono, *Magnetic Vortex Core Observation in Circular Dots of Permalloy*, Science **289**, 930 (2000).

[182] P. Siffalovic, E. Majkova, L. Chitu, M. Jergel, S. Luby, I. Capek, A. Satka, A. Timmann, and S. V. Roth, *Real-Time Tracking of Superparamagnetic Nanoparticle Self-Assembly*, Small **4**, 2222 (2008). Figure 2.1 contains material reprinted with kind permission from this article. Copyright ©2008, Wiley-VCH Verlag GmbH & Co. KGaA, Weinheim. Online article: dx.doi.org/10.1002/smll.200800353.

[183] J. L. Soret, *Über die durch Kreisgitter erzeugten Diffractionsphänomene*, Ann. Phys. (Berlin) **232**, 99 (1875).

[184] T. Srinivasan-Rao, J. Fischer, and T. Tsang, *Photoemission studies on metals using picosecond ultraviolet laser pulses*, J. Appl. Phys. **69**, 3291 (1991).

[185] T. Srinivasan-Rao, J. Schill, I. B. Zvi, and M. Woodle, *Sputtered magnesium as a photocathode material for rf injectors*, Rev. Sci. Instrum. **69**, 2292 (1998).

[186] C. Stamm, T. Kachel, N. Pontius, R. Mitzner, T. Quast, K. Holldack, S. Khan, C. Lupulescu, E. F. Aziz, M. Wietstruk, H. A. Dürr, and W. Eberhardt, *Femtosecond modification of electron localization and transfer of angular momentum in nickel*, Nat. Mater. **6**, 740 (2007).

[187] C. D. Stanciu, F. Hansteen, A. V. Kimel, A. Kirilyuk, A. Tsukamoto, A. Itoh, and T. Rasing, *All-Optical Magnetic Recording with Circularly Polarized Light*, Phys. Rev. Lett. **99**, 047601 (2007). Figure 2.1 contains material from this article reprinted with kind permission from Daniel Stanciu. Copyright ©2007 by the American Physical Society. Online abstract: link.aps.org/abstract/PRL/v99/p047601.

[188] S. E. Stevenson, C. Moutafis, G. Heldt, R. V. Chopdekar, C. Quitmann, L. J. Heyderman, and J. Raabe, *Dynamic stabilization of nonequilibrium domain configurations in magnetic squares with high amplitude excitations*, Phys. Rev. B **87**, 054423 (2013).

[189] J. Stöhr, *Exploring the microscopic origin of magnetic anisotropies with X-ray magnetic circular dichroism (XMCD) spectroscopy*, J. Magn. Magn. Mater. **200**, 470 (1999).

[190] J. Stöhr, H. Padmore, S. Anders, T. Stammler, and M. Scheinfein, *Principles of X-ray magnetic dichroism spectromicroscopy*, Surf. Rev. Lett. **5**, 1297 (1998).

[191] J. Stöhr and H. C. Siegmann, *Magnetism: From Fundamentals to Nanoscale Dynamics*, Springer, Berlin Heidelberg, first ed., (2006). Figure 2.14b reprinted from this book. With kind permission from Joachim Stöhr and Springer Science and Business Media. Online eBook chapter: dx.doi.org/10.1007/978-3-540-30283-4_10.

[192] D. Strickland and G. Mourou, *Compression of amplified chirped optical pulses*, Opt. Commun. **56**, 219 (1985).

[193] C. Sun, J. S. Lee, and M. Zhang, *Magnetic nanoparticles in MR imaging and drug delivery*, Adv. Drug Delivery Rev. **60**, 1252 (2008). Inorganic Nanoparticles in Drug Delivery.

[194] A. A. Thiele, *Steady-State Motion of Magnetic Domains*, Phys. Rev. Lett. **30**, 230 (1973).

[195] A. C. Thompson, D. T. Attwood, E. M. Gullikson, M. R. Howells, K.-J. Kim, J. Kirz, J. B. Kortright, I. Lindau, Y. Liu, P. Pianetta, A. R. Robinson, J. H. Scofield, J. H. Underwood, G. P. Williams, and H. Winick, *X-Ray Data Booklet*, Lawrence Berkeley National Laboratory, University of California, Berkeley, California 94720, third ed., Sep 2009.

[196] J.-N. Tödt. Private communication, (2013).

[197] I. Tudosa, C. Stamm, A. B. Kashuba, F. King, H. C. Siegmann, J. Stöhr, G. Ju, B. Lu, and D. Weller, *The ultimate speed of magnetic switching in granular recording media*, Nature **428**, 831 (2004).

[198] E. Turgut, C. La-o vorakiat, J. M. Shaw, P. Grychtol, H. T. Nembach, D. Rudolf, R. Adam, M. Aeschlimann, C. M. Schneider, T. J. Silva,

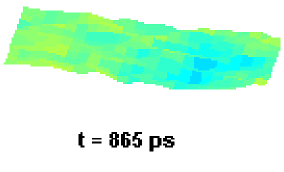

M. M. Murnane, H. C. Kapteyn, and S. Mathias, *Controlling the Competition between Optically Induced Ultrafast Spin-Flip Scattering and Spin Transport in Magnetic Multilayers*, Phys. Rev. Lett. **110**, 197201 (2013).

[199] V. Uhlíř, M. Urbianek, L. Hladiik, J. Spousta, M.-Y. Im, P. Fischer, N. Eibagi, J. J. Kan, E. E. Fullerton, and T. Šikola, *Dynamic switching of the spin circulation in tapered magnetic nanodisks*, Nat. Nanotechnol. **8**, 341 (2013).

[200] University of Hamburg (Group of Prof. Dr. Roland Wiesendanger), *Nanoscience.de Homepage.* nanoscience.de, Dez 2013. Figure 2.1 contains material from this website reprinted with kind permission from the group of Prof. Dr. Roland Wiesendanger, University of Hamburg.

[201] B. Van Waeyenberge, A. Puzic, H. Stoll, K. W. Chou, T. Tyliszczak, R. Hertel, M. Fähnle, H. Brückl, K. Rott, G. Reiss, I. Neudecker, D. Weiss, C. H. Back, and G. Schütz, *Magnetic vortex core reversal by excitation with short bursts of an alternating field*, Nature **444**, 461 (2006).

[202] J. Viefhaus, F. Scholz, S. Deinert, L. Glaser, M. Ilchen, J. Seltmann, P. Walter, and F. Siewert, *The Variable Polarization XUV Beamline P04 at PETRA III: Optics, mechanics and their performance*, Nucl. Instrum. Methods Phys. Res., Sect. A **710**, 151 (2013). Figure 4.14 reprinted from this publication with kind permission from Jens Viefhaus. Copyright ©2013, with permission from Elsevier. Online journal: www.sciencedirect.com/science/journal/01689002.

[203] B. Vodungbo, J. Gautier, G. Lambert, A. B. Sardinha, M. Lozano, S. Sebban, M. Ducousso, W. Boutu, K. Li, B. Tudu, M. Tortarolo, R. Hawaldar, R. Delaunay, V. Liopez-Flores, J. Arabski, C. Boeglin, H. Merdji, P. Zeitoun, and J. Lüning, *Laser-induced ultrafast demagnetization in the presence of a nanoscale magnetic domain network*, Nat. Commun. **3**, 999 (2012).

[204] A. Vogel. Private communication, (2012).

[205] A. Vogel, T. Kamionka, M. Martens, A. Drews, K. W. Chou, T. Tyliszczak, H. Stoll, B. Van Waeyenberge, and G. Meier, *Coupled Vortex Oscillations in Spatially Separated Permalloy Squares*, Phys. Rev. Lett. **106**, 137201 (2011).

[206] A. Vogel, S. Wintz, T. Gerhardt, L. Bocklage, T. Strache, M.-Y. Im, P. Fischer, J. Fassbender, J. McCord, and G. Meier, *Field- and current-induced domain-wall motion in permalloy nanowires with magnetic soft spots*, Appl. Phys. Lett. **98**, 202501 (2011).

[207] U. Vogt, M. Lindblom, P. Charalambous, B. Kaulich, and T. Wilhein, *Condenser for Koehler-like illumination in transmission x-ray microscopes at undulator sources*, Opt. Lett. **31**, 1465 (2006).

[208] W. Voigt, *Magneto- und Elektrooptik*, B. G. Teubner, Poststraße 3, Leipzig, first ed., (1908).

[209] A. Wachowiak, J. Wiebe, M. Bode, O. Pietzsch, M. Morgenstern, and R. Wiesendanger, *Direct Observation of Internal Spin Structure of Magnetic Vortex Cores*, Science **298**, 577 (2002).

[210] L. R. Walker, *Magnetostatic Modes in Ferromagnetic Resonance*, Phys. Rev. **105**, 390 (1957).

[211] M. Weigand, B. Van Waeyenberge, A. Vansteenkiste, M. Curcic, V. Sackmann, H. Stoll, T. Tyliszczak, K. Kaznatcheev, D. Bertwistle, G. Woltersdorf, C. H. Back, and G. Schütz, *Vortex Core Switching by Coherent Excitation with Single In-Plane Magnetic Field Pulses*, Phys. Rev. Lett. **102**, 077201 (2009).

[212] C. Wen, *Coplanar Waveguide: A Surface Strip Transmission Line Suitable for Nonreciprocal Gyromagnetic Device Applications*, IEEE T. Microw. Theory **17**, 1087 (1969).

[213] G. Wentzel, *Über strahlungslose Quantensprünge*, Z. Phys. A **43**, 524 (1927).

[214] P. Wessels, J. Ewald, M. Wieland, T. Nisius, G. Abbati, S. Baumbach, J. Overbuschmann, A. Vogel, A. Neumann, J. Viefhaus, H. P. Oepen, G. Meier, T. Wilhein, and M. Drescher, *Time-resolved soft X-ray microscopy of magnetic nanostructures at the P04 beamline at PETRA III*, J. Phys.: Conf. Ser. **499**, 012009 (2014).

[215] P. Wessels, M. Schlie, M. Wieland, J. Ewald, G. Abbati, S. Baumbach, J. Overbuschmann, T. Nisius, A. Vogel, A. Neumann, A. Meents, J. Viefhaus, H. P. Oepen, G. Meier, T. Wilhein, and M. Drescher, *XMCD microscopy with synchronized soft X-ray and laser pulses at PETRA III for time-resolved studies*, J. Phys.: Conf. Ser. **463**, 012023 (2013).

[216] M. Wieland, C. Spielmann, U. Kleineberg, T. Westerwalbesloh, U. Heinzmann, and T. Wilhein, *Toward time-resolved soft X-ray microscopy using pulsed fs-high-harmonic radiation*, Ultramicroscopy **102**, 93 (2005).

[217] T. Wilhein, S. Rehbein, D. Hambach, M. Berglund, L. Rymell, and H. M. Hertz, *A slit grating spectrograph for quantitative soft x-ray spectroscopy*, Rev. Sci. Instrum. **70**, 1694 (1999). Figure 5.6 reprinted with permission from this article. Copyright ©1999, AIP Publishing LLC. Online article: dx.doi.org/10.1063/1.1149653.

[218] S. A. Wolf, D. D. Awschalom, R. A. Buhrman, J. M. Daughton, S. von Molniar, M. L. Roukes, A. Y. Chtchelkanova, and D. M. Treger, *Spintronics: A Spin-Based Electronics Vision for the Future*, Science **294**, 1488 (2001).

[219] L. F. Yin, D. H. Wei, N. Lei, L. H. Zhou, C. S. Tian, G. S. Dong, X. F. Jin, L. P. Guo, Q. J. Jia, and R. Q. Wu, *Magnetocrystalline Anisotropy in Permalloy Revisited*, Phys. Rev. Lett. **97**, 067203 (2006).

[220] S. Yu, G. Santoro, K. Sarkar, B. Dicke, P. Wessels, S. Bommel, R. Döhrmann, J. Perlich, M. Kuhlmann, E. Metwalli, J. F. H. Risch,

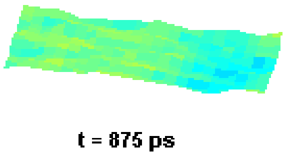

M. Schwartzkopf, M. Drescher, P. Müller-Buschbaum, and S. V. Roth, *Formation of Al Nanostructures on Alq3: An in Situ Grazing Incidence Small Angle X-ray Scattering Study during Radio Frequency Sputter Deposition*, J. Phys. Chem. Lett. **4**, 3170 (2013).

[221] Z. M. Yusof, M. E. Conde, and W. Gai, *Schottky-Enabled Photoemission in a rf Accelerator Photoinjector: Possible Generation of Ultralow Transverse Thermal-Emittance Electron Beam*, Phys. Rev. Lett. **93**, 114801 (2004).

[222] J. Zak, E. R. Moog, C. Liu, and S. D. Bader, *Universal approach to magneto-optics*, J. Magn. Magn. Mater. **89**, 107 (1990).

[223] J. Zak, E. R. Moog, C. Liu, and S. D. Bader, *Magneto-optics of multilayers with arbitrary magnetization directions*, Phys. Rev. B **43**, 6423 (1991).

[224] ——, *Erratum: Magneto-optics of multilayers with arbitrary magnetization directions*, Phys. Rev. B **46**, 5883 (1992).

[225] A. H. Zewail, *Femtochemistry: Atomic-Scale Dynamics of the Chemical Bond Using Ultrafast Lasers (Nobel Lecture)*, Angew. Chem. Int. Ed. **39**, 2586 (2000).